

***J/ψ Production and Suppression in Au+Au Collisions at***

**$\sqrt{s_{NN}}=200$  GeV**

by

**Matthew Gerad Wysocki**

B.S., University of Notre Dame, 2003

A thesis submitted to the

Faculty of the Graduate School of the

University of Colorado in partial fulfillment

of the requirements for the degree of

Doctor of Philosophy

Department of Physics

2011

This thesis entitled:  
 $J/\psi$  Production and Suppression in Au+Au Collisions at  $\sqrt{s_{NN}}=200$  GeV  
written by Matthew Gerard Wysocki  
has been approved for the Department of Physics

---

James Nagle

---

Ed Kinney

---

John Cumalat

---

Oliver DeWolfe

---

Andrew Hamilton

Date \_\_\_\_\_

The final copy of this thesis has been examined by the signatories, and we find that both the content and the form meet acceptable presentation standards of scholarly work in the above mentioned discipline.

Wysocki, Matthew Gerad (Ph.D., Physics)

$J/\psi$  Production and Suppression in Au+Au Collisions at  $\sqrt{s_{NN}}=200$  GeV

Thesis directed by Prof. James Nagle

In high-energy heavy ion collisions a partonic state of matter known as the quark-gluon plasma is expected to be formed. The suppression of  $J/\psi$  meson production in high-energy heavy ion collisions is expected to be a strong signature for the formation of the quark-gluon plasma, due to Debye screening of the quark-antiquark potential. To investigate the state of matter produced in Au+Au collisions at  $\sqrt{s_{NN}}=200$  GeV at the PHENIX experiment, we have analyzed forward rapidity  $J/\psi \rightarrow \mu^+\mu^-$  production and find that  $J/\psi$  production is significantly suppressed in collisions at small impact parameter.

The analysis methods are presented here, as well as results for  $J/\psi$  invariant yields and nuclear modification factors as functions of impact parameter and  $J/\psi$  transverse momentum. The results are compared to previous  $J/\psi$  measurements in heavy ion collisions, as well as to current theoretical models, and the implications for our understanding of  $J/\psi$  production and suppression in heavy ion collisions are discussed.

## Dedication

To my family, without whom I could not have accomplished any of this, and especially Grandpa Wysocki, who shared his love of science with me.

"The scientist does not study nature because it is useful; he studies it because he delights in it, and he delights in it because it is beautiful. If nature were not beautiful, it would not be worth knowing, and if nature were not worth knowing, life would not be worth living."

-Henri Poincaré

"Happy is he who gets to know the reasons for things."

-Virgil, *Georgics*

## Acknowledgements

I would like to take this opportunity to thank all those who made this work possible. There are many more people I should thank than I could possibly fit on one page, so apologies to those I have missed.

Many thanks to my advisor Jamie Nagle, a consummate scientist and exceptional mentor. You set the bar high enough that we all have to strive for it, but that's how excellence is brought about. Your passion for the truth and your unflagging dedication to searching it out is an example I can only hope to match.

To all of the post-docs that have guided me along the way, including Sean Kelly, Abby Bickley, Andy Glenn, Alex Linden Levy, and Mike McCumber. To Andrew Adare for putting up with me as a roommate, asking all the right questions, and being a friend when I needed one. And thanks to all of the other CU students I've helped and who have helped me over the years.

To Chun Zhang, for being my cubicle-mate, friend, and answerer of all questions at BNL, and to the BNL DAQ Group for showing me a whole new side to being an experimental physicist.

To Howard, Anne, and the rest of the Group, for giving me myself back when I needed it most.

And finally, I am eternally grateful to my parents, who encouraged my education and endeavors at every turn, and have never wavered in their love and support. Many thanks to my sister, who alternately keeps me grounded or lifts me up as needed. To Grandpa Wysocki, whose scientific curiosity is as infectious as it is boundless. And to the entire rest of my family, I wouldn't be where I am without all of you.

## Contents

### Chapter

<b>1</b>	<b>Introduction</b>	<b>1</b>
1.1	High Temperature QCD Matter . . . . .	4
<b>2</b>	<b>Charmonia and the <math>J/\psi</math></b>	<b>9</b>
2.1	$J/\psi$ Production Mechanisms . . . . .	10
2.2	$J/\psi$ s as probes of the QGP . . . . .	16
2.3	Cold Nuclear Matter . . . . .	18
2.3.1	SPS $p+A$ Measurements . . . . .	21
2.3.2	PHENIX $d+\text{Au}$ Measurements . . . . .	22
2.4	$A+A$ Collisions . . . . .	24
2.4.1	NA50 Pb+Pb Program . . . . .	24
2.4.2	PHENIX Au+Au Program . . . . .	26
2.4.3	$J/\psi$ Regeneration . . . . .	27
2.4.4	Sequential Charm Dissociation . . . . .	28
2.4.5	Cold Nuclear Matter Contribution . . . . .	31
2.4.6	Suppression vs. Transverse Momentum . . . . .	32
2.5	Motivation for the Current Analysis . . . . .	35
<b>3</b>	<b>Experimental Setup</b>	<b>38</b>
3.1	The Relativistic Heavy Ion Collider . . . . .	38

3.2	PHENIX . . . . .	40
3.2.1	Muon Tracker . . . . .	44
3.2.2	Muon Identifier . . . . .	46
3.2.3	Beam-Beam Counter . . . . .	48
3.2.4	The Data Acquisition System . . . . .	49
3.3	Event Reconstruction . . . . .	54
3.3.1	Collision Centrality and Number of Binary Collisions . . . . .	54
3.3.2	Track Reconstruction in the Muon Arms . . . . .	57
<b>4</b>	<b>Data Analysis</b> . . . . .	<b>61</b>
4.1	Dataset and Quality Assurance . . . . .	61
4.2	Analysis Cuts . . . . .	63
4.2.1	Event $z$ -vertex . . . . .	63
4.2.2	MUTR and MUID Track Agreement . . . . .	63
4.2.3	MUTR and MUID Number of Hits per Track . . . . .	64
4.2.4	Minimum $p_z$ . . . . .	64
4.2.5	Tracking $\chi^2/\text{ndf}$ . . . . .	64
4.2.6	Kinematic Cut . . . . .	64
4.2.7	Event Mixing Cuts . . . . .	65
4.3	Signal Extraction . . . . .	65
4.3.1	Combinatoric Background Estimation and Subtraction . . . . .	66
4.3.2	Mass Fits . . . . .	75
4.3.3	Final Values . . . . .	78
4.4	Detector Acceptance and Efficiency Correction . . . . .	81
4.4.1	Particle Generation . . . . .	81
4.4.2	PISA and Detector Response . . . . .	82
4.4.3	Time-averaged $\text{Acc} \times \text{Eff}$ . . . . .	84

<b>5</b>	<b>Experimental Uncertainties and Results</b>	<b>88</b>
5.1	Systematic Uncertainties . . . . .	88
5.1.1	Signal Extraction (Type A and B) . . . . .	88
5.1.2	Acceptance (Type B) . . . . .	89
5.1.3	Acceptance Input Distributions (Type B) . . . . .	91
5.1.4	MUTR and MUID Efficiencies (Type B) . . . . .	91
5.1.5	Monte Carlo and Data Matching (Type B) . . . . .	92
5.1.6	North/South Matching (Type B) . . . . .	92
5.1.7	Number of Binary Collisions (Type B or C) . . . . .	93
5.1.8	$p+p$ Reference Data . . . . .	93
5.2	Invariant Yields . . . . .	95
5.3	Nuclear Modification Factor $R_{AA}$ . . . . .	99
<b>6</b>	<b>Comparison to Theoretical Models and Discussion</b>	<b>104</b>
6.1	Model Comparisons vs. Centrality . . . . .	104
6.2	Model Comparisons vs. Transverse Momentum . . . . .	108
<b>7</b>	<b>Summary and Outlook</b>	<b>113</b>
<b>Bibliography</b>		<b>116</b>
<b>Appendix</b>		
<b>A</b>	<b>Tables</b>	<b>120</b>
A.1	Signal Tables . . . . .	120
A.2	Acc $\times$ Eff Tables . . . . .	135
A.3	Invariant Yield Tables . . . . .	141
A.4	$R_{AA}$ Tables . . . . .	147



## Tables

### Table

2.1	Several charmonia states, with their masses, binding energies, and spin states. . . . .	9
2.2	A comparison of the screening radius $\lambda_D$ and the Bohr radius of the $J/\psi$ . . . . .	18
3.1	RHIC Running Periods . . . . .	40
3.2	Orientations of the stereo planes . . . . .	46
3.3	Largest DCM average packet sizes and RMS values at the end of Run 7 . . . . .	54
3.4	Mean $N_{\text{part}}$ , $N_{\text{coll}}$ , and impact parameter from Glauber simulation . . . . .	58
4.1	Mass Fit Parameters . . . . .	76
4.2	Fit parameters for the low-mass vector mesons. . . . .	78
4.3	Pythia $J/\psi$ s generated for embedding in real data. . . . .	82
4.4	Reference runs and their corresponding periods . . . . .	85
5.1	Systematic Uncertainties for invariant yields and $R_{\text{AA}}$ . . . . .	89
5.2	Run 5 $p+p$ invariant yields as a function of $p_{\text{T}}$ . . . . .	100
A.1	$J/\psi$ signal in 10% centrality bins . . . . .	120
A.2	$J/\psi$ signal in 5% centrality bins . . . . .	121
A.3	$J/\psi$ signal in 20% centrality and 1 GeV/c $p_{\text{T}}$ bins . . . . .	122
A.4	$J/\psi$ signal RMS variation, listed in 10% and 5% centrality bins . . . . .	123
A.5	$J/\psi$ signal RMS variation, listed in 20% centrality and 1 GeV/c $p_{\text{T}}$ bins. . . . .	124

A.6 $J/\psi$ signal/background in 10% and 5% centrality bins . . . . .	125
A.7 $J/\psi$ signal/background in 20% centrality and 1 GeV/c $p_T$ bins . . . . .	126
A.8 Comparison of $J/\psi$ signal summed across bins . . . . .	126
A.9 Subtracted ++ and -- counts in the $J/\psi$ mass region for the South Arm vs. cent. .	127
A.10 Subtracted ++ and -- counts in the $J/\psi$ mass region for the South Arm vs. $p_T$ . .	128
A.11 Subtracted ++ and -- counts in the $J/\psi$ mass region for the North Arm vs. cent. .	129
A.12 Subtracted ++ and -- counts in the $J/\psi$ mass region for the North Arm vs. $p_T$ . .	130
A.13 $J/\psi$ signal from both mixed and like-sign subtraction in 10% and 5% centrality bins	131
A.14 $J/\psi$ signal from both mixed and like-sign subtraction in 1 GeV/c $p_T$ bins . . . . .	132
A.15 $J/\psi$ signal from both mixed and like-sign subtraction in 10% and 5% centrality bins, -30 cm < $z$ < 0 cm for South, 0 cm < $z$ < 30 cm for North . . . . .	133
A.16 $J/\psi$ signal from both mixed and like-sign subtraction in 1 GeV/c $p_T$ bins, -30 cm < $z$ < 0 cm for South, 0 cm < $z$ < 30 cm for North . . . . .	134
A.17 Acc $\times$ Eff correction factors for run-to-run variations for six reference runs . . . . .	135
A.18 $J/\psi$ embedded acc $\times$ eff as a function of centrality . . . . .	136
A.19 $J/\psi$ embedded acc $\times$ eff as a function of $p_T$ in 0-20% centrality . . . . .	137
A.20 $J/\psi$ embedded acc $\times$ eff as a function of $p_T$ in 20-40% centrality . . . . .	138
A.21 $J/\psi$ embedded acc $\times$ eff as a function of $p_T$ in 40-60% centrality . . . . .	139
A.22 $J/\psi$ embedded acc $\times$ eff as a function of $p_T$ in 60-93% centrality . . . . .	140
A.23 South Arm $J/\psi$ invariant yields vs. centrality . . . . .	141
A.24 North Arm $J/\psi$ invariant yields vs. centrality . . . . .	142
A.25 Arm-averaged $J/\psi$ Invariant Yields vs. Centrality . . . . .	143
A.26 South Arm $J/\psi$ Invariant Yields vs. $p_T$ . . . . .	144
A.27 North Arm $J/\psi$ Invariant Yields vs. $p_T$ . . . . .	145
A.28 Arm-averaged $J/\psi$ Invariant Yields vs. $p_T$ . . . . .	146
A.29 Arm-averaged $J/\psi$ $R_{AA}$ vs. Centrality . . . . .	147
A.30 Arm-averaged $J/\psi$ $R_{AA}$ vs. $p_T$ in four bins of centrality. . . . .	148

## Figures

### Figure

1.1	The fundamental constituents of matter in the Standard Model. . . . .	1
1.2	Feynman diagrams for the vertices of QED and QCD. . . . .	2
1.3	Running of $\alpha_s$ with respect to $Q^2$ . . . . .	3
1.4	QCD phase diagram of matter. . . . .	5
1.5	Energy density/ $T^4$ near the transition temperature from lattice calculations. . . . .	7
1.6	The stages of a high-energy nuclear collision. . . . .	7
2.1	Major charmonia states and decay modes . . . . .	10
2.2	Feynman diagram for the Color Singlet Model . . . . .	11
2.3	CDF $J/\psi$ cross section compared to both CSM and COM calculations . . . . .	12
2.4	$\alpha$ vs. $p_T$ as measured by CDF for prompt $J/\psi$ and $\psi'$ production. . . . .	13
2.5	Predictions from the CSM with the $s$ -channel cut, compared to experimental results. .	14
2.6	$J/\psi$ production in $p+p$ collisions at PHENIX. . . . .	15
2.7	Cartoon of a $J/\psi$ in (a) vacuum and (b) the QGP. . . . .	17
2.8	The color singlet $q\bar{q}$ free energy, calculated in (2+1)-flavor QCD on the lattice. . .	19
2.9	Ratio of gluon PDF in an $A=208$ nucleus to the gluon PDF in a proton. . . . .	20
2.10	Left: $J/\psi$ modification vs. $L$ from NA60. Right: $\sigma_{br}$ vs. $x_F$ . . . . .	21
2.11	$R_{dAu}$ as a function of rapidity and $N_{coll}$ . . . . .	23
2.12	$x_2$ vs. $y$ distributions for $2 \rightarrow 1$ and $2 \rightarrow 2$ production processes. . . . .	24

2.13	NA50 measurements of anomalous $J/\psi$ suppression in Pb+Pb collisions. . . . .	25
2.14	$J/\psi$ $R_{AA}$ in 200 GeV/u Au+Au collisions at PHENIX. . . . .	26
2.15	$J/\psi$ $R_{AA}$ from both PHENIX and NA50 with several models for comparison. . . . .	27
2.16	$J/\psi$ suppression at NA50 and PHENIX using the model of Zhao and Rapp. . . . .	28
2.17	Rapidity distributions of $J/\psi$ s with and without $J/\psi$ s from regeneration. . . . .	29
2.18	$J/\psi$ survival probability as used in Sequential Charmonium Dissociation. . . . .	29
2.19	$R_{AA}$ projections using the 2003 PHENIX $d$ +Au data. . . . .	31
2.20	Left: $N_{\text{coll}}$ and Au nucleus radial impact position for the $d$ +Au centrality classes. Right: $R_{AA}$ projections using the 2003 PHENIX $d$ +Au data. . . . .	33
2.21	PHENIX Au+Au $R_{AA}$ vs. $p_T$ at forward and mid-rapidities, in four centrality bins. .	34
2.22	$J/\psi$ dissociation temperature vs. transverse momentum in the Hot Wind model. .	35
2.23	$J/\psi$ $R_{AA}$ vs. $p_T$ as calculated by Zhao and Rapp. . . . .	36
2.24	$J/\psi$ $R_{AA}$ vs. $p_T$ in 200 GeV/u Cu+Cu collisions at STAR . . . . .	37
3.1	Aerial photograph of RHIC (top) and other accelerator facilities taken in 2010. . . .	39
3.2	PHENIX detector configuration . . . . .	41
3.3	Stopping power $\langle dE/dx \rangle$ for $\mu^+$ in copper . . . . .	43
3.4	Integrated nuclear interaction lengths of steel in the South Muon Arm . . . . .	44
3.5	Left: Magnet field lines in PHENIX. Right: Cutaway view of South MUTR. . . . .	45
3.6	PHENIX side view with distances to MUTR tracking layers included. . . . .	47
3.7	Cutaway view of MUID two-pack made up of Iarocci tubes. . . . .	47
3.8	Layout of MUID panels in the South Arm as seen from the interaction point . . . .	48
3.9	BBC Photos . . . . .	49
3.10	The data collecting portion of the PHENIX data acquisition system. . . . .	50
3.11	Layout of a DCM board with FPGA daughtercards attached . . . . .	51
3.12	Block diagram of data flow through a DCM board . . . . .	52
3.13	Comparison of DAQ performance of Run 4 vs. Run 7 . . . . .	53

3.14	The BBC charge distribution from data and the best-fit result from Glauber MC . . . . .	55
3.15	$N_{\text{part}}$ and $N_{\text{coll}}$ distributions from the Glauber MC . . . . .	56
4.1	Number of disabled MUTR channels . . . . .	62
4.2	Example unsubtracted mass distribution . . . . .	66
4.3	Example same-sign mass plots from South Arm 0-10% centrality . . . . .	69
4.4	Example same-sign mass plots from South Arm 60-70% centrality . . . . .	70
4.5	Example mass plots from South Arm 0-20% centrality, selected $p_{\text{T}}$ bins . . . . .	71
4.6	Example mass plots from South Arm 40-60% centrality, selected $p_{\text{T}}$ bins . . . . .	72
4.7	Example like-sign subtracted mass plots from South Arm 0-10% and 50-60% centrality	74
4.8	Acceptance functions used to modulate the mass fits . . . . .	76
4.9	Example subtracted mass plots with overlaid fits for selected centrality and $p_{\text{T}}$ bins .	77
4.10	Relative errors for each bin. . . . .	80
4.11	Acc $\times$ eff vs. centrality . . . . .	84
4.12	Run-by-run acc $\times$ eff for pure PYTHIA $J/\psi$ s . . . . .	86
4.13	Run-averaged acc $\times$ eff vs. centrality . . . . .	86
4.14	Run-averaged acc $\times$ eff vs. $p_{\text{T}}$ . . . . .	87
5.1	Track $\phi$ distributions from MC and data. . . . .	90
5.2	$J/\psi$ $p_{\text{T}}$ and rapidity distributions used as input to calculated acc $\times$ eff systematic . .	91
5.3	$J/\psi$ invariant yield vs. centrality in 10% bins . . . . .	96
5.4	$J/\psi$ invariant yield vs. centrality in 5% bins . . . . .	97
5.5	$J/\psi$ invariant yield vs. $p_{\text{T}}$ in four centrality bins . . . . .	98
5.6	Ratio of $J/\psi$ invariant yield in 2007 to 2004 vs. $p_{\text{T}}$ . . . . .	99
5.7	$J/\psi$ $R_{\text{AA}}$ vs. centrality in 5% bins . . . . .	101
5.8	$J/\psi$ $R_{\text{AA}}$ vs. centrality in 10% bins . . . . .	102
5.9	$J/\psi$ $R_{\text{AA}}$ vs. $p_{\text{T}}$ in four centrality bins . . . . .	103

6.1	PHENIX $J/\psi$ $R_{AA}$ vs. $N_{\text{part}}$ , compared to the Comover Interaction Model	105
6.2	Predicted $R_{AA}$ at forward rapidity for the model of Zhao and Rapp	107
6.3	Suppression curves at forward and mid-rapidity as calculated in the CGC framework	108
6.4	Predicted $R_{AA}$ vs. $p_{\text{T}}$ at forward rapidity for the model of Zhao and Rapp	109
6.5	Predicted $R_{AA}$ at mid-rapidity in the model of Kopeliovich <i>et al.</i>	110
6.6	$R_{AA}$ vs. $p_{\text{T}}$ in Cu+Cu and Au+Au collisions as calculated by Kopeliovich <i>et al.</i>	111
6.7	$R_{AA}$ vs. $p_{\text{T}}$ as calculated using the Hot Wind model in central and semi-peripheral centralities	112
7.1	Cartoon of sequential dissociation of charmonia and bottomonia	114
B.1	Subtracted dimuon spectra for 10% centrality bins.	150
B.2	Subtracted dimuon spectra for 10% centrality bins.	151
B.3	Subtracted dimuon spectra for 10% centrality bins.	152
B.4	Subtracted dimuon spectra for 10% centrality bins.	153
B.5	Subtracted dimuon spectra for 10% centrality bins.	154
B.6	Subtracted dimuon spectra for 5% centrality bins.	155
B.7	Subtracted dimuon spectra for 5% centrality bins.	156
B.8	Subtracted dimuon spectra for 5% centrality bins.	157
B.9	Subtracted dimuon spectra for 5% centrality bins.	158
B.10	Subtracted dimuon spectra for 5% centrality bins.	159
B.11	Subtracted dimuon spectra for 5% centrality bins.	160
B.12	Subtracted dimuon spectra for 5% centrality bins.	161
B.13	Subtracted dimuon spectra for 5% centrality bins.	162
B.14	Subtracted dimuon spectra for 1 $\text{GeV}/c$ $p_{\text{T}}$ bins.	163
B.15	Subtracted dimuon spectra for 1 $\text{GeV}/c$ $p_{\text{T}}$ bins.	164
B.16	Subtracted dimuon spectra for 1 $\text{GeV}/c$ $p_{\text{T}}$ bins.	165
B.17	Subtracted dimuon spectra for 1 $\text{GeV}/c$ $p_{\text{T}}$ bins.	166

B.18 Subtracted dimuon spectra for 1 $\text{GeV}/c$ $p_{\text{T}}$ bins. . . . .	167
B.19 Subtracted dimuon spectra for 1 $\text{GeV}/c$ $p_{\text{T}}$ bins. . . . .	168
B.20 Subtracted dimuon spectra for 1 $\text{GeV}/c$ $p_{\text{T}}$ bins. . . . .	169
B.21 Subtracted dimuon spectra for 1 $\text{GeV}/c$ $p_{\text{T}}$ bins. . . . .	170
B.22 Subtracted dimuon spectra for 1 $\text{GeV}/c$ $p_{\text{T}}$ bins. . . . .	171
B.23 Subtracted dimuon spectra for 1 $\text{GeV}/c$ $p_{\text{T}}$ bins. . . . .	172

## Chapter 1

### Introduction

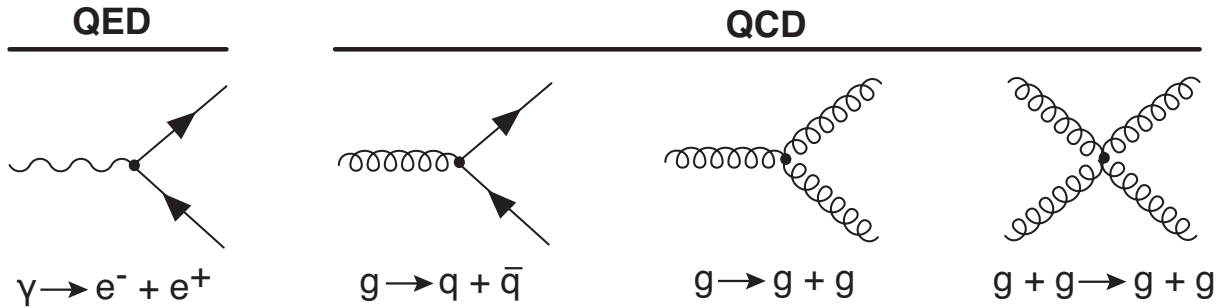
The modern Standard Model of particle physics states that the matter of the universe is made up of six flavors of quarks and six types of leptons, along with anti-particles for each of these. These fundamental particles interact via four forces: gravitational, electromagnetic, and the weak and strong nuclear interactions. The latter three are known to be mediated by photons,  $W$  and  $Z$  bosons, and gluons, respectively [1, 2]. The particles and several of their properties are shown in Figure 1.1.

Quantum field theory calculations using the Standard Model have been astoundingly accurate in describing EM and weak interactions, typically with perturbative calculations that expand in powers of  $\alpha_{EM} \sim 1/137$  and can be graphically described by Feynman diagrams.

Figure 1.1: The fundamental constituents of matter in the Standard Model. Masses taken from the Particle Data Book [3].

Quarks		Leptons		Force-carrying Bosons	
mass charge spin	1.7-3.3 MeV 2/3 1/2 <b>u</b> up	4.1-5.8 MeV -1/3 1/2 <b>d</b> down	0.511 MeV -1 1/2 <b>e</b> electron	0 0 1 <b><math>\gamma</math></b> photon	91.2 GeV 0 1 <b><math>Z^0</math></b>
1.27 GeV 2/3 1/2 <b>c</b> charm	101 MeV -1/3 1/2 <b>s</b> strange	105.66 MeV -1 1/2 <b><math>\mu</math></b> muon	0 0 1 <b><math>\nu_\mu</math></b> muon neutrino	172 GeV 0 1 <b>g</b> gluon	80.4 GeV 0 1 <b><math>W^\pm</math></b>
172 GeV 2/3 1/2 <b>t</b> top	4.19 GeV -1/3 1/2 <b>b</b> bottom	1.777 GeV -1 1/2 <b><math>\tau</math></b> tau	0 0 1 <b><math>\nu_\tau</math></b> tau neutrino		

Figure 1.2: Feynman diagrams for the vertices of QED and QCD.



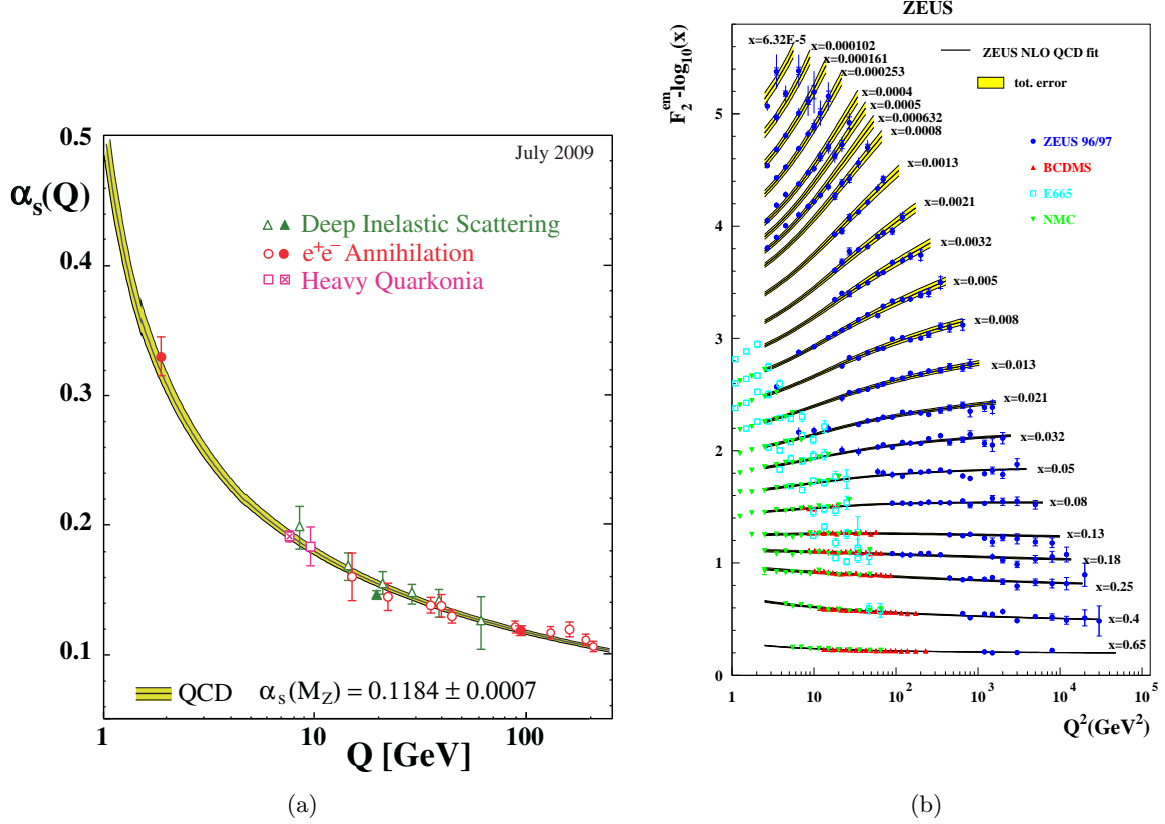
To describe the strong interaction, we turn to Quantum Chromodynamics (QCD). QCD was so named because quarks have an additional quantum number that can take three values, analogous to red-green-blue light in optics. Therefore, this quantum number is known as color charge, and the theory was given the name Chromodynamics. The quarks can be red, green, or blue, while the gluons have eight color states known as the color octet. The color-neutral singlet state is not allowed for gluons.

The quark-quark and quark-antiquark interactions induce a color charge-screening effect analogous to that found between electromagnetic charges. In the EM case, at large distance scales vacuum polarization effects screen the electric charge, and at large enough distances the effective charge is the typical value  $e$ . However, as the distance scale of the interaction goes to zero, the effects of vacuum polarization diminish and the “bare” charge is seen by the interaction.

However, in the QCD case gluons are allowed to interact with other gluons, as shown in the basic Feynman diagram vertices of Figure 1.2. This feature adds an additional term to the QCD field tensor  $F_{\mu\nu}$  compared to the EM field tensor, which leads to important physical consequences.

Contrary to the EM case described above, the introduction of gluon-gluon interactions creates an overall anti-screening effect for color charges in QCD interactions, whereby the interaction becomes **stronger** at larger distance scales. As the distance between a pair of quarks grows and the potential energy increases, it eventually becomes energetically favorable for a new quark-antiquark pair to tunnel out of the vacuum, and the original pair splits into new pairs. This is known as confinement, and this is the reason that free quarks are not observed in nature.

Figure 1.3: Running of  $\alpha_s$  with respect to  $Q^2$ , taken from [4]. The points are various measurements, while the curves represent the world average as calculated in [4], evolved over the range of  $Q^2$ .



Confinement also makes some of the traditional perturbative calculations from QED difficult or impossible in QCD. The coupling constant  $\alpha_s$  varies depending on the  $Q^2$  (momentum-transfer between particles) and distance of the interaction in question. Measurement of this “running” of  $\alpha_s$  are shown in Figure 1.3(a) along with their average extrapolated over the  $Q^2$  range. As a result, expansions in terms of  $1/\alpha_s$  may not converge quickly or at all for interactions at low energies. Additionally, unlike the mediating bosons of QED, the gluons of QCD may interact with other gluons, leading to additional terms/diagrams that must be accounted for in the perturbative expansions.

At short distance scales or large  $Q^2$ , however, the effective coupling constant becomes small enough that partons are essentially moving freely, and their interactions may be calculated with perturbation theory [5, 6]. This effect is known as **asymptotic freedom**, and the Nobel Prize in

Physics was awarded to Gross, Wilczek, and Politzer in 2004 for its discovery.

One successful application of perturbative QCD has been to the  $Q^2$ -dependence of proton structure functions. In Figure 1.3(b) the pQCD curves are overlaid on the measured values of  $F_2$  over five orders of magnitude in  $Q^2$  [7].

## 1.1 High Temperature QCD Matter

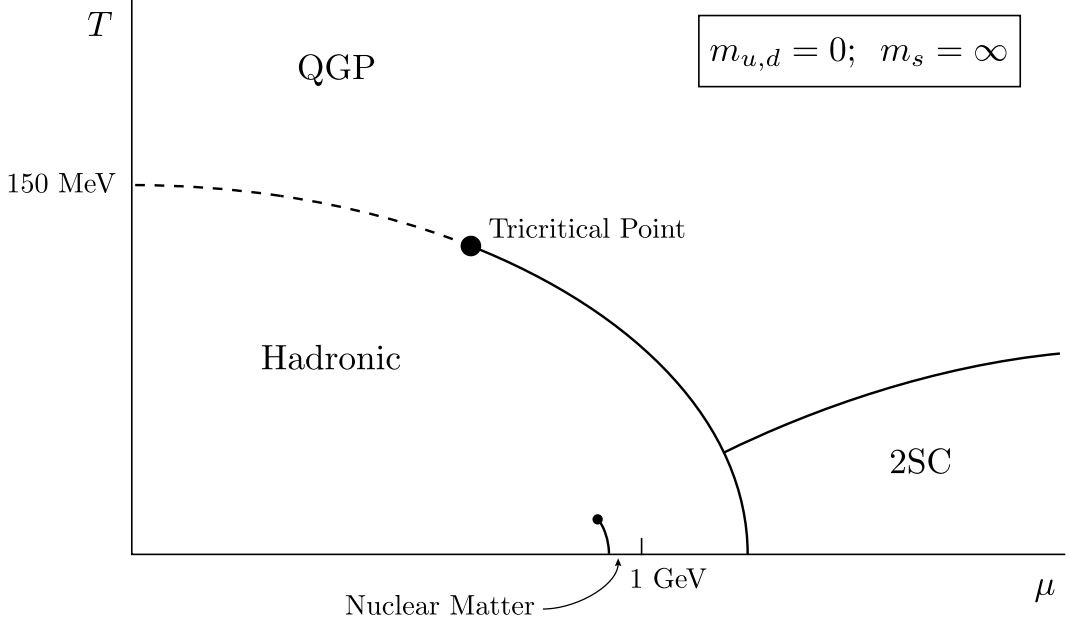
The behavior of QCD at high temperatures or densities has long been of interest. In the first few microseconds after the Big Bang, the universe would have had an enormous energy density, and hence a very high temperature. It is expected that at such temperatures the component quarks and gluons of normal hadronic matter have enough energy that they are no longer confined to their usual bound states. This results in a phase transition between normal matter and a new state, known as the Quark-Gluon Plasma (QGP) in analogy to electromagnetic plasmas in which the electrons and ions are freed of their atomic bound states. A corresponding phase diagram can be constructed, as shown in Figure 1.4, which includes normal nuclear and hadronic matter, as well as the QGP phase. In addition, other phases are expected to exist at higher net baryon chemical potential, such as in neutron stars.

Unfortunately, the QGP near the transition temperature is an inherently non-perturbative regime, and other methods must be used to perform calculations. One way around this difficulty is to perform numerical calculations using lattice QCD, which makes use of a Euclidean space-time grid to calculate the path integral of the QCD partition function. From there statistical and thermodynamic properties such as temperature and free energy can be calculated.

Recently lattice QCD has been used to examine the phase transition to a QGP. It was found that the transition temperature is  $T_c \approx 170$  MeV. This happens to lie very close to the Hagedorn temperature  $T_H \approx 160$  MeV, the limiting temperature in high-energy hadronic collisions, above which only the entropy of the thermodynamic system is increased (*i.e.* the number of hadronic states produced) [8].

In order to create such a state of matter in the laboratory, heavy nuclei are collided at

Figure 1.4: QCD phase diagram of matter.



relativistic velocities such that a portion of the large kinetic energy is converted to thermal energy. In  $\sqrt{s_{NN}}=200$  GeV/u (per nucleon) Au+Au collisions at the Relativistic Heavy Ion Collider (RHIC) at Brookhaven National Laboratory, for example, there is as much as 28.8 TeV of the 39.4 TeV total kinetic energy converted to thermal energy [9].

The temperature dependence of the energy density can be naively calculated by assuming the QGP is a Stefan-Boltzmann gas of massless, non-interacting particles [10, 11]. The partition function for fermions (+) and bosons (-) is:

$$\ln Z(T, \mu, V) = \frac{gV}{2\pi^2 T} \int_0^\infty \frac{dk}{3E} \left[ \frac{1}{e^{(E-\mu)/T} \mp 1} + \frac{1}{e^{(E+\mu)/T} \mp 1} \right] \quad (1.1)$$

If we assume that the number of quarks and anti-quarks are equal, then it can be shown that  $\mu=0$ .

For gluons (or other bosons), this becomes

$$\ln Z = \begin{cases} g \frac{\pi^2}{90} V T^3 & \text{(bosons)} \\ g \frac{7\pi^2}{720} V T^3 & \text{(fermions)} \end{cases} \quad (1.2)$$

Now, since energy density is  $\epsilon = (T^2/V)(\partial \ln Z / \partial T)$ , we can calculate:

$$\epsilon = (g_b + \frac{7}{8}g_f) \frac{\pi^2}{30} T^4 \quad (1.3)$$

where  $g_{b,f}$  are the degeneracy numbers of the bosons, fermions as calculated below for gluons and quarks+antiquarks:

$$g_b = g_{gluon} = (8 \text{ color states})(2 \text{ spin}) \quad (1.4)$$

$$g_f = (g_q + g_{\bar{q}}) = 2(3 \text{ color})(2 \text{ spin})(n \text{ flavor}) \quad (1.5)$$

This gives us

$$\epsilon = \begin{cases} 37\frac{\pi^2}{30}T^4 & (2 \text{ quark flavors}) \\ 47.5\frac{\pi^2}{30}T^4 & (3 \text{ quark flavors}) \end{cases} \quad (1.6)$$

for the energy density of a gas of massless partons.

Using lattice QCD it is possible to perform a more realistic calculation of the energy density. Figure 1.5 shows such a calculation of the energy density [12]. At sufficient temperature, this result shows the same  $T^4$ -scaling of the plasma energy density as calculated above. It should be noted that the calculation plateaus at  $\sim 80\%$  of the Stefan-Boltzmann gas of non-interacting partons. This has sometimes been taken as evidence that the plasma weakly-interacting, but other calculations have shown that even a strongly-interacting plasma could approach this limit [13].

As the medium expands and cools, it passes through several phases, as shown in Figure 1.6. First hadronization will occur once the temperature becomes low enough that partons are confined again. Next, kinetic freeze-out occurs when the expanding hadrons are too sparse to interact with one another. At this point they will continue along their trajectories to be experimentally observed. In order to extract any properties of the QGP medium, the evolution through other phases must be accounted for as well. Hadronization in particular is not understood very well.

Topics of interest for the produced medium include the amount of thermalization of the medium, how strongly-interacting the medium is, the nature of the phase transition itself, among others.

Unfortunately, we are limited in our capabilities to experimentally study the properties of the medium, due to its exceedingly short lifetime. Because of this we are constrained to probes that are produced in the same collision as the medium, such as jets or heavy quarks from a hard scattering.

Figure 1.5: Energy density in units of  $T^4$  as calculated in lattice QCD as calculated in [12]. The sharp rise at  $T \approx T_c$  corresponds to the phase transition to the QGP. On the right side the energy density of a simple Stefan-Boltzmann gas of partons (as calculated in the text) is labeled.

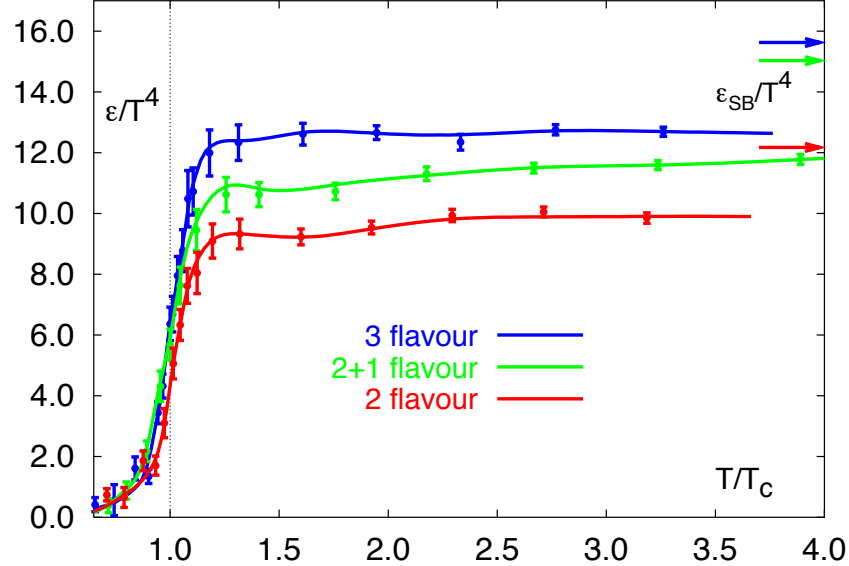
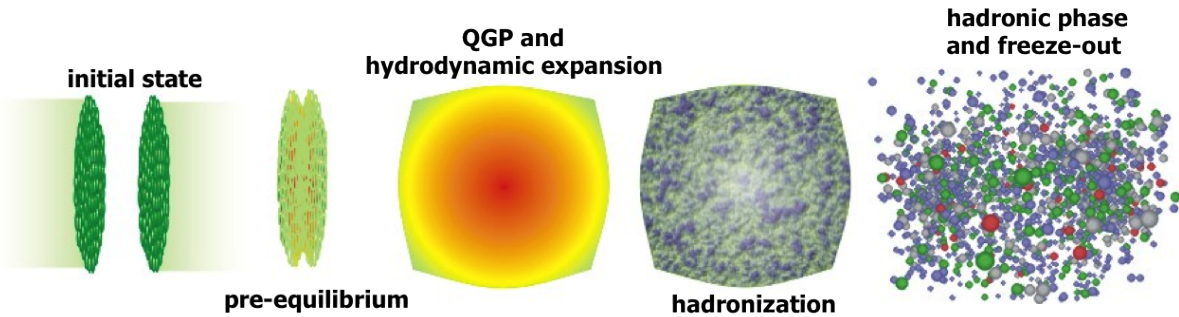


Figure 1.6: The stages of a high-energy nuclear collision.



To understand the experimental measurements of these probes, however, we must understand their initial production cross sections as well.

Our available probes and observables for studying the QGP medium include:

- Elliptic flow of particles to study on the shear viscosity/entropy of the medium.
- Jet modification due to in-medium scattering and energy loss.
- Heavy quark flow as a measure of the medium thermalization.

- Hanbury-Brown-Twiss interferometry to evaluate the distribution of matter.
- $J/\psi$  suppression above the QGP transition temperature as a signature of deconfinement.

For a detailed review of experimental and theoretical status, see [14, 15].

To expand upon the last bullet item in the list, the QGP is expected to exhibit screening of the interactions between color charges, similar to Debye screening of electric charges in electromagnetic plasmas. Calculations of the screening length near the transition temperature have led to the conclusion that the  $J/\psi$  meson (a charm-anticharm bound state) is the right size to have its constituent quarks Debye-screened from one another just above  $T_c$ . This is the core of the proposal that the disappearance of the  $J/\psi$  bound state is a signature of the QGP. This effect is the topic of the current analysis, and is discussed further in the next chapter.

## Chapter 2

### Charmonia and the $J/\psi$

The  $J/\psi$ , with mass  $\approx 3.1$  GeV/ $c^2$  and spin of 1, was discovered concurrently and independently by groups at Brookhaven National Laboratory (BNL) [16] and the Stanford Linear Accelerator Center (SLAC) [17], and the discoveries were announced together on November 11, 1974. It was the first discovered hadron containing charm quarks ( $D$  mesons, though much lighter, were not discovered until 1976), as well as the first discovered charm-anticharm meson (charmonium). The BNL group used the reaction  $p + \text{Be} \rightarrow J/\psi + X \rightarrow e^+ + e^- + X$ , while the SLAC group used  $e^+ + e^- \rightarrow J/\psi \rightarrow \{\text{hadrons}, e^+ e^-, \mu^+ \mu^-\}$ . Since that discovery, many more charmonium states have been observed, such as the  $\psi'$ ,  $\eta_c$ , and  $\chi_c^1$ <sup>1</sup>, as well as hadrons containing a mixture of charm and other quarks (*e.g.*  $D$  mesons and the  $\Lambda_c$ ). Several of the most common charmonia states are listed in Table 2.1. Charmonia which have mass below the energy threshold for producing two  $D$  mesons (3.73 GeV) are shown in Figure 2.1 with their major decay modes.

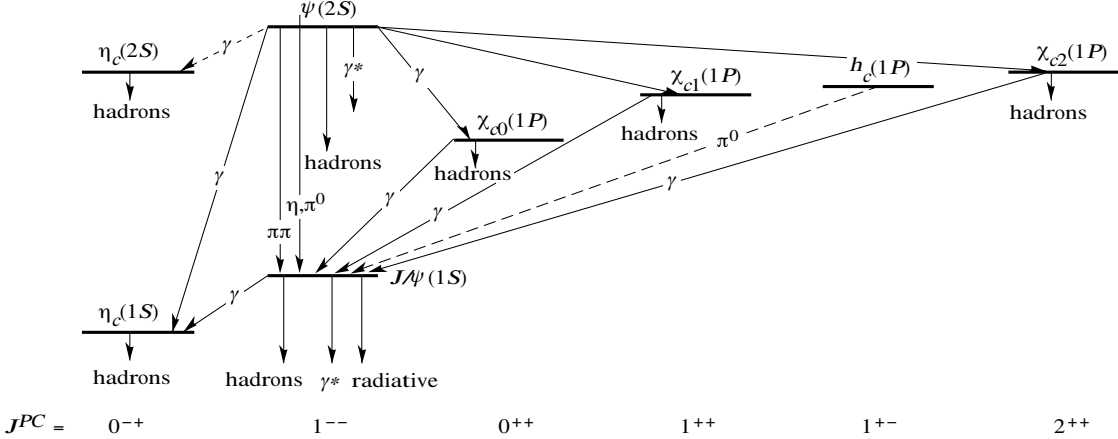
Table 2.1: Several charmonia states, with their masses, binding energies, and spin states.

state	$\eta_c$	$J/\psi$	$\chi_{c0}$	$\chi_{c1}$	$\chi_{c2}$	$\eta_c(2S)$	$\psi'$
mass (GeV/ $c^2$ )	2.98	3.10	3.42	3.51	3.56	3.64	3.69
$\Delta E$ (GeV)	0.75	0.64	0.32	0.22	0.18	0.10	0.05
$2S+1L_J$	$^1S_0$	$^3S_1$	$^3P_0$	$^3P_1$	$^3P_2$	$^1S_0$	$^3S_1$

One advantage to a bound state of heavy quarks is that it is relatively well-described by the non-relativistic Schrodinger equation. We can write the QCD potential energy of the bound

<sup>1</sup> The  $\chi_{c0,1,2}$  are often listed as a spin-averaged state  $\chi_c$ .

Figure 2.1: Major charmonia states and decay modes [3].



state as having two components, one similar to a typical Coulomb potential and a second linear term for confinement that increases as the quarks are pulled apart. This is known as a “Cornell potential” [18] and is written:

$$V(r) = \kappa r - \frac{\alpha}{r} \quad (2.1)$$

Following the procedure of [19] and plugging this potential into the non-relativistic Schrodinger equation:

$$\left\{ 2m_c - \frac{1}{m_c} \nabla^2 + V(r) \right\} \Phi_i(r) = M_i \Phi_i(r) \quad (2.2)$$

and using  $\kappa \simeq 0.2$ ,  $\alpha \simeq \pi/12$ , and  $m_c \simeq 1.3 \text{ GeV}/c^2$  one can reproduce the experimental masses of the  $J/\psi$ ,  $\chi_c$ , and  $\psi'$  to within 1%. The resulting calculated mass of the  $J/\psi$  is  $3.10 \text{ GeV}/c^2$  (compare to the Particle Data Book [20] value of  $3.0969 \text{ GeV}/c^2$ ) and the average radius is 0.25 fm. The calculated  $\psi'$  mass is  $3.68 \text{ GeV}/c^2$ , as compared to the PDB value of  $3.68609 \text{ GeV}/c^2$ .

## 2.1 $J/\psi$ Production Mechanisms

There have been several models put forward to calculate the direct  $J/\psi$  (and other heavy quarkonia) production rates. The Color Evaporation Model (CEM) was introduced in 1977 [21, 22], and was later revived in 1996 by Halzen *et al.* [23]. It is able to reproduce a number of experimental results very well, such as the  $J/\psi$  cross section from  $p+p$  or  $p+\bar{p}$  collisions as a function of  $\sqrt{s}$ , as

well as the polarized production cross sections.

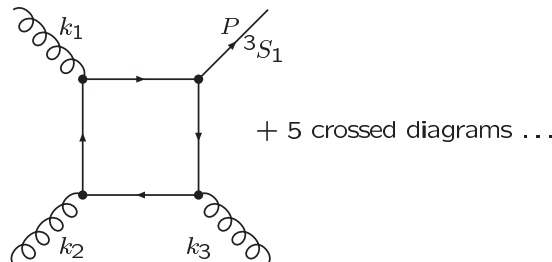
The model assumes that the color state of the produced  $c\bar{c}$  is completely random, and consequently there is a 1/9 chance of ending up with a colorless (singlet state) meson (the other cases are assumed to result in open charm mesons). This can be written as:

$$\sigma(J/\psi) = \frac{\rho}{9} \int_{2m_c}^{2m_D} dm \frac{d\sigma_{c\bar{c}}}{dm} \quad (2.3)$$

where  $d\sigma_{c\bar{c}}/dm$  is the differential  $c\bar{c}$  production cross section with respect to mass, and the natural value of  $\rho$  is the inverse of the number of quarkonia states between  $2m_c$  and  $2m_D$ . However, in practice the determination of  $\rho$  is usually done from the data, leaving the CEM rather phenomenological.

The Color Singlet Model (CSM) is based on the postulate that the creation of the two heavy quarks and the formation of the meson state can be factorized. The first process is considered to be perturbative due to the heavy mass of the quarks, allowing the cross section to be calculated using the usual Feynman diagram techniques. The second step is assumed to happen with the quarks at rest in the meson frame, and this is known as the *static approximation*. Finally, it is assumed that the color and spin of the  $q\bar{q}$  do not change during binding, and therefore the  $q\bar{q}$  pair is required to be produced in the color singlet state. In high energy hadronic collisions, two-gluon fusion is the leading contribution, and the diagram for this is shown in Figure 2.2.

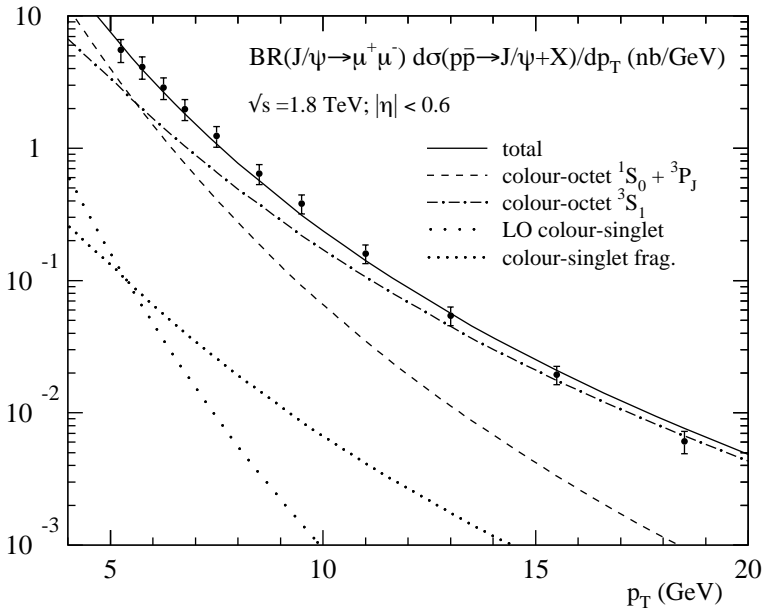
Figure 2.2: Feynman diagram for the Color Singlet Model [24].



However, in 1997 the CDF collaboration showed that the direct  $J/\psi$  cross section exceeds the CSM prediction by a factor of  $\sim 30$  in  $p+\bar{p}$  collisions at  $\sqrt{s}=1.8$  TeV [25], [26], as shown in

Figure 2.3. CDF had also already shown that the  $\psi'$  predictions did not match the data. These results left the CSM in a state of disrepute, and other models were turned to.

Figure 2.3: CDF  $J/\psi$  production differential cross section compared to both CSM and COM calculations [27]. The large (factor  $\sim 30$ ) disagreement with the CSM can be seen.



The Color Octet Model (COM) was proposed in 1995 [28], and offers an alternative to the CSM-CDF puzzle. It takes the large mass of the charm quark as reason to neglect relativistic effects and perform calculations within the effective field theory of Non-Relativistic QCD (NRQCD). This involves expansions in both  $\alpha_s$  and  $v/c$ , the relative quark velocity within the bound state. This expansion is written as:

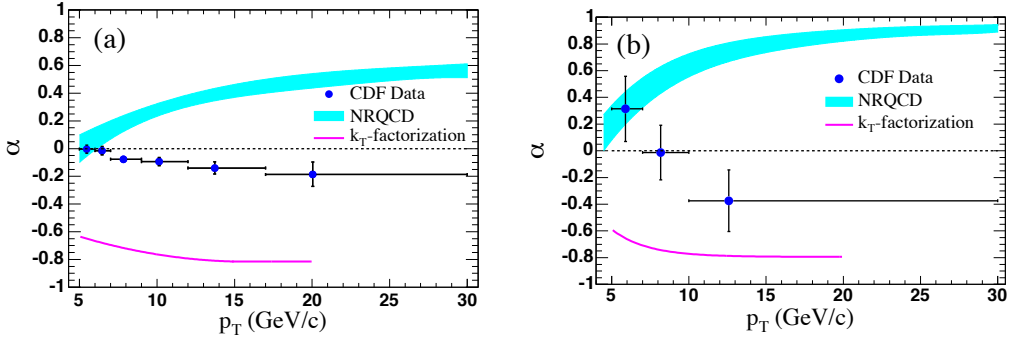
$$d\sigma[J/\psi] = \sum_n d\sigma[c\bar{c}(n)] \langle O_n^{J/\psi} \rangle \quad (2.4)$$

where  $n$  are the color (single/octet) and angular momentum Fock states,  $d\sigma[c\bar{c}]$  is the  $c\bar{c}$  production cross section in state  $n$ , and  $\langle O_n^{J/\psi} \rangle$  are NRQCD matrix elements. Factorization is assumed to hold, so that the  $c\bar{c}$  cross sections are expanded in powers of  $\alpha_s$  and calculated perturbatively, while the transition probability from the  $c\bar{c}(n)$  state to the  $J/\psi$  is encapsulated in the matrix elements, which

can be expanded in powers of  $v/c$ . The inclusion of color-octet production cross sections for the  $J/\psi$  are what led to the name ‘‘Color Octet Model’’. Unlike the CSM, the COM is very successful at reproducing the  $J/\psi$  and  $\psi'$  cross sections at the Tevatron, as seen in Figure 2.3. However, the matrix elements are tuned to the data, as it is not currently known how to calculate them on the lattice.

In 2007 CDF published the polarization of prompt (not from  $b$ -decays)  $J/\psi$  and  $\psi'$  mesons [29], which disagrees strongly with COM predictions. If  $\theta^*$  is the angle between the decay  $\mu^+$  and the boost direction (in the lab frame) of the meson in the meson’s rest frame, then the decay angle distribution is  $dN/d\cos\theta^* \propto 1 + \alpha \cos^2\theta^*$ , where  $\alpha$  determines the magnitude and direction of the polarization. The CDF measurements of  $\alpha$  are shown in Figure 2.4, along with the COM predictions. As can be seen, CDF measured  $J/\psi$  production to be slightly longitudinally polarized ( $\alpha < 0$ ), while the COM predicts a strong transverse polarization ( $\alpha > 0$ ).

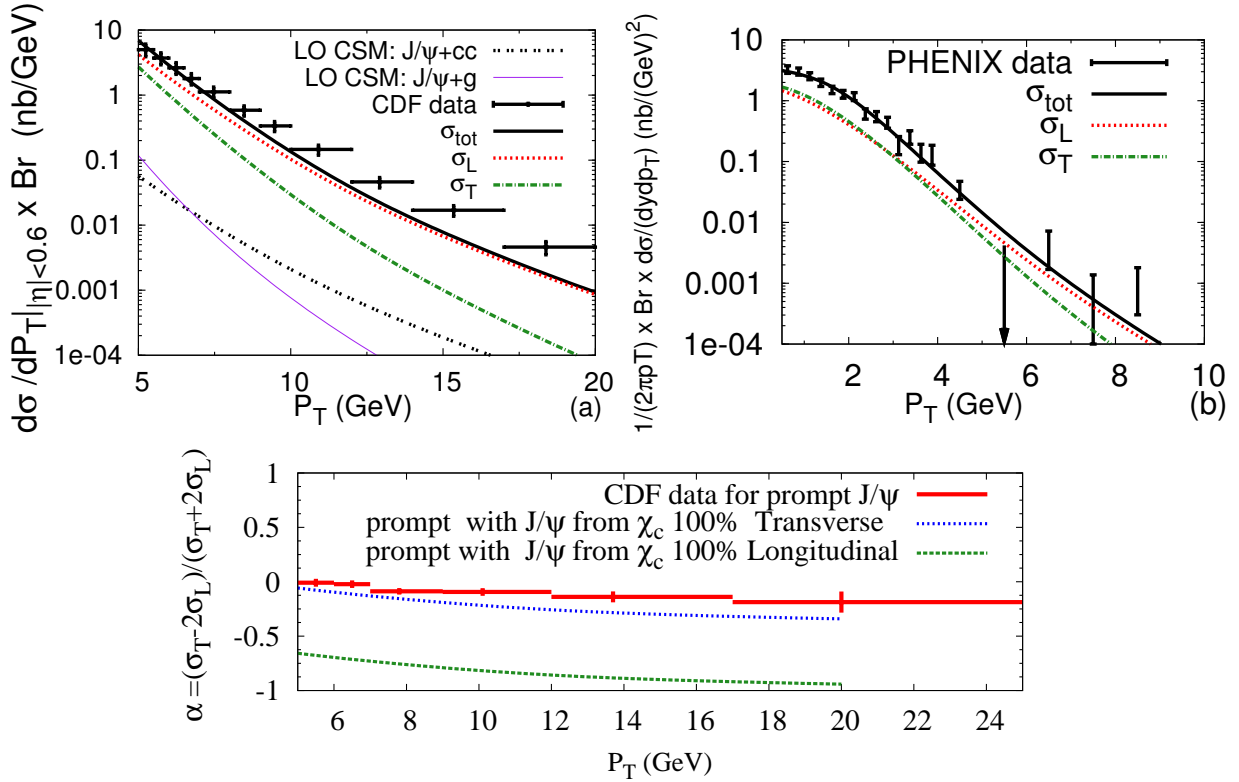
Figure 2.4: The polarization parameter  $\alpha$  as measured by CDF for prompt (a)  $J/\psi$  and (b)  $\psi'$  production [29]. Overlaid as blue bands are the predictions from the COM, which disagree with the data.



Recently work has been done to extend the CSM by including additional diagrams. Lansberg *et al.* [30, 31] include terms corresponding to an  $s$ -channel cut of  $\hat{s} = 4m^2$ . These diagrams are similar to those in Figure 2.2, but with different kinematic requirements. The function chosen to represent  $c\bar{c}Qg$  nodes in the calculation contains two free parameters, which were chosen to match the CDF total cross section up to  $p_T \sim 10$  GeV/ $c$ . The resulting large contribution from including the  $s$ -channel cut terms results in predictions that agree much better with the CDF data

on both the  $J/\psi$  cross section and the polarization, as shown in Figures 2.5, although higher-order diagrams than those currently included are expected to contribute significantly further out in  $p_T$ . The predicted polarization varies due to the large  $J/\psi$  feed-down contribution from  $\chi_c$  decays, but the case of a transversely polarized  $\chi_c$  agrees with the data much better than previous models.

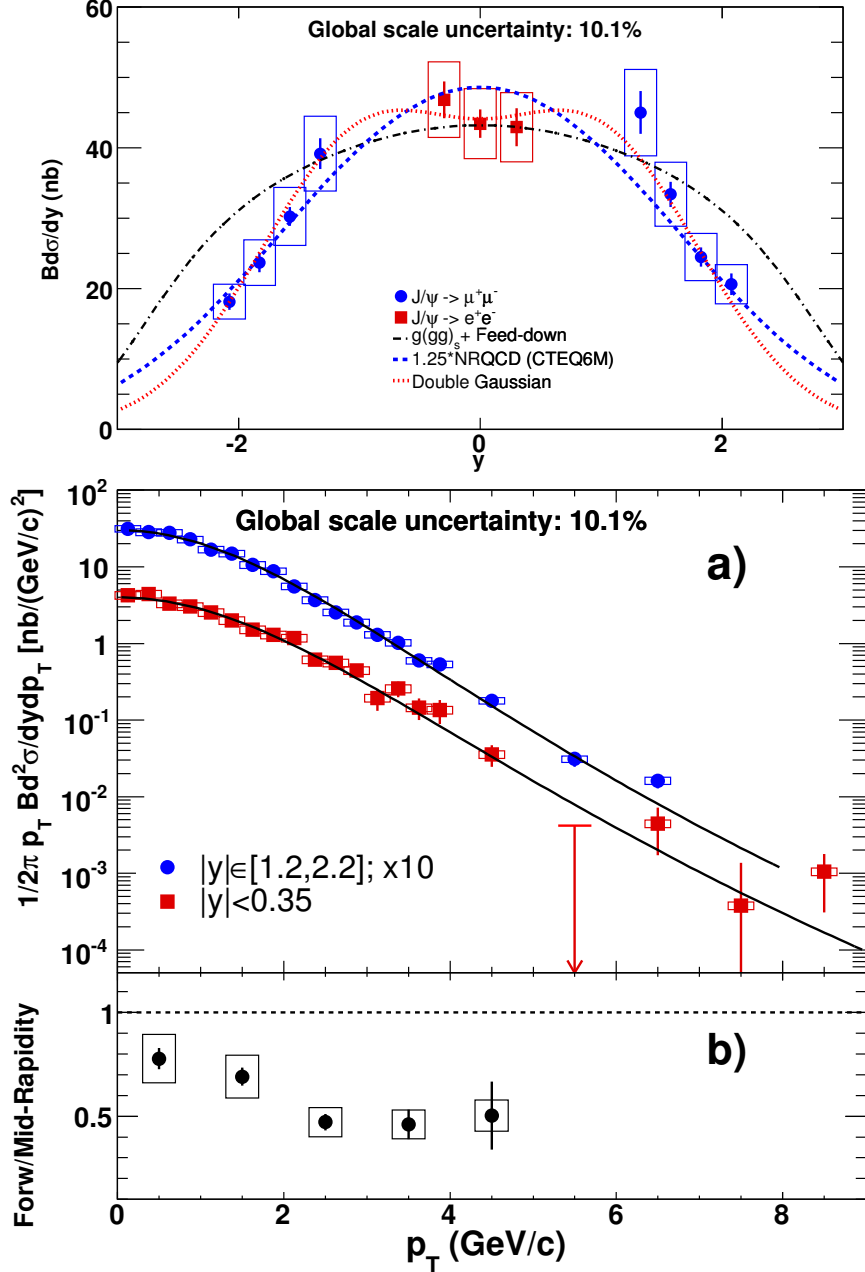
Figure 2.5: Predictions from the CSM with the  $s$ -channel cut [32, 31], parametrized to the CDF total  $J/\psi$  cross section, (Top Left) compared to CDF  $J/\psi$  production cross sections at  $\sqrt{s}=1.8$  TeV (Top Right) compared to PHENIX  $J/\psi$  production cross sections at  $\sqrt{s}=200$  GeV, (Bottom) compared to CDF measurement of the  $J/\psi$  polarization parameter  $\alpha$ .



PHENIX has also measured  $J/\psi$  production in  $\sqrt{s}=200$  GeV  $p+p$  collisions using the 2005 dataset [33]. The cross sections as functions of rapidity and  $p_T$  are shown in Figure 2.6. These have also been compared to predictions of the CSM model with the  $s$ -channel cut, as shown in Figure 2.5.

There has been much work done on understanding  $J/\psi$  production, but there is still a ways to go before it is completely understood in  $p+p$  and  $p+\bar{p}$  environments, let alone in the more

Figure 2.6:  $J/\psi$  production in  $p+p$  collisions at  $\sqrt{s}=200$  GeV at PHENIX [33]. Top: rapidity distribution. Bottom:  $p_T$  distributions.



complicated domain of nuclear collisions.

## 2.2 $J/\psi$ s as probes of the QGP

In 1986, Matsui and Satz proposed that Debye screening of color charge would take place in a deconfined quark-gluon medium, just as in an electromagnetic plasma [34]. Further, they calculated that the radius of the  $J/\psi$  bound state is larger than the Debye screening radius just above the transition temperature  $T_c$  of the plasma. This would lead to the dissolution of the  $J/\psi$  bound state within the plasma, which would be a clear signal of the existence of such a plasma.

In a medium of charged particles, Debye screening occurs when the interactions of one charge are reduced or cancelled out by the surrounding charges. Though, this was originally defined for electromagnetic plasmas, it can be extended to plasmas of color charge as well. It is parametrized by the Debye screening radius, the radius at which the effective charge of a particle is reduced by a factor of  $1/e$ .

Inside the QGP, the linear term in our potential model (Equation 2.1) will disappear as the plasma temperature  $T$  approaches the transition temperature, and a screening factor will be introduced to the Coulombic term, giving rise to the modified potential

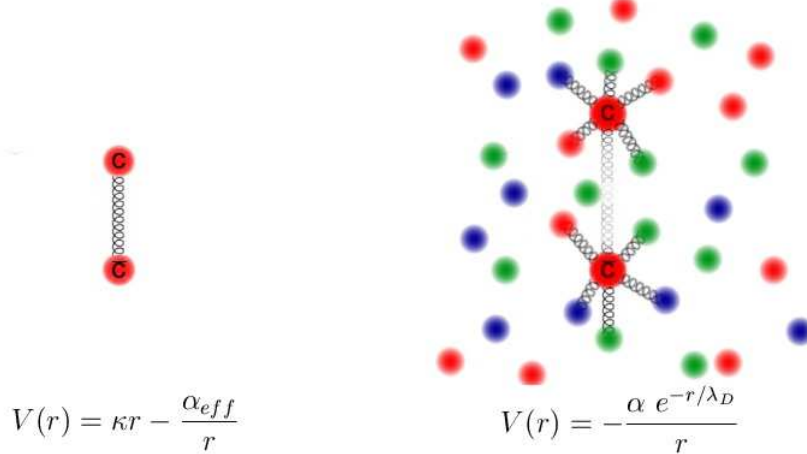
$$V(r) = -\frac{\alpha_{eff} e^{-r/\lambda_D}}{r} \Big|_{T=T_c} \quad (2.5)$$

The net result is a much shallower potential well, where even small perturbations can knock the  $c\bar{c}$  out of the bound state.

Qualitatively, this change can be thought of as the short-range strong interactions in the medium predominating over the long-range interactions. The key is that the relative scale of long-range versus short-range for the  $c\bar{c}$  changes when it is immersed in the plasma, such that the binding interaction is no longer dominant. This is expressed pictorially in Figure 2.7.

Some simple calculations can express this quantitatively, as detailed in [10]:

- First, noting that  $\alpha_{eff}$  is dependent on the temperature of the medium, the lattice QCD results of  $\alpha=0.52$  and  $0.2$  at  $T=0$  and  $200$  MeV, respectively, are used.

Figure 2.7: Cartoon of a  $J/\psi$  in (a) vacuum and (b) the QGP.

- Next, the screening radius from lowest-order perturbative QCD is used:

$$\lambda_D(T) = \sqrt{\frac{2}{9\pi\alpha_{eff}} \frac{1}{T}} \quad (2.6)$$

- Finally, the semi-classical Bohr radius of the  $c\bar{c}$  comes from minimizing the energy equation for a  $c\bar{c}$  system ( $\mu = 1840/2$  MeV) with the screened potential (Eq. 2.5) and  $\langle p^2 \rangle \sim 1/r^2$ , in the limit  $\lambda_D \rightarrow \infty$ :

$$\begin{aligned} E(r) &= \frac{p^2}{2m} + V(r) \\ &= \frac{1}{2\mu r^2} - \frac{\alpha_{eff}(T)e^{-r/\lambda_D(T)}}{r} \end{aligned} \quad (2.7)$$

The results of these calculations are listed in Table 2.2.

It is clear that the screening radius is much smaller than the  $J/\psi$  radius at  $T=200$  MeV in this model, and it should also be noted that the radius of the  $c\bar{c}$  system has become quite large in the medium. It is also pointed out in [10] that the lowest-order pQCD estimate of  $\lambda_D$  are about a factor of 2 larger than those from lattice calculations.

The effect of Debye screening is also borne out by lattice calculations of the binding energy of the  $c\bar{c}$  system. Shown in Figure 2.8 is the result of a lattice calculation by the RBC-Bielefeld Collaboration [35] of the free energy as a function of the radial separation of the quarks in (2+1)-

Table 2.2: A comparison of the screening radius  $\lambda_D$  and the Bohr radius of the  $J/\psi$ 

$T_{\text{plasma}}$	0	200 MeV
$\alpha_{\text{eff}}$	0.52	0.2
$\lambda_D$	$\infty$	0.59 fm
$R_{\text{Bohr}}$	0.41 fm	1.07 fm

flavor QCD. As can be seen, the energy required to break the binding drops with the increase in the medium temperature, until it becomes negligible above  $2T_c$ .

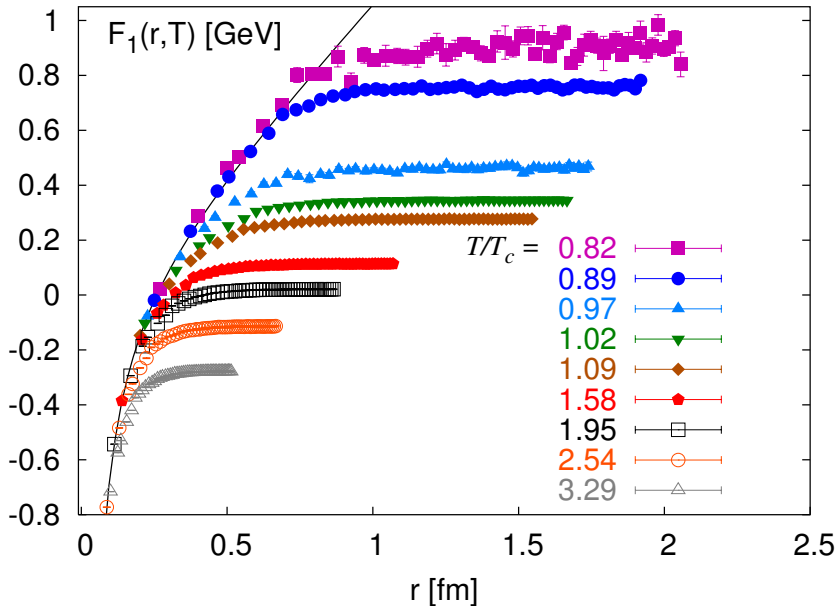
Though a number of lattice calculations show the  $J/\psi$  peak in the spectral function surviving as high as  $2T_c$ , recently Mócsy and Petreczky [36] argued that even though the spectral functions exist at higher temperatures, the binding energy still becomes low enough that any  $c\bar{c}$  bound state can be broken simply by interactions with the thermal medium. For example, they calculate that at  $1.1T_c$  the  $J/\psi$  spectral functions still has a resonance peak, but the binding energy has already been reduced to 0.014 GeV. They also note that the existence of the spectral function peak at higher temperatures could mean that the  $c\bar{c}$ -pair is still correlated in phase space, which could encourage later-stage regeneration of  $J/\psi$ s after the plasma has cooled.

In any case, the  $c\bar{c}$  interaction will be almost entirely screened away in a hot enough medium, causing the component charm quarks to become unbound from one another. Experimentally, this would manifest in the suppression of the  $J/\psi$  state and would clearly indicate the formation of a QGP. However, the picture is no longer as straightforward as that laid out by Matsui and Satz and described here.

### 2.3 Cold Nuclear Matter

The “smoking gun” quality of  $J/\psi$  suppression has become more complex in the past 15 years due to results on suppression of  $J/\psi$ s within normal nuclear matter (usually referred to as “cold” nuclear matter), which was not accounted for in the original Matsui and Satz paper. We know that there is significant modification of the parton distribution functions (PDFs) when the nucleons are bound in the nucleus, compared to the PDFs of free nucleons. This plays a

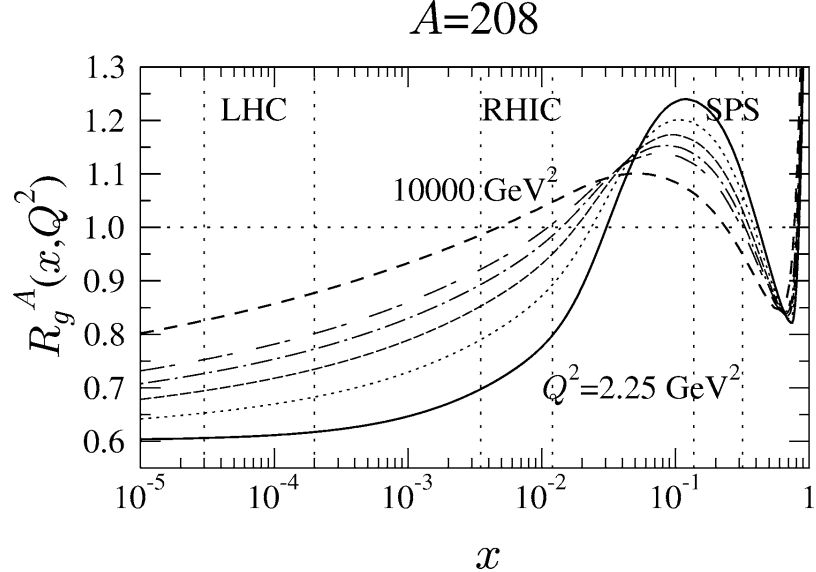
Figure 2.8: The color singlet  $q\bar{q}$  free energy as a function of their radial separation, as calculated in (2+1)-flavor QCD on the lattice [35]. As can be seen, the energy needed to separate the pair decreases as the medium temperature approaches and then exceeds  $T_c$ . The solid line represents the heavy quark potential  $V(r)$  at  $T=0$ .



significant role in quantitatively extracting the cold nuclear effects from the data. For example, because  $J/\psi$  production is dominated by gluon-gluon fusion, when  $p+A$  or  $d+A$  data is compared to  $p+p$  data the gluon distribution in the nucleus must be contrasted to the gluon distribution of the proton. Experiments at the CERN-SPS have taken a different route by comparing the  $p+A$   $J/\psi$  production to Drell-Yan production in the same data-set. However, in that case the gluon PDF must be compared to the quark PDFs in the nucleus over the respective  $x$ -ranges of the two measurements, and the difference must still be accounted for in any analysis of cold nuclear matter (CNM) effects.

The ratio of the gluon PDF in a heavy nucleus ( $A=208$ ) to that in a free proton is shown in Figure 2.9, as calculated by Eskola *et al.* in [37]. The depletion in the region  $x \lesssim 10^{-2}$  is known as “shadowing”, while the enhancement at  $x \sim 10^{-1}$  is known as “anti-shadowing”. In  $\sqrt{s_{NN}}=200$  GeV  $d+Au$  collisions PHENIX covers a range of  $x$ -values in the gold nucleus of roughly  $0.002 < x < 0.2$ . This includes both the shadowing and anti-shadowing regions. It should be noted

Figure 2.9: Ratio of gluon PDF in an  $A=208$  nucleus to the gluon PDF in a proton as calculated in [37]. The solid line is for  $Q^2=2.25 \text{ GeV}^2$ , while the dashed line is for  $Q^2=10000 \text{ GeV}^2$ . Vertical lines delineate the dominant regions of  $x$  probed at SPS, RHIC, and the LHC.



that the exact modification of the gluon PDF is very model-dependent at present.

In addition to the modified PDFs, there is a significant chance that the  $J/\psi$  final state will fail to form due to the  $c\bar{c}$ -pair interacting with the nucleus after production. This is usually represented by a break-up (or absorption) cross section, and the  $J/\psi$  production cross section in  $p+A$  collisions can be written in the Glauber formalism as [38]:

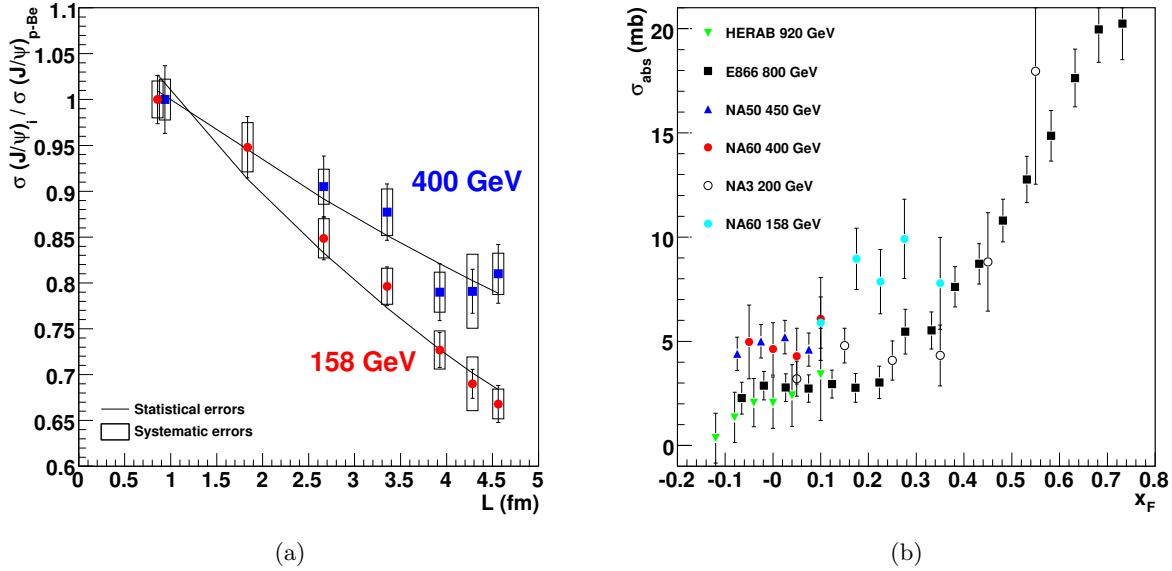
$$\sigma_{pA} = \frac{\sigma_0}{\sigma_{br}} \int d\mathbf{b} [1 - (1 - T_A(\mathbf{b})\sigma_{br})^A] \quad (2.8)$$

where  $\sigma_0$  is the nucleon-nucleon charmonium production cross section,  $\sigma_{br}$  is the  $c\bar{c}$  break-up cross section,  $T_A(\mathbf{b}) = \int \rho_A(\mathbf{b}, z) dz$  is the nuclear thickness seen by the impacting proton, as a function of impact parameter  $\mathbf{b}$ . Thus far there is no first-principles calculation of  $\sigma_{br}$ , so it remains a free parameter that must be extracted from the data.

### 2.3.1 SPS $p+A$ Measurements

A number of experiments at CERN-SPS have measured  $J/\psi$  production in  $p+A$  collisions, recently including the NA50 and NA60 experiments, in addition to several previous experiments such as NA3. The nuclear targets have included Be, Al, Cu, Ag, W, and Pb, with proton beam energies of 158, 400, and 450 GeV. The different nuclei provide a varying path length for the  $c\bar{c}$  through the nucleus.

Figure 2.10: From [39]: Left: ratio of  $J/\psi$  production cross sections in  $p+A$  collisions divided by  $p+Be$  collisions as a function of the path length  $L$  from NA60. Right: compilation of  $\sigma_{br}$  as a function of  $x_F$  from various experiments.



NA60 recently published results for  $J/\psi$  production from  $p+A$  collisions with  $E_{beam}=158$  GeV and 400 GeV [39]. These are presented in Figure 2.10(a) as the ratio of  $J/\psi$  production off of a heavier nucleus to the production off Be. As can be seen, the nuclear break-up of the  $c\bar{c}$  is stronger in the 158 GeV case for the same average path length. This is in line with the break-up cross sections extracted from this data,  $\sigma_{br}[158 \text{ GeV}] = 7.6 \pm 0.7 \text{ (stat.)} \pm 0.6 \text{ (syst.) mb}$  and  $\sigma_{br}[400 \text{ GeV}] = 4.3 \pm 0.8 \text{ (stat.)} \pm 0.6 \text{ (syst.) mb}$ . A comparison is also done between the  $\sigma_{br}$  extracted by a variety of experiments over a range of  $x_F$  values, as is shown in Figure 2.10(b).

### 2.3.2 PHENIX $d+\text{Au}$ Measurements

In 2003, PHENIX recorded  $d+\text{Au}$  collisions at  $\sqrt{s_{NN}}=200$  GeV/u in order to study cold nuclear matter effects on  $J/\psi$ s [40]. It was found that  $J/\psi$  production is significantly suppressed in the deuteron-going direction (forward rapidity in this case), as compared to production in  $p+p$  collisions scaled up by the mean number of binary collisions in a given  $d+\text{Au}$  centrality bin:

$$R_{d\text{Au}} = \frac{1}{\langle N_{\text{coll}} \rangle} \frac{d\sigma^{d\text{Au}}/dy}{d\sigma^{pp}/dy} \quad (2.9)$$

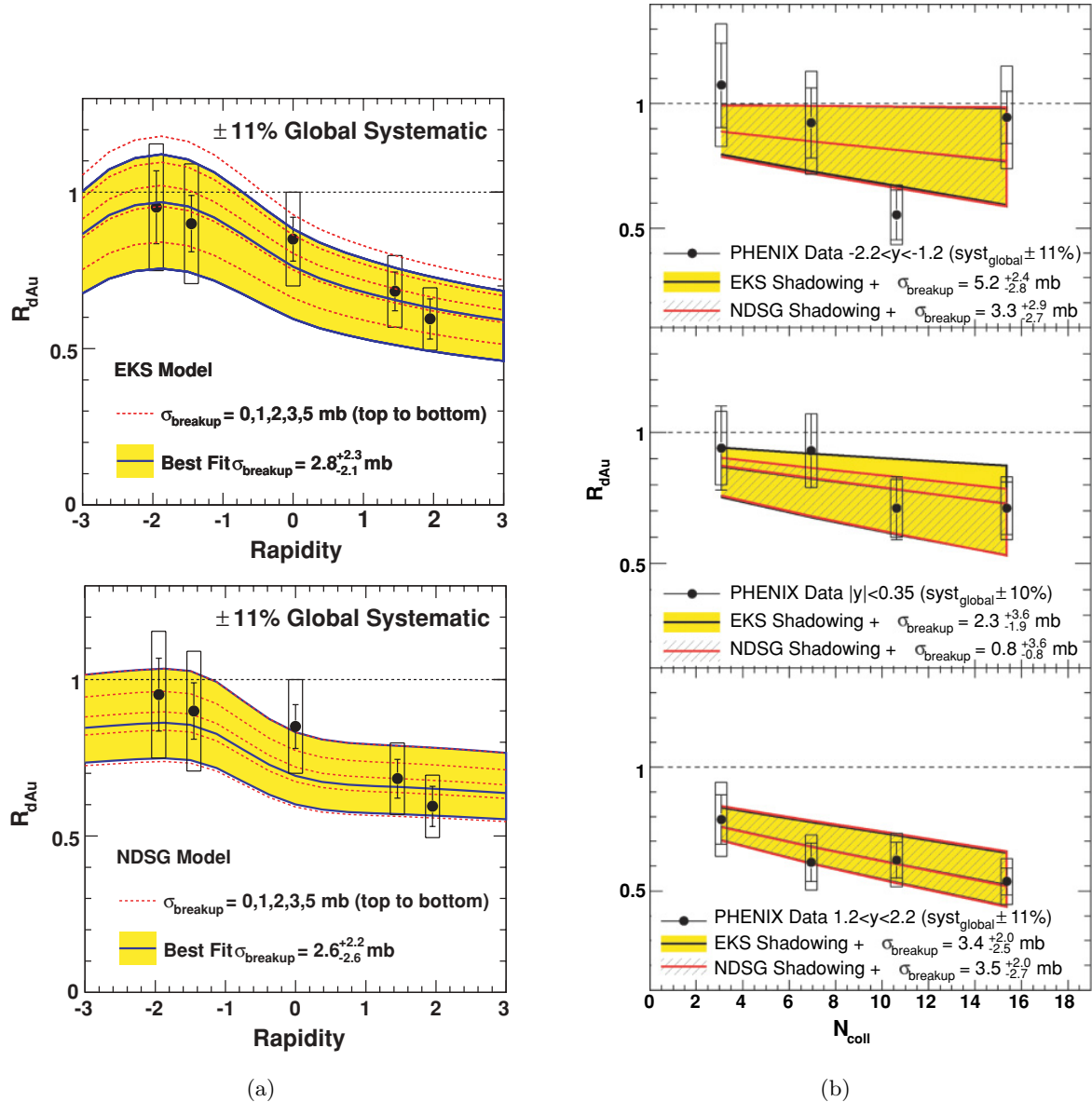
The rapidity dependence of  $R_{d\text{Au}}$  is shown in Figure 2.11(a), and the  $N_{\text{coll}}$ -dependence is shown in Figure 2.11(b) in three bins of rapidity. It can be seen that the suppression at forward rapidity also increases with  $N_{\text{coll}}$ , as would be expected simply due to increased path length through the thicker part of the nucleus in collisions at small impact parameter.

Also shown in Figure 2.11(a) is a calculation of  $R_{d\text{Au}}$  [41] incorporating the EKS [37] (top) and NDSG [42] (bottom) nuclear shadowing-modified PDFs. An additional break-up cross section (chosen to be constant for simplicity) is included as a free parameter. Curves are shown in the Figure for several values of  $\sigma_{br}$ , along with the best-fit curve, which yields  $\sigma_{br} = 2.8_{-2.3}^{+2.1}$  mb for EKS shadowing, and  $\sigma_{br} = 2.6_{-2.6}^{+2.2}$  mb for NDSG shadowing. The fits take into account both statistical and systematic uncertainties in the data, and the 1-sigma region is shown as a band around the central value.

In Figure 2.11(b) the EKS and NDSG models are fit to  $R_{d\text{Au}}$  as a function of  $N_{\text{coll}}$ , using a geometric parametrization based on the path of the parton through the nucleus to calculate the  $N_{\text{coll}}$ -dependence. Those fits are used to extract the break-up cross section independently in the three rapidity bins. The identical appearance of the EKS and NDSG bands is due to using the same geometric dependence for both cases, so that the only difference is the relative contribution from the nuclear PDFs vs. the break-up cross section.

Recently, it was pointed out by Ferreiro *et al.* [43] that the choice of a  $2 \rightarrow 1$  or  $2 \rightarrow 2$  process for  $J/\psi$  production can have a significant effect on the  $x$ -values in the nucleus probed by  $J/\psi$ s of a given  $p_{\text{T}}$  and  $y$ . This has implications for extracting CNM effects from data, where the  $p_{\text{T}}$ ,  $y$  of

Figure 2.11: From [40]:  $R_{dAu}$  as a function of (a) rapidity and (b)  $N_{coll}$ , compared to both the EKS and NDSG shadowing models with an additional nuclear break-up term.



the  $J/\psi$  is mapped to the  $x_2$  within the nucleus. The two cases are shown in Figure 2.12, where “Intrinsic” refers to the  $2 \rightarrow 1$  case in which the  $J/\psi p_T, y$  are determined entirely by the incoming gluons, while “Extrinsic” refers to the  $2 \rightarrow 2$  where the  $J/\psi$  kinematics also depend on those of the outgoing gluon. As would be expected, for a given rapidity in the extrinsic case there is a much wider range of  $x_2$  values sampled due to the extra freedom introduced by the additional outgoing parton.

## 2.4 $A+A$ Collisions

### 2.4.1 NA50 Pb+Pb Program

NA50 was a fixed-target experiment at the CERN Super Proton Synchrotron (SPS) that studied dimuon production in Pb+Pb collisions, including  $J/\psi$ ,  $\psi'$ , and Drell-Yan production. As a fixed-target experiment it had lower  $\sqrt{s_{NN}}$  than collider experiments, but an advantage in statistics due to the higher collision probability, a boon for rare physics processes such as  $J/\psi$  production.

Using  $E_{\text{beam}}=158$  GeV/u Pb+Pb data ( $\sqrt{s_{NN}}=17.2$  GeV/u) taken in 1998 and 2000, NA50 measured [44] both the  $J/\psi$  and the Drell-Yan cross sections. The total  $J/\psi$  production cross section should nominally (absent medium effects) scale with the Drell-Yan cross section for all

Figure 2.12:  $x_2$  vs.  $y$  distribution from [43] for  $J/\psi$ s in simulated  $\sqrt{s_{NN}}=200$  GeV  $d+\text{Au}$  collisions. Left: Intrinsic case of the  $2 \rightarrow 1$  production process. Right: Extrinsic case of the  $2 \rightarrow 2$  process.

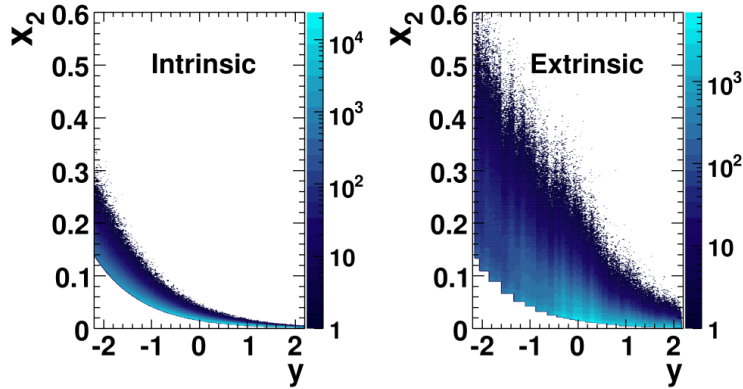
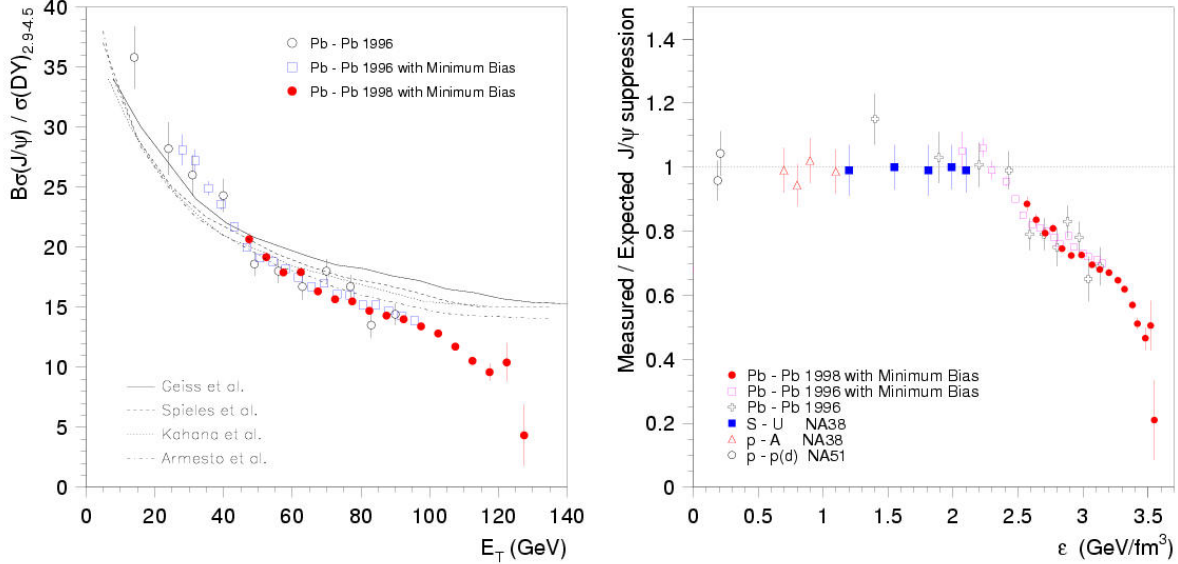


Figure 2.13: Left: NA50 measurement of the ratio of  $J/\psi$  to Drell-Yan production as a function of the transverse energy of the collision,  $E_T = \sum_{\text{particles}} E_i \sin \theta_i$ . Right: NA50 and previous results for  $J/\psi$ /Drell-Yan production divided by the expectations based on  $p+A$  data, mapped to the energy density of the system. Both from [44].



impact parameters, and Drell-Yan processes are not expected to be modified by medium effects, so the ratio of  $\sigma_{J/\psi}/\sigma_{DY}$  is a measure of  $J/\psi$  suppression by the medium. This ratio is shown as a function of transverse energy  $E_T = \sum_{\text{particles}} E_i \sin \theta_i$  in Figure 2.13, compared to the expected ratio based on CNM effects measured in  $p+A$  collisions. The total transverse energy is a direct observable that can be mapped to impact parameter or energy density. Also shown is the previous ratio divided by the CNM expectation, plotted against the energy density as calculated in the Bjorken energy density formula:

$$\epsilon = \frac{dE_T/dy}{c\tau \times A_T} \quad (2.10)$$

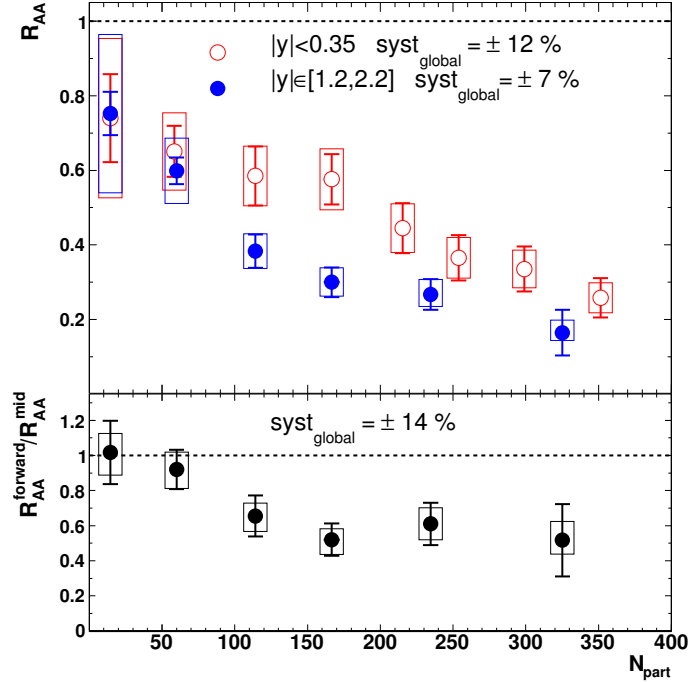
with a medium lifetime of  $\tau=1$  fm/c, where  $A_T$  is the transverse area of the collision, and  $c$  is the speed of light. The significant suppression beyond expected CNM effects has been referred to as “anomalous suppression”, and helped form the basis of a CERN announcement in 2000 that they had observed the quark-gluon plasma at the CERN-SPS in Pb+Pb collisions [45, 46]. It should be mentioned that in the right-hand plot of Figure 2.13 (1) the  $x$ -axis is dependent on that equation

for the medium energy density, and (2) none of the plotted datasets have large statistics on both sides of the turn-on point of the anomalous suppression ( $\epsilon \sim 2.4 \text{ GeV/fm}^3$ ). Nonetheless, the NA50 anomalous  $J/\psi$  suppression remains an intriguing result.

#### 2.4.2 PHENIX Au+Au Program

Following the  $d+\text{Au}$  run of 2003, PHENIX recorded its first statistically significant  $J/\psi$  sample from Au+Au collisions in 2004 [47]. The  $J/\psi$  nuclear modification factor ( $R_{\text{AA}}$ ) as a function of the number of participant nucleons ( $N_{\text{part}}$ ) is shown in Figure 2.14. As can be seen in the figures,  $J/\psi$ s are significantly suppressed in Au+Au collisions compared to the naïve  $N_{\text{coll}}$ -scaling of  $J/\psi$  production in  $p+p$  collisions.

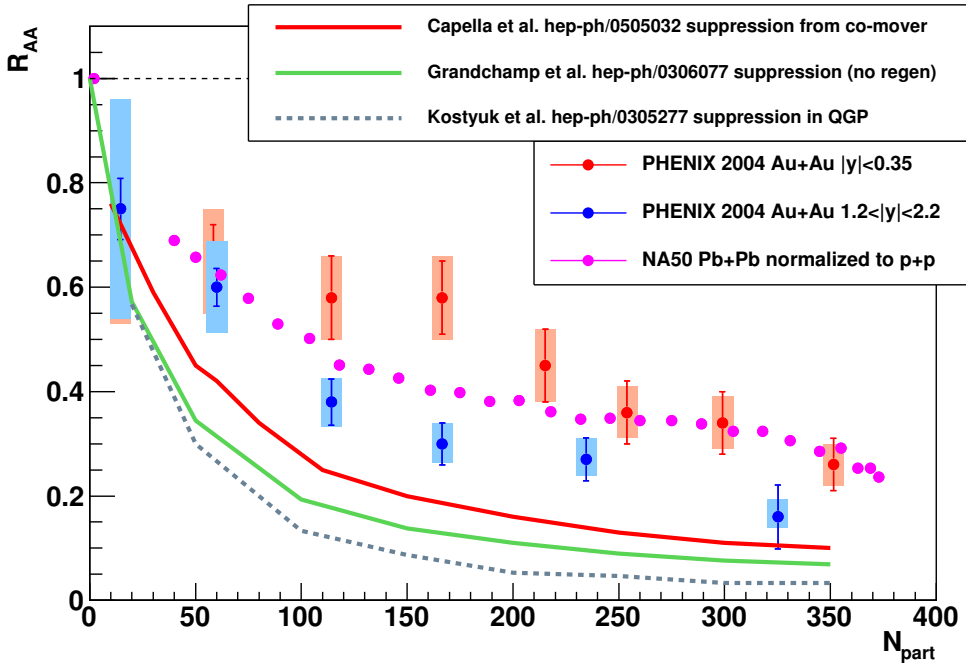
Figure 2.14: Top: PHENIX  $J/\psi$   $R_{\text{AA}}$  as a function of  $N_{\text{part}}$  at (blue) forward and (red) mid-rapidities [47]. Bottom: ratio of  $R_{\text{AA}}$  at mid-rapidity to forward rapidity.



The PHENIX  $R_{\text{AA}}$  points, however, are of the same order of suppression as that seen by NA50, as can be seen in Figure 2.15. This came as something of a surprise, since the higher energy density and temperature at RHIC were expected to lead to greater suppression than was seen at

the CERN-SPS. The NA50 data and PHENIX data are overlaid in Figure 2.15, along with several model calculations.

Figure 2.15:  $R_{AA}$  data as a function of  $N_{\text{part}}$  from NA50 and PHENIX. Overlaid are several models from the same time period. It should be noted that Grandchamp *et al.* also included a regeneration component which is not plotted here, but is discussed in the next section.



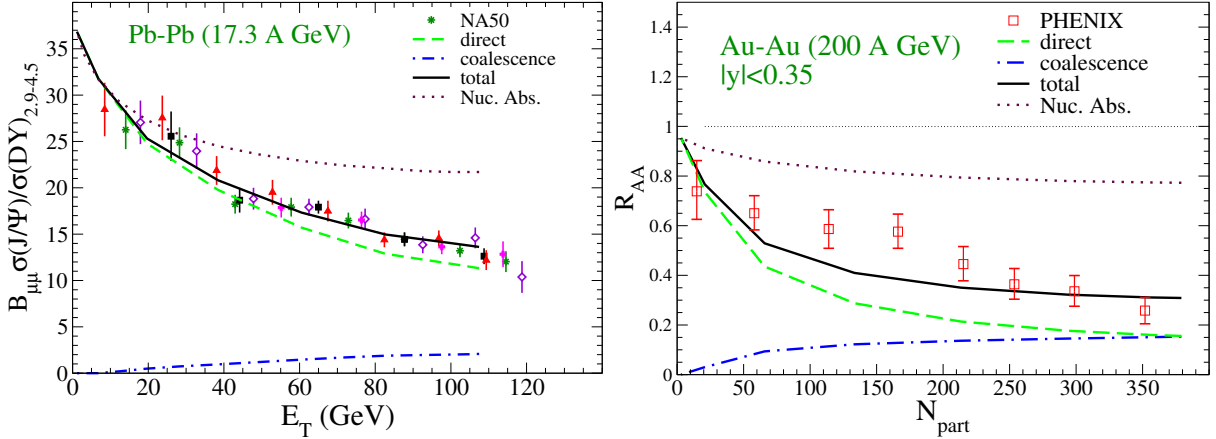
Additionally, PHENIX found that  $J/\psi$ s are more suppressed at forward rapidity than at mid-rapidity in central collisions, as can be seen from the ratio of the two rapidities in the lower panel of Figure 2.14. This would seem to be in contradiction to a simple energy-density picture of suppression, where  $J/\psi$ s at forward rapidity would be subject to lower energy densities and therefore *less* suppressed.

#### 2.4.3 $J/\psi$ Regeneration

$J/\psi$  regeneration (also sometimes referred to as “statistical hadronization” or  $J/\psi$  coalescence) has seen much interest due to its ability to explain both the similarity in suppression between SPS and RHIC, as well as the difference in suppression at forward and mid-rapidity measured by

PHENIX. In this picture the larger number of  $c\bar{c}$ -pairs produced at RHIC (of order 10 in central Au+Au collisions) are allowed to recombine at the hadronization stage of medium evolution to form new  $J/\psi$ s. In such a scenario  $J/\psi$ s are still more suppressed at RHIC than at the SPS by the higher medium temperature, but the  $c\bar{c}$ -pairs recombining into  $J/\psi$ s lead to an enhancement that balances out the Debye screening contribution in the overall  $J/\psi$  measurement. A model calculation by Zhao and Rapp from [48] which includes the two contributions is shown in Figure 2.16 for both NA50 and PHENIX.

Figure 2.16:  $J/\psi$  suppression at NA50 (left) and PHENIX (right) using the model of Zhao and Rapp [48]. Shown for both is the suppression of direct  $J/\psi$ s, as well as the contribution from regeneration (AKA coalescence), which is much larger at RHIC.

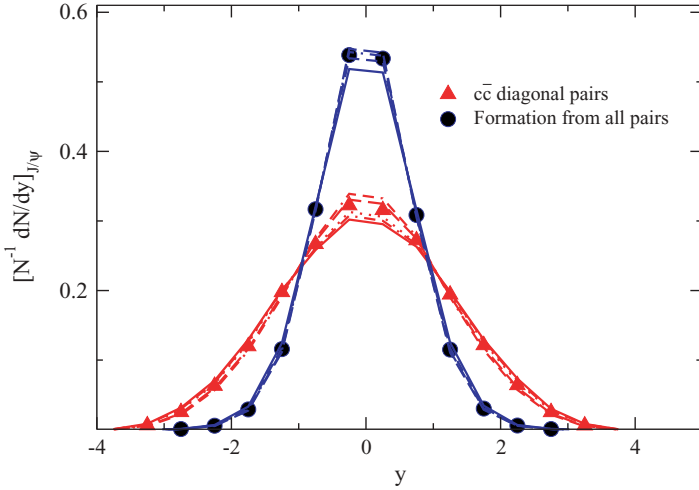


Since the amount of regeneration would statistically increase as  $\sim N_{\text{charm}}^2$ , the rapidity distribution for recombined  $J/\psi$ s would be narrower than that of direct  $J/\psi$ s. The rapidity distribution shown in Figure 2.17 is based on a calculation of  $J/\psi$  regeneration by Thews [49]. The difference in the distributions implies that even if the suppression of direct  $J/\psi$ s is identical at forward and mid-rapidity, the enhancement from regeneration at mid-rapidity will be greater and lead to higher  $R_{AA}$  there than at forward rapidity, as is seen by PHENIX.

#### 2.4.4 Sequential Charm Dissociation

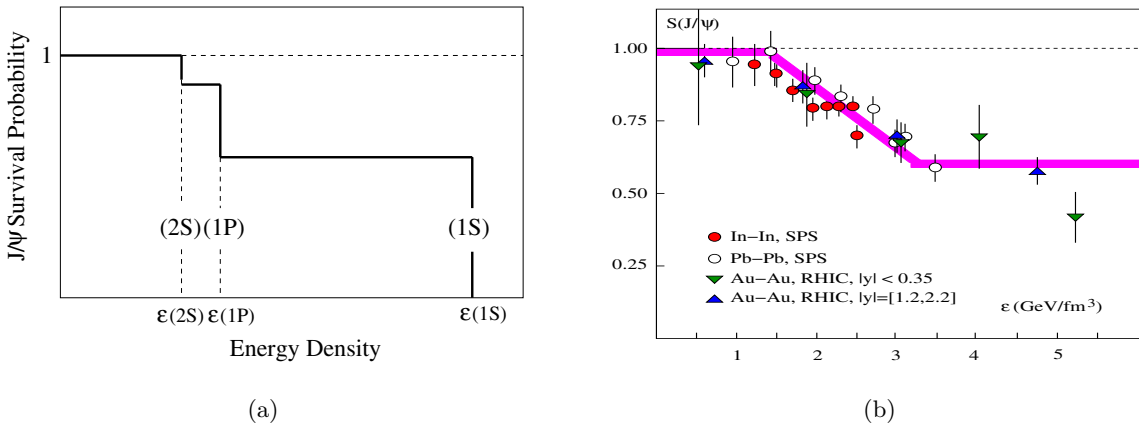
Sequential charm dissociation is another model that attempts to explain the similarity in suppression between NA50 and PHENIX. As proposed by Karsch, Kharzeev, and Satz [50], it is

Figure 2.17: Rapidity distribution of  $J/\psi$ s from [49], where ‘‘diagonal pairs’’ refers to  $c\bar{c}$  pairs produced together in the initial collisions, while ‘‘all pairs’’ includes  $J/\psi$ s from regeneration.



based on the significant feed-down contribution to  $J/\psi$  production from higher-energy  $c\bar{c}$  states like the  $\psi'$  and  $\chi_c$ . In this picture it is argued that the  $J/\psi$  itself does not melt until temperatures above  $2T_c$ , or energy densities above  $25$  GeV/fm $^3$ , which is not achieved at the SPS or RHIC.

Figure 2.18: Left:  $J/\psi$  survival probability vs. energy density, showing the broad range of  $\epsilon$  where the  $\psi'$  and  $\chi_c$  are melted, but not the  $J/\psi$ . Right: Survival probability as calculated from the SPS and RHIC data [19], as described in the text. It should be noted that the PHENIX points are based on the preliminary 2004 results, not the final published values.



Instead, the observed suppression in both cases is caused by the  $\psi'$  and  $\chi_c$  melting, and the

resulting loss of their feed-down  $J/\psi$ s that would have been produced. It is assumed that the feed-down rates are the same as those in  $p+p$  collisions, *i.e.* 60% direct  $J/\psi$ , 30% decay from  $\chi_c$ , and 10% decay from  $\psi'$ . For this model the  $\chi_c$  and  $\psi'$  melting points are taken to be just above  $T_c$ , or  $\gtrsim 1$  GeV/fm<sup>3</sup> based on lattice QCD spectral functions, while the  $J/\psi$  dissociation temperature is assumed to be  $>1.5T_c$ , or  $\sim 10\text{--}30$  GeV/fm<sup>3</sup>. With these melting temperatures, the  $\chi_c$  and  $\psi'$  states should melt in quick succession, followed by a broad range in energy density where only the direct  $J/\psi$  contribution remains. This is shown in cartoon form in Figure 2.18(a).

In order to compare to the data, the authors combine the measured  $R_{AA}$  vs.  $N_{\text{part}}$  with a break-up cross section for the  $J/\psi$  passing through the nuclei, and extract the survival probability as a function of energy density. The resulting values are shown in Figure 2.18(b). To verify this picture of sequential charm dissociation at RHIC, measurements of  $\chi_c$  production in Au+Au collisions are probably needed to demonstrate the  $\chi_c$  suppression occurs over the same range of energy density as the  $J/\psi$  suppression.

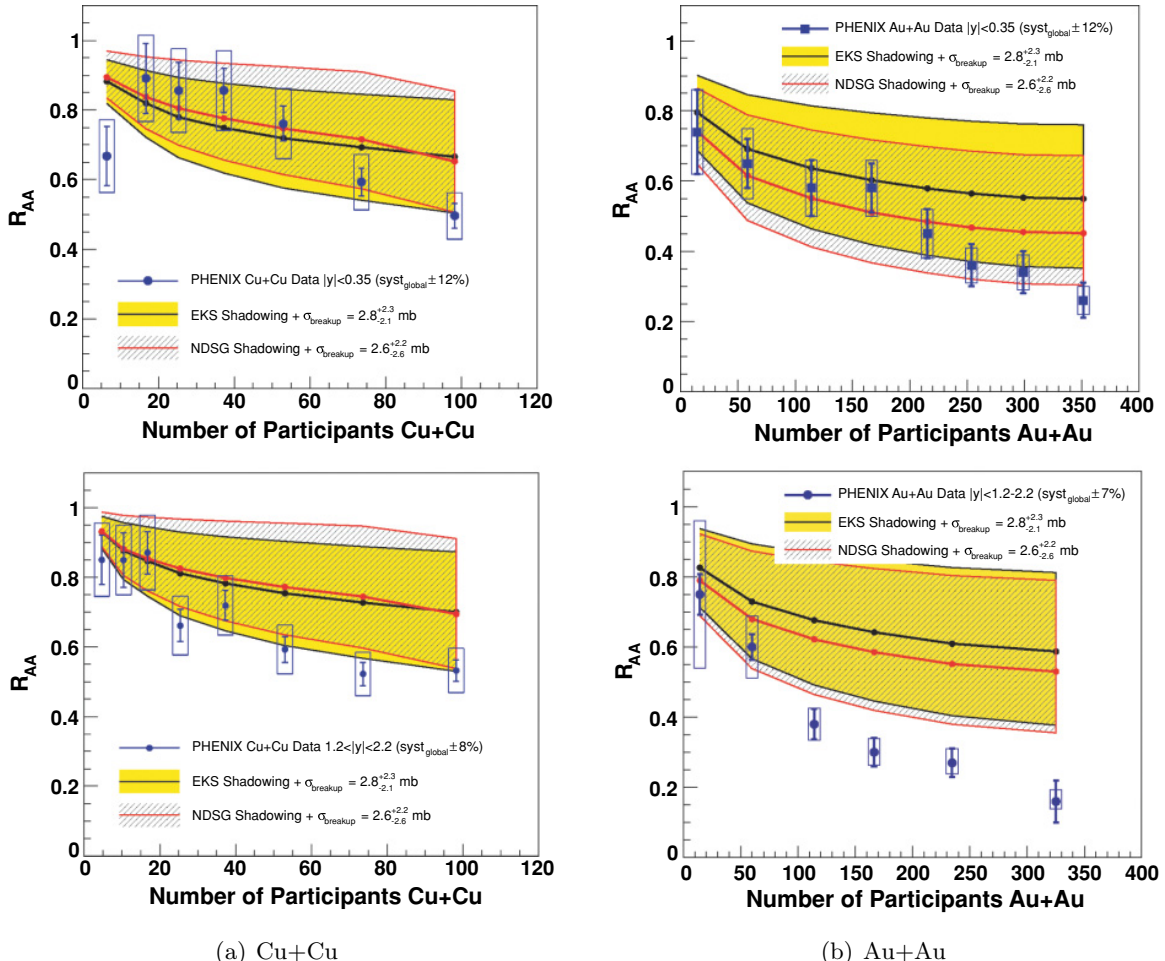
To determine whether regeneration or sequential dissociation is the explanation behind the comparable results at RHIC and SPS we can make use of the fact that  $J/\psi$ s from regeneration are expected to have a softer  $p_{\text{T}}$ -distribution than direct  $J/\psi$ s, due to the  $N_{\text{charm}}^2$ -dependence of the enhancement. However, to distinguish the two cases at RHIC a precision measurement of the  $p_{\text{T}}$ -distribution in Au+Au collisions is needed. Current measurements extend to only  $p_{\text{T}}=5$  GeV/ $c$ , and even there have large uncertainties (as will be further discussed in Section 2.4.6), resulting in a poor constraint on the slope parameter of the  $p_{\text{T}}$ -distribution at present.

Within the authors' assumption that direct  $J/\psi$ s are not dissociated at RHIC, the LHC  $J/\psi$  measurements should be conclusive on the matter. The LHC is expected to achieve sufficient energy density in nuclear collisions to cause the melting of the direct  $J/\psi$  contribution even if  $T_{\text{dissoc}} \approx 2T_c$ , while regeneration models typically predict a large enhancement at the LHC with respect to RHIC, due to the larger number of  $c\bar{c}$  pairs produced. It is believed that these opposite behaviors at higher energy will allow discrimination between the regeneration and sequential dissociation pictures.

#### 2.4.5 Cold Nuclear Matter Contribution

In order to unequivocally refer to the measured  $J/\psi$  suppression as coming from a quark-gluon plasma, it is essential to compare to the suppression that is known to be caused by the interaction of the  $c\bar{c}$  with normal cold nuclear matter. This has been done in two ways in [40], first by projecting the nuclear PDF and break-up cross section model of the  $d$ +Au data to Au+Au collisions, and secondly by using the  $d$ +Au data itself to form a prediction.

Figure 2.19:  $R_{AA}$  projections using the 2003  $d$ +Au data for both (a) Cu+Cu and (b) Au+Au, overlaid on the PHENIX data points from the 2004 Au+Au Run and 2005 Cu+Cu Run. Taken from [40].



In the first case, the  $\sigma_{br}$  extracted from fits to the  $d$ +Au data is combined with a Glauber

Monte Carlo simulation of the  $A+A$  collision and a simulation of the PHENIX trigger and centrality selection to extrapolate to  $R_{AA}$  in Cu+Cu and Au+Au collisions. The resulting curves and one-sigma uncertainty regions are shown in Figure 2.19. As can be seen, due to the large uncertainties the suppression in Cu+Cu collisions and at mid-rapidity in Au+Au collisions is statistically consistent with cold nuclear matter suppression. It is only at forward rapidity in Au+Au that the suppression exceeds that of the CNM projection by at least 2-sigma.

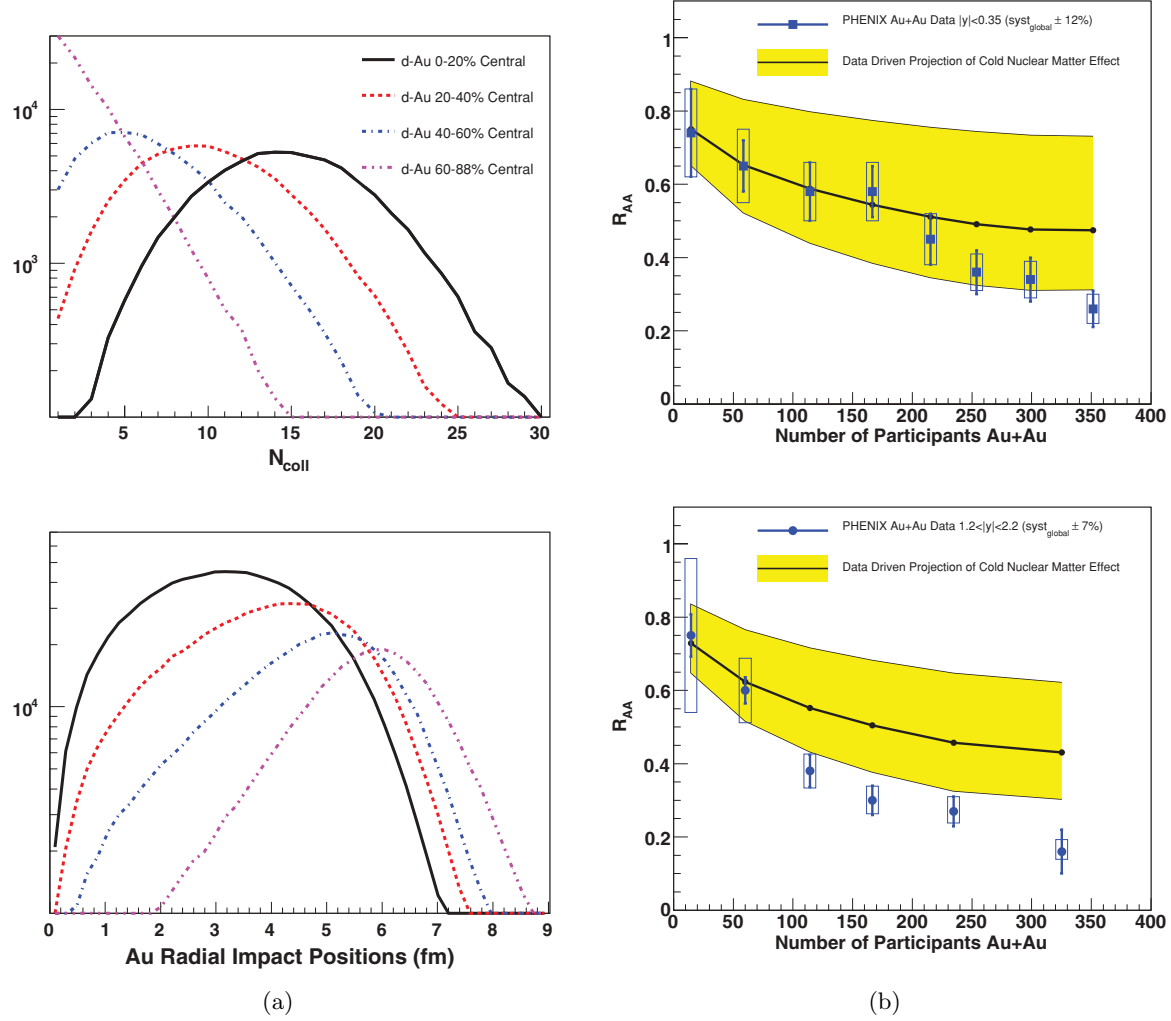
In the second case it is assumed that the CNM effects at a given rapidity in a Au+Au collision would be the product of the measured  $R_{dAu}$  at that rapidity in  $d+Au$  collisions and the  $R_{dAu}$  at the opposite rapidity (equivalent to a Au+ $d$  collision). This model has the advantage of not assuming a particular shadowing model or break-up cross section, but instead relies directly upon the impact parameter-dependence of the measured data. This is combined with a Au+Au Glauber MC in which the radial position of a given nucleon-nucleon collision is explicitly known, and the total  $R_{AA}$  is calculated for various centrality bins (or  $N_{part}$  bins). The distributions of  $N_{coll}$  and the radial impact position are shown in Figure 2.20(a) for the four  $d+Au$  centrality bin. The parametrization of the modification factor as a function of the radial position is widely varied in order to produce a one-sigma uncertainty band for the projected  $R_{AA}$ . The resulting projections are shown in Figure 2.20(b). Similar to the previous case, the suppression at mid-rapidity is consistent with CNM effects. The forward rapidity suppression is consistent with the CNM projection at about the two-sigma level.

Both of the previous two projections would benefit greatly from higher-precision  $d+Au$  data. In 2008 PHENIX recorded a factor of  $\sim 30$  more  $d+Au$  data than in the 2003 run. The final analysis of this data should yield much better CNM projections for comparison to Au+Au suppression.

#### 2.4.6 Suppression vs. Transverse Momentum

In addition to the  $N_{part}$  distributions of Figure 2.14, in 2004 PHENIX also measured  $J/\psi$   $R_{AA}$  as a function of transverse momentum. The results are shown in Figure 2.21 in four broad bins of centrality, for both forward and mid-rapidities.

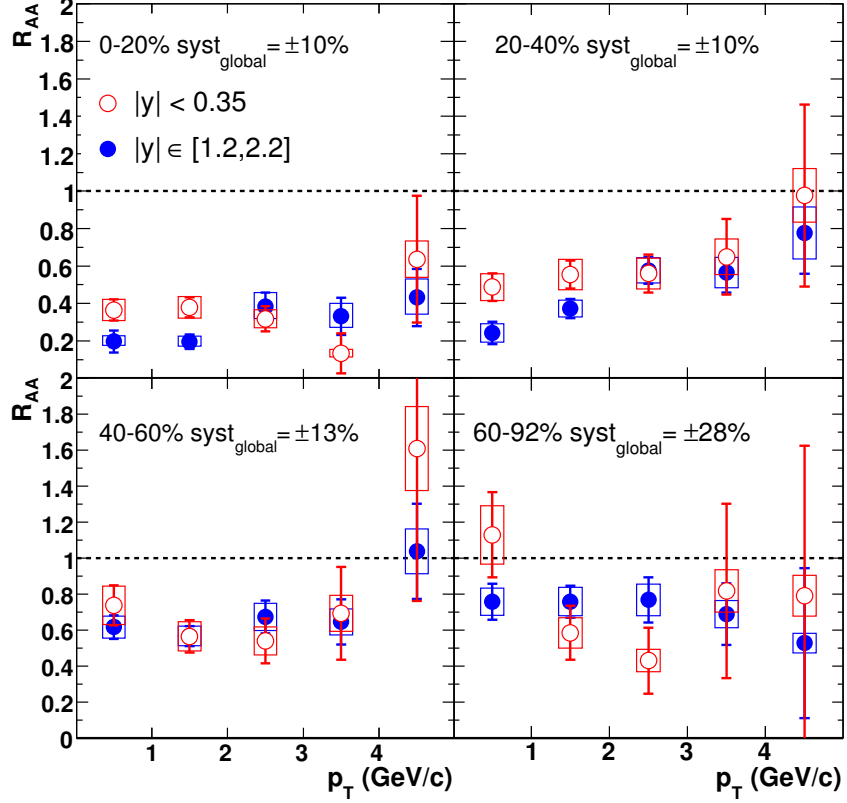
Figure 2.20: Left (a):  $N_{\text{coll}}$  (top) and Au nucleus radial impact position (bottom) for the four broad  $d+\text{Au}$  centrality classes. Right (b):  $R_{\text{AA}}$  projections using the 2003  $d+\text{Au}$  data for both  $\text{Cu}+\text{Cu}$  and  $\text{Au}+\text{Au}$ , overlaid on the PHENIX data points from the 2004  $\text{Au}+\text{Au}$  Run and 2005  $\text{Cu}+\text{Cu}$  Run.



Recent theoretical predictions and experimental results have driven interest in whether  $J/\psi$   $R_{\text{AA}}$  at high  $p_{\text{T}}$  ( $> 5$  GeV/c) flattens out, drops further, or increases to 1.

One source of such interest is the so-called “Hot Wind Model” of Liu, Rajagopal, and Wiedemann [51]. They make use of AdS/CFT correspondence to calculate the screening length  $L$  in a hot medium for a moving heavy  $q\bar{q}$ -pair in  $\mathcal{N}=4$  super Yang-Mills theory. As a result, they find a  $1/\sqrt{\gamma}$ -dependence in the screening length, resulting in  $J/\psi$ s at higher  $p_{\text{T}}$  being more suppressed.

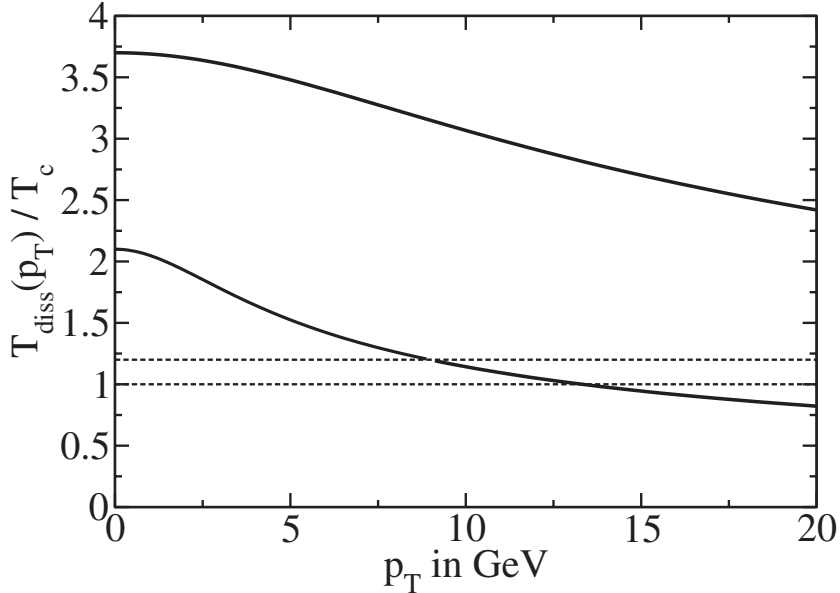
Figure 2.21:  $R_{AA}$  as a function of transverse momentum at (blue) forward and (red) mid-rapidities, in four centrality bins.



This is plotted as a modification to the dissociation temperature in Figure 2.22. As the screening length shrinks with increasing momentum, the  $c\bar{c}$  will become unbound at lower and lower temperatures, implying that  $R_{AA}$  should decrease as a function of  $p_T$ . Additionally, it was pointed out by T. Gunji *et al.* [52] that there should be a relatively sharp turn-on in the suppression at the  $p_T$  where the dissociation temperature is less than the temperature of the medium.

The two-component model of Zhao and Rapp [53] is the source of another recent prediction of  $J/\psi$   $R_{AA}$  vs.  $p_T$ . They incorporate both direct  $J/\psi$  production and coalescence of  $c\bar{c}$  pairs at hadronization time. For the direct component they use a Glauber model with a nuclear break-up cross section to initially distribute the  $J/\psi$ s, and a transport model to propagate them through the medium. The normalization of the coalescence component is determined by the number of  $c\bar{c}$  pairs produced in the collision, while the kinematics of the resulting  $J/\psi$ s are calculated via a blast-wave

Figure 2.22: The dissociation temperature as a function of transverse momentum in the Hot Wind model [51]. The top curve is the dissociation temperature for the  $\Upsilon$ , while the bottom curve is for the  $J/\psi$ .



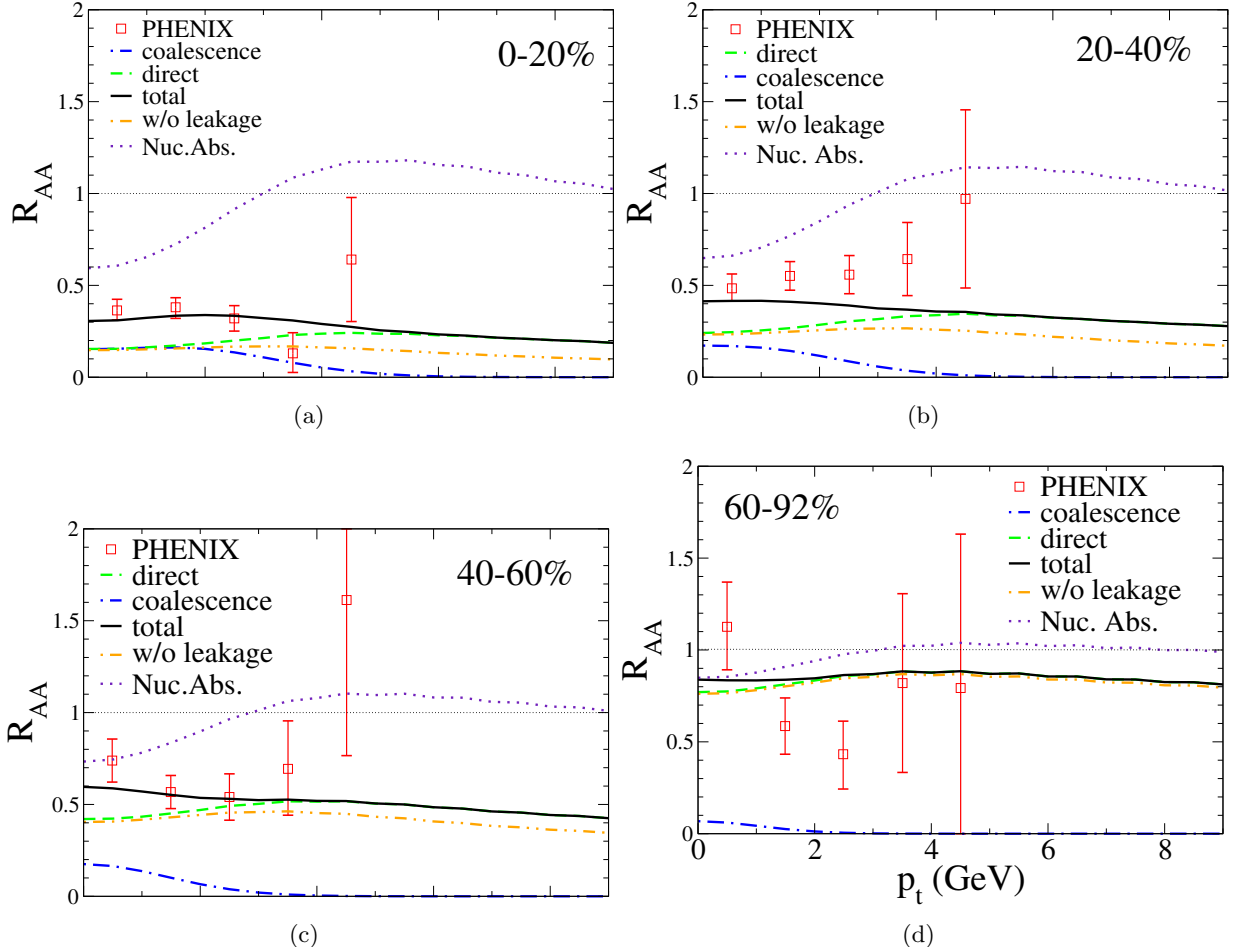
formula, which assumes the charm quarks flow along with the thermalized medium. The resulting  $p_T$  distributions from both components, as well as the sum, are shown in Figure 2.23 and compared to PHENIX Au+Au data.

While experiments have struggled to collect enough Au+Au data to measure  $R_{AA}$  at high  $p_T$ , there have been recent results from Cu+Cu data for  $R_{AA}$  at  $p_T > 5$  GeV/c. STAR measured  $J/\psi$   $R_{AA}$  using the 2005 Cu+Cu dataset in two bins covering  $5 < p_T < 8$  GeV/c [54], and found  $R_{AA}$  to be above unity for both 0-60% and 0-20% centralities. This result is shown in Figure 2.24, with the PHENIX Cu+Cu data for comparison. It should be noted, however, that due to the large uncertainties the STAR points are still compatible with  $R_{AA} \sim 0.6$ -0.8 at the 1-sigma level. More statistics will be needed for a precise determination of the high- $p_T$  behavior of  $R_{AA}$ .

## 2.5 Motivation for the Current Analysis

The overview presented in this chapter summarized the current state of  $J/\psi$  affairs, both experimental and theoretical. It is clear that more precise models and measurements are needed

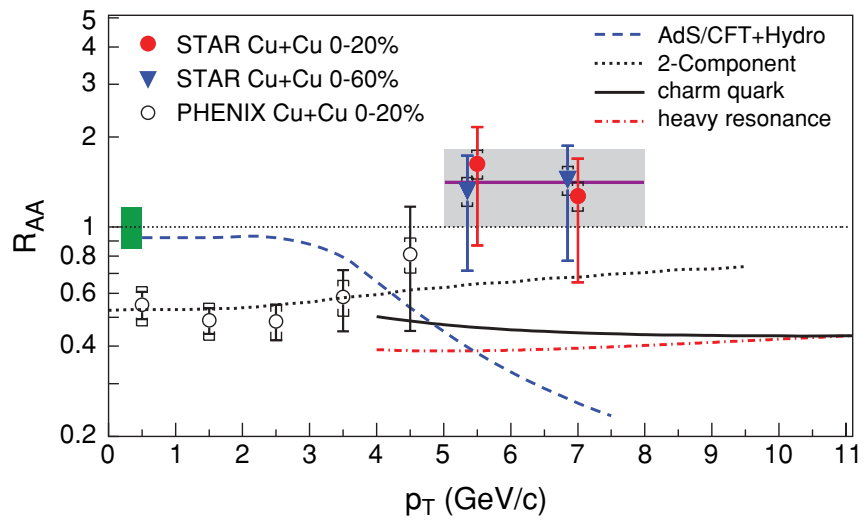
Figure 2.23:  $J/\psi R_{AA}$  vs.  $p_T$  as calculated in a two-component model [53]. Also shown are the separated components of  $J/\psi$ s from direct production and those from coalescence. Overlaid are the PHENIX 2004 Au+Au data.



before we can fully disentangle the various effects involved in  $J/\psi$  production in heavy ion collisions. Therefore there is ample motivation to make more precise measurements of  $J/\psi$  suppression as functions of both impact parameter and transverse momentum.

To this end, the current analysis makes use of PHENIX Au+Au data recorded during 2007 that has roughly 3 times the integrated luminosity as the previously-published 2004 dataset. It is hoped that the increase in statistics will lead to better constraints on the various theoretical models, as well as encourage further refinement of said models.

Figure 2.24:  $J/\psi R_{AA}$  vs.  $p_T$  in  $\sqrt{s_{NN}}=200$  GeV/u Cu+Cu collisions as measured by STAR [54] in 0-20% and 0-60% centralities. Also included is the curve from the two-component model of Zhao and Rapp [53], as well as the Hot Wind Model. Included for comparison are the PHENIX 2005 Cu+Cu data points.



## Chapter 3

### Experimental Setup

#### 3.1 The Relativistic Heavy Ion Collider

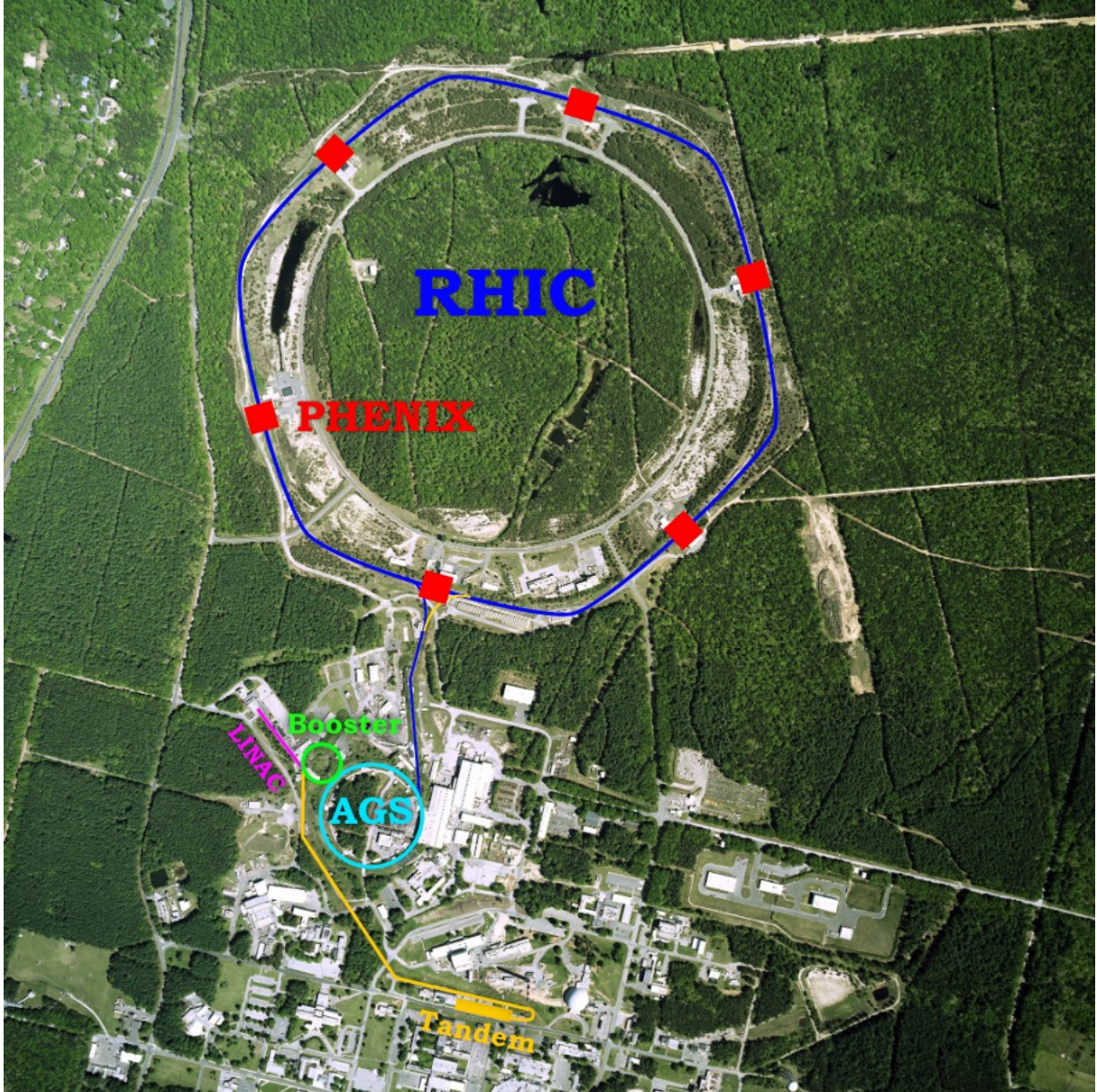
The Relativistic Heavy Ion Collider (RHIC) is a superconducting hadron collider located at Brookhaven National Laboratory in Upton, New York. It is capable of colliding gold ions over a range of nucleon-nucleon center-of-mass energies  $\sqrt{s_{NN}} = 7.7\text{--}200$  GeV/u, as well as protons up to  $\sqrt{s} = 500$  GeV. There are six points of intersection of the twin concentric beamlines, four of which are occupied by experiments. Figure 3.1 is a recent aerial view of RHIC and its supporting facilities.

The process for accelerating ions to RHIC energies is as follows: gold ions are first accelerated by a Tandem Van de Graaff to 1 MeV/u, then by the Booster Synchrotron to 95 MeV/u, and finally by the Alternating Gradient Synchrotron (AGS) to 10.8 GeV/u, the injection energy for RHIC. At this point, the ions have been stripped of all electrons, and are injected into the RHIC rings, and finally accelerated to the desired energy for collisions.

RHIC runs for several months per year, typically in the winter but occasionally going all the way through June. The convention at RHIC is to refer to the running period of each year as a “Run”, and the sequential numbering of the Runs fortuitously corresponds to the winter/spring in which the data was taken (*e.g.* Run 7 corresponds to the data taken in spring of 2007). The RHIC running periods to date are listed in Table 3.1.

There are four major experiments located at RHIC: BRAHMS, PHENIX, PHOBOS, and STAR. BRAHMS makes use of two small, mobile spectrometers to cover a wide kinematic range.

Figure 3.1: Aerial photograph of RHIC (top) and other accelerator facilities taken in 2010.



PHOBOS is optimized for measuring charged-particle multiplicity over almost the full  $4\pi$  solid angle, charged-particle tracking in two spectrometers, and particle identification (PID) for low- $p_T$  ( $\lesssim 2$  GeV/c)  $\pi, K, p$ . STAR is based around a large time projection chamber (TPC) and solenoidal magnet, which provides excellent tracking and PID. PHENIX is the focus of this analysis, and is described in more detail below.

Table 3.1: RHIC Running Periods with colliding species, CMS energy, and luminosity delivered (to all experiments).

Dates	Designation	Colliding Species	$\sqrt{s_{NN}}$ (GeV/u)	Delivered Luminosity
3/00-9/00	Run 1	Au+Au	130	$20 \mu\text{b}^{-1}$
5/01-1/02	Run 2	Au+Au	200	$258 \mu\text{b}^{-1}$
		Au+Au	19.6	$0.4 \mu\text{b}^{-1}$
		p+p	200	$1.4 \text{ pb}^{-1}$
12/02-5/03	Run 3	d+Au	200	$73 \text{ nb}^{-1}$
		p+p	200	$5.5 \text{ pb}^{-1}$
11/03-5/04	Run 4	Au+Au	200	$3.53 \text{ nb}^{-1}$
		Au+Au	62.4	$67 \mu\text{b}^{-1}$
		p+p	200	$7.1 \text{ pb}^{-1}$
11/04-6/05	Run 5	Cu+Cu	200	$42.1 \text{ nb}^{-1}$
		Cu+Cu	62.4	$1.5 \text{ nb}^{-1}$
		Cu+Cu	22.4	$0.02 \text{ nb}^{-1}$
		p+p	200	$29.5 \text{ pb}^{-1}$
2/06-6/06	Run 6	p+p	200	$88.6 \text{ pb}^{-1}$
		p+p	62.4	$1.05 \text{ pb}^{-1}$
2/07-6/07	Run 7	Au+Au	200	$7.25 \text{ nb}^{-1}$
11/07-3/08	Run 8	d+Au	200	$437 \text{ nb}^{-1}$
		p+p	200	$38.4 \text{ pb}^{-1}$
2/09-7/09	Run 9	p+p	500	$110.4 \text{ pb}^{-1}$
		p+p	200	$114 \text{ pb}^{-1}$
12/09-6/10	Run 10	Au+Au	200	$10.3 \text{ nb}^{-1}$
		Au+Au	62.4	$0.544 \text{ nb}^{-1}$
		Au+Au	39	$0.206 \text{ nb}^{-1}$
		Au+Au	7.7	$2.1 \mu\text{b}^{-1}$
		Au+Au	11.5	$4.7 \mu\text{b}^{-1}$

### 3.2 PHENIX

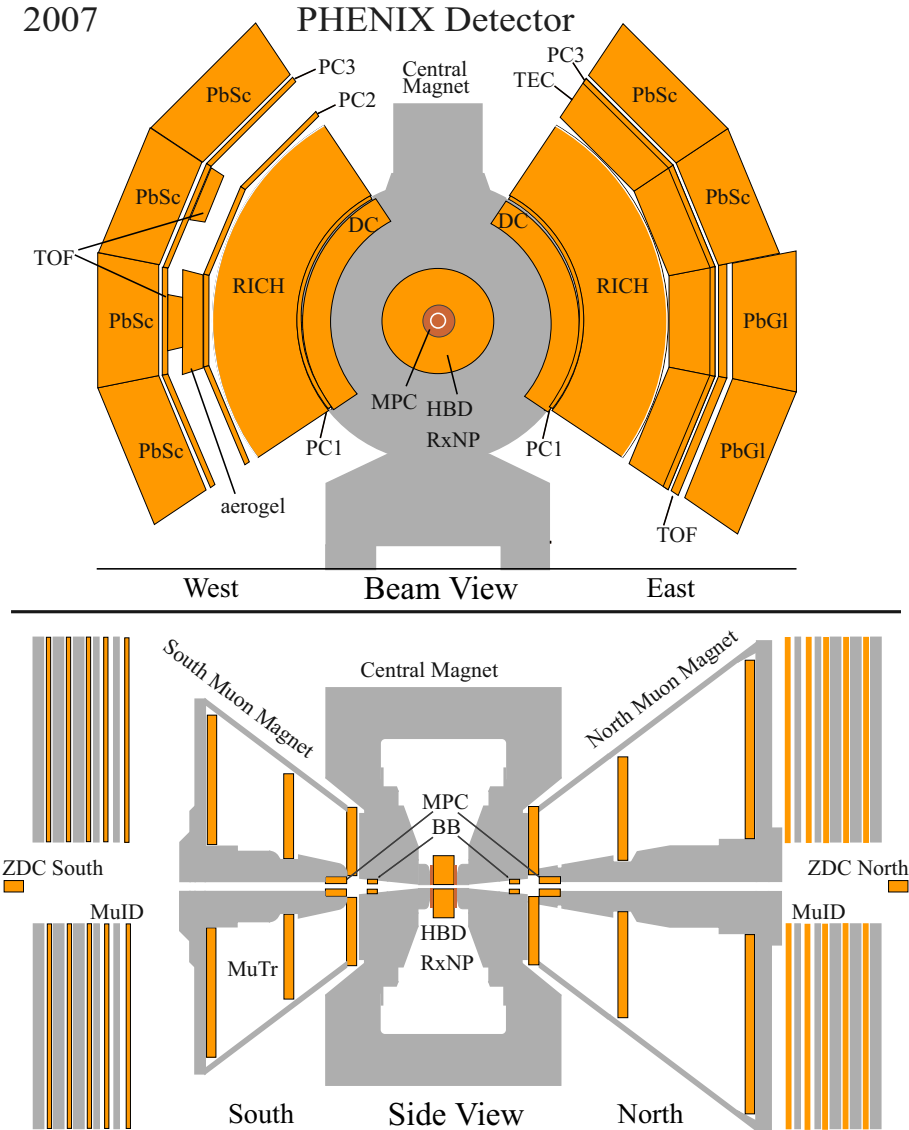
The PHENIX<sup>1</sup> experiment consists of a multitude of detectors, mostly as part of four spectrometers or “arms”: the East and West Central Arm detectors, and the North and South Muon Arm detectors. There are also several “global” detectors for measuring global event characteristics such as multiplicity and collision vertex. For a general overview, see [55].

The Central Arm detectors are located on either side of the interaction region, so that they

<sup>1</sup> Pioneering High-Energy Nuclear Interaction eXperiment

are centered around  $y = 0$  with a coverage of roughly  $-0.35 < \eta < 0.35$  in pseudo-rapidity. They consist of the Pad Chambers and Drift Chambers for particle tracking [56], the ElectroMagnetic Calorimeter [57] and Time-of-Flight detectors for general particle ID, and the Ring-Imaging Cherenkov Detector for electron ID [58]. A beams-eye view of the Central Arm detector layout is shown in the top of Figure 3.2.

Figure 3.2: PHENIX detector configuration for Run-7, where the orange regions are the actual detector volumes. Top half is the x-y plane at  $z = 0$ , which shows the Central Arm detectors. Bottom half is the y-z plane cutaway view, showing the Muon Arms and global detectors.



The Muon Arm spectrometers are located further out along the beam line in order to cover

an angular range from the beam-line of about  $12^\circ$ – $35^\circ$ , which corresponds to forward and backward rapidity ranges of roughly  $1.2 < |y| < 2.2$  for  $J/\psi \rightarrow \mu\mu$  [59]. Both arms consist of a Muon Tracker (MUTR) for tracking and Muon Identifier (MUID) for muon identification. As these detectors are used in the current analysis, they are described in more detail below.

Additionally, there are several detectors used for measuring global variables and for triggering [60]. The Beam Beam Counters (BBCs) cover roughly  $3.0 < |\eta| < 3.9$ , while the Zero-Degree Calorimeters (ZDCs) are located along the  $z$ -axis. Finally, the Reaction Plane detector (RXNP) was first added for Run 7 specifically for measuring the event-by-event reaction plane (the plane formed by the impact parameter vector and the  $z$ -axis). A cutaway side view of the Muon Arm detector layout is shown in the bottom of Figure 3.2, along with the BBC, ZDC, and RXNP.

The Muon Arms are designed in the traditional muon detector fashion, with plenty of steel to absorb the hadronic background particles and take advantage of the penetrating ability of muons. For this purpose the pole tips of the Central Magnet (which are located between the interaction point and the Muon Tracker; see Figure 3.2) consist of 60 cm of low-carbon steel and a 20 cm brass “nosecone” pointed towards the interaction region. The back-plate of the Muon Magnets adds 20 cm of low-carbon steel in the South Arm, and 30 cm in the North Arm. Finally, there are four layers of steel in the MUID, with thicknesses of (in order) 10 cm, 10 cm, 20 cm, and 20 cm, that particles must pass through to reach the last detecting layer.

The minimum momentum required for a muon to penetrate to the last gap can be calculated by integrating the Bethe-Bloch formula for electronic energy loss for heavy particles passing through matter [20]. That formula is:

$$-\left\langle \frac{dE}{dx} \right\rangle = K z^2 \frac{Z}{A} \left[ \frac{1}{2\beta^2} \ln \frac{2m_e c^2 \beta^2 \gamma^2 T_{max}}{I^2} - 1 - \frac{\delta(\beta\gamma)}{2} \right] \quad (3.1)$$

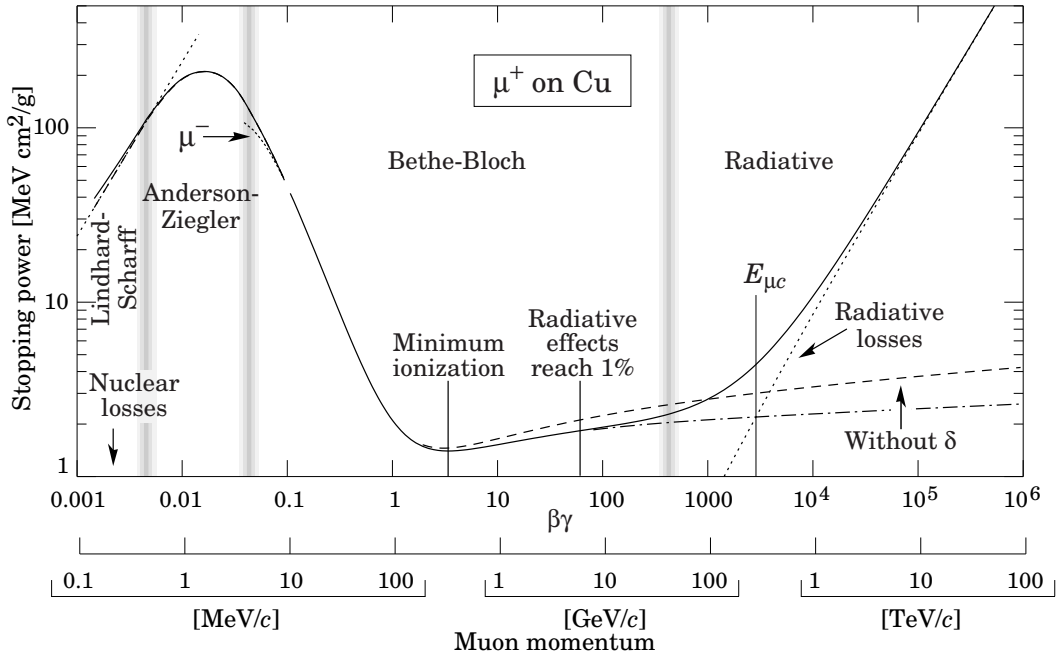
where  $E$  is the energy of the incident particle in MeV,  $K$  is 0.307075 MeV cm<sup>2</sup>,  $ze$  is the charge of the incident particle,  $\beta$  and  $\gamma$  are  $v/c$  and  $1/\sqrt{1-\beta^2}$  for the incident particle,  $Z$  and  $A$  are the atomic number and atomic mass of the absorber,  $I$  is the mean excitation energy of the absorber (286 eV for iron),  $T_{max}$  is the maximum kinetic energy which can be imparted to a free electron in

a single collision, and  $\delta(\beta\gamma)$  is the density effect correction.  $T_{max}$  is given by:

$$T_{max} = \frac{2m_e c^2 \beta^2 \gamma^2}{1 + 2\gamma m_e/M + (m_e/M)^2} \quad (3.2)$$

for an incident particle of mass  $M$ .

Figure 3.3: Stopping power  $\langle dE/dx \rangle$  for  $\mu^+$  in copper, as detailed in [20]. The region between the shaded bands labeled Bethe-Bloch is where Equation 3.1 is applicable.



One of the primary goals of the many layers of steel is to reduce the background of pions from the event vertex that are mis-reconstructed as muons. The  $\mu/\pi$  ratio due to weak decays before the nosecone and absorber is  $\sim 10^{-3}$ , and the design goal was to reduce this further to  $2.5 \times 10^{-4}$  so that the background muons are the largest remaining contributor. The total thickness of steel was chosen to achieve this level of suppression for the punch-through pions.

For a muon to penetrate to the last gap of the South Muon Arm, it must pass through 140 cm of steel and 20 cm of brass, while the North Muon Arm has 150 cm of steel with 20 cm of brass. This results in a minimum momentum of 2.31  $\text{GeV}/c$  in the South Arm and 2.45  $\text{GeV}/c$  in the North Arm, assuming the average  $dE/dx$  of the Bethe-Bloch equation. Of course, muons going into the Muon Arm acceptance see more material due to their non-zero incident angle, but

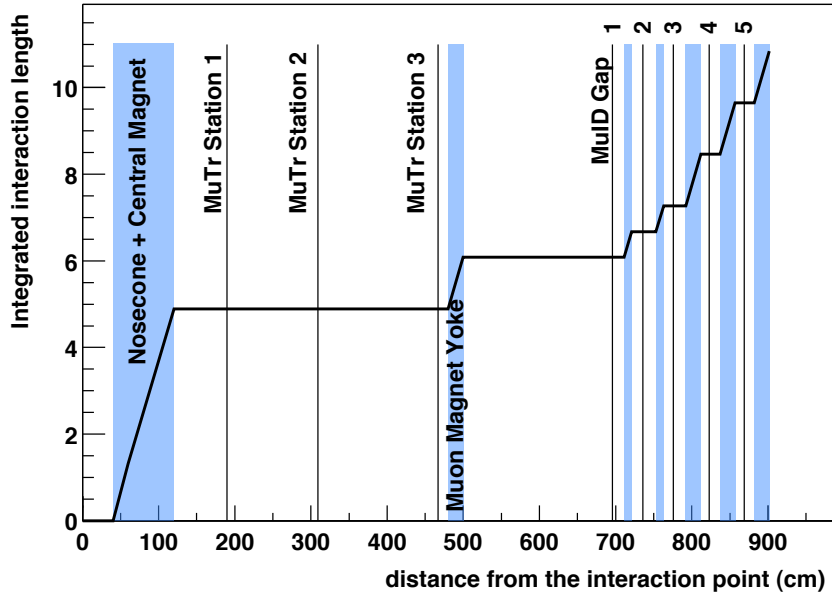
the factor of  $\cos \theta$  for additional material cancels with that in  $p_z = p \cos \theta$ , such that we can treat these numbers as the minimum  $p_z$  instead of total momentum. The number of nuclear interaction lengths contributed by each layer of absorber is shown graphically in Figure 3.4.

### 3.2.1 Muon Tracker

The Muon Trackers (MUTR) are spectrometers situated at forward and backward rapidities with acceptance for  $J/\psi \rightarrow \mu^+ \mu^-$  of roughly  $1.2 < |y| < 2.2$ . The North Arm actually goes out to  $y \approx 2.4$ , but the anodes closest to the beam-line are turned off during Au+Au running to help reduce the high North Arm occupancy, and that is the region that extends the acceptance further out in rapidity.

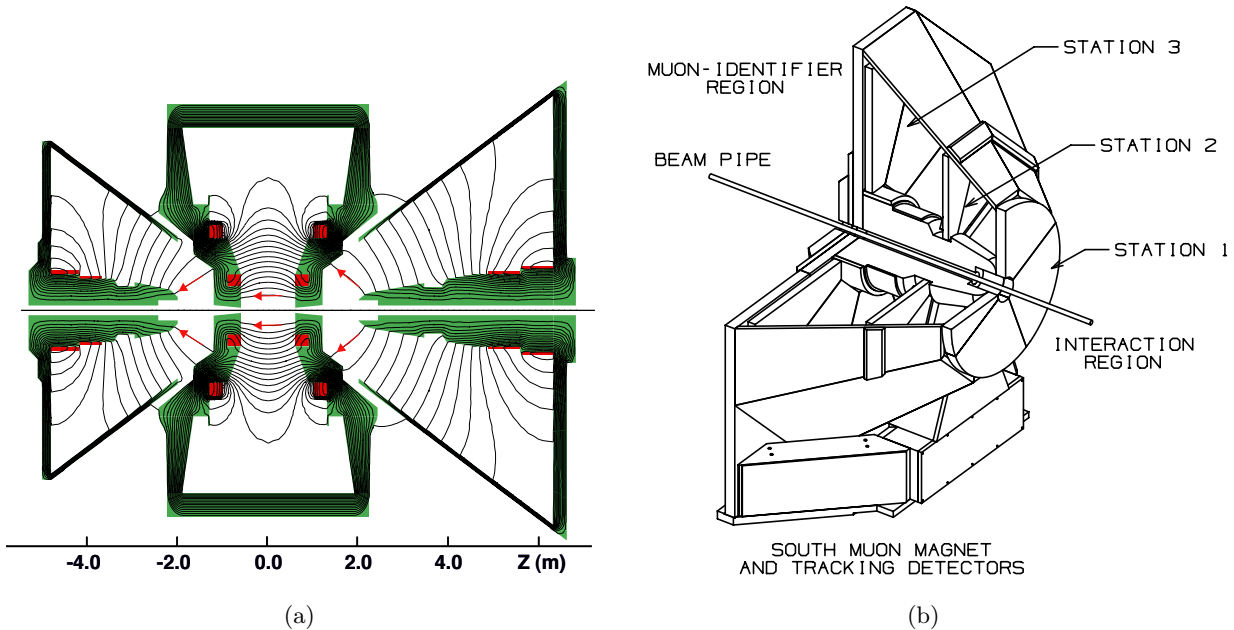
The MUTRs consist of multiple tracking layers in a roughly radial magnetic field (see Figure 3.5(a)), such that particles coming from the interaction point will bend mostly in the  $\phi$ -direction. The tracking layers are made up of two layers of 5 mm-wide cathode strips on either side of a layer of

Figure 3.4: Integrated nuclear interaction lengths of steel in the South Muon Arm as a function of the distance from the interaction point. Hatched regions represent absorber layers, while lines indicate the rough position of tracking layers [61].



anode wires, the combination of which is referred to as a gap or gas gap. The layers are grouped into three Stations, with Stations 1 and 2 having three gaps and Station 3 having two gaps, for a total of 8 gaps and 16 cathode planes. A cutaway view of the South MUTR is shown in Figure 3.5(b).

Figure 3.5: Left: Magnet field lines in PHENIX [62]. Red regions represent the coils used to generate the fields. Right: Drawing of the South MUTR with a portion of the detector cut out to show the internal structure.



The anode wires are oriented in the azimuthal direction, and are not included in the data output stream. The cathode strips of one plane in each gap are perpendicular to the wires (roughly radially outward from the beam pipe), while the other plane are set at a small ( $< 12^\circ$ ) “stereo” angle with respect to the non-stereo plane. The stereo angle for each gap is listed in Table 3.2. This was done to maximize the measurement of the  $\phi$ -position, since that is the bending direction in the  $B$ -field. The gas mixture that flows within the gaps is 50% Ar + 30% CO<sub>2</sub> + 20% CF<sub>4</sub>, and the nominal operating high voltage for the anode wires is 1850 V.

Stations 2 and 3 were constructed as separate octants, with the strips oriented together within each half-octant. Due to Station 1’s smaller size, it was constructed in quadrants, but the strip layout was still done in octants to match the other Stations. In order to maintain good momentum

Table 3.2: Orientations of the stereo planes

Station	Gap	angle (degrees)
1	1	-11.25
	2	+6
	3	+11.25
2	1	+7.5
	2	+3.75
	3	+11.25
3	1	-11.25
	2	-11.25

resolution, Station 2 was required to be  $\leq 0.1\%$  of a radiation length to minimize interactions with muons passing through. To accomplish this, the cathodes of Station 2 are made of etched copper-coated Mylar foil, held taut by a thick outer aluminum support frame. Station 1 is 1.25m from inner radius to outer radius, while Station 3 is 2.4m. The Muon Arm dimensions in the  $z$ -direction can be seen in the schematic of Figure 3.6.

### 3.2.2 Muon Identifier

The Muon Identifiers (MUID) consist of layers of Iarocci streamer tubes interleaved with layers of steel. The purpose of the MUID is to reject hadron tracks by requiring the candidate tracks to pass through multiple layers of steel, and to provide fast muon and dimuon triggers, although these are not used in Au+Au collisions due to their low rejection power in high multiplicity events, and because the Au+Au collision rate is low enough that the minimum bias BBC trigger (which doesn't select any specific physics process) is adequate.

Iarocci tubes were chosen for the detector layers for their reliability and inexpensiveness when covering a large area. Within each 8.35 cm x 1.3 cm plastic casing are eight channels, each with a 100  $\mu\text{m}$  CuBe anode wire down the center and graphite coating to form the cathode. The eight wires are electrically connected to form a single output. The tubes are arranged in “two-packs” of two staggered tubes offset by half a channel’s width, and are logically ORed together, allowing one tube to cover the other’s dead area, resulting in higher overall efficiency. A cutaway view of a

Figure 3.6: PHENIX side view with distances to MUTR tracking layers included.

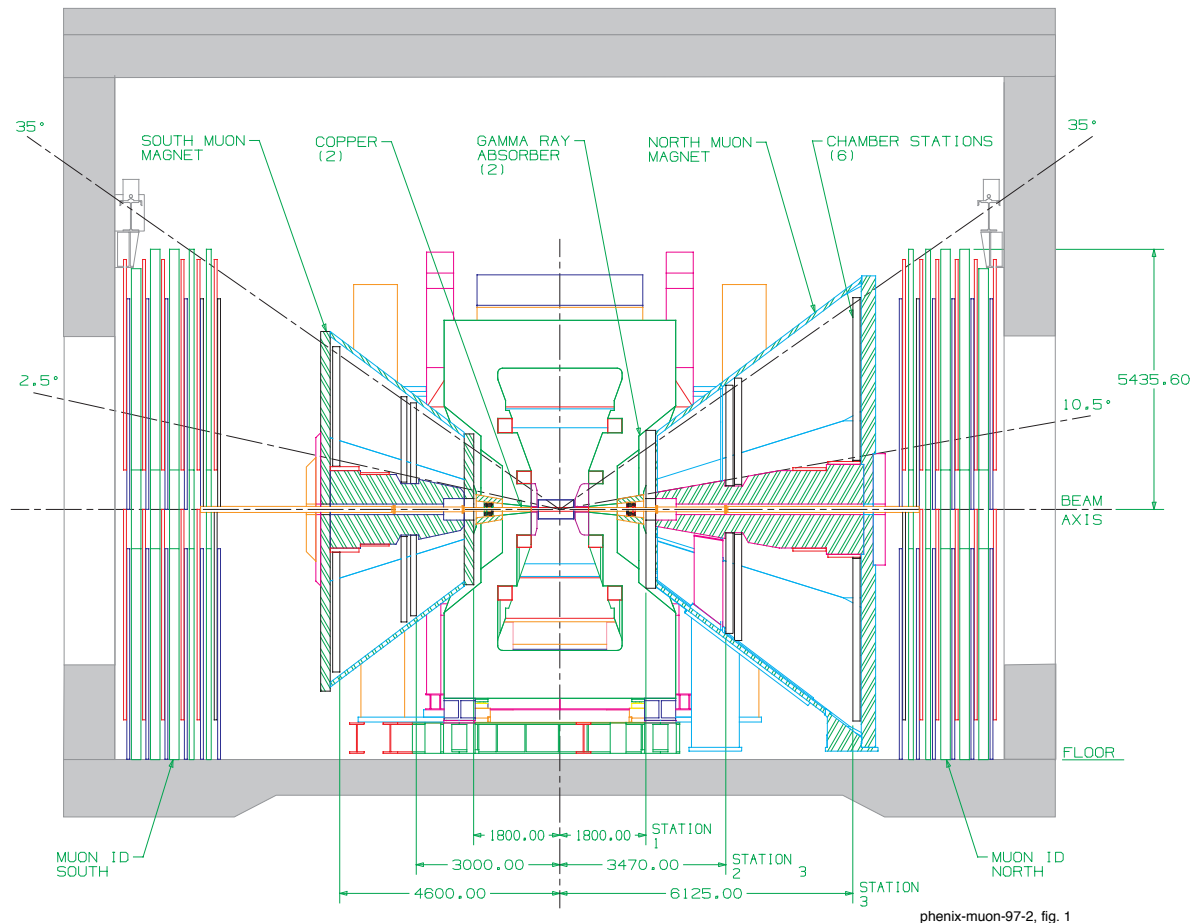
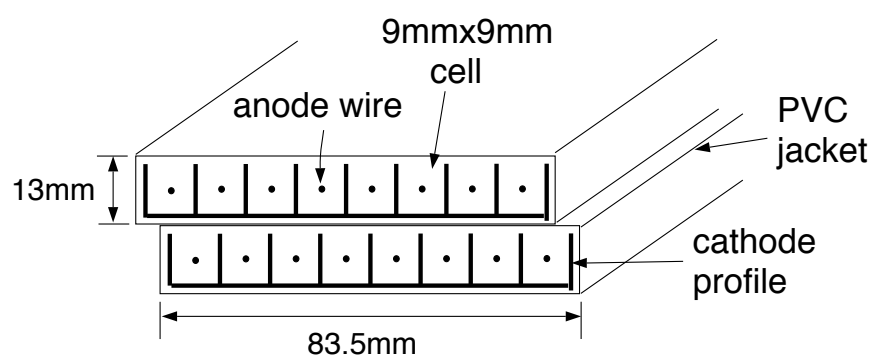


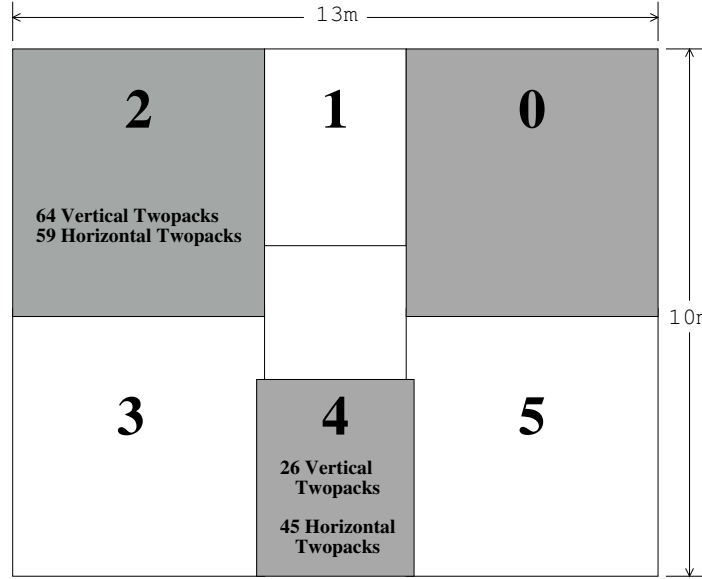
Figure 3.7: Cutaway view of MUID two-pack made up of Iarocci tubes.



two-pack is shown in Figure 3.7.

The two-packs are combined into panels, each with a horizontal layer and a vertical layer of tubes. Six panels are located in each gap between layers of steel in the MUID, and the panels slightly overlap so as to reduce dead area. An example gap is shown in Figure 3.8.

Figure 3.8: Layout of MUID panels in the South Arm as seen from the interaction point. Panels are hung in two layers, with the shaded panels mounted closer to the interaction point.

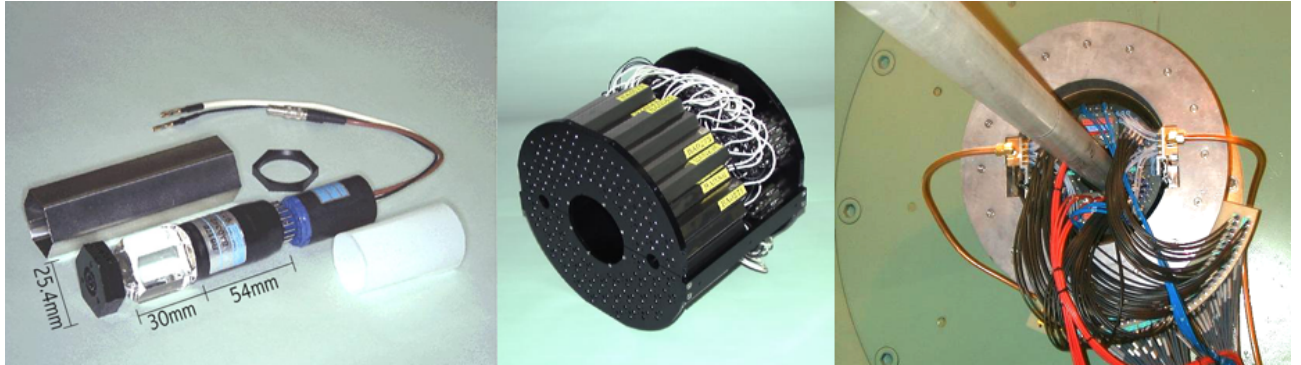


### 3.2.3 Beam-Beam Counter

The North and South Beam-Beam Counters (BBC) are located 144 cm from the center of the interaction region, directly behind the Central Magnet. They are also located with their inner radius only 1 cm away from the beam-line, so that they lie at very forward rapidity ( $3.0 < |\eta| < 3.9$ ). They consist of an arrangement of 64 1-inch diameter photo-multiplier tubes (PMTs) arranged behind 3-inch quartz radiators to provide Cherenkov light as particles impact the Counter.

The primary function of the BBCs is to provide high-resolution time measurements of the collision. The time-difference between the BBCs is used to find the  $z$ -position, and the average gives time of the collision. The crossing time is then used in conjunction with the time-of-flight detectors in the Central Arms to calculate the particle velocity. Particle ID can then be done using

Figure 3.9: Left: single BBC photo-multiplier tube. Middle: Fully constructed BBC. Right: BBC installed behind the Central Magnet.



that velocity and the momentum from the spectrometer. The timing resolution of one BBC is  $52 \pm 4$  ps.

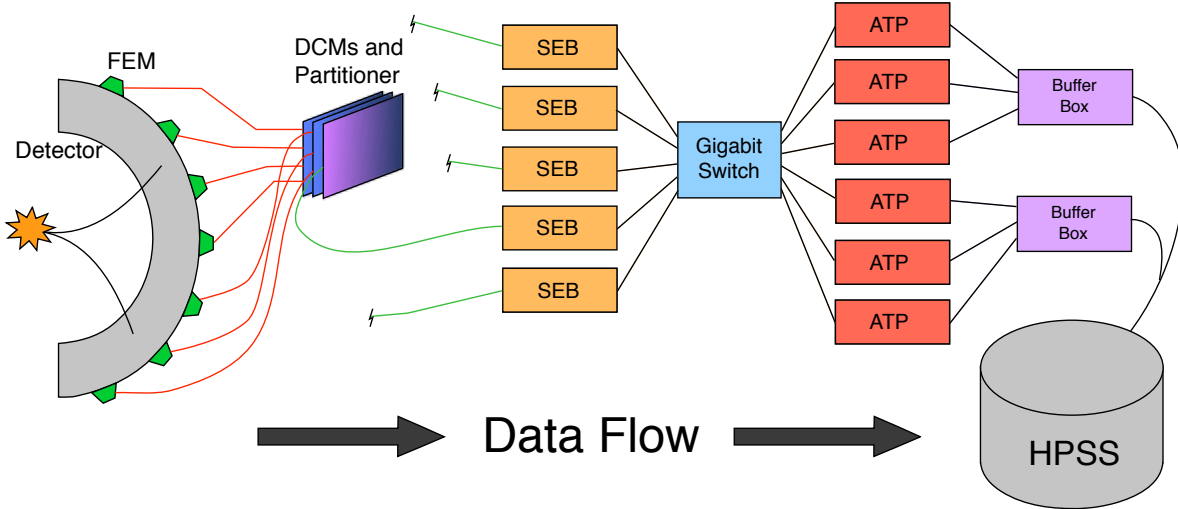
The BBCs are also used as a minimum-bias trigger in Au+Au events, where a requirement of two tubes firing in each Counter allows us to record 93% of inelastic collisions. Additionally, the charge deposited in the BBC is used to gauge the impact parameter of the collision in  $d$ +Au and Au+Au events. The procedure for this is described in Section 3.3.1.

### 3.2.4 The Data Acquisition System

The PHENIX Data Acquisition System (DAQ) is designed to record data at high rates and volumes for the large-multiplicity environment at RHIC. The overall layout of the data-flow is shown in Figure 3.10. Front End Modules (FEMs) located on or near each detector collect and process the analog signals, such as the charge deposited on a cathode wire, or the electron avalanche in a photo-multiplier tube.

Hardware-based triggers are used to quickly decide whether there was a collision for a given bunch crossing, and whether interesting physics processes took place and the event should be recorded. The individual triggers, known as Local Level 1 (LL1) triggers, decide based on the output of one or two detector subsystems, *e.g.* the minimum bias trigger using the BBC, or the dimuon trigger using the MUID. They therefore receive the data from those detectors for every

Figure 3.10: The data collecting portion of the PHENIX data acquisition system.

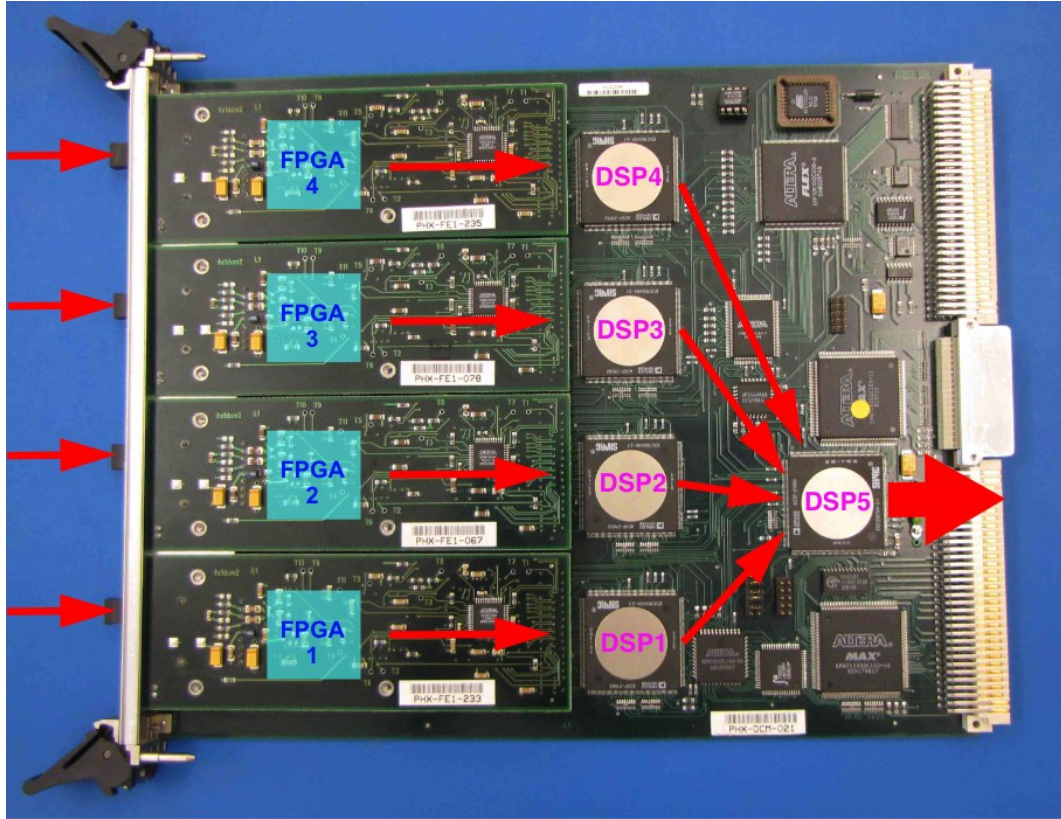


bunch crossing and send their decision to the Global Level 1 (GL1), which decides whether the event should be recorded or not. The decision to record is then passed back to the FEMs, which send their data over fiber optic connections to the Data Collection Modules (DCMs).

The detector signal from each crossing is stored in either analog or digital buffers in the FEMs for up to 40 crossings. Within this time, the triggers must decide whether to issue an “accept” signal to the FEMs, at which point they would send up the signal from the buffer corresponding to the same bunch crossing as the trigger. The RHIC crossing frequency is 9.4 MHz, so there is a bunch crossing in the interaction region every 106 ns. This is too fast for the detector data to be read out (the time to transfer a full event to the DCMs is  $\approx 40 \mu\text{s}$ ), so it was decided to limit the PHENIX trigger accept rate to 12.5kHz, and require the FEMs to buffer enough events to cover the latency between the collision time and the accept-event signal time.

The DCMs consist of four daughtercards with Altera FPGAs attached to the main board, which are piped into four Analog Devices ADSP-21062 SHARC DSPs (1-4), and the data is funneled to a final DSP (DSP5) before being output from the board. An example DCM board is shown in Figure 3.12. The boards are designed to output the data over a custom backplane using the VME64X standard. The FPGAs on the daughtercards are responsible for zero-suppression of the

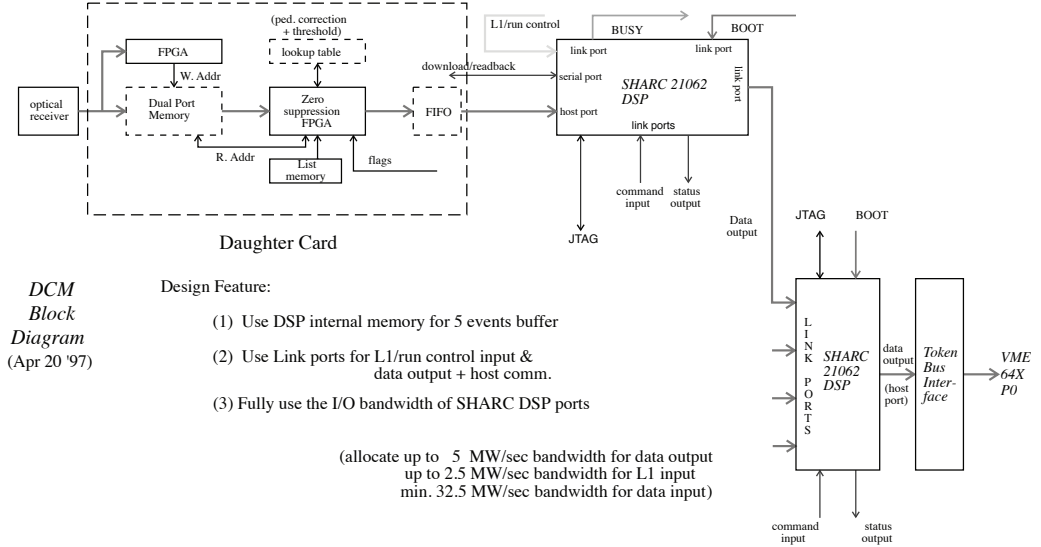
Figure 3.11: Layout of a DCM board with FPGA daughtercards attached. Fiber optic inputs are on the left, connector for VME64X backplane is on the right.



data, which removes samples that are below a threshold low enough to be considered zero signal. They also repackage the data into more efficient formats for some subsystems. The DSPs run at 40 MHz and use binaries programmed in C and assembler, and compiled with Analog Devices VisualDSP. They are typically the throughput-limiting component of the DCMs, so their only task is to repackage the data into the standard PHENIX packet format. The data is transferred from DSPs 1-4 to DSP 5 through the link ports of the DSP, which are capable of transferring 4 bits per clock cycle. This leads to a theoretical maximum throughput of 19.1 MB/s for each of DSP1-4, and a total from the board of 76.4 MB/s.

The event data from several DCMs is collected by a Partitioner board and transferred to a Sub-Event Builder (SEB), which combines the data from a single partition of DCM boards. At this point the data for a single event is spread across many SEBs, which are connected to ATPs via

Figure 3.12: Block diagram of data flow through a DCM board from optical inputs on the left, to the back-plane connector on the right.

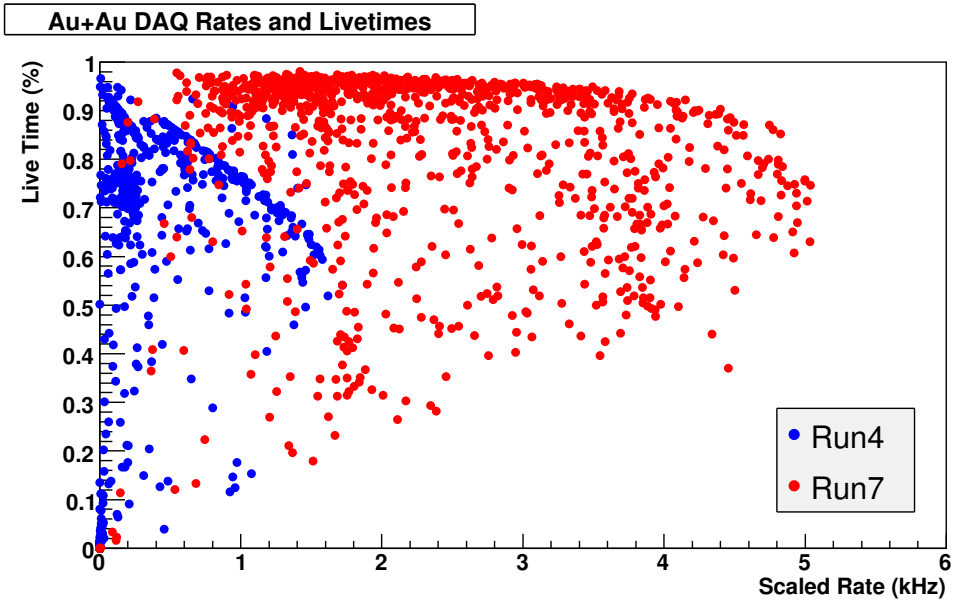


a gigabit Ethernet switch. An ATP is assigned an event number, requests the data for that event from each SEB, and combines all the data for that event. Software Level-2 filters may also be run in the ATPs. The event data is collected from the ATPs and merged into files by six buffer boxes, which are Linux-based storage devices with sixteen hard drives in a RAID array. The buffer boxes store the data locally at the experiment hall until it can be transferred to permanent tape storage in the RHIC High Performance Storage System (HPSS).

Work was done before and during Run 7 to increase the DAQ rate for Au+Au running. As the DAQ is a large parallel, pipelined system, the overall throughput is determined by the slowest component. The DCM throughput is set by the size of the event data, so efforts were made to reduce the size by using more efficient data formats. Although LZO compression is applied to the final data files that are written to disk, this step is too late to affect DAQ performance. The MUTR and EMCAL are two subsystems with large data volume that were found to have formats that could be rearranged to hold the data more compactly with no loss of information. To accomplish this, the DSP output routines were rewritten in assembly code to repack the data before placing it in the link port. The original MUTR format stored one 12-bit ADC sample per 32-bit word, while

the repacked format held two ADC samples per word, resulting in an almost 2-to-1 improvement in data size. The EMCAL data holds one TDC and four ADC 12-bit samples per detector element, so in that case five samples are repacked into three words. The remaining space in both cases is used for the unique 8-bit channel identifier, which is needed when zero suppression is applied and channels are no longer strictly sequential.

Figure 3.13: Comparison of DAQ performance of Run 4 vs. Run 7, both of which were  $\sqrt{s_{NN}}=200$  GeV Au+Au Runs. Plotted is the live time (% of events where the DAQ was ready to record the event) vs. the DAQ archiving rate.



In addition, the per-event overhead in DSP5 was reduced by eliminating extraneous data being transferred in the event header from DSP1-4, and instead loading it into DSP5 at run-time. As a result of these changes the DAQ up through the DCMs was capable of running at or above 5 kHz, and by the end of Run 7 the entire DAQ could run at these rates, as can be seen in the right-most points of Figure 3.13. This is significant, because the min bias trigger rate was at or below 5 kHz for the majority of a store. In Table 3.3, the sizes of the largest packets are listed as they were at the end of the Run. As can be seen, the limiting subsystems were the Hadron Blind Detector (HBD) and Reaction Plane Detector (RXNP), which were newly installed that year, and hot channels in the Drift Chamber (DC). It was found that removing the packets larger than the

Table 3.3: Largest DCM average packet sizes and RMS values at the end of Run 7. Each fiber carries one or two packets to the DCM, and flows through the FPGA and DSP before being combined with other packets from the same event.

Subsystem	Packet Number	Avg Size (bytes)	RMS (bytes)
HBD	22006	1272.8	923.6
DC	3145	1177.6	196.4
DC	3011	1154.4	167.2
DC	3125	1153.2	169.2
HBD	22011	1093.6	795.6
RXNP	23001	1032.0	0.0
HBD	22010	955.6	839.2
MPC	21031	932.0	345.2
MPC	21032	907.2	299.2
MPC	21022	876.8	340.0
BBC	1003	860.0	0.0
BBC	1002	860.0	0.0

RXNP packet increased the DAQ rate to 6.4 kHz, so additional work was done after Run 7 to reduce the data sizes of the HBD, MPC, and RXNP, and fix or remove the hot channels of the DC.

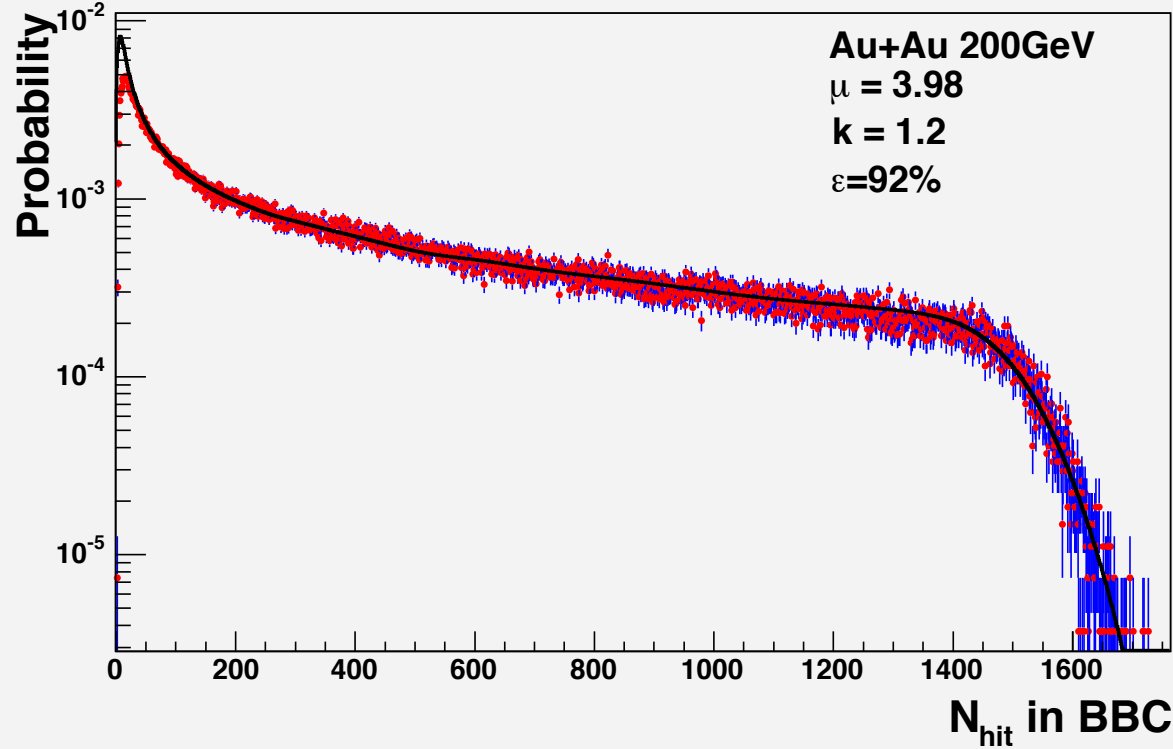
### 3.3 Event Reconstruction

Before a physics analysis of the data can be performed, the physical properties of the events must be reconstructed from the raw data. This typically involves converting the charge deposited on the detector elements back to spatial coordinates of where the particle passed through the detector, followed by combining the coordinates into the particle trajectories, known as tracking. Within a magnetic field, the bending of the trajectory tells us the momentum of the particle. This is the principle behind most spectrometers in high-energy particle physics.

#### 3.3.1 Collision Centrality and Number of Binary Collisions

Because global geometric variables like impact parameter ( $b$ ), the number of participant nucleons ( $N_{\text{part}}$ ), and the number of binary nucleon-nucleon collisions ( $N_{\text{coll}}$ ) are not direct observables, PHENIX categorizes events into percentile bins of multiplicity, ranging from 0-100%, and referred

Figure 3.14: The red and blue histogram is the BBC charge distribution from data, while the black line is the best-fit result from the Glauber simulation.

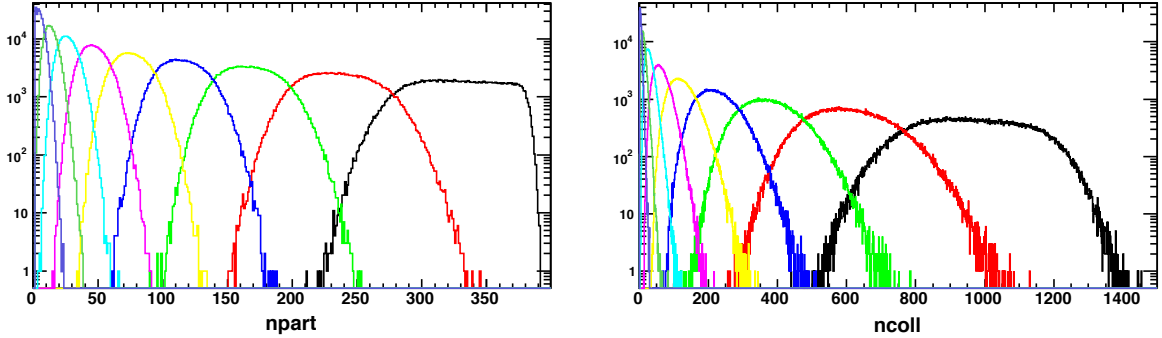


to as “centrality”. This takes advantage of the monotonic scaling between mean multiplicity and  $N_{\text{part}}$ . In other words, the 0-10% centrality bin corresponds to the 10% of collisions with the largest multiplicity in some region. Therefore, by definition, the (per-event) centrality distribution should be flat.

In PHENIX, the centrality is calculated for each event using a mapping of BBC charge to centrality, calculated separately for different running periods to account for variations in BBC gain, etc. This assumes that the charge deposited on the BBC is proportional to the multiplicity of charged particles going into the BBC ( $3.0 < |\eta| < 3.9$ ), and this is done on an event-by-event basis.

The mapping of centrality back to the geometric quantities like impact parameter and  $N_{\text{coll}}$  is done by using a Glauber Monte Carlo simulation [63] of Au+Au collisions in which the geometric quantities are exactly known event by event. The multiplicity within the BBC is randomly generated by assuming that for each nucleon-nucleon collision the multiplicity fluctuates as a negative binomial

Figure 3.15:  $N_{\text{part}}$  (left) and  $N_{\text{coll}}$  (right) distributions for 10% centrality bins in the Glauber Monte Carlo.



distribution (NBD). W. Knox discussed in [64] why a NBD matched the multiplicity distribution of negative particles in 405 GeV (fixed target) p+p collisions at Fermilab much better than a Poisson distribution. He proposed that it was due to identical mesons being produced within phase-space cells of size  $\Delta x^3 \Delta p^3 = h^3$ . Bose-Einstein statistics apply within each phase-space cell, and the overall multiplicity will follow a NBD, or generalized Bose-Einstein distribution for  $k$  identical cells [65]:

$$P_{\mu,k}(n) = \frac{\Gamma(n+k)}{\Gamma(n+1)\Gamma(k)} \frac{(\mu/k)^n}{(\mu/k+1)^{n+k}} \quad (3.3)$$

For  $k=1$ , Eq 3.3 becomes the usual Bose-Einstein distribution, while for  $k \gg \mu$  it approaches a Poisson distribution.  $\mu$  is the mean number of particles, and  $k$  is related to the variance via  $k = \frac{\mu^2}{Var(n)-\mu}$ . The PHENIX BBC charge distribution and the Glauber MC BBC charge distribution convoluted with a NBD are in good agreement, as shown in Figure 3.14.

It was found that values of  $\mu=4$  and  $k=1.4$  reproduce the PHENIX BBC multiplicity distribution in 200 GeV Au+Au collisions relatively well. Applying the minimum bias trigger requirement (two tubes fired in both BBC North & South) to the Glauber collisions shows that PHENIX sees 93% of the total inelastic cross section when using this trigger. It would be expected that the NBD parameters vary with the  $z$ -vertex of the collision, due to the changing solid angle seen by the BBC detectors as the collision is closer or further away. However, it was found that even when the  $z$ -vertex dependence is taken into account, there is little variation (<2%) in  $\langle N_{\text{part}} \rangle$  or  $\langle N_{\text{coll}} \rangle$ .

For each Glauber-simulated collision, the BBC response for the thrown multiplicity is modeled, and the BBC charge is used to assign a centrality for the simulated event. After running many events, the mean impact parameter, eccentricity,  $N_{\text{part}}$ , and  $N_{\text{coll}}$  are calculated for several binnings of centrality, as well as the standard deviation.  $N_{\text{part}}$  and  $N_{\text{coll}}$  distributions for 10% centrality bins can be seen in Figure 3.15. Systematics are calculated by varying the parameters of the Glauber simulation. The resulting quantities for Run 7 are listed in Table 3.4 for 5%, 10% and 20% centrality bins.

### 3.3.2 Track Reconstruction in the Muon Arms

Reconstruction and tracking in the Muon Arms is performed using the MUTOO package, an object-oriented C++ collection of modules that run within the standard PHENIX Fun4All data-processing framework. MUTOO makes extensive use of the C++ Standard Template Library, the GNU Scientific Library, and the Boost Libraries. One design goal was simplifying access to objects that are associated with one another, and to that end the ability to “associate” one object with another was built into the base class for all tracking objects. For example, a cluster object is associated with the hit objects that make it up, and a track object is associated with the cluster objects that it is fit to. A MUTR track is associated with a MUID track, and when running simulations, a Monte Carlo particle can be associated with a reconstructed track. Making an association between objects is as simple as:

```
PHKey::associate( some_object, some_other_object );
```

Likewise, getting the associated objects is quite simple. For example:

```
cluster_pointer->get_associated<TMutHit>();
```

returns a container of hit objects that make up that particular cluster.

MUTOO, like most PHENIX software, uses schema evolution to allow class definitions to be modified while still maintaining the ability read/write older versions of that class. This works by deriving different versions of a class from a common abstract base class, and then writing analysis code that only makes use of base class pointers. Thanks to the built-in polymorphism of objects

Table 3.4: Mean  $N_{\text{part}}$ ,  $N_{\text{coll}}$ , and impact parameter values and systematic uncertainties in each of 5%, 10%, and 20% centrality bins, as calculated in the Glauber Monte Carlo simulation.

Centrality (%)	$\langle N_{\text{part}} \rangle$	$\langle N_{\text{coll}} \rangle$	$\langle b \rangle$ (fm)
0-5	$350.8 \pm 3.092$	$1067 \pm 107.7$	$2.284 \pm 0.0746$
5-10	$301.7 \pm 4.665$	$857.8 \pm 85.45$	$3.949 \pm 0.1421$
10-15	$255.7 \pm 5.426$	$680.2 \pm 67.26$	$5.161 \pm 0.1923$
15-20	$216.4 \pm 5.619$	$538.7 \pm 52.39$	$6.13 \pm 0.2258$
20-25	$182.4 \pm 5.743$	$424.4 \pm 40.37$	$6.96 \pm 0.2666$
25-30	$152.7 \pm 5.903$	$330.9 \pm 32.68$	$7.705 \pm 0.2919$
30-35	$126.8 \pm 5.945$	$254.7 \pm 25.78$	$8.385 \pm 0.3193$
35-40	$104.2 \pm 5.758$	$193.1 \pm 20.71$	$9.014 \pm 0.3426$
40-45	$84.59 \pm 5.639$	$143.9 \pm 16.51$	$9.603 \pm 0.3798$
45-50	$67.73 \pm 5.405$	$105.4 \pm 13.50$	$10.15 \pm 0.4027$
50-55	$53.16 \pm 4.960$	$75.22 \pm 10.53$	$10.69 \pm 0.4180$
55-60	$40.96 \pm 4.478$	$52.52 \pm 8.164$	$11.19 \pm 0.4369$
60-65	$30.77 \pm 3.911$	$35.67 \pm 6.135$	$11.69 \pm 0.4549$
65-70	$22.64 \pm 3.406$	$23.77 \pm 4.658$	$12.16 \pm 0.4844$
70-75	$16.14 \pm 2.791$	$15.37 \pm 3.323$	$12.63 \pm 0.5007$
75-80	$11.15 \pm 2.194$	$9.686 \pm 2.323$	$13.09 \pm 0.5223$
80-93	$5.601 \pm 0.810$	$4.193 \pm 0.761$	$13.92 \pm 0.5059$
0-10	$325.8 \pm 3.810$	$960.2 \pm 96.14$	$3.132 \pm 0.1079$
10-20	$236.1 \pm 5.517$	$609.5 \pm 59.81$	$5.645 \pm 0.2092$
20-30	$167.6 \pm 5.811$	$377.6 \pm 36.39$	$7.333 \pm 0.2783$
30-40	$115.5 \pm 5.841$	$223.9 \pm 23.20$	$8.699 \pm 0.3311$
40-50	$76.15 \pm 5.502$	$124.6 \pm 14.94$	$9.877 \pm 0.3908$
50-60	$47.07 \pm 4.726$	$63.90 \pm 9.359$	$10.94 \pm 0.4278$
60-70	$26.72 \pm 3.669$	$29.75 \pm 5.410$	$11.92 \pm 0.4699$
70-80	$13.67 \pm 2.492$	$12.55 \pm 2.822$	$12.86 \pm 0.5104$
80-90	$6.153 \pm 1.359$	$4.688 \pm 1.252$	$13.80 \pm 0.5484$
0-20	$280.5 \pm 4.58$	$783.2 \pm 77.47$	$4.401 \pm 0.1584$
20-40	$141.5 \pm 5.817$	$300.8 \pm 29.64$	$8.016 \pm 0.3049$
40-60	$61.6 \pm 5.08$	$94.23 \pm 12.03$	$10.41 \pm 0.4089$
60-93	$14.4 \pm 2.148$	$14.48 \pm 2.75$	$12.99 \pm 0.4949$

in C++ , this allows new versions of a class with new functionality to be added without breaking older code in most cases.

Event reconstruction in the Muon Arms begins in the MUID, where the tracks are more spread out and occupancy is lower, and progresses backwards towards the event vertex. First, hit Iarocci two-packs are combined into clusters if they are adjacent, but only two two-packs are

allowed per cluster since tracks that come from the interaction region must be almost perpendicular to the plane of the tubes. Next, 2D tracks are found separately in the  $x$ - $z$  and  $y$ - $z$  planes using vertically and horizontally oriented two-packs, respectively. Finally, the 2D tracks are combined into three-dimensional tracks, and the clusters of the 3D track are fit to a straight line (since there is no magnetic field in the MUID).

In the MUTR, adjacent hit strips are first combined into clusters. The cluster charge distributions are fit to a Mathieson distribution to extract the centroid along the axis perpendicular to the strips, usually referred to as the  $w$ -axis. The cathode planes on either side of each gas gap are compared, and nearby clusters (with their 2-D coordinates) are combined into a 3-D “gap coordinate”.

To seed the MUTR tracking, the MUID tracks are projected to Station 3 of the MUTR, and the gap coordinates within a specific window can be combined across planes into track “stubs” that span only that Station. Due to the very small  $z$ -distance covered by a Station, the stub pointing resolution is quite bad. At this point, there is still no momentum estimate, so in spite of the magnetic field a straight-line project is done to Station 2. Again, stubs are built within a window around the projected position, but now the bend-plane approximation is applied to the magnetic field between Stations 2 and 3, and is combined with the stub coordinates in each station to update the track momenta. This allows a more accurate projection to Station 1, where the occupancy is highest, without the time required for a full Kalman-fit trajectory calculation within the magnetic field. Stubs are built in Station 1 around the track projection.

At this point there may be multiple tracks that share the same cluster in one or more stations, so-called “ghost tracks”. To eliminate these, the bend-plane fit is again performed, this time using all three Stations. Tracks which share hits are then compared, and the candidate with larger  $\chi^2/\text{NDF}$  and fewer hits is deleted. Candidates are also deleted if they have the same number of hits but  $\chi^2/\text{NDF}$  worse by at least a factor of 5.

Once the set of track candidates has been narrowed down, a full Kalman fit [66] is performed using all of the MUTR cluster coordinates associated with the track, as well as the position of the

event vertex. The particle's momentum vector and position are calculated at each MUTR Station, and extrapolated to both the collision vertex and the first gap of the MUID. At this point the tracking is complete, and physics analysis can be performed using the calculated momentum vectors and trajectories of the particles.

## Chapter 4

### Data Analysis

In order to arrive at the physical quantity we are interested in, *i.e.* the  $J/\psi$  production rate in  $\sqrt{s_{NN}}=200$  GeV Au+Au collisions, we must correct the measured  $J/\psi$  counts by the number of observed collisions, as well as the PHENIX acceptance and efficiency for  $J/\psi \rightarrow \mu^+\mu^-$ . We can calculate this invariant yield (times the  $\mu\mu$  branching fraction) as:

$$B_{\mu\mu} \frac{dN_{J/\psi}}{dy} = \frac{1}{\Delta y} \frac{N_{J/\psi}}{A\epsilon N_{evts}} \quad (4.1)$$

where  $N_{evts}$  is the number of BBC minimum bias-triggered events that were processed,  $N_{J/\psi}$  is the extracted signal counts,  $A\epsilon$  is the detector acceptance  $\times$  efficiency correction, and  $\Delta y$  is the rapidity bin width. The will be described in Sections 4.1, 4.3, and 4.4, respectively. The invariant yields themselves will be presented in the next chapter.

#### 4.1 Dataset and Quality Assurance

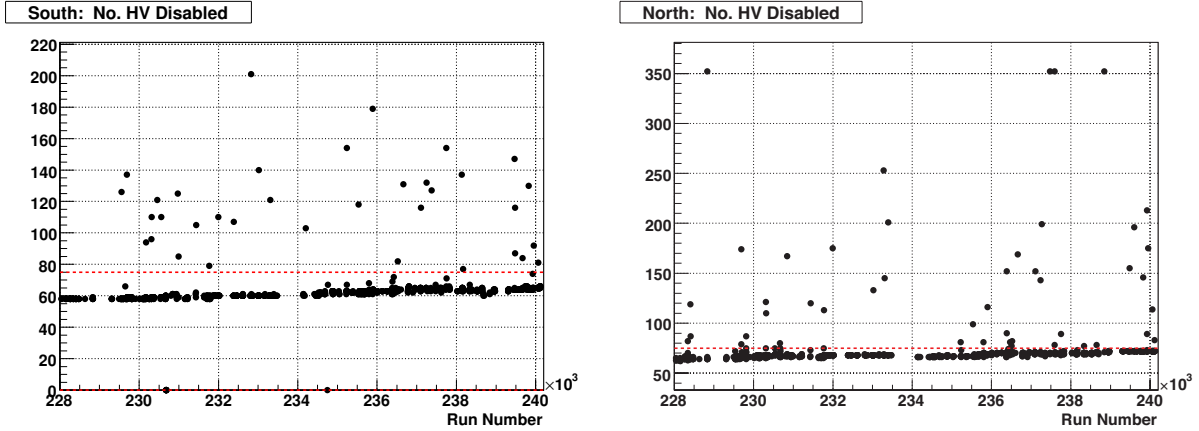
The full reconstruction of the Run 7 Muon Arm data was done using the pro.80 version of the PHENIX software library (PHENIX CVS tag: run07\_production\_C\_01) running within the ROOT software framework. The dataset consists of 5.236 billion events recorded with the BBC minimum bias trigger during  $\sqrt{s_{NN}}=200$  GeV Au+Au collisions, and includes DAQ runs 228042-240121.

Quality Assurance (QA) checks were performed on the data to ensure that running periods with poor detector performance were removed from the analyzed sample. In addition, it is desirable that the detector performance be roughly uniform over as long a running period as possible to make simulations more representative of the real data.

Initial QA was performed by using the online monitoring information and shift crew logs to remove runs in which essential detectors were deactivated or misbehaving. These runs were rejected before data reconstruction took place in order to save time. In addition, 428 runs were rejected because they had less than 500,000 events, as that usually meant the shift crew detected problems within the first few minutes and stopped the DAQ. Of 1005 physics runs taken during the 2007 Au+Au running period, 917 were reconstructed, comprising 4911663621 events.

Next, runs with a large number ( $> 75$ ) of disabled MUTR channels are removed. The run-by-run distributions for the South and North MUTRs are shown in Figure 4.1. These runs are not necessarily “bad”, but removing runs that deviate largely from the average detector efficiency makes the overall calculation of yields more robust.

Figure 4.1: Number of disabled MUTR channels in the South (left) and North (right) Muon Arms. The red dashed lines demarcate the cutoff values for “bad” runs,  $> 75$  disabled channels.



Additional QA cuts were applied to remove runs with a large number of dead channels or hot channels in the North and South MUTRs. Finally, 5- or 10-sigma cuts are applied to the average charge of the cluster peak strip, the number of clusters per MUTR station, and the number of MUTR hits per event.

Lastly, it was found after the full reconstruction had been completed that there were 39 (104) runs in the South (North) Arm for which the gain calibrations for the MUTR were incorrect in the calibrations database. These runs were also removed, although they could be reconstructed at

some later date now that the database has been corrected.

The remaining runs are fairly uniform in detector performance. The resulting good runs lists comprise 3951695369 events for the South Arm and 3826584595 for the North Arm.

## 4.2 Analysis Cuts

After QA cuts are applied, the remaining runs are listed in the “good run list” for each arm separately, since the arms are completely independent sets of detectors. The analysis software, which forms track pairs, calculates the pair mass and kinematics, and estimates the combinatoric background, is then run over all of the reconstructed events in the good runs. At this point track-, pair-, and event-level quality cuts are applied. These cuts are explained in the following subsections.

### 4.2.1 Event $z$ -vertex

Events where the event vertex  $z$ -position is outside  $\pm 30$  cm are rejected. Events which are outside of this range deviate from the NBD hit distributions for the BBC and thus a reliable event centrality is not +possible. Because the majority of collisions fall within  $\pm 30$  cm, the others are simply rejected.

### 4.2.2 MUTR and MUID Track Agreement

Tracks in the MUTR and MUID are associated during reconstruction by projecting the MUID track to the MUTR, which has relatively poor pointing precision, and looking within a large window. In low-occupancy collisions such as  $p+p$  this is probably sufficient, but in Au+Au events where there may be multiple tracks in both detectors, it is possible that associations are made between tracks that did not come from the same particle.

Therefore, at the analysis stage we reevaluate the associated tracks by projecting the MUTR track to the first gap of the MUID. The association is rejected if the radial distance between the projection and the MUID track is greater than 20 cm in the South Arm or 15 cm in the North Arm. Additionally, the two associated tracks are required to have the same  $\theta$ -slope to within 9 degrees.

#### 4.2.3 MUTR and MUID Number of Hits per Track

We require tracks to have a minimum number of hits to reduce the chance of tracks being built from a few random hits. MUTR tracks are required to have at least 8 of 16 possible planes hit. MUID tracks are required to have at least 8 of 10 possible planes hit, with at least one hit in the last gap to ensure the muon passed through the maximum amount of steel.

#### 4.2.4 Minimum $p_z$

Muons must have a minimum  $p_z$  in order to penetrate to the last gap of the MUID, as described in Section 3.2. The minimum values are different from those listed previously because the momentum is measured by the MUTR *after* the muon has passed through the front absorber. Muons are rejected if they have  $|p_z| < 1.17 \text{ GeV}/c$  in the South Arm, or  $< 1.05 \text{ GeV}/c$  in the North Arm.

#### 4.2.5 Tracking $\chi^2/\text{ndf}$

When the tracks are fit to the MUTR hit positions, the  $\chi^2/\text{ndf}$  is also calculated and saved for each track. Unfortunately, the distribution is very broad, and so good tracks are only required to have  $\chi^2/\text{ndf} < 30$ .

A simultaneous fit is also done for each pair of tracks with the event vertex from the BBC. The  $\chi^2/\text{ndf}$  from this fit gives a much narrower distribution, so that we reject pairs for which  $\chi^2/\text{ndf} > 4$ .

#### 4.2.6 Kinematic Cut

$J/\psi$  candidate pairs are required to have rapidity within  $1.2 < |y| < 2.2$ . This ensures that false pairs that have a rapidity outside the actual acceptance are rejected. It also makes the rapidity bin of the two arms symmetric, so that the forward and backward rapidity results can be averaged in symmetric colliding species such as Au+Au.

#### 4.2.7 Event Mixing Cuts

The above cuts are identical to the Run-4 Au+Au analysis, with the exception of two new cuts. A requirement was added that the two MUTR tracks come from different octants, and that the MUID roads do not share a hit tube. Since only the hit position is stored for the MUID roads, we required the hits to either be in different MUID panels, or to be separated by at least 100 cm in x (for vertical tubes) or y (for horizontal tubes).

These cuts have essentially no effect on pairs from the same event, since the offline reconstruction already requires that tracks don't overlap. The pairs from mixed events, however, may contain overlapping hits that would not occur in the normal reconstructed event, so these cuts were added to enforce the same requirements in same-event and mixed-event pairs. Their largest effect is at small opening angles and therefore low mass.

### 4.3 Signal Extraction

To extract the  $J/\psi$  yield from the data, the recipe is as follows:

- (1) Create the mass spectrum
- (2) Estimate and subtract the combinatoric background
- (3) Fit the spectra and extract the  $J/\psi$  yield

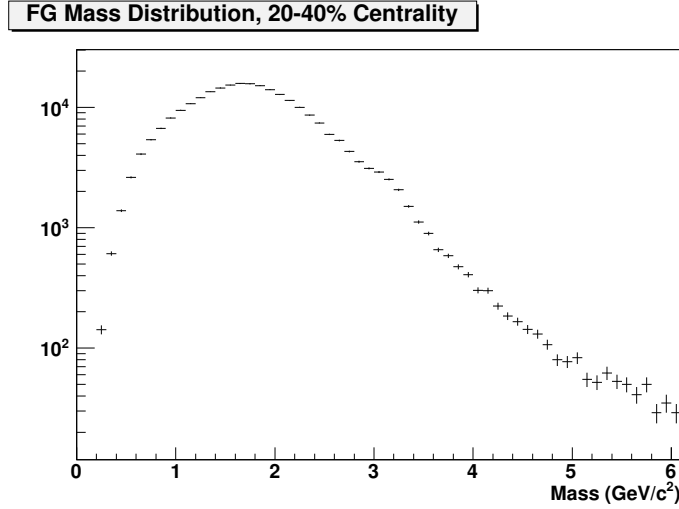
Each of these steps will be described below.

The mass spectrum we are interested in is that of the parent-particles that decayed into two muons. The parent invariant mass is calculated by conservation of energy and momentum:

$$E^2 = p^2 + m^2 \quad (4.2)$$

$$\begin{aligned} M^2(\text{pair}) &= E^2(\text{pair}) - p^2(\text{pair}) \\ &= (E^+ + E^-)^2 - (p_x + q_x)^2 - (p_y + q_y)^2 - (p_z + q_z)^2 \\ &= \left( \sqrt{m_\mu^2 + |p|^2} + \sqrt{m_\mu^2 + |q|^2} \right)^2 - (p_x + q_x)^2 - (p_y + q_y)^2 - (p_z + q_z)^2 \\ &= 2m_\mu^2 + 2\sqrt{(m_\mu^2 + |p|^2)(m_\mu^2 + |q|^2)} - 2p \cdot q \end{aligned} \quad (4.3)$$

Figure 4.2: Unsubtracted mass distribution from the South Arm, 20-40% centrality.



where  $p$  and  $q$  are the  $\mu^+$  and  $\mu^-$  momentum vectors, and  $M(\text{pair})$  is the invariant mass of the parent particle. Of course, not all of the possible pairs of tracks came from an actual parent particle, and we need to subtract this ‘‘combinatoric’’ pair background from the spectrum. As can be seen in the mass histogram of Figure 4.2, the combinatoric background is quite significant compared to the  $J/\psi$  peak in Au+Au collisions.

#### 4.3.1 Combinatoric Background Estimation and Subtraction

The combinatoric background is estimated first through the standard PHENIX event mixing software with a Muon Arm-specific module to apply the event- and track-level cuts and fill the invariant mass histograms. The events which pass analysis cuts are stored in mixing pools, up to ten at a time. Each pool has only events within a 2.5% centrality and 1 cm  $z$ -vertex bin, so that particle multiplicity and position are roughly the same between mixed events. As each event is added, replacing the oldest event in the mixing pool, all two-track combinations are made within that event. Any pair which passes the track and pair cuts is written to the output histograms (2D histograms of invariant mass vs. pair  $p_T$ ). The newly-added event is then mixed with all the currently stored events, *i.e.* pairs are made with one track from the new event and one track from a stored event. Again, any pair passing track and pair cuts is stored to the output histograms (a

separate set are kept for mixed events). The process then moves on to the next event.

The mixed-pair histograms should have no resonance peak, since no mixed pair could have come from an actual  $J/\psi$  decay. Therefore, the mixed event invariant mass spectra should only be representative of the combinatoric background, and we refer to it as the “mixed background”.

The mixed background can be normalized either by absolute or relative methods. The absolute normalization method is based on the ratio of real to mixed events that were processed, while relative normalization uses the real and mixed like-sign (++) and (--) pairs (in which there is no  $J/\psi$  signal) to determine the normalization level. Absolute normalization also requires correction factors to account for the fact that the mixed events did not actually have the same impact parameter or collision vertex, even though they are required to be similar. Because these correction factors introduce additional uncertainties compared to the relative normalization, the latter is used in this analysis.

To calculate the normalization, we make use of the like-sign estimate of the combinatoric background (derived later)  $N_{+-} = 2\sqrt{N_{++} \cdot N_{--}}$ . We calculate this for both the foreground (same-event) and background (mixed) pairs over the mass range 1.7–10  $\text{GeV}/c^2$ . We ignore the low-mass region because in the past there have been distortions in the spectra down there, and it is below the region we are interested in. We can write this as:

$$\text{combinatoric bgnd} = (\text{mixed bgnd}) \frac{2\sqrt{FG_{++}FG_{--}}}{2\sqrt{BG_{++}BG_{--}}} \quad (4.4)$$

We also subtract the ++ and -- pair histograms, with the mixed background simply normalized to the ratio of the foreground/background counts, since there is no signal to worry about in this case. The resulting spectra should be flat, as there is no same-sign muon background in the  $J/\psi$  mass region. Two example like-sign spectra are shown in Figure 4.3 for 0-10% centrality, and Figure 4.4 for 60-70% centrality. As would be expected, the largest fluctuations are where combinatoric background is greatest, around  $M \sim 1.5\text{--}2 \text{ GeV}/c^2$ .

Figures 4.5 and 4.6 show example background-subtracted mass distributions for two centrality and two  $p_T$  bins in the South Arm. Additional curves are overlaid that are the  $\pm 1\%$  and  $\pm 2\%$  times

the mixed background to demonstrate the sensitivity of the subtracted spectra to the background normalization. Of course the effect is much smaller for peripheral collisions, where there is little combinatoric background due to the lower multiplicity.

Figure 4.3: Example same-sign mass plots from South Arm 0-10% centrality, all  $p_{\text{T}}$ s. The mixed background contribution is shown scaled by  $\pm 1\%$  and  $\pm 2\%$  (blue points), and the residual counts in the  $J/\psi$  mass region [2.6,3.6] are listed.

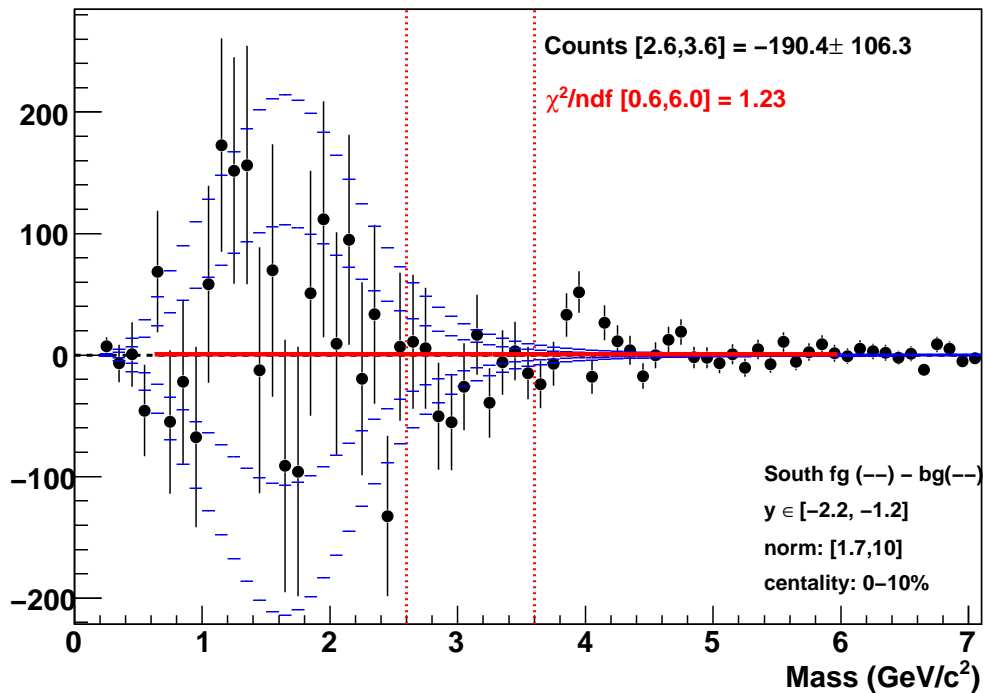
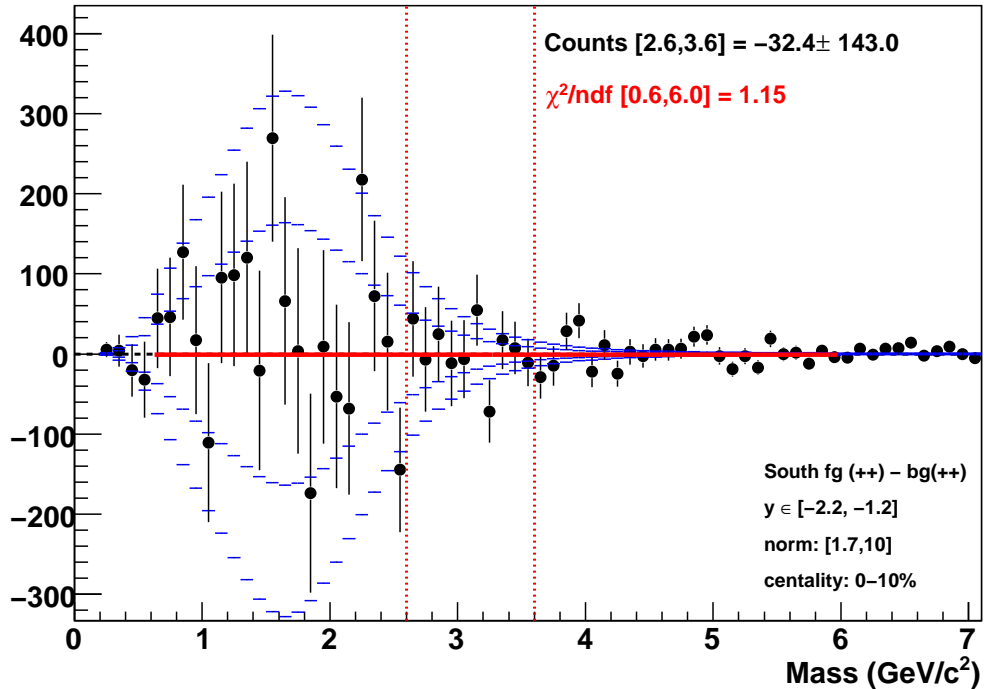


Figure 4.4: Example same-sign mass plots from South Arm 60-70% centrality, all  $p_{\text{T}}$ s. The mixed background contribution is shown scaled by  $\pm 1\%$  and  $\pm 2\%$  (blue points), and the residual counts in the  $J/\psi$  mass region [2.6,3.6] are listed.

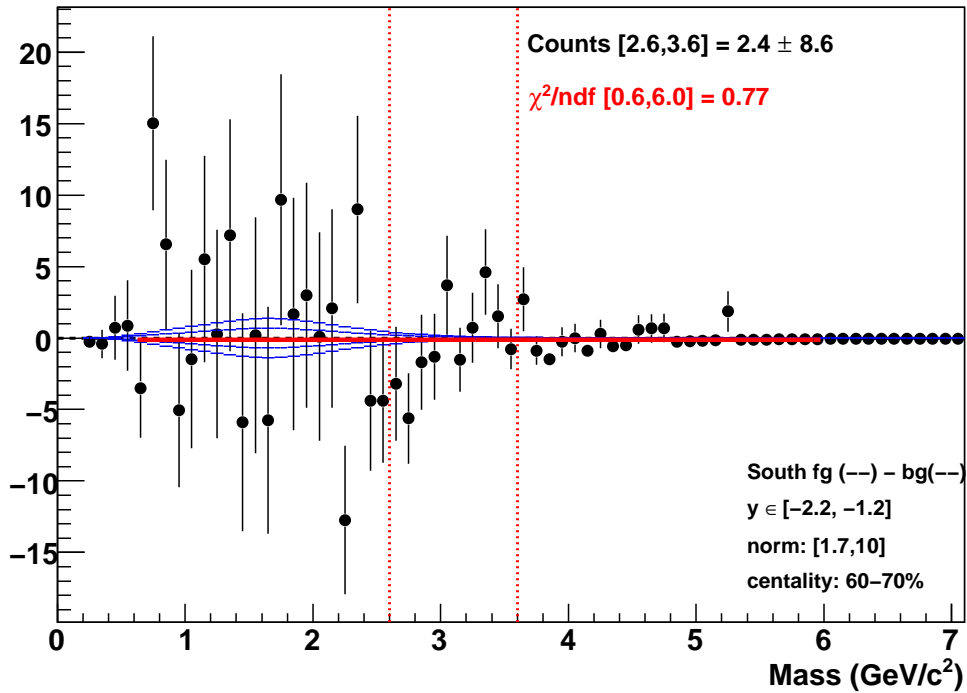
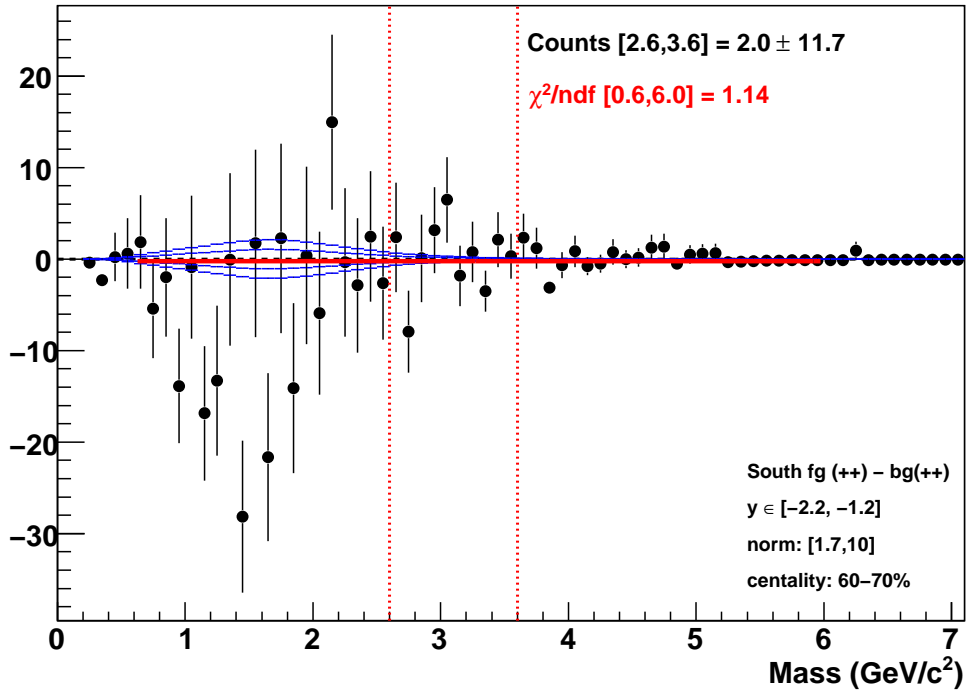


Figure 4.5: Example mass plots from South Arm 0-20% centrality,  $p_T=0-1$  and  $p_T=2-3\text{GeV}/c$ . The mixed background contribution is shown scaled by  $\pm 1\%$  and  $\pm 2\%$  (blue points).

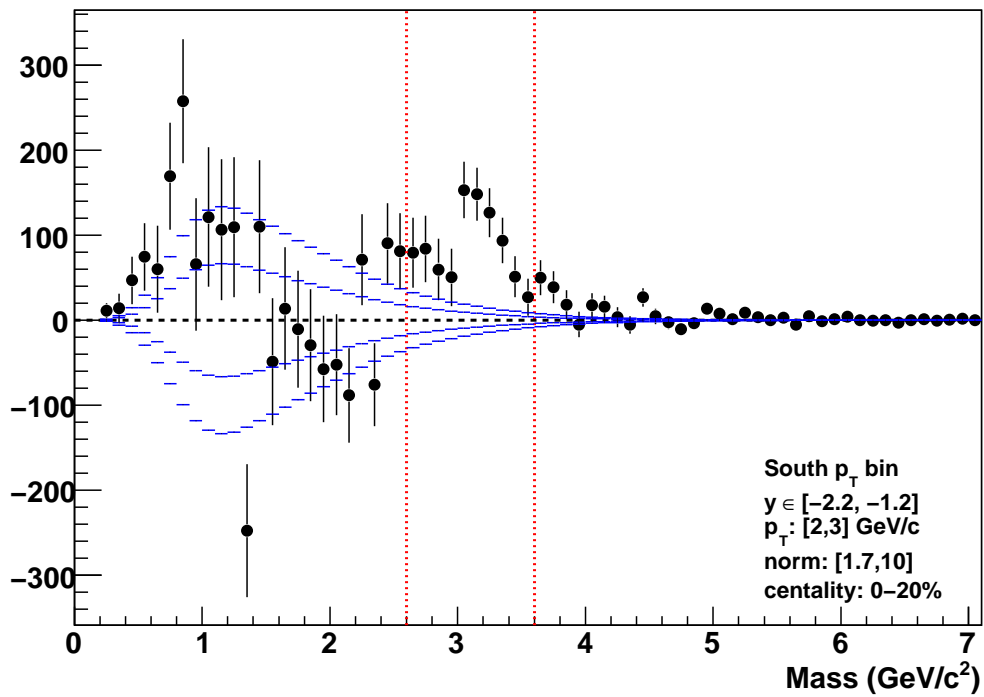
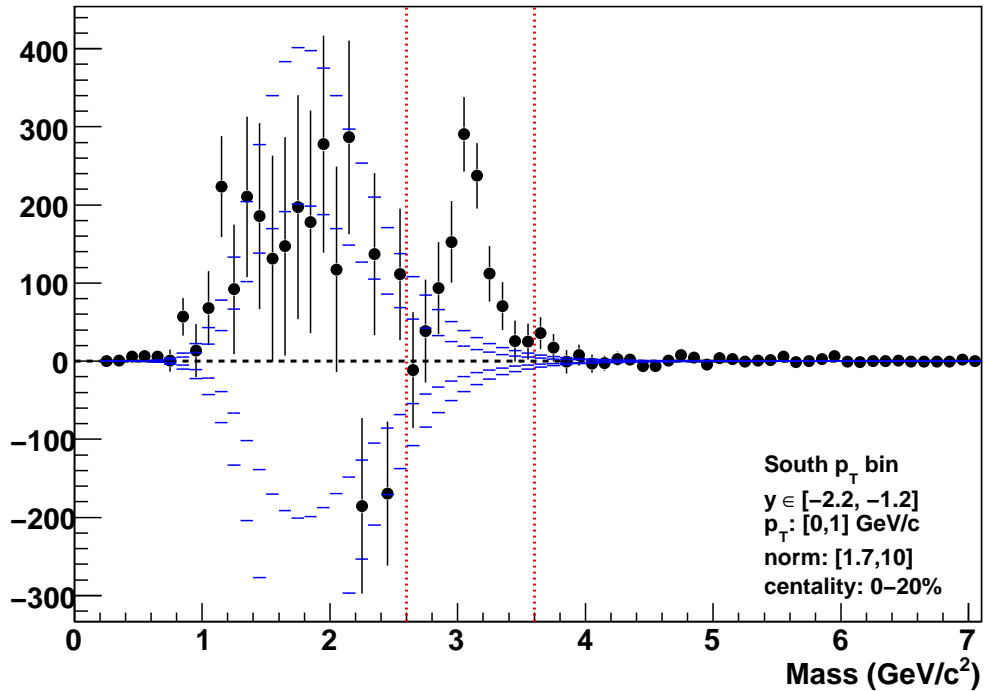
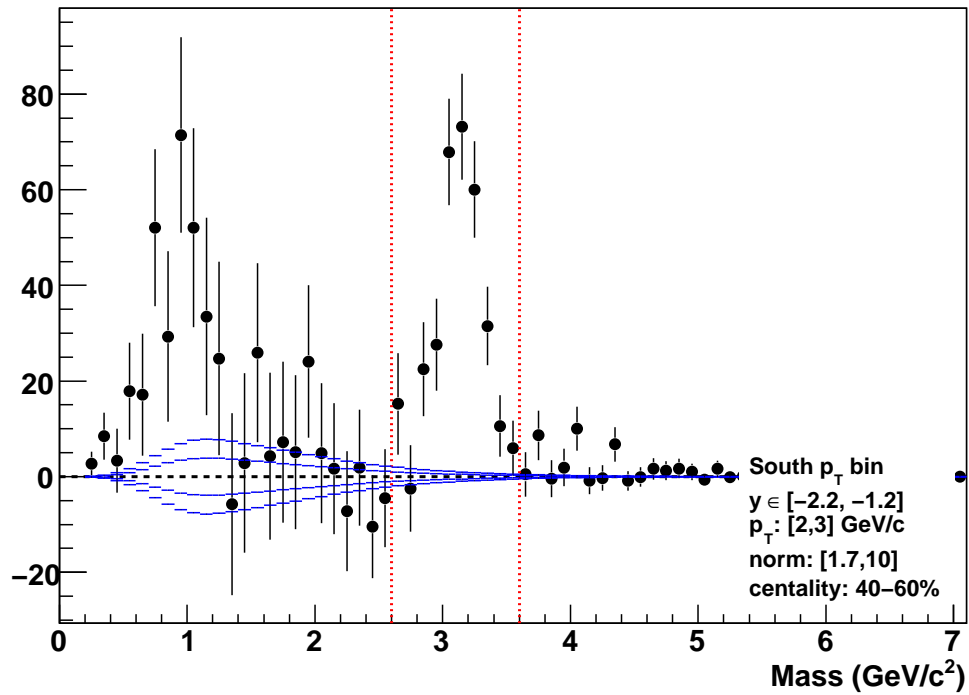
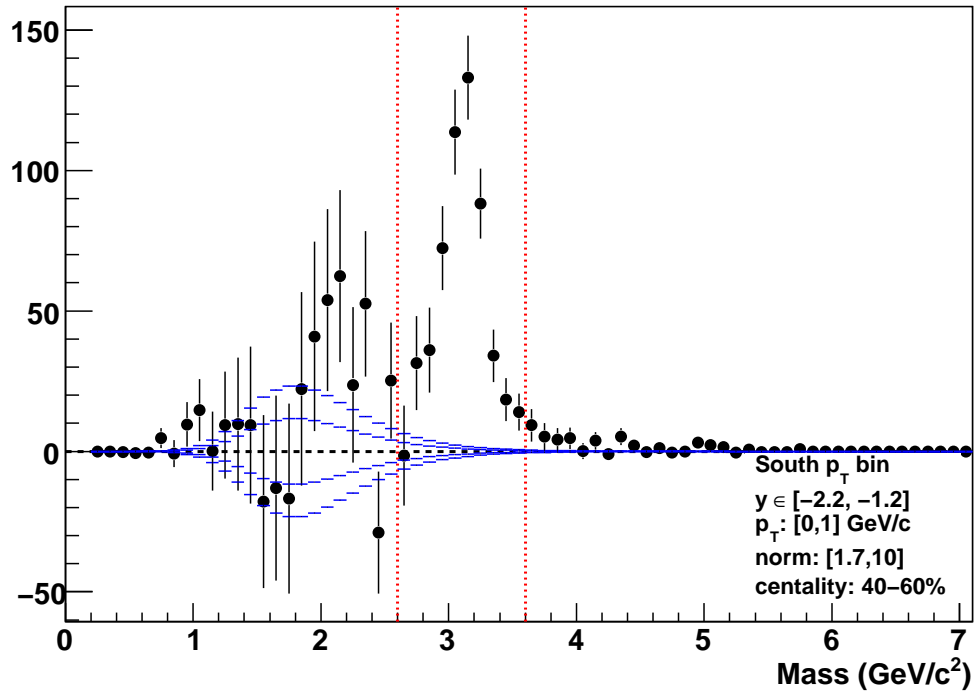


Figure 4.6: Example mass plots from South Arm 40-60% centrality,  $p_T=0-1$  and  $p_T=2-3\text{GeV}/c$ . The mixed background contribution is shown scaled by  $\pm 1\%$  and  $\pm 2\%$  (blue points).



As mentioned above, the background can also be estimated directly from like-sign pairs using the usual formula ( $2\sqrt{N_{++}N_{--}}$ ). For large  $N$ , this converges to the unlike-sign combinatoric background, although it does not work well when the per-mass-bin counts are  $\sim 0$  or 1. In this analysis, this method appears to leave more distortion in the subtracted spectra (see, for example, Figure 4.7), but it is unclear which method produces a more accurate signal. Therefore, we will proceed with both methods.

The like-sign background formula can be arrived at via two assumptions. If we assume that all tracks are from  $J/\psi$ s, then

$$\begin{aligned} N_{+-}^{comb} &= N_+N_- - N_{signal} \\ &= N_{sig}^2 - N_{sig} \\ &= N_{sig}(N_{sig} - 1) \end{aligned} \tag{4.5}$$

$$\begin{aligned} 2\sqrt{N_{++}N_{--}} &= 2\sqrt{\frac{N_+(N_+ - 1)}{2} \frac{N_-(N_- - 1)}{2}} \\ &= \sqrt{(N_{sig}(N_{sig} - 1))^2} \\ &= N_{+-}^{comb} \end{aligned} \tag{4.6}$$

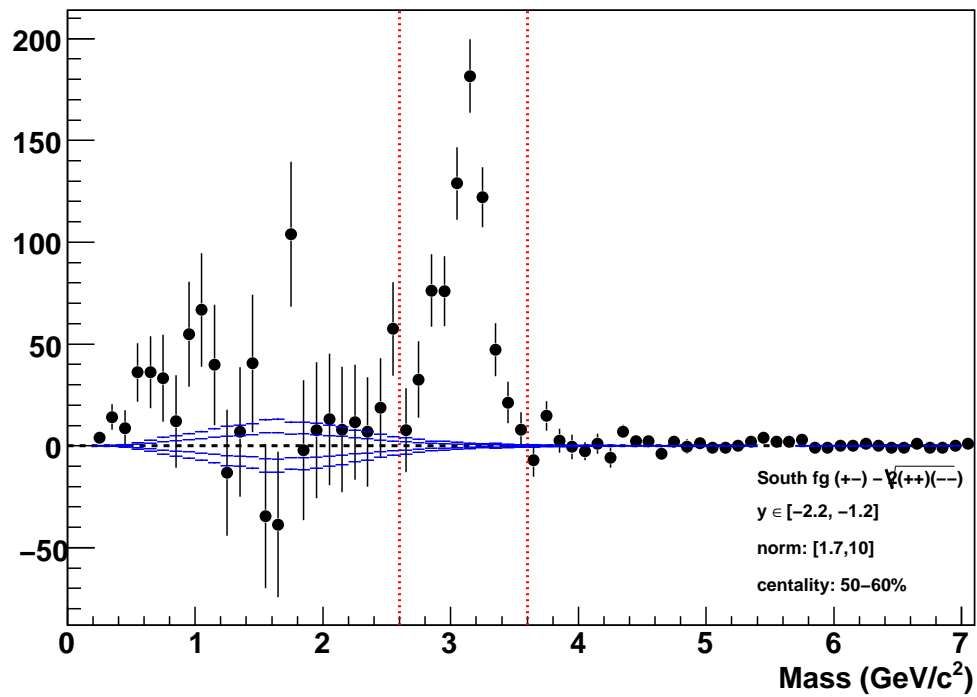
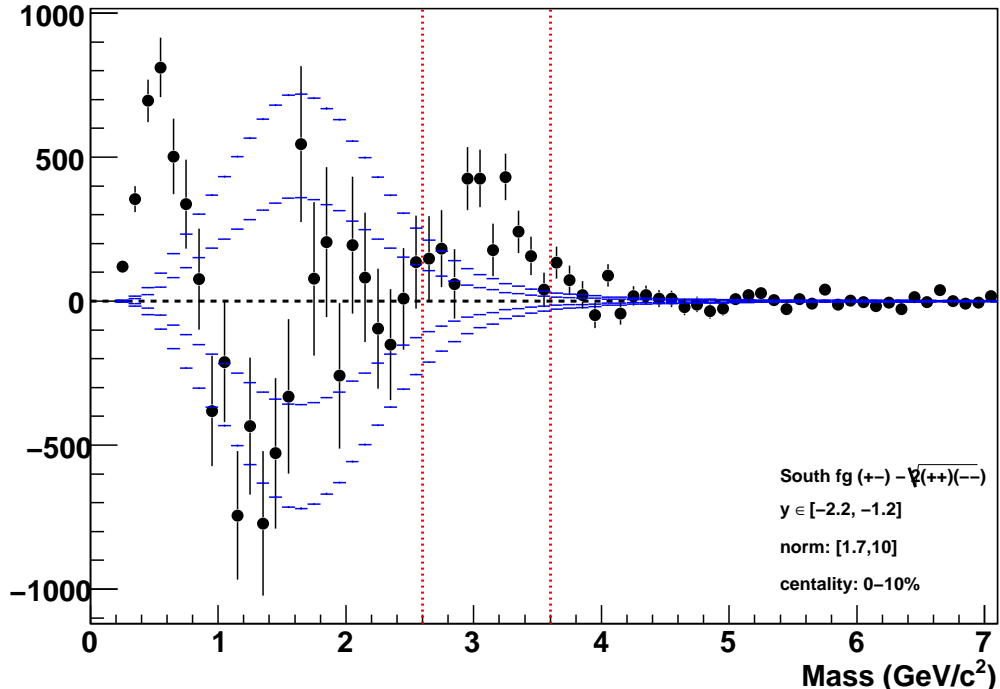
Alternatively, if we assume that  $N_+ \approx N_-$ , both are  $\gg 1$ , and the signal/background is very low, then:

$$\begin{aligned} N_{+-}^{comb} &= N_+N_- - N_{signal} \\ &\approx N_+N_- \\ &\approx N_+^2 \end{aligned} \tag{4.7}$$

$$\begin{aligned} 2\sqrt{N_{++}N_{--}} &= 2\sqrt{\frac{N_+(N_+ - 1)}{2} \frac{N_-(N_- - 1)}{2}} \\ &= \sqrt{(N_+(N_+ - 1))^2} \\ &\approx N_+^2 \\ &\approx N_{+-}^{comb} \end{aligned} \tag{4.8}$$

The latter case should hold true in central Au+Au collisions, and the former in peripheral events.

Figure 4.7: Example like-sign subtracted mass plots from South Arm 0-10% and 50-60% centrality, all  $p_{\text{TS}}$ . As can be seen, while the peripheral bin looks reasonable, the central bin has large distortions.



### 4.3.2 Mass Fits

Once the background is calculated and subtracted, several different fits are performed independently on the resulting invariant mass histograms for both methods of background subtraction. The background-subtracted spectra and several associated fits can be seen in Appendix B.

A log-likelihood fit is performed such that proper Poisson statistical errors are used for each mass bin. Because the ROOT log-likelihood fitter expects a histogram of raw counts, it is incorrect to apply it to a subtracted distribution. A custom TVirtualFitter class was written to instead apply the log-likelihood method to the foreground histogram of same-event pairs (which is a histogram of counts), and the sum of the signal fit function and the background distribution are treated as the total fit function, also in counts.

The actual fit function builds upon those used in previous PHENIX Muon Arm analyses. Two Gaussians are used for the  $J/\psi$  peak, and the non-combinatorial background is accounted for by an exponential. The total fit function is convoluted with a function representing the acceptance as a function of mass. We can write out the fit function as:

$$g(M) = A(M) N_{J/\psi} \{(1 - f) \text{Gaus}(M; \mu_1, \sigma_1) + f \text{Gaus}(M; \mu_2, \sigma_2)\} + A(M) a \text{Exp}(M; b)$$

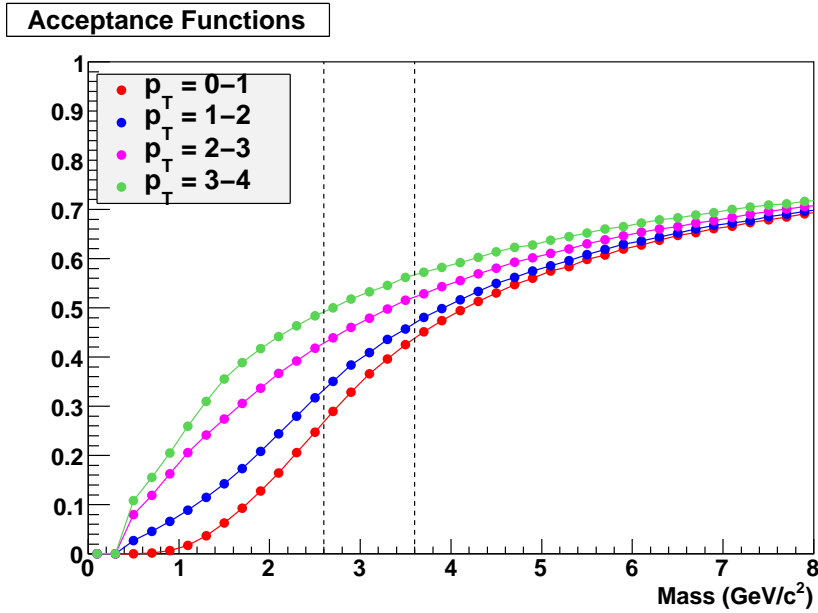
The seven fit parameters are constrained using PHENIX  $p+p$  data to the values in Table 4.1. We allow the normalization of the exponential to be negative, even though this may be unphysical, because in some bins with large fluctuations the positive-constrained exponential will hit the limits of the parameters and lead to very large errors on the fit result.

The acceptance function is generated by a toy Monte Carlo simulation of dimuons going into the Muon Arms. The  $p_z$  required to penetrate to the last gap of the MUID is accounted for, as well as the effect of the event mixing cuts described in Section 4.2.7. Some examples of the acceptance functions are shown in Figure 4.8.

Since the functional form is not exactly known for the Au+Au dimuon spectra, the fit is

Table 4.1: Mass Fit Parameters

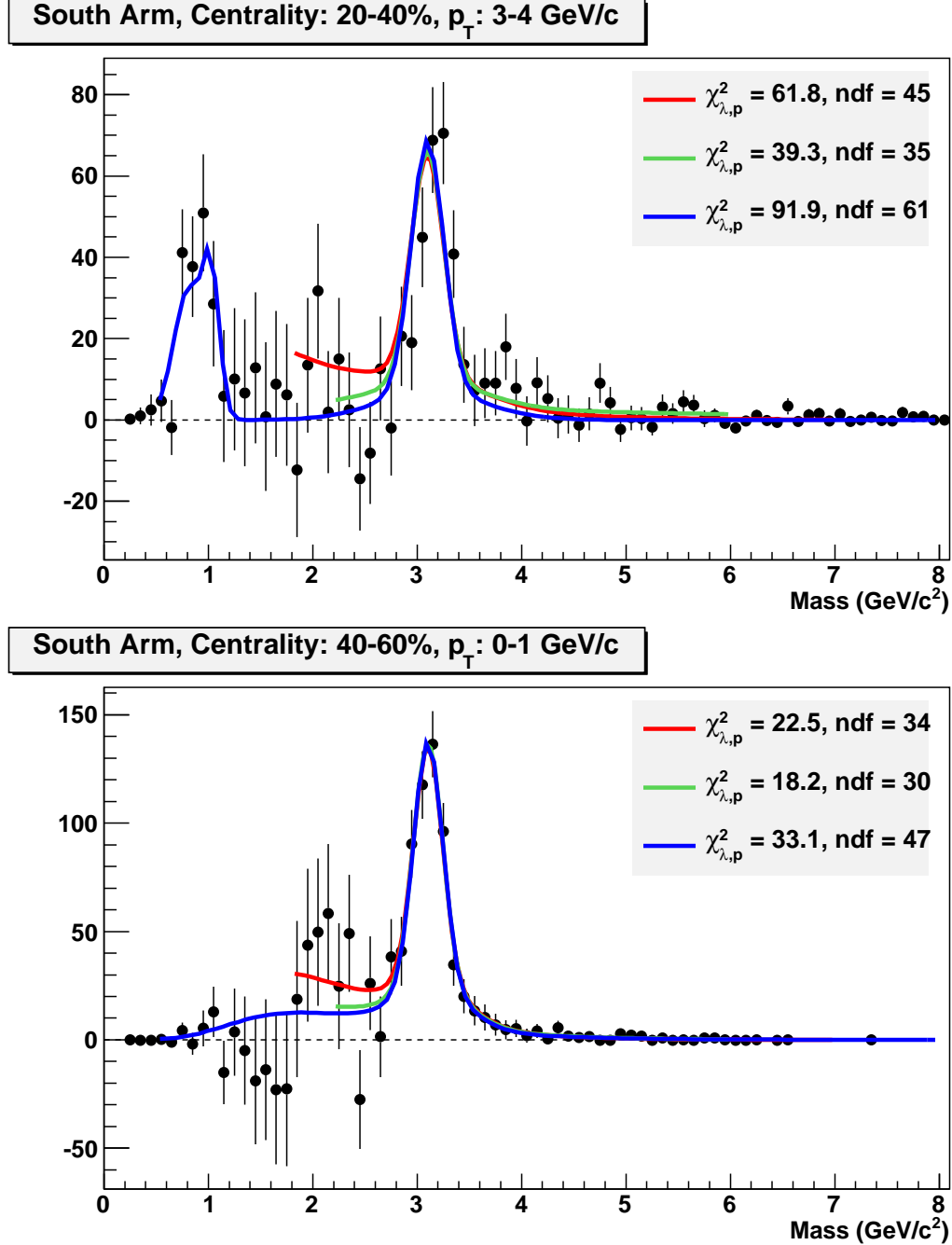
Parameter	Description	Limits	
		South	North
$p_0$	Integral of Both Gaus	0.0-1.e7	0.0-1.e7
$p_1$	Gaus One Mean	$M_{J/\psi}$	$M_{J/\psi}$
$p_2$	Gaus One Sigma	0.138	0.136
$p_3$	Gaus Two Fraction	0.267	0.210
$p_4$	Gaus Two Sigma	0.310	0.409
$p_5$	Exp Norm	$ p_5  < 1e9$	$ p_5  < 1e9$
$p_6$	Exp Slope	0-25.0	0-25.0
$p_7$	Gaus Two Mean – Gaus One Mean	0.0	0.0

Figure 4.8: Acceptance functions used to modulate the mass fits, generated by the fast MC in several  $J/\psi$   $p_T$  bins. The dashed lines delineate the  $J/\psi$  peak region.

performed multiple times while varying several parameters. The background normalization is varied by  $\pm 2\%$ , the relative fractions of the two Gaussians is varied by  $\pm 25\%$  from their nominal value, and three different fit ranges (of invariant mass in  $\text{GeV}/c^2$ ) are used: [0.5,8.0], [1.8,7.0], and [2.2,6.0]. The variation in fit range can be seen in the example fits of Figure 4.9.

A common problem with the Au+Au dimuon spectra is that there are very few counts above

Figure 4.9: Example subtracted mass plots with overlaid fits for South Arm 20-40% centrality,  $p_T=3\text{-}4 \text{ GeV}/c$  (top), and 40-60% centrality,  $p_T=0\text{-}1 \text{ GeV}/c$  (bottom). The large peak at low mass due to the vector mesons can be seen in the top plot, but in the lower plot  $p_T=0\text{-}1 \text{ GeV}/c$  there is no acceptance for the vector mesons.



the  $J/\psi$  mass region, as well as large uncertainties on the points just below the  $J/\psi$  peak due to the large background being subtracted in that region. This gives very little leverage with which to

establish the amount of physical background, and leaves the results sensitive to the fit range that is chosen. Therefore multiple fit ranges are used to try to account for this.

When fitting down below masses of  $\sim 1.5$  GeV/ $c^2$ , there are additional resonances in the spectra due to the low-mass vector mesons  $\phi$ ,  $\rho$ , and  $\omega$ . The acceptance for dimuon decays from these mesons is greatly reduced by the absorber, and there is essentially no peaks present at  $p_T \lesssim 1$  GeV/ $c$ . The mesons need to be added to the fit in the kinematic bins where their acceptance is non-negligible, which is  $\approx 1 < p_T < 4$ . The parameters for the vector meson peaks were taken from a Muon Arms simulation and are listed in Table 4.2. The  $\rho$  and  $\omega$  are too close in mass to be resolved, and so are fit to a single Gaussian. An additional Gaussian is used for the  $\phi$  meson. The fit including the vector mesons can be seen in the top plot of Figure 4.9.

Table 4.2: Fit parameters for the low-mass vector mesons.

Parameter	South Arm	North Arm
$\rho, \omega$ mean (GeV/ $c^2$ )	0.781	0.785
$\rho, \omega$ width (GeV/ $c^2$ )	0.143	0.143
$\phi$ mean (GeV/ $c^2$ )	1.021	1.020
$\phi$ width (GeV/ $c^2$ )	0.078	0.076

### 4.3.3 Final Values

The final signal value we quote for each kinematic bin is the average of the various fits, with their RMS included as a point-to-point uncorrelated systematic error. The signals extracted using the two background subtraction methods are averaged, with  $|S_{mixed} - S_{likesign}|/\sqrt{12}$  taken to be the systematic uncertainty due to their disagreement. This uncertainty is chosen because it is not clear which method is more correct, so a (worst-case) flat probability distribution between the two measurements is assumed, for which the RMS is  $|x_1 - x_2|/\sqrt{12}$ . The signal counts are listed in Tables A.2 and A.3, along with the statistical errors and the uncorrelated systematic from the RMS of the different fit methods. The relative errors for each bin are also graphically tabulated in Figure 4.10. The different contributions to the RMS systematic error are listed separately in Tables A.4 and A.5. The signal-to-background for the  $J/\psi$  mass region (2.6–3.6 GeV/ $c^2$ ) and the

(subtracted counts)/background for a region of background only (1.8–2.0 GeV/ $c^2$ ) are listed in Tables A.6 and A.7.

There are several bins where the signal is statistically insignificant. The procedure chosen is to use only a 90% confidence level upper limit (CLUL) for bins where  $N_{J/\psi} < \sqrt{\sigma_{stat}^2 + \sigma_{sys}^2}$ . This is reflected in Tables A.2, A.3. The CLUL was calculated using the likelihood function for Poisson-distributed foreground and background counts [67],[68]:

$$L(N, M; \nu_f, \nu_b) = \text{Poisson}(N, \nu_f) \text{Poisson}(M, \nu_b) \quad (4.9)$$

$$= \frac{\nu_f^N e^{-\nu_f}}{N} \cdot \frac{\nu_b^M e^{-\nu_b}}{M} \quad (4.10)$$

$$L(\nu_s; N, M) = \frac{\int_0^\infty L(N, M; \nu_s + \nu_b, \nu_b) d\nu_b}{\int_0^\infty \int_0^\infty L(N, M; \nu_s + \nu_b, \nu_b) d\nu_b d\nu_s} \quad (4.11)$$

$$0.9 = \int_0^{x_{CL}} L(\nu_s; N, M) d\nu_s \quad (4.12)$$

where  $N$  is the foreground counts and  $M$  is the background counts in the mass range [2.6,3.6],  $\nu_f$ ,  $\nu_b$ , and  $\nu_s$  are the foreground, background, and signal expected values, and  $x_{CL}$  is the CLUL we are trying to calculate. A Runge-Kutta algorithm with adaptive step-sizing, taken from Numerical Recipes [69], is used to calculate the integrals.

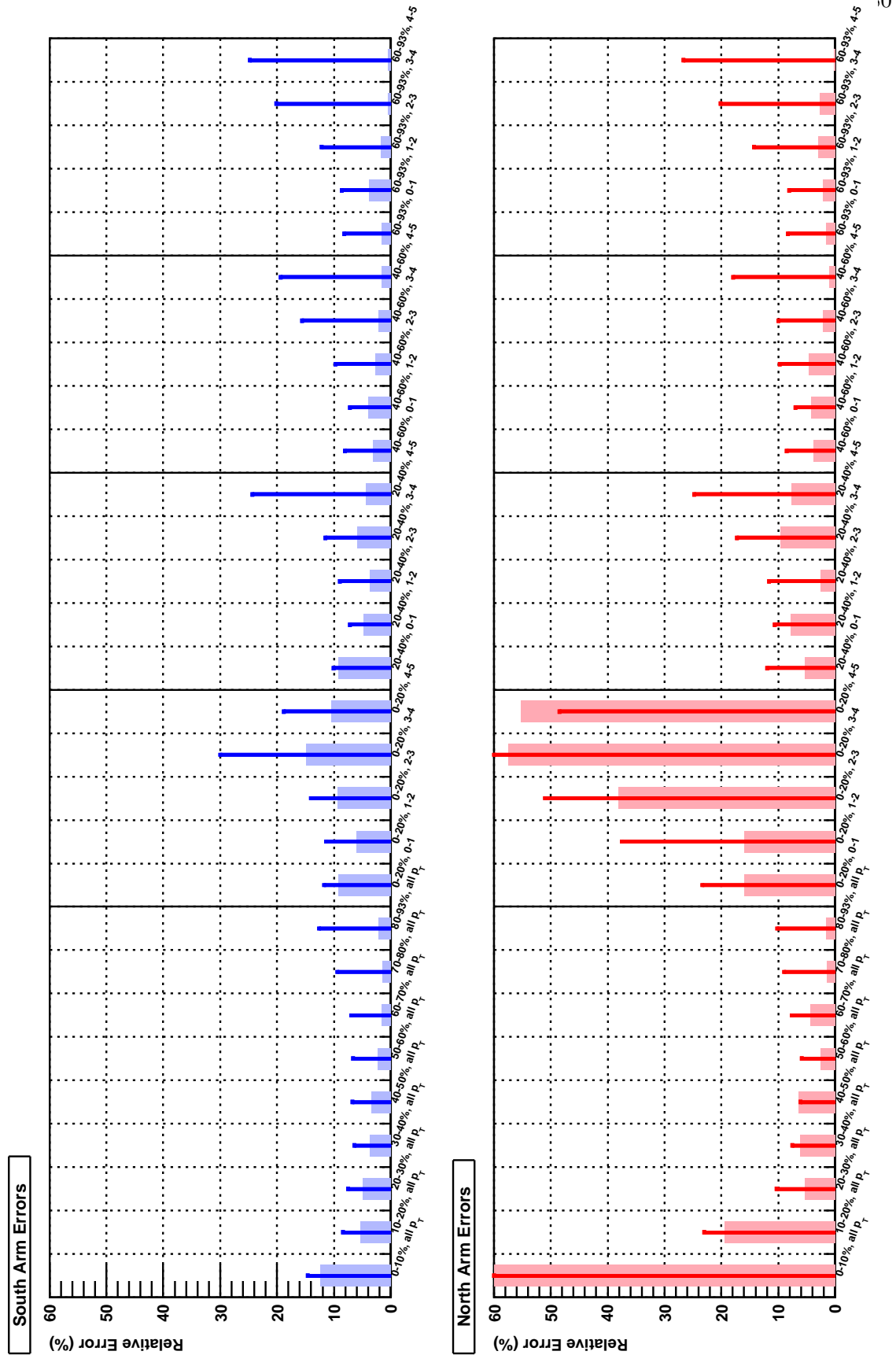
A simple consistency check of the signal extraction method is to compare the signal summed over  $p_T$  bins to the signal summed over centrality bins within 20% centrality bins. These values are listed in Table A.8 using mixed background subtraction, and shows good agreement in all bins except for the most central North Arm bin, where there is very little signal to fit one way or another.

Included in the mass plots are the non-standard  $\chi^2$  values as calculated for Poisson distributions in [70]:

$$\chi_{\lambda, p}^2 = 2 \sum_i y_i - n_i + n_i \ln(n_i/y_i) \quad (4.13)$$

In our case  $y_i$  represents the fit function + mixed background, while  $n_i$  is the number of foreground counts in that bin. This  $\chi^2$  test is used in place of the standard version, which assumes that the values are Gaussian-distributed, and therefore is invalid for small-valued Poisson quantities.

Figure 4.10: Relative errors for each bin. Bars are statistical errors, while bands are the uncorrelated systematics due to varying the fit parameters. First the 10% centrality bins (integrated over  $p_T$ ) are shown, followed by the 20% centrality and 1 GeV/ $c$   $p_T$  bins.



## 4.4 Detector Acceptance and Efficiency Correction

The detector geometric acceptance and reconstruction efficiencies for a  $J/\psi$  in the Muon Arms are calculated as a single quantity (often written  $\text{acc} \times \text{eff}$ ) as described below. The PYTHIA event generator [71] is used to simulate  $J/\psi$  samples, which are then fed through a GEANT3-based [72] simulation of the PHENIX detectors (known as PISA). They are next embedded in a Au+Au event sample (to add detector occupancy-related effects) and then run through the usual PHENIX reconstruction software. The overall  $\text{acc} \times \text{eff}$  is simply the number of reconstructed  $J/\psi$ s in a particular kinematic ( $p_T$ ,  $y$ ) bin, divided by the number of  $J/\psi$ s thrown in that bin. Note that this quantity does not include trigger efficiencies, only detector-related effects. However, because the minimum bias trigger was the only trigger used during Run 7, there is no separate dimuon trigger efficiency to account for as there has been in PHENIX  $p+p$  and  $d+\text{Au}$  datasets.

### 4.4.1 Particle Generation

Simulated  $J/\psi$  samples were generated using PYTHIA version 6.205, with the  $g+g \rightarrow J/\psi+g$  process selected (MSUB(86)=1) and the  $\mu\mu$  decay channel activated (MDME(859,1)=1) while throwing  $\sqrt{s}=200$  GeV  $p+p$  collisions. The output was filtered prior to the GEANT stage by requiring at least one muon to go into  $143^\circ < \theta < 171^\circ$  for the South Arm, or  $9^\circ < \theta < 37^\circ$  for the North Arm, and only the two muons descended from a  $J/\psi$  parent are written out. The PYTHIA statistics used for embedding are listed in Table 4.3.

When embedding PYTHIA  $J/\psi$ s into real data events, the collision spatial coordinates are first read out from the data events into a text file, and then used to shift the PYTHIA event to the same  $z$ -coordinate. Because the collision  $z$ -position (as determined by the BBC North-South timing difference) is only known to about  $\pm 0.5$  cm, we blur the  $J/\psi$   $z$ -position event-by-event by a Gaussian distribution of  $\sigma = 0.5$  cm.

For unembedded PYTHIA events where there is no data vertex to read in, a vertex is thrown event-by-event with a  $z$ -distribution (from data) of  $\sigma = 24.4\text{cm}$ . A redistribution of the  $J/\psi$ s with

Table 4.3: Pythia  $J/\psi$ s generated for embedding in real data.

Arm	$p_T$ cut	$J/\psi$ s Generated	$J/\psi$ s Embedded
South	$> 0$	32,101,727	2,393,807
North	$> 0$	32,150,330	2,393,807
South	$> 2.5$	31,044,298	2,393,807
North	$> 2.5$	31,075,599	2,393,807

respect to the collision vertex is done similarly to above. The collision  $z$ -position is relevant, because the geometric acceptance changes with the distance between the collision and the detectors. The signal to background also changes as a function of  $z$ , because background particles like pions and kaons have more time to decay to muons when the collision is further from the detector in question, while the number of  $J/\psi$ s (and muons from  $J/\psi$ s) remains constant. This feature has been used in single muon heavy flavor analyses, where the “decay muon” component must be subtracted.

#### 4.4.2 PISA and Detector Response

The PHENIX GEANT3 simulation (PISA) propagates the initial particles through the detectors and other materials, and accounts for both  $dE/dx$  and deflections in the materials and bending in the magnetic field.

The MUTR response to a particle is simulated as follows: the particle’s  $dE/dx$  through each of the MUTR gas gaps is thrown using a Landau distribution. The energy deposited is converted into a Mathieson distribution of charge on the cathode strips on either side of the gap, centered on the intersection point. The charge is then converted to ADC values and zero-suppression applied, in order to simulate the electronics of the actual detector.

The MUTR response also accounts for disabled high voltage modules, dead anode wires, dead FEMs, the scratched cathodes in the North Arm, and the gain and pedestal calibrations. A run number is chosen when the simulation is run, and the disabled high voltage and calibrations are loaded from the PHENIX database for that particular run. That way the simulation represents the detector state at a given point in time, and this is used in the next section to account for the

time-variation of the  $\text{acc} \times \text{eff}$ .

The MUID simulated response is much simpler, since the tubes are merely hit or not hit. For each MC particle, the MUID two-packs that it passes through are found. Whether each two-pack fires is thrown randomly with a probability equal to the two-pack efficiency that is input into the simulation. The two-pack efficiency is calculated from the real data tracks themselves. For any two-pack, we select the tracks which passed through it, and rerun the track-finding algorithm to require that the track would have been found with or without a hit in that two-pack. Then the efficiency for that two-pack is simply the fraction of tracks in the sample that actually did have a hit in the two-pack.

Cases where the particle passes through two or more two-packs are also accounted for in the full calculation. The effect of random hits on the measured efficiency was studied and was found to be only a few percent effect or less.

If the simulated event is being embedded into a real data event, at this point the MUTR charge and ADC values for MC and real data are merged into a single hit strip-by-strip. If both the MC and real data have a hit on the same strip, the charges are literally added. Also, the MUID hits are merged such that a tube is listed as having fired if either a real data or MC hit occurred there.

From here the event is a collection of hit strips and tubes just as in the real data, and the reconstruction proceeds just as for real data. It is important to use the same version of the reconstruction code as was used for the real data, otherwise other effects may be inadvertently included if the reconstruction algorithms have been modified.

Unfortunately, the embedded event samples cannot exactly recreate the signal-to-background (combinatoric or physical) levels seen in real events, because  $J/\psi$ s are literally being injected into every event, while in real data they exist in only a small fraction of events. Because of this, after the event-mixing stage we use a modified signal extraction procedure for simulated events. The biggest difference is that no background exponential is used for unembedded data or embedded data with centrality  $\geq 30\%$ . In addition, the fit to the  $\phi, \rho, \omega$  mesons is excluded, because they

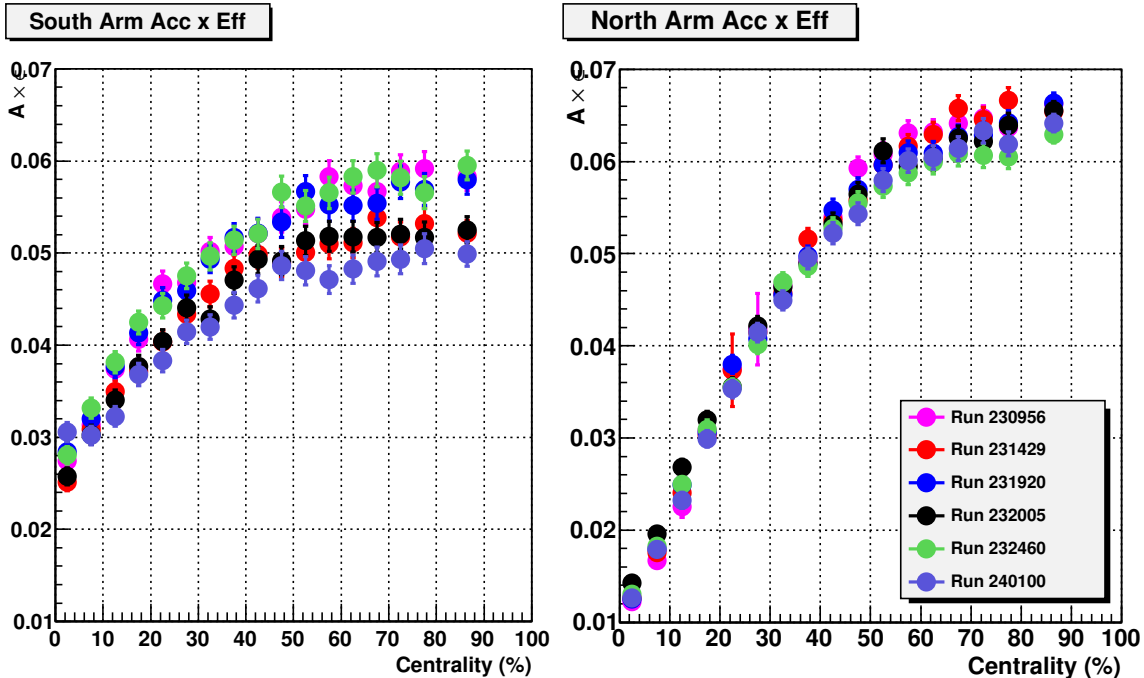
don't appear in large enough quantity relative to the  $J/\psi$  in the embedded events.

With the number of reconstructed  $J/\psi$ s in hand, we can calculate the  $\text{acc} \times \text{eff}$  in a given bin as:

$$\epsilon = N_{J/\psi}^{\text{reconst.}} / N_{J/\psi}^{\text{thrown}} \Big|_{\text{cent, } p_{\text{T}}, y \text{ bin}} \quad (4.14)$$

#### 4.4.3 Time-averaged Acc $\times$ Eff

Figure 4.11: Acc $\times$ eff vs. centrality for both the North and South Arms for the six reference runs.



The dataset (after quality cuts) consists of  $>700$  individual runs, with variations due to HV channels that are tripped and disabled and FEMs that are disabled, along with environmental effects such as humidity and barometric pressure. Ideally, the  $\text{acc} \times \text{eff}$  using the embedding method would be calculated for each run and then averaged, to account for all variations in the detectors between runs. Because this is computationally prohibitive (due to the size of the Au+Au events being used for the embedding), instead we divide the data into six periods of similar detector performance, mainly due to changes in the number of disabled MUTR HV channels in the South Arm (the North Arm performance was much more stable). Within each period a representative run

is chosen to be the reference for that particular time period. These runs and their corresponding periods are listed in Table 4.4, along with the number of events for each. The embedded acc $\times$ eff is calculated for each reference run, and the values are shown in Figure 4.11 and Tables A.18-A.22.

Table 4.4: Reference runs and their corresponding periods, where '[' and ')' are the inclusive and exclusive set delimiters, respectively.

Run	Events	Period	Events in period
230956	4168993	[228042,231100)	669212982
231429	5270319	[231100,231850)	232499773
231920	13399077	[231850,231970)	75131222
232005	1076450	[231970,232050)	55732027
232460	8476600	[232050,236700)	1326274554
240100	3208425	[236700,240200)	1607881326

To account for the relative run-to-run variations within each time period, the acc $\times$ eff calculation was performed for each individual run using purely PYTHIA  $J/\psi$ s (not embedded) and is shown in Figure 4.12. This is used to calculate a correction factor for the embedded acc $\times$ eff of the reference run. Note the this only includes  $p_T$ - and  $y$ -dependence, since there is no centrality variable for PYTHIA  $J/\psi$  events. This correction factor assumes that the centrality distributions of acc $\times$ eff for each run are related by a simple scale factor, at least within each time period. For reference run  $i$ , in each kinematic bin of  $p_T$  and  $y$ , we average the runs  $j$  in that period and calculate the correction factor:

$$c_i = \sum_j N_j^{evts} (\epsilon_j / \epsilon_i^{embed}) / \sum_j N_j^{evts} \quad (4.15)$$

The correction factors are typically less than 5%, and are listed in Table A.17.

We then average across the reference runs  $i$  in a similar fashion to get the total acc $\times$ eff for that bin:

$$\epsilon = \sum_i N_i^{evts} c_i \epsilon_i^{embed} / \sum_i N_i^{evts} \quad (4.16)$$

The resulting values are shown for centrality bins in Figure 4.13 and for  $p_T$  bins Figure 4.14. listed in the last column of Tables A.18-A.22. As can be seen, the acc $\times$ eff is lowest in the most central collisions, due to the higher occupancy in the detectors. The North Arm has worse occupancy

Figure 4.12: Run-by-run  $\text{acc} \times \text{eff}$  for pure PYTHIA  $J/\psi$ s, for both the South (top) and North (bottom) Arms. The blue dashed lines delineate the time periods used for averaging the  $\text{acc} \times \text{eff}$  values.

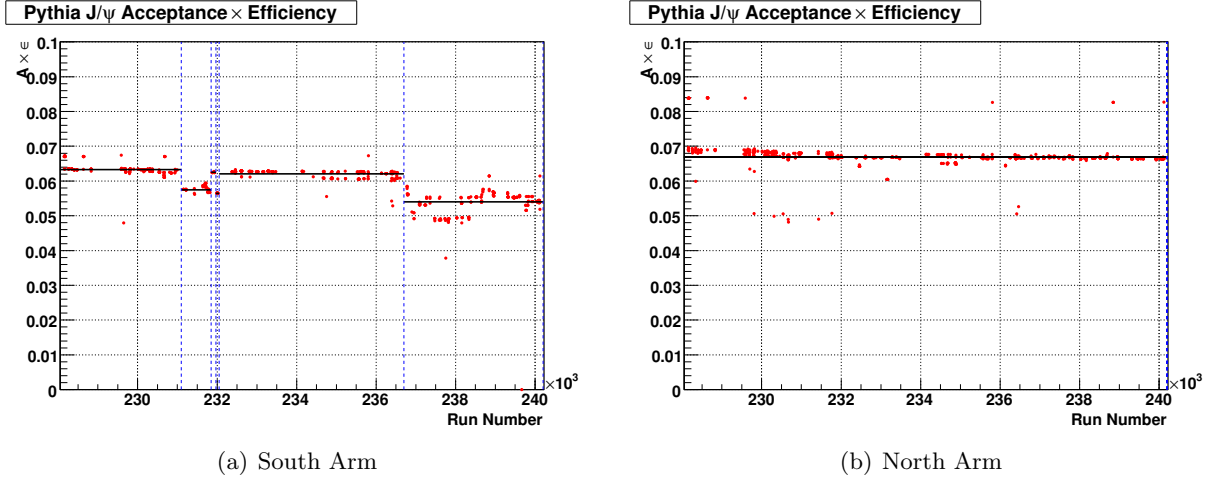
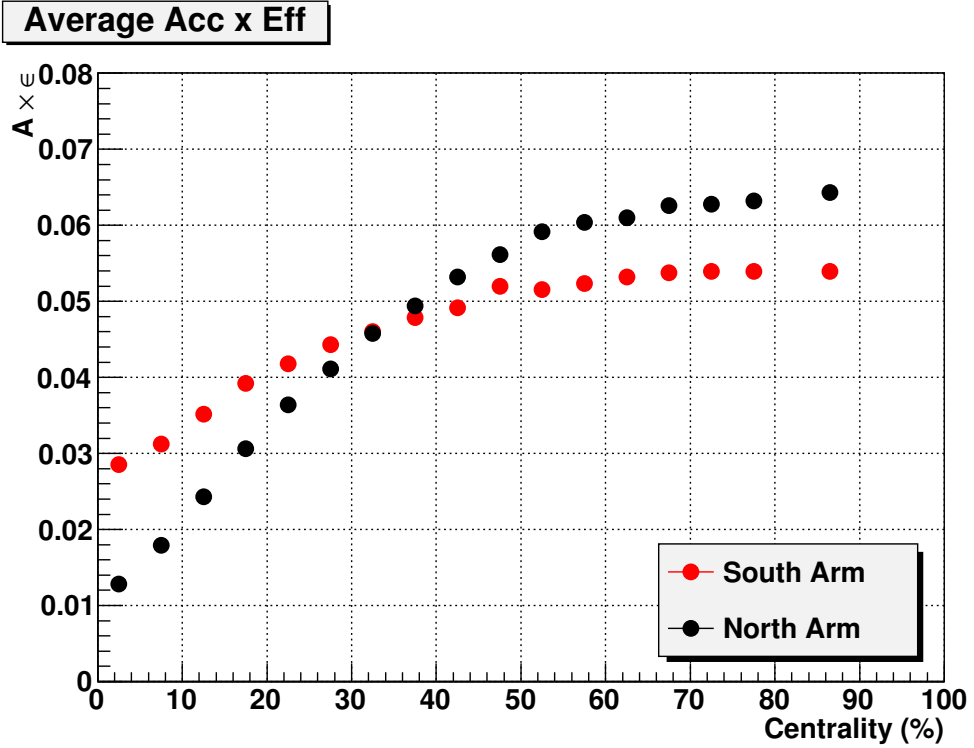
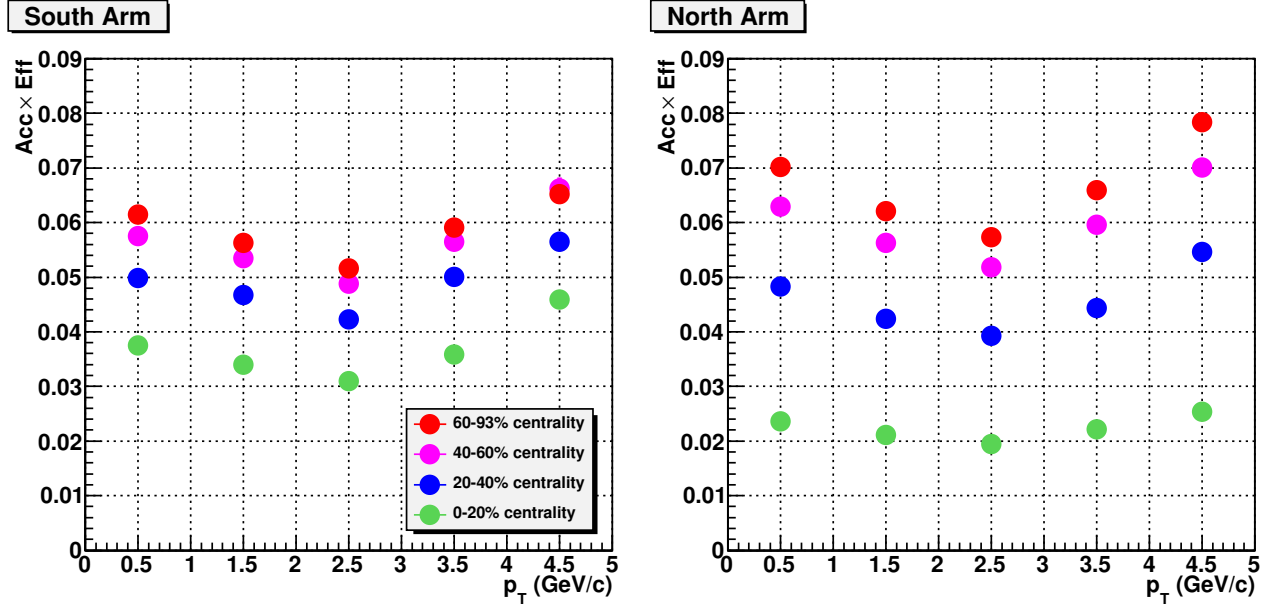


Figure 4.13: Run-averaged  $\text{acc} \times \text{eff}$  vs. centrality for both the North and South Arms.



than the South Arm in central events, and hence a steeper drop in efficiency. The  $\text{acc} \times \text{eff}$  vs.  $p_T$  is very similar in shape between the two arms, with the only difference being the occupancy-related

Figure 4.14: Run-averaged  $\text{acc} \times \text{eff}$  vs.  $p_T$  for both the North and South Arms in 20% centrality bins.



centrality effect.

## Chapter 5

### Experimental Uncertainties and Results

#### 5.1 Systematic Uncertainties

The various systematic uncertainties in this analysis are classified as either Type A, B, or C. Type A refers to uncertainties which are uncorrelated between points, Type B refers to uncertainties which are correlated between points to some degree (*i.e.* the points would move in some coherent fashion), and Type C refers to “global” uncertainties which are identical and completely correlated across all points. The Type A uncertainties are added in quadrature with the statistical uncertainties and displayed as error bars, the Type B uncertainties are displayed as boxes behind the points, and the total Type C uncertainty is labeled in text on the plots. The systematics and their Type when plotting vs. centrality,  $p_T$ , or rapidity are listed in Table 5.1.

##### 5.1.1 Signal Extraction (Type A and B)

The systematic uncertainty on the extracted signal is estimated as described in Section 4.3.3. The RMS of the 27 various fits (3 fit functions, 3 Gaussian relative normalizations, 3 background normalizations) is taken to be the systematic on the signal extraction. It is considered to be uncorrelated point-to-point.

In addition, the difference between the signal extracted using mixed background and like-sign background is taken as the limits of the real signal. This error is calculated as the difference between the signals divided by  $\sqrt{12}$ . The sign of the difference appears to be correlated between points, so this is taken to be type B.

Table 5.1: Systematic uncertainties for arm-averaged invariant yields and  $R_{AA}$ . The bottom section only applies to  $R_{AA}$ . How the uncertainties are treated as functions of centrality,  $p_T$ , and rapidity are included, as well as how they are treated when averaging South Arm and North Arm invariant yields.

Systematic	Value		Type of Uncertainty			Arm-to-arm
	Peripheral	Central	vs. Cent.	vs. $p_T$	vs. Rap.	
Signal Extr.	1.6%	9.8%	A	A	A	uncorrelated
Background Est.	0.6%	5.0%	B	B	B	correlated
Acceptance	2.2%	3.6%	B	B	B	uncorrelated
MC Input Dists.	4%	4%	B	B	B	correlated
MUTR Eff.	1.4%	2%	B	B	B	uncorrelated
MUID Eff.	2.8%	4%	B	B	B	uncorrelated
MC and Data match	0%	16%	B	C	C	correlated
$N_{coll}$	19%	10%	B	C	C	-
$p+p$ Errors	varies		C	A/B/C	A/B/C	-

### 5.1.2 Acceptance (Type B)

The uncertainty on the acceptance between octants is measured by comparing the  $\phi$ -distribution of tracks in the MUTR. The Monte Carlo (MC) distribution of tracks is compared to that of the real data (RD) tracks, where the MC histogram is normalized to the RD total integral. Examples of these distributions can be seen in Figure 5.1 for runs 230956 and 231429. The RMS of the relative octant-by-octant difference is taken to be the uncertainty for one track passing through one octant of the detector. The RMS about the mean is calculated for one reference run as:

$$X_j = \frac{MC_j - RD_j}{RD_j} \quad (5.1)$$

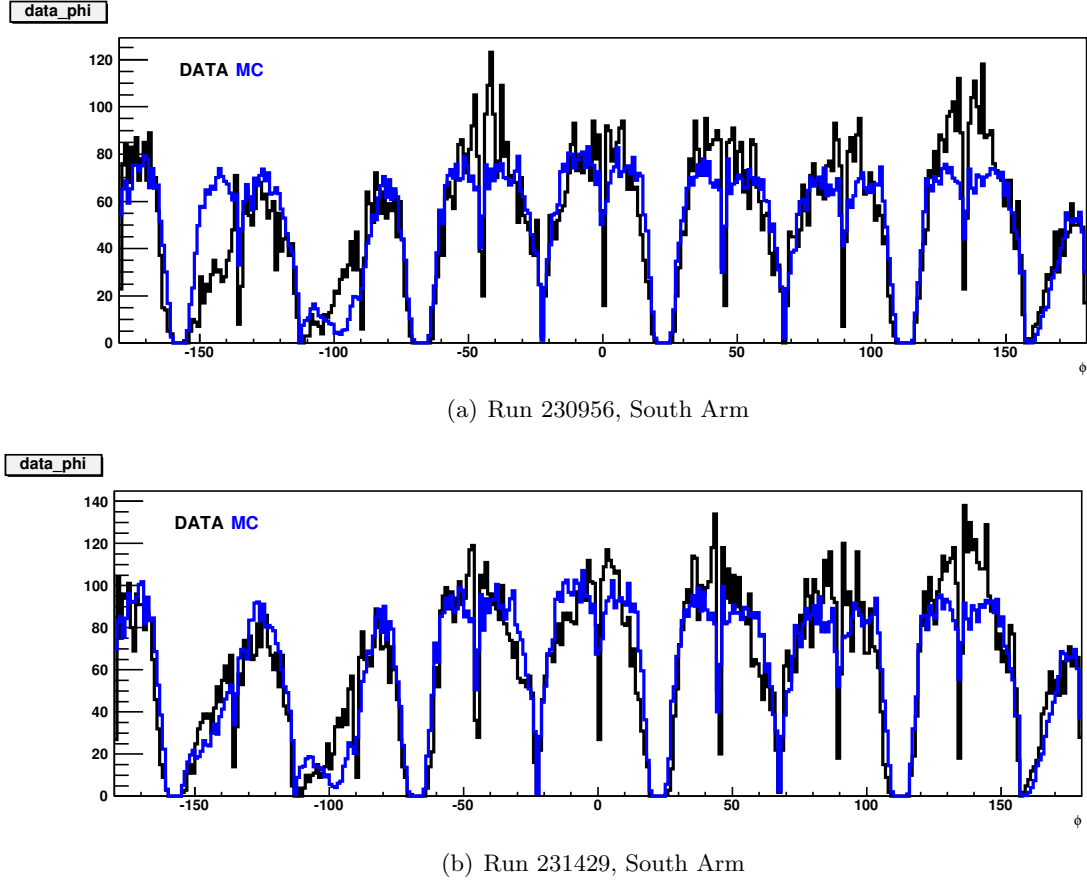
$$RMS_i = \sqrt{\frac{1}{N-1} \sum_j^{octs} (X_j - \bar{X})^2} \quad (5.2)$$

The uncertainty determined for each particular reference run is then averaged, weighting by the number of events in the corresponding period of running.

$$\langle RMS \rangle = \sum_i^{runs} N_i^{evts} RMS_i / \sum_i^{runs} N_i^{evts} \quad (5.3)$$

This is the uncertainty for a single track in one octant of the MUTR. Because the total  $J/\psi$  acceptance is the average of the acceptance of the octants for single tracks, and then squared to

Figure 5.1: Track  $\phi$  distributions from both simulation (blue) and data (black). The distributions have been normalized to the same integral.



get the pair acceptance, the uncertainty on the total pair acceptance is found by dividing by  $\sqrt{8}$  because the total acceptance is an average across the eight octants, and multiplying by 2 because the total is for pairs of tracks. This is written out below:

$$A_{pair} = \frac{1}{N_{oct}} \sum_{oct} A_{single,oct}^2 \quad (5.4)$$

$$\sigma_{pair}^2 = \sum_{oct} \left( \frac{\partial A_{pair}}{\partial A_{single,oct}} \right)^2 \sigma_{single}^2 = (2\sigma_{single}/8)^2 \quad (5.5)$$

$$\sigma_{total} = \langle RMS \rangle / 2 \quad (5.6)$$

This results in a 3.8% systematic uncertainty for the South Arm, and 2.5% for the North Arm. The one section of the detector not accurately described by the simulation is the half-octant near  $-150^\circ$  in the South Arm, as can be seen in the top plot of Figure 5.1. This disagreement only

existed for the first running period, with reference run 230956. In later periods the detector is better described, as can be seen in the lower plot of the Figure.

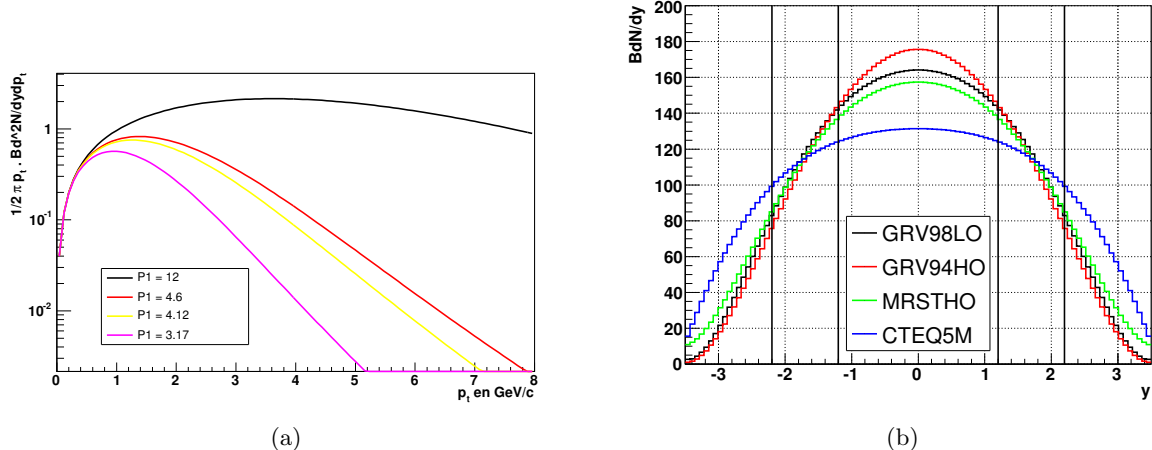
### 5.1.3 Acceptance Input Distributions (Type B)

The uncertainty in the acceptance due to the  $J/\psi$  distribution which is input to the simulation was determined in [47] to be 4%. This value was derived by varying the input  $p_T$  and rapidity distributions, as well as the  $z$ -distribution of the  $J/\psi$  production vertex. This is considered correlated point-to-point, as it would affect all the acceptance values similarly. The  $p_T$  distributions were varied by changing the  $P_1$  parameter in the phenomenological function:

$$\frac{1}{2\pi p_T} \frac{d^2N}{dy dp_T} = A \times \left( 1 + \left( \frac{p_T}{P_1} \right)^2 \right)^{-6} \quad (5.7)$$

as shown in Figure 5.2(a). The rapidity distributions were derived from empirical fits to several PDFs, and are shown in Figure 5.2(b).

Figure 5.2:  $J/\psi$   $p_T$  (left) and rapidity (right) distributions used as input to calculated  $\text{acc} \times \text{eff}$  systematic.



### 5.1.4 MUTR and MUID Efficiencies (Type B)

There is additional uncertainty on the  $\text{acc} \times \text{eff}$  from the MUTR and MUID detector efficiencies that are used in the simulation, and these were calculated for [47]. The uncertainty on the MUTR

efficiency was determined to be 2%. This includes the effect due to hot packets in the detector which are not accounted for (runs with many hot packets are removed from the dataset before analysis).

A 2.2% uncertainty on the individual MUID tube efficiencies was propagated to the overall detector efficiency by varying the efficiencies in the simulation. This resulted in a 4% uncertainty on the overall  $\text{acc} \times \text{eff}$ . Both of the MUID and MUTR uncertainties are correlated point-to-point.

### 5.1.5 Monte Carlo and Data Matching (Type B)

This uncertainty attempts to encompass the difference between the acceptance  $\times$  efficiency calculated by embedding PYTHIA  $J/\psi$ s in real data and the efficiency of actual  $J/\psi$ s in the data. This was done by embedding  $p+p$  events with excellent  $J/\psi$  candidates into Au+Au events, and comparing the resulting  $\text{acc} \times \text{eff}$ . It was found that the embedded  $p+p$  sample always had a lower efficiency than PYTHIA  $J/\psi$ s, and only in the 0-40% centrality range. Therefore, the difference was used as a systematic error on the  $\text{acc} \times \text{eff}$ , but only in the negative direction. The values are listed below:

- 0-10% Centrality: 16.3%
- 10-20% Centrality: 8.9%
- 20-30% Centrality: 3.8%
- 30-40% Centrality: 0.8%

### 5.1.6 North/South Matching (Type B)

Because the North and South Arm invariant yields systematically differ by more than the uncorrelated errors, as will be shown in the next section, we apply a systematic uncertainty to account for this. We fit the ratio of North/South for peripheral points (30-93% centrality) to a flat line, which gives  $0.77 \pm 0.04$ . So we take 23% to be the typical difference between North and South.

Since it is not known which result is more correct, we use a flat probability distribution of width 23%, which gives  $\sigma = 23\%/\sqrt{12} = 6.6\%$ . The fit line is shown in Figure 5.4.

### 5.1.7 Number of Binary Collisions (Type B or C)

The uncertainty on  $\langle N_{\text{coll}} \rangle$  for a given centrality bin is estimated by varying the parameters of the Glauber Monte Carlo simulation described in Section 3.3.1. The resulting uncertainties are taken to be type B as a function of centrality, but as a function of  $p_{\text{T}}$  or rapidity are type C because only one value of  $\langle N_{\text{coll}} \rangle$  is used for all bins (in a given centrality). The full  $\langle N_{\text{coll}} \rangle$  uncertainties are listed in Table 3.4.

### 5.1.8 $p+p$ Reference Data

There is a 7.6% type C systematic on the  $p+p$  invariant yields, which must also be applied to all the  $R_{\text{AA}}$  quantities. This includes a 7.1% systematic on the inelastic cross section that is sampled by the  $p+p$  BBC minimum bias trigger, a 2.5% systematic on the BBC triggering efficiency for events containing a  $J/\psi$  (or any hard scattering), and a 1% uncertainty on the sampled luminosity. This does **not** include the 4.5% uncertainty on the total  $p+p$  inelastic cross section of 42.2 mb, because that uncertainty also applies to the  $\langle N_{\text{coll}} \rangle$  systematic. However, the  $p+p$  invariant yield goes as  $1/\sigma_{\text{inel}}$ , while the  $\langle N_{\text{coll}} \rangle$  roughly scales with  $\sigma_{\text{inel}}$ , so systematic deviations will roughly cancel.

There is a 7.1% type B systematic on the  $p+p$  points from the absolute normalization of the acceptance. This systematic should cancel when taking the ratio with Au+Au data, as they use the same technique for calculating acc $\times$ eff.

It should be noted that when plotting  $R_{\text{AA}}$  vs.  $p_{\text{T}}$  or rapidity, the type A and B uncertainties on the  $p+p$  points in the ratio are combined in quadrature with the corresponding Au+Au uncertainties, as would be expected. However, only one  $p_{\text{T}}$ -integrated  $p+p$  point is used when plotting  $R_{\text{AA}}$  vs. centrality, and therefore the total error (of all types added in quadrature) on that point is taken to be an additional type C uncertainty on  $R_{\text{AA}}$  points. This adds another 7.3% (without the

acceptance systematic) in quadrature with the type C listed above, for a total type C uncertainty of 10.6%.

## 5.2 Invariant Yields

The  $J/\psi$  signal extraction reported in previous chapters is presented here as invariant per-event yields, corrected for the acceptance and efficiency of the PHENIX detectors. The formula for the  $p_{\text{T}}$ -integrated yields can be written out as:

$$B_{\mu\mu} \frac{dN_{J/\psi}}{dy} = \frac{1}{\Delta y} \frac{N_{J/\psi}}{N_{\text{evts}} A \epsilon} \quad (5.8)$$

and the formula for the  $p_{\text{T}}$ -dependent yields is:

$$B_{\mu\mu} \frac{d^3 N_{J/\psi}}{dp_{\text{T}}^2 dy} = B_{\mu\mu} \frac{d^2 N_{J/\psi}}{2\pi p_{\text{T}} dp_{\text{T}} dy} = \frac{1}{2\pi p_{\text{T}} \Delta p_{\text{T}} \Delta y} \frac{N_{J/\psi}}{N_{\text{evts}} A \epsilon} \quad (5.9)$$

where  $N_{J/\psi}$  is the extracted signal counts,  $N_{\text{evts}}$  is the number of BBC minimum bias-triggered events that were processed,  $A\epsilon$  is the acceptance  $\times$  efficiency (all described in Chapter 4),  $\Delta y$  and  $\Delta p_{\text{T}}$  are the  $y$  and  $p_{\text{T}}$  bin widths, and  $p_{\text{T}}$  is the center of the  $p_{\text{T}}$  bin in question.

The invariant yields calculated from the quantities described and tabulated in previous chapters are shown as functions of centrality in Figure 5.3 in 10% bins and in Figure 5.4 in 5% bins, and are tabulated in Tables A.23-A.25. The invariant yield as a function of  $p_{\text{T}}$  in 20% centrality bins is shown in Figure 5.5 and listed in Tables A.26-A.28.

By virtue of using symmetric colliding species, the forward and backward rapidity invariant yields may be averaged to produce a more precise result. To take into account the difference in the uncertainties on the two results, the correct weights must be used when averaging. As detailed in [73], the proper weights for Gaussian-distributed errors are the inverse square of the uncertainties that are uncorrelated between the two results:

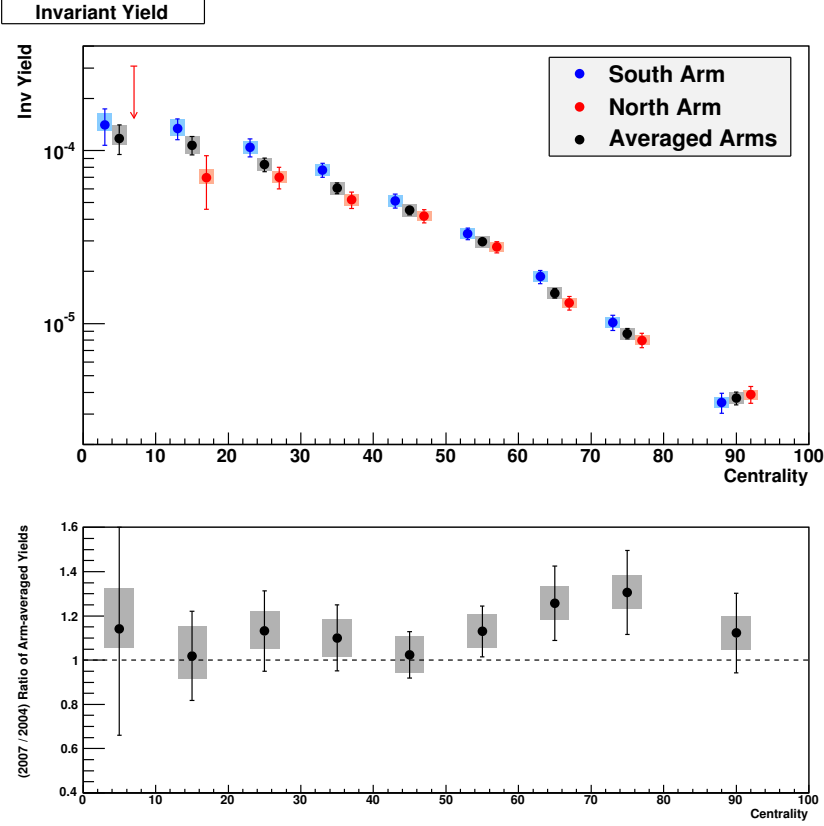
$$w_{\text{arm}} = 1/\sigma_{\text{arm,uncorr}}^2 \quad (5.10)$$

and the average invariant yields are then calculated as:

$$Y_{\text{ave}} = \frac{w_N Y_N + w_S Y_S}{w_N + w_S} \quad (5.11)$$

The statistical and systematic uncertainties are likewise combined using the weight factors, such that the average uncorrelated error is smaller than that of the separate values (as one would

Figure 5.3:  $J/\psi$  invariant yield vs. centrality in 10% bins, for both the South and North Arms, as well as the Arm-averaged values. The ratio of yields from this dataset to those from 2004 is shown in the lower panel for comparison.



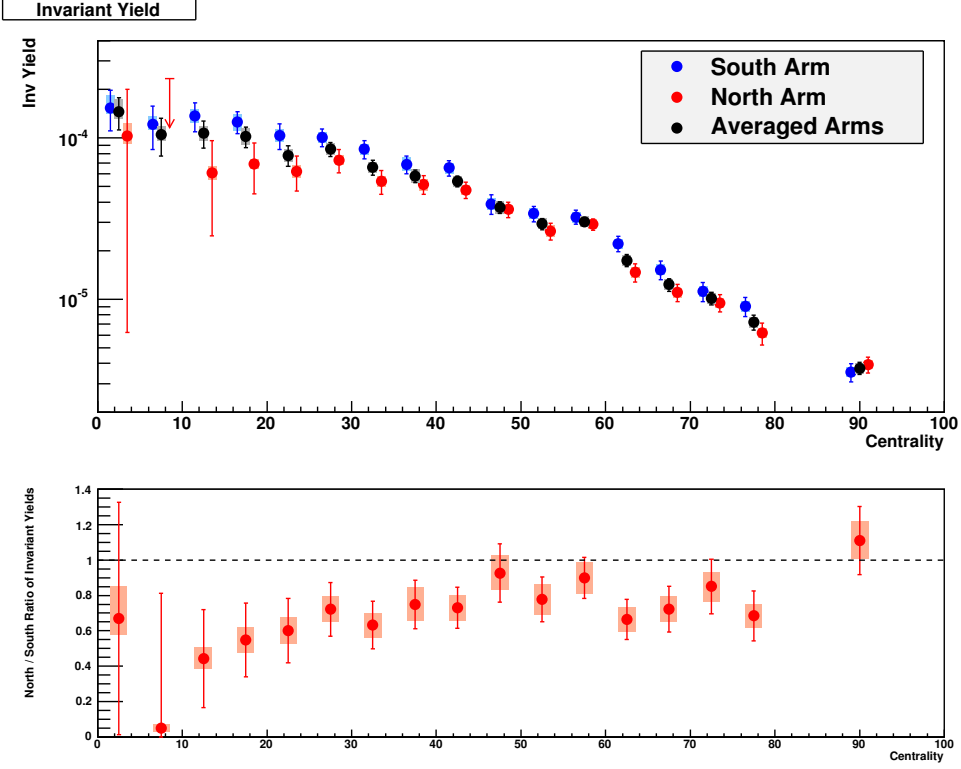
expect when averaging two measurements). Uncertainties that are 100% correlated, however, remain the same for the averaged quantity. We apply this worst-case scenario to the systematic uncertainties for which the amount of correlation is unknown. This results in the following two formulas for calculating the average uncertainties:

$$\sigma_{stat} = \sqrt{\frac{(w_N \sigma_{N,stat})^2 + (w_S \sigma_{S,stat})^2}{(w_N + w_S)^2}} \quad (5.12)$$

$$\sigma_{sys} = \sqrt{\frac{(w_N \sigma_{N,uncorr})^2 + (w_S \sigma_{S,uncorr})^2}{(w_N + w_S)^2} + \sigma_{corr}^2} \quad (5.13)$$

The resulting arm-averaged invariant yields are shown in 10% centrality bins in Figure 5.3. The ratio of the Run 7 to Run 4 invariant yields are shown in the lower panel of the Figure, and it can be seen that the two results are in agreement at the one-sigma level in all but the 60-80%

Figure 5.4:  $J/\psi$  invariant yield vs. centrality in 5% bins, for both the South and North Arms, as well as the Arm-averaged values. The ratio of North/South yields is shown in the lower panel for comparison, along with a fit to the 30-93% most peripheral bins. The fit result is used to formulate the systematic uncertainty due to North/South disagreement in Section 5.1.6.



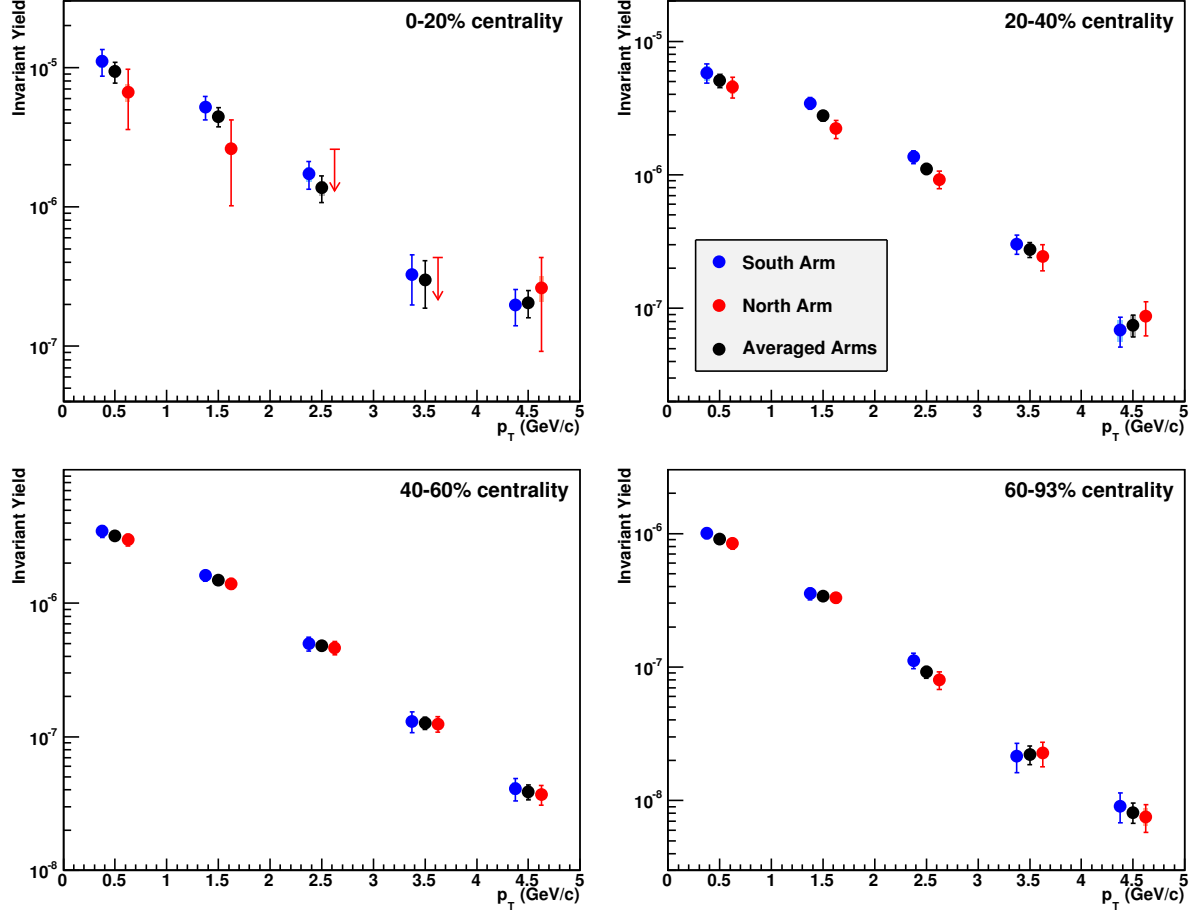
centrality bins. However, the Run 7 yields are systematically somewhat larger than the Run 4 yields if the points are compared as a whole.

The invariant yield in 5% centrality bins is shown in Figure 5.4, and the ratio of the North Arm to the South Arm yields is shown in the lower panel. It can be seen that the two results disagree on the order of 20%, and this is accounted for by a systematic uncertainty, as was described in Section 5.1.6.

Finally, the invariant yield as a function of  $p_T$  is shown in Figure 5.5 in 20% centrality bins. In the 0-20% centrality bin, there were two  $p_T$  bins in the North Arm that did not satisfy our significance criteria on the signal of:

$$N_{J/\psi} \geq \sqrt{\sigma_{stat}^2 + \sigma_{sys}^2} \quad (5.14)$$

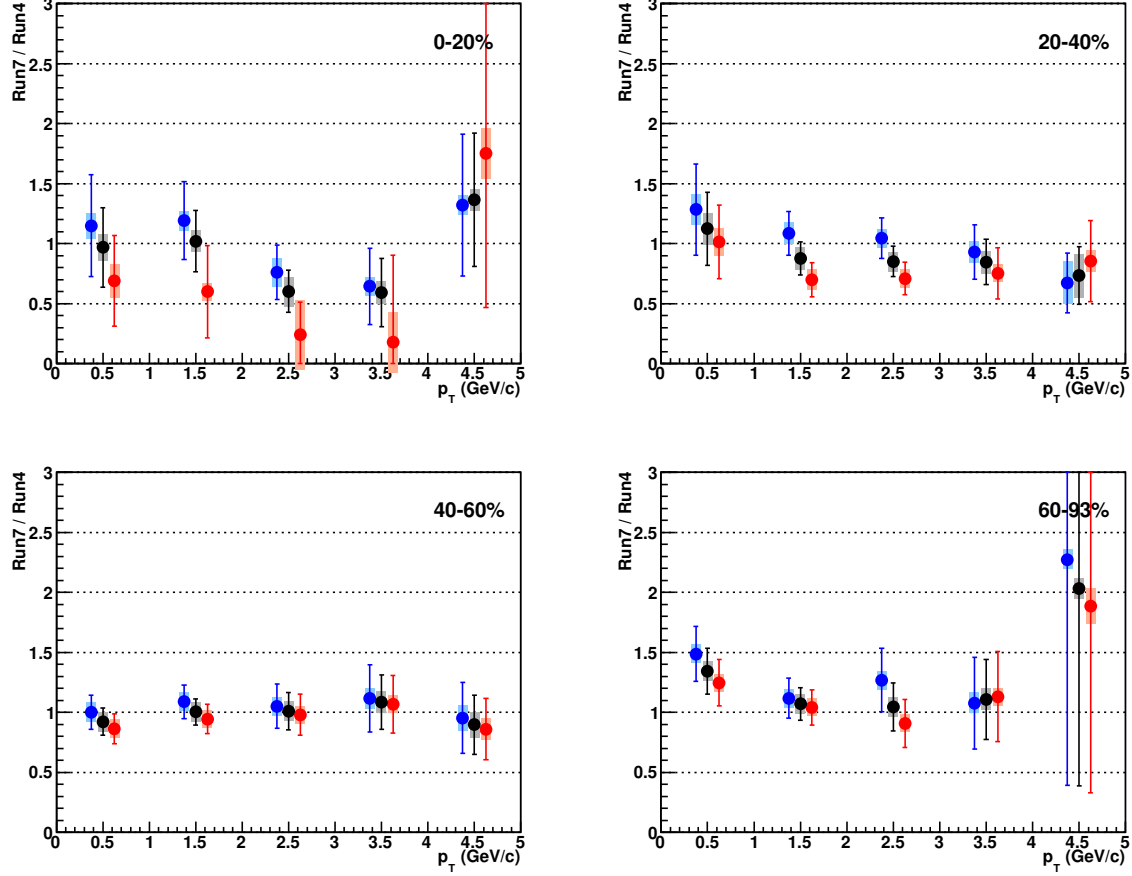
Figure 5.5:  $J/\psi$  invariant yield vs.  $p_T$  in four centrality bins, for both the South and North Arms, as well as the Arm-averaged values.



For these bins, only 90% confidence-level upper limits are reported. Because we cannot simply average two points in these bins, the likelihood functions are combined numerically and the maximum and one-sigma central confidence interval are found and used for the averaged invariant yield and error bar.

Shown in Figure 5.6 are the ratios of the Run 7/Run 4 invariant yields vs.  $p_T$ . As can be seen in the Figure, most bins agree within one-sigma and all agree within two-sigma.

Figure 5.6: Ratio of  $J/\psi$  invariant yield in 2007 to 2004 vs.  $p_T$  in four centrality bins, for both the South and North Arms, as well as the Arm-averaged values.



### 5.3 Nuclear Modification Factor $R_{AA}$

The nuclear modification factor  $R_{AA}$  measures the amount of deviation in heavy ion collisions from the naïve scenario of  $p+p$  collisions scaled up by the number of binary nucleon-nucleon collisions ( $N_{\text{coll}}$ ) in the centrality bin of interest. It is written as:

$$R_{AA} = \frac{1}{\langle N_{\text{coll}} \rangle} \frac{Y_{\text{Au+Au}}}{Y_{p+p}} \quad (5.15)$$

where  $Y_{xx}$  represents the Au+Au or  $p+p$  invariant yields in the bin of interest and  $\langle N_{\text{coll}} \rangle$  is the average value of  $N_{\text{coll}}$  in that centrality bin (see Table 3.4).

The PHENIX Run 5  $\sqrt{s}=200$  GeV  $p+p$  results [33] are used for these  $R_{AA}$  calculations. The

$p+p$   $p_T$ -integrated cross section for the  $1.2 < |y| < 2.2$  rapidity bin is  $B_{\mu\mu}d\sigma/dy = 27.61 \pm 2.81$  nb. To get the invariant yield we simply divide by the total  $p+p$  inelastic cross section of 42.2 mb, giving us  $B_{\mu\mu}dN/dy = (6.5427 \pm 0.6658) \times 10^{-7}$ . This value is used for all of the  $p_T$ -integrated  $R_{AA}$  points. For the separate  $p_T$  bins, the  $p+p$  invariant yield for the same bin is used. The full invariant yields are listed in Table 5.2.

Table 5.2: Run 5  $p+p$  invariant yields as a function of  $p_T$  from [33].

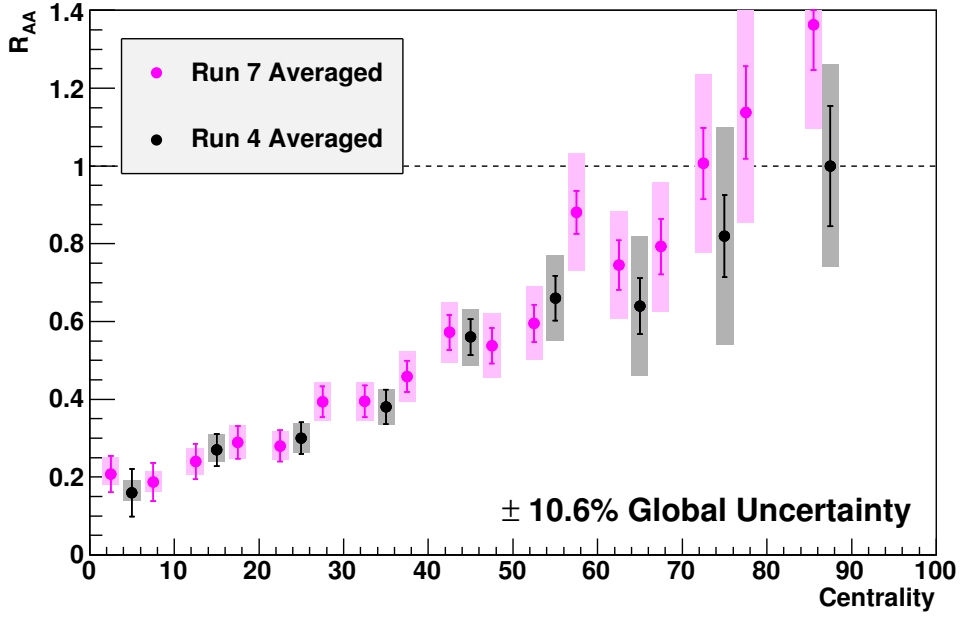
$p_T$ (GeV/c)	Inv. Yield ( $\times 10^{-8}$ )	Uncorr. Error ( $\times 10^{-8}$ )	Corr. Error ( $\times 10^{-8}$ )
all	65.427	2.153	6.303
0-1	6.16114	0.21847	0.59242
1-2	2.89100	0.11848	0.28436
2-3	0.78199	0.03188	0.07583
3-4	0.20095	0.01049	0.01943
4-5	0.04550	0.00420	0.00427
5-6	0.00791	0.00170	0.00076
6-7	0.00408	0.00084	0.00045

$R_{AA}$  as a function of centrality is shown in Figure 5.7 in 5% centrality bins, and Figure 5.8 in 10% centrality bins. Both sets of values are listed in Table A.29. It can be seen in the lower panel of Figure 5.8 that the  $p_T$ -integrated  $R_{AA}$  is very similar to those measured in Run 4 in central collisions. In peripheral collisions, by comparison of the bottom panel of Figure 5.8, the variation from Run 4 is mostly due to the Run 7 invariant yield values.

In the most peripheral bin, however there is a significant contribution due to a  $\sim 15\%$  smaller  $\langle N_{\text{coll}} \rangle$  value than was used for the Run 4 results. This is believed to be due to changes in how the BBC trigger efficiency is calculated from the data and changes to the centrality calculation itself. As opposed to the methods described in Section 3.3.1, in the Run 4 analysis the matching of the Glauber simulation to the BBC data was done using Poisson statistics instead of a negative binomial distribution. In addition, the centrality in Run 4 was determined using the so-called “clock method”, which incorporated both the BBC and the ZDC hits to divide the data into centrality bins. This method was later shown to be less accurate than using the BBC alone.

$R_{AA}$  as a function of  $p_T$  is shown in Figure 5.9 in four broad centrality bins, and values

Figure 5.7:  $J/\psi R_{AA}$  vs. centrality in 5% bins. Also shown are the PHENIX 2004 Au+Au data.



are listed in Table A.30. As can be seen, the Run 7 measured  $R_{AA}$   $p_T$  distributions are in good agreement with the Run 4 results.

Figure 5.8:  $J/\psi R_{AA}$  vs. centrality in 10% bins. Also shown are the PHENIX 2004 Au+Au data.

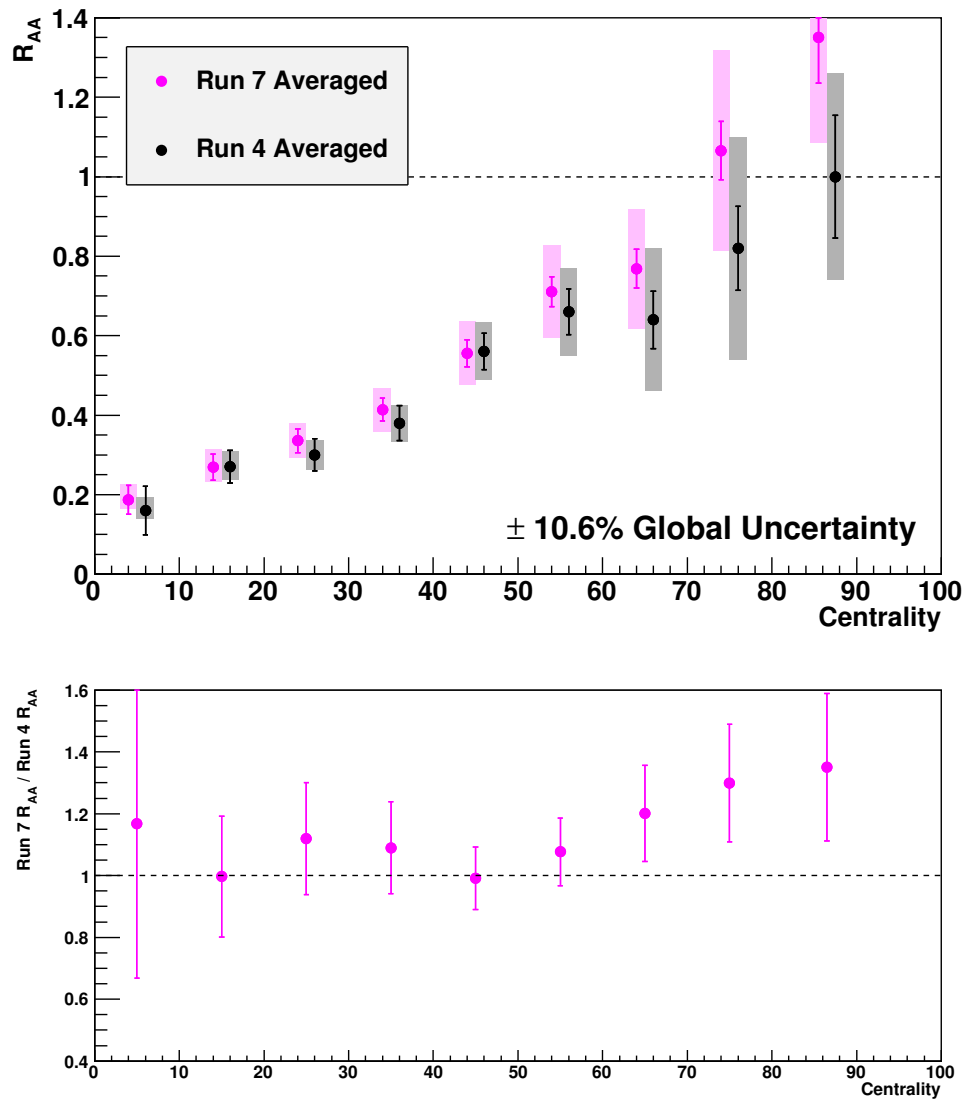
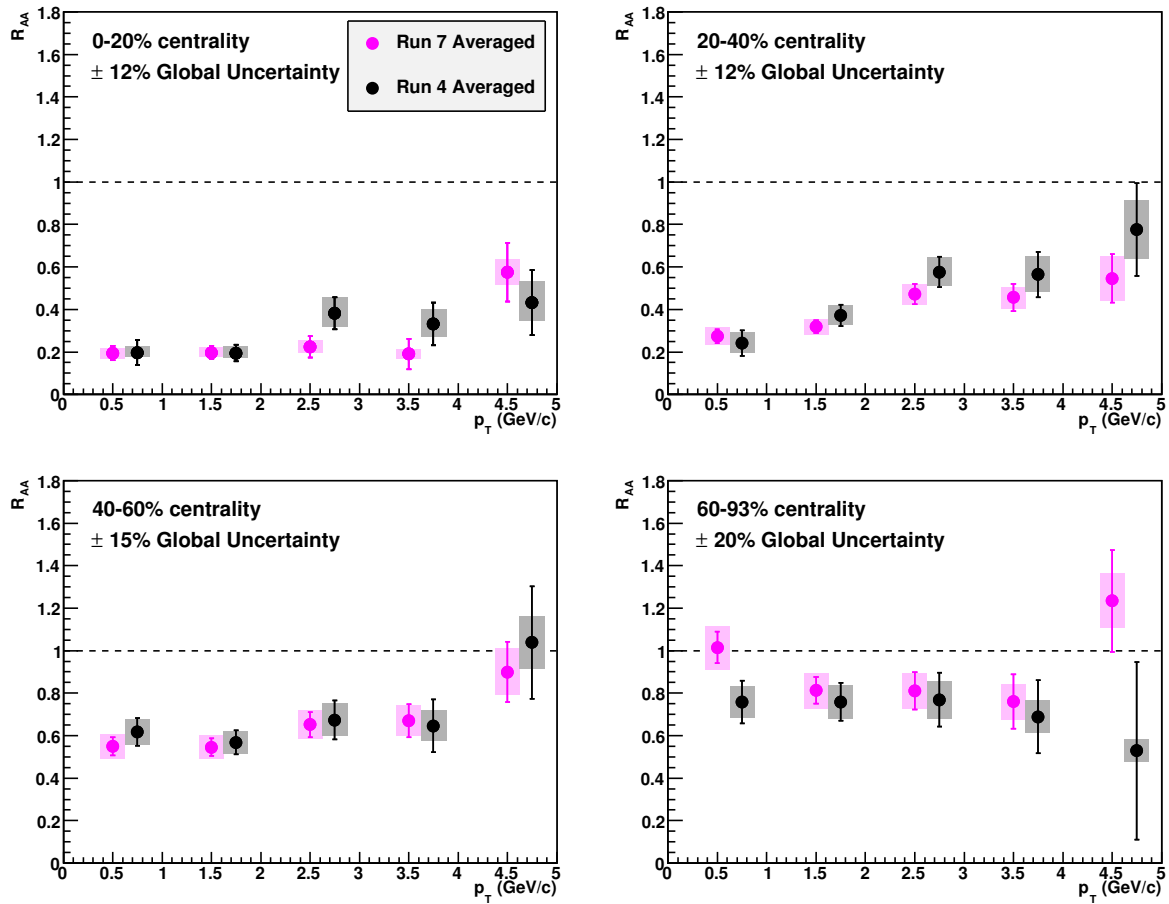


Figure 5.9:  $J/\psi$   $R_{AA}$  vs.  $p_T$  in four centrality bins. Also shown are the PHENIX 2004 Au+Au data.



## Chapter 6

### Comparison to Theoretical Models and Discussion

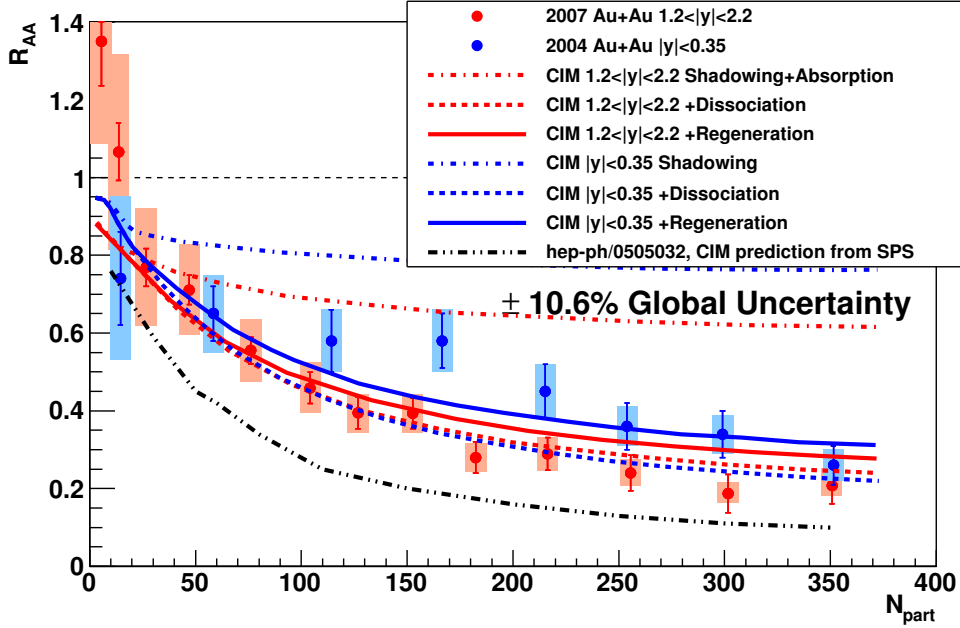
#### 6.1 Model Comparisons vs. Centrality

$J/\psi$  production in high-energy Au+Au collisions stands as a measurement by itself, but it is most interesting when interpreted in terms of  $J/\psi$  suppression by a hot partonic medium. In order to extract meaningful information about the medium we must compare to models that incorporate the various effects described in Chapter 2.

Calculations involving the Comover Interaction Model (CIM) use a rate equation which accounts for  $J/\psi$  break-up due to interactions with a co-moving medium. No assumptions about whether the medium is partonic or hadronic are made, nor whether the transition is smooth or abrupt; it is only assumed that some overall average cross section can be used. However, the cross section extracted from SPS data is assumed to be the same at RHIC. This prediction, based on SPS measurements, far exceeded the measured suppression at RHIC; however, it did not include any regeneration effects, and used a break-up cross section of  $\sigma_{br}=4.5$  mb [74], much larger than measured in  $d$ +Au collisions at RHIC. The prediction for mid-rapidity can be seen in Figure 6.1.

An updated calculation [75] was released after the PHENIX Run 4 data came out, and replaced the constant break-up cross section with an  $x$ -dependent function  $\xi(x_{\pm})\sigma_{Q\bar{Q}}$ , where  $x_{\pm} = 0.5 \left( \sqrt{x_F^2 - 4M^2/s} \pm x_F \right)$ , that accounts for both absorption and energy-momentum conservation. The regeneration component is normalized to the ratio of open charm production to  $J/\psi$  production, with the open charm cross section from  $p$ + $p$  data at mid-rapidity and PYTHIA at forward rapidity. The newer curves are in better agreement with the data at mid and forward rapidities, as shown

Figure 6.1: PHENIX  $J/\psi$   $R_{AA}$  measurements vs.  $N_{\text{part}}$ , compared to calculations of the Comover Interaction Model (CIM) at forward and mid-rapidity. Nuclear absorption is much stronger at forward rapidity, but the suppression from comover interactions and the enhancement from regeneration are both less, leading to similar predictions for both rapidities. Also included is the previous CIM prediction based on SPS data from [74], which over-predicted the suppression seen at RHIC.



in Figure 6.1. As can be seen in the Figure, the non-medium effects are much stronger at forward rapidity, due in part to the assertion that nuclear absorption is negligible at mid-rapidity. On the other hand, the effects of comover dissociation and regeneration are stronger at mid-rapidity, leading to predictions which are overall very similar at forward and mid-rapidity, with the forward rapidity curve slightly under-predicting the suppression seen in the data. In the end, it is questionable how much information can be extracted using a model that makes almost no assumptions about the properties of the medium.

Another model is put forward by Zhao and Rapp in [53] and [48] which incorporates both a QGP phase and a Hadron Gas (HG) phase. They begin by using two scenarios of CNM effects. In the first scenario, nuclear absorption is calculated in the usual Glauber formalism, shadowing and anti-shadowing are assumed to roughly cancel, such that the overall shadowing effects are encapsulated in  $\sigma_{br}$ , and Gaussian smearing of the  $J/\psi$   $p_T$  is used to simulate the Cronin effect.

In scenario 2 the CNM effects are treated as in [75], which leads to larger CNM suppression at forward rapidity, and Cronin effect is treated the same as scenario 1.

The thermal dissociation is modeled via a Boltzmann transport equation for both QGP and HG phases. The QGP is assumed to be an isentropically expanding cylindrical fireball.  $J/\psi$ -medium interactions are assumed to stop at a freeze-out temperature of 120 MeV. The final  $J/\psi$ - $p_T$ -distribution is calculated by spatially integrating the final phase-space distribution. The regeneration component assumes that the  $c\bar{c}$  is thermally equilibrated with the medium when it coalesces into a  $J/\psi$ , and so their  $p_T$  is given by a blastwave equation for the transverse flow velocity:

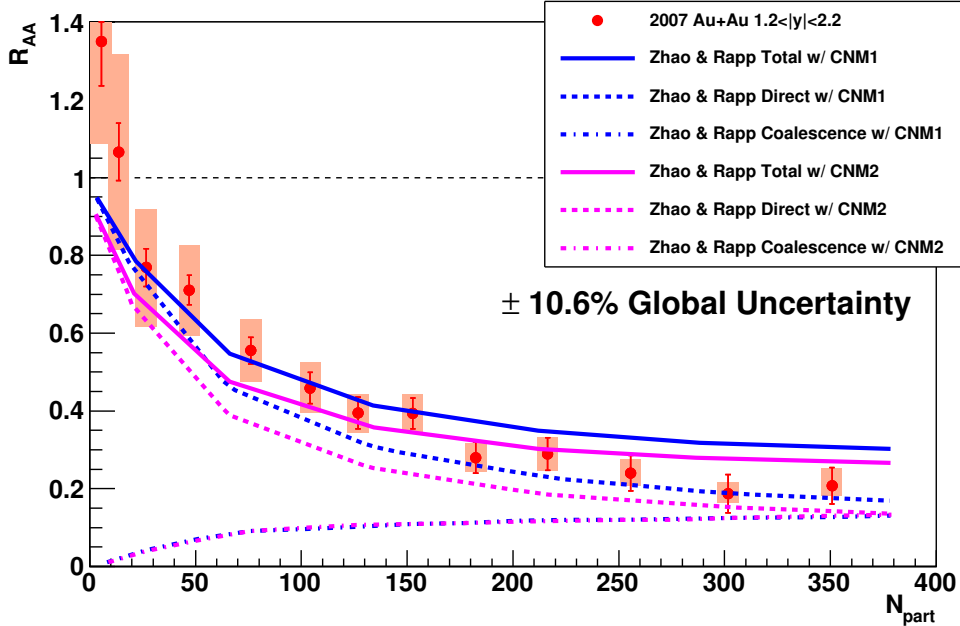
$$\frac{1}{p_T} \frac{dN}{dp_T} \propto m_T \int_0^R r dr K_1 \left( \frac{m_T \cosh y_T}{T} \right) I_0 \left( \frac{p_T \sinh y_T}{T} \right) \quad (6.1)$$

where  $m_T^2 = m_{J/\psi}^2 + p_T^2$ ,  $y_T = \tanh v_T^{-1}$ , and the transition to the HG phase occurs at 180 MeV (beyond which regeneration does not occur). The normalization of this component is performed by plugging the initial charm densities into a rate equation with both gain and loss terms, and solving at the freeze-out time.

The resulting curves for both CNM scenarios at forward rapidity are shown in Figure 6.2, along with the separate dissociation and regeneration components. The larger CNM suppression in scenario 2 leads to a more suppressed overall  $R_{AA}$ , but in general the total difference between the two scenarios is small. It is noteworthy that the regeneration component is only slightly larger at mid-rapidity in this model than at forward rapidity. This implies that the  $c\bar{c}$  pairs involved in regeneration are mostly diagonal pairs, *i.e.* produced together in the original collision. However, increasing the contribution of off-diagonal pairs would only increase the amount of regeneration, and lead to worse agreement with the data for central collisions.

A more unusual model is described by Kharzeev *et al.* in [76], in which they assume that the nuclear wave functions in very high energy nuclear collisions can be described by the Color Glass Condensate (CGC). The primary effect in the CGC picture is the saturation of the gluon fields as  $x \rightarrow 0$ , and calculations are done in a quasi-classical approximation. The key consequences for  $J/\psi$  production are the enhancement of the 3-gluon fusion process  $g + g + g \rightarrow J/\psi$  over the

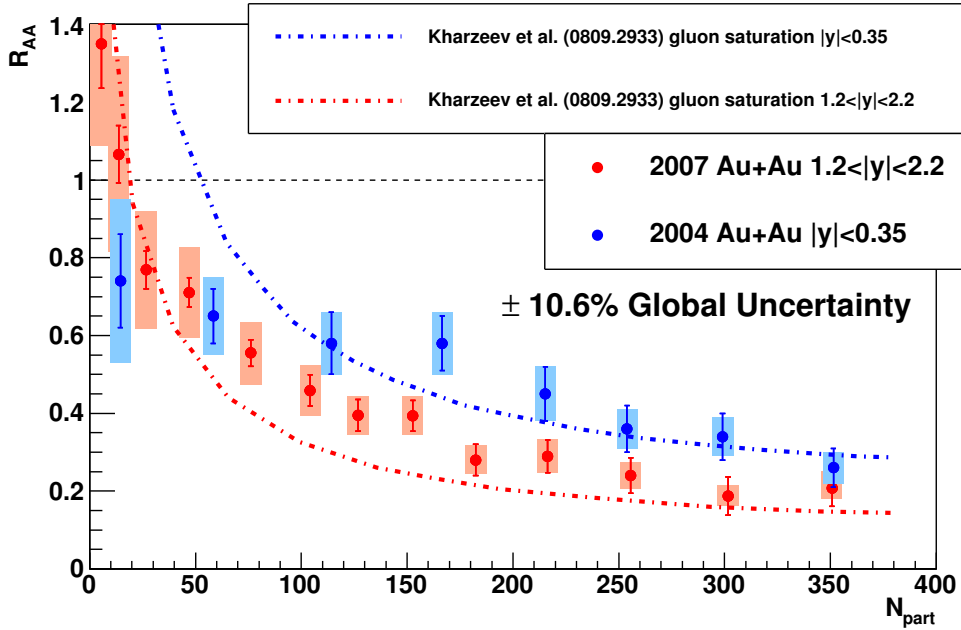
Figure 6.2: Predicted  $R_{AA}$  at forward rapidity for the model of Zhao and Rapp [53, 48] for two different scenarios of CNM effects. The results of the current analysis are shown for comparison. In addition, the contributions of dissociation and regeneration are shown separately.



2-gluon fusion process  $g + g \rightarrow J/\psi + g$ , and the suppression of  $J/\psi$  production and narrowing of the rapidity distribution due to saturation of the gluon fields in heavy ion collisions relative to  $p+p$  collisions. It should be noted that this model does not include any hot medium effects.

The calculated  $R_{AA}$  is shown in Figure 6.3 for both forward and mid-rapidity, along with the latest PHENIX data for both. The difference in suppression between the two rapidities is qualitatively reproduced by this model, and the large amount of suppression in central events as well. However, it should be noted that the model includes an overall normalization factor that is determined from fitting the measured rapidity distributions. While it is conceptually interesting that the model is able to roughly reproduce the data without invoking medium effects, a more realistic calculation including medium-induced suppression would be more plausible, although it would require independent determination of the normalization constant. Furthermore, this calculation is only valid for central nuclear collisions, so the large enhancement seen at small  $N_{\text{part}}$  should be ignored as outside the valid range of the model (it is unclear at what point the model becomes

Figure 6.3: Suppression curves at forward and mid-rapidity as calculated in the CGC framework involving gluon saturation, but not including hot medium effects [76]. PHENIX data at both rapidities is shown for comparison.



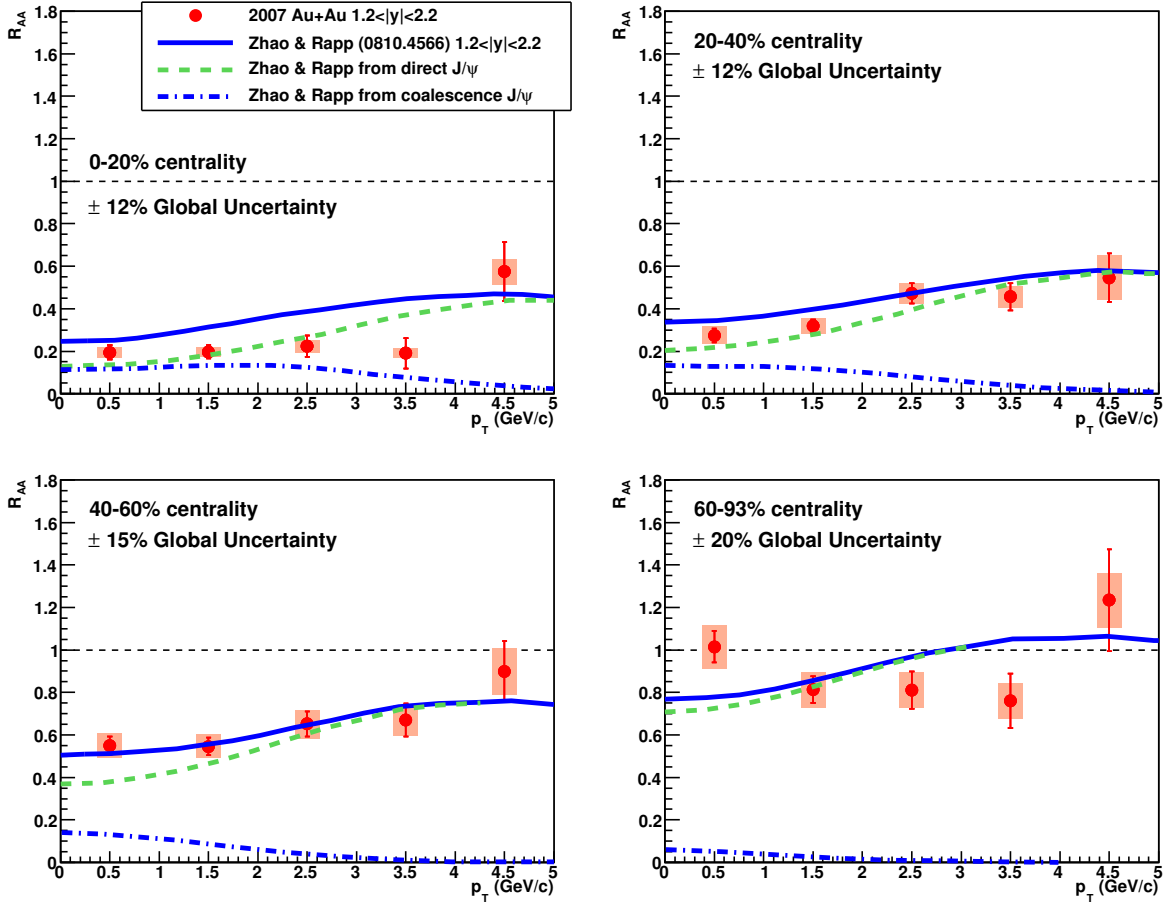
valid).

## 6.2 Model Comparisons vs. Transverse Momentum

The model of Zhao and Rapp, described in the previous section, was also used to calculate  $R_{AA}$  vs.  $p_T$  at forward and mid-rapidity. The forward rapidity results are compared to the results of this analysis in Figure 6.4. It can be seen that in the most central bin, the model underpredicts the amount of suppression for  $p_T < 4$  GeV/ $c$ . However, the model agrees qualitatively well with the data in the other three centrality bins. In the most peripheral bin, the level of modification is roughly reproduced, although the  $p_T$  shape is harder to get a handle on from the data.

Another model of interest is described by Kopeliovich, *et al.* in [77]. They calculate initial-state effects due to attenuation of the  $c\bar{c}$  dipole propagating through both nuclei, leading-twist gluon shadowing, and higher-twist shadowing of charm quarks. They also include Cronin broadening of the  $p_T$ -distribution in two different forms: the first uses a simple shift of  $\langle p_T^2 \rangle \rightarrow \langle p_T^2 \rangle + \delta$  in the

Figure 6.4: Predicted  $R_{AA}$  at forward rapidity for the model of Zhao and Rapp [53, 48]. The results of the current analysis are shown for comparison. In addition, the contributions of dissociation and regeneration are shown separately.

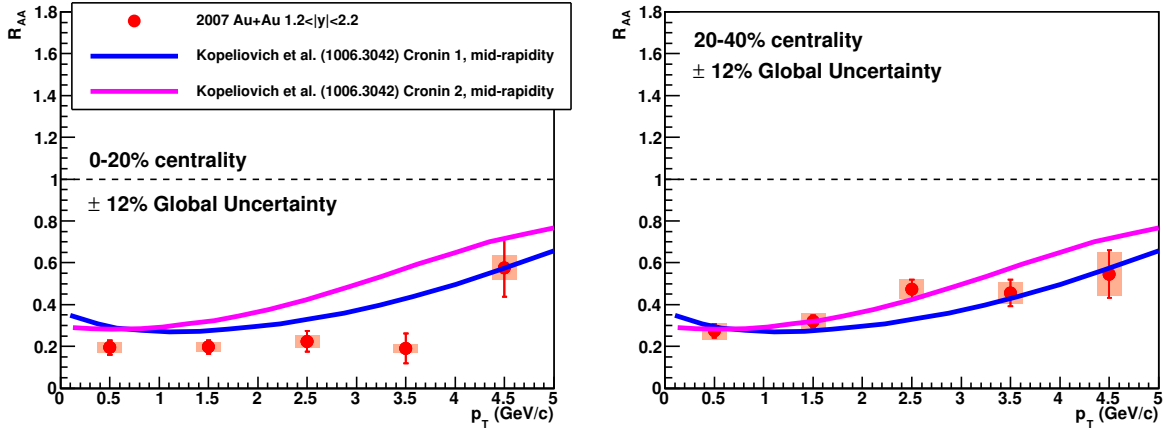


$p_T$ -distribution parametrization that matches  $p+p$  relatively well:

$$\frac{d\sigma}{dp_T^2} \propto \left(1 + \frac{p_T^2}{6\langle p_T^2 \rangle}\right)^{-6} \quad (6.2)$$

Unfortunately, this leads to  $R_{AA}$  that steadily increases with  $p_T$ , which is most likely unrealistic. The second Cronin model is a simple Gaussian smearing of the  $p_T$ -distribution, which leads to  $R_{AA}$  that rises initially but trends downward  $\gtrsim 6$  GeV/c. Within the  $p_T$ -range of the current data, however, the two cases give similar results, as can be seen in Figure 6.5. The final effect that is included is medium-induced suppression, which is formulated in terms of a transport coefficient,  $\hat{q}_0$ , that represents the broadening of the  $c\bar{c}$  dipole in the medium per unit length traversed. They

Figure 6.5: Predicted  $R_{AA}$  at mid-rapidity for  $b = 0$  Au+Au collisions in the model of Kopeliovich *et al.* [77]. The results of the current analysis are shown for comparison, although the rapidity and centrality selections are not identical.



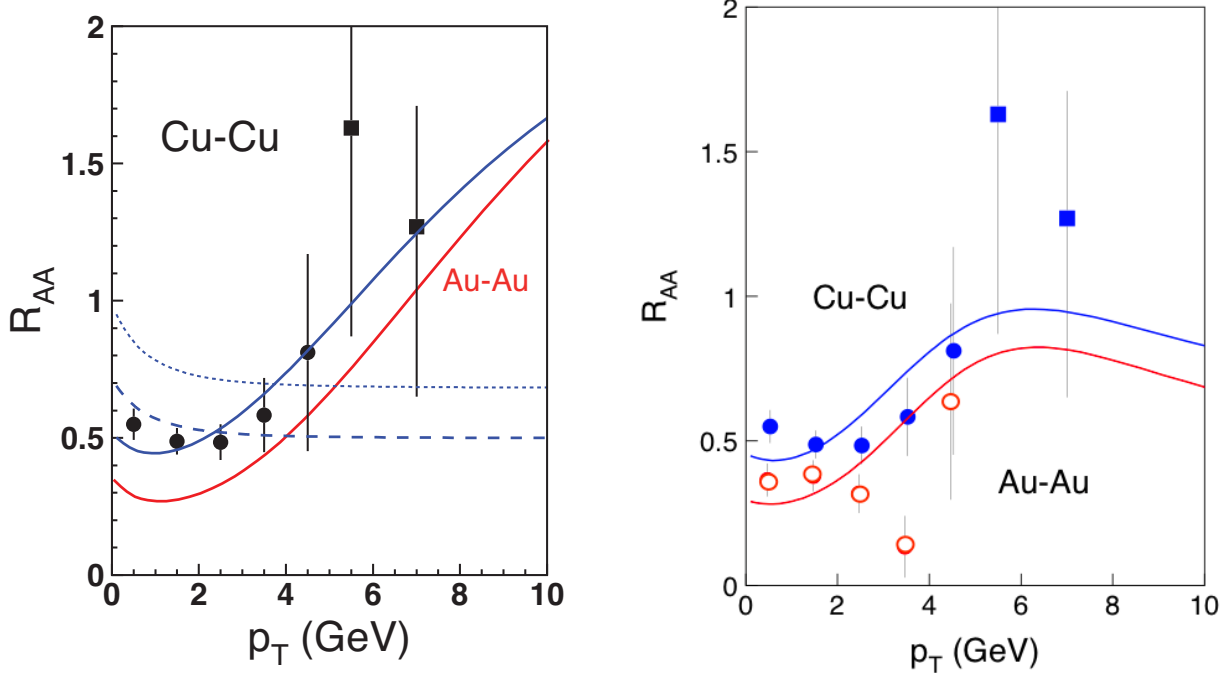
find that values of  $\hat{q}_0 \approx 0.3\text{--}0.5$  GeV $^2$ /fm agree with the data.

The calculations that result in the curves of Figure 6.5 are done at  $b=0$ , and should really only be compared to the most central events, but we have plotted the curves over both 0-20% and 20-40% centralities and it can be seen that there is better, though still imperfect, agreement for the 20-40% bin. However, the curves are also not calculated at forward rapidity, which would lower them by an additional factor (based on the difference between forward and mid-rapidity data).

It should be noted that almost all of the  $p_T$ -dependence of this model comes from the Cronin effect. This can be seen in Figure 6.6, where the various contributions to Cu+Cu  $R_{AA}$  are plotted separately. Because this model is so dependent on the shape of the Cronin effect, much more precise measurements of the  $J/\psi$   $p_T$ -distributions at  $>3$  GeV/c in heavy ion collisions are needed before the medium-induced effects can be separated.

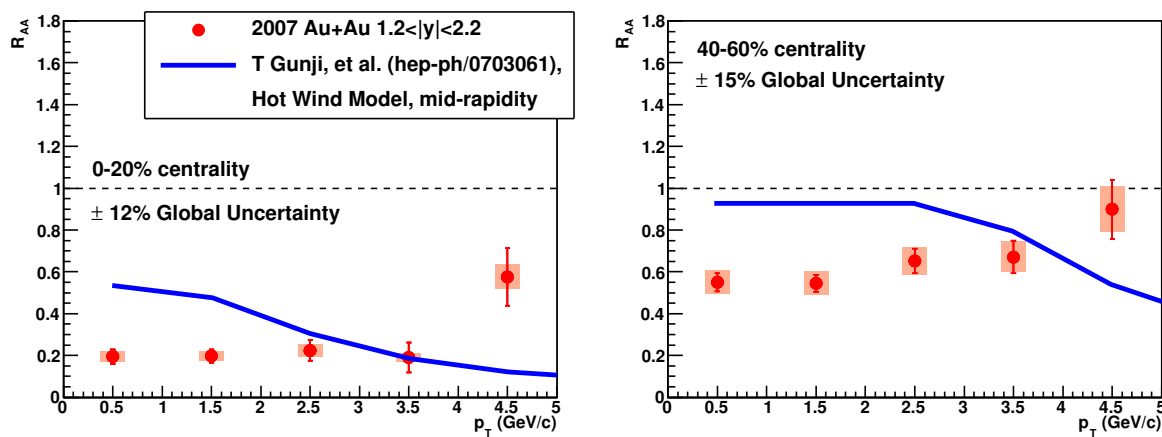
Finally, as mentioned in Section 2.4.6, in the ‘‘Hot Wind Model’’ of Liu, Rajagopal, and Wiedemann [51], it was found that the screening length goes as  $1/\sqrt{\gamma}$ , resulting in increased suppression at high- $p_T$ . This effect was modeled by T. Gunji *et al.* [52] using (3+1)-dimensional ideal relativistic hydrodynamics to model the medium’s space-time evolution. They then assume that the charmonia bound states disappear immediately if their melting temperature is reached, and

Figure 6.6:  $R_{AA}$  vs.  $p_T$  in Cu+Cu and Au+Au collisions as calculated with Cronin method 1 (left) and Cronin method 2 (right) in [77]. The divergence between the two calculations can be seen at  $p_T > 5$  GeV/c. In the left figure, the dotted curve includes only the medium-induced effects, the dashed curve adds the shadowing and absorption, while the final curve adds the Cronin effect.



use the Hot Wind model to modify the melting temperatures based on the velocity of the particle. This results in  $J/\psi R_{AA}$  where the suppression increases above some  $p_T$  where the effective melting temperature has been reduced to the medium temperature. This trend is at odds with the data, as can be seen in Figure 6.7. It should be noted that because of the immediate suppression at a certain temperature, the entire  $p_T$ -shape of the curve is due to the Hot Wind effect.

Figure 6.7:  $R_{AA}$  vs.  $p_T$  as calculated using the Hot Wind model in central (left) and semi-peripheral (right) centralities.



## Chapter 7

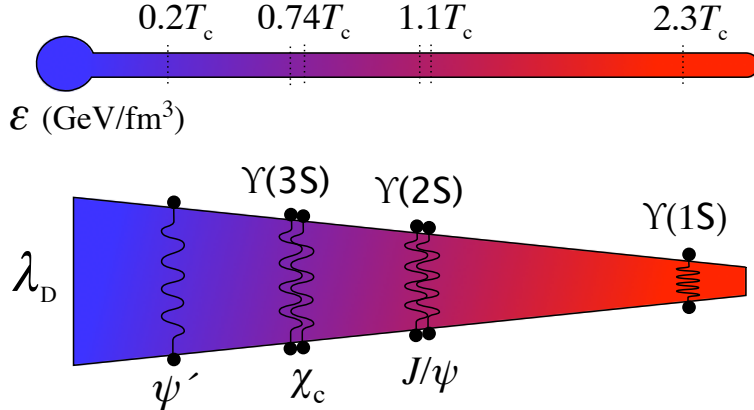
### Summary and Outlook

In this work a full analysis of  $J/\psi \rightarrow \mu^+ \mu^-$  has been presented using the PHENIX Run 7  $\sqrt{s_{NN}}=200$  GeV/u Au+Au data. The results are compatible with the previous Run 4 PHENIX results, and are able to rule out simple  $J/\psi$  suppression models, but are unable to discern between current models that make use of multiple charmonium states or both suppression and regeneration. A future (very) high-statistics measurement may be able to distinguish between these models, but the systematic uncertainties will have to be reduced as well. More likely, a combination of  $R_{AA}$  with different observables and kinematic bins not currently feasible will be used to distinguish between models, as well as additional data at higher energies from the LHC.

One effect that could be very useful in gauging the medium temperature is sequential charmonium dissociation, *i.e.* dissociation of the  $\chi_c$  and  $\psi'$  and the resulting suppression of the feed-down  $J/\psi$ s. The lower dissociation temperatures of the excited states could at least allow a bracketing of the medium temperature. In order to quantify this effect, separate measurements of  $\chi_c$  and  $\psi'$   $R_{AA}$  in Au+Au collisions will be needed. Once the modification of the  $\chi_c$  and  $\psi'$  is known, the effect on  $J/\psi$   $R_{AA}$  can be calculated using the feed-down fractions. This can also be combined with bottomonia sequential dissociation to more precisely bracket the medium temperature, as shown in the cartoon diagram of Figure 7.1.

Regeneration of  $J/\psi$ s is also an intriguing effect that needs to be mapped out better. It needs to be understood whether regeneration is dominated by diagonal pairs or off-diagonal pairs, which should scale with  $N_{\text{charm}}$  and  $N_{\text{charm}}^2$  respectively. One of driving motivations of regeneration cal-

Figure 7.1: Cartoon of sequential dissociation of charmonia and bottomonia.



culations is the greater  $J/\psi$  suppression seen at forward rapidities at RHIC, but this was expected from the narrowing of the rapidity distribution due to combining off-diagonal pairs. If most regeneration is from diagonal pairs, another explanation must be found for the rapidity difference, such as stronger shadowing at forward rapidity or gluon saturation effects. More precise experimental measurements of the rapidity and  $p_T$  distributions could help clarify the picture. The LHC Pb+Pb program will also help in understanding the different contributions, as the charm-quark density is expected to be about an order of magnitude larger than in RHIC Au+Au collisions. Extreme calculations even predict less suppression of  $R_{AA}$  compared to the RHIC values, due to the increase in charm-quark density [78].

There is also some debate about the interpretation of the survival of  $J/\psi$  spectral functions up to  $2T_c$  in lattice QCD. This is important for medium-evolution calculations which must input a particular melting point for the  $J/\psi$  and other charmonium states. In some cases this is treated as meaning the  $J/\psi$  bound state survives well above the transition temperature, while other recent interpretations point out that the binding energy can be negligible even while the spectral peak still exists. This needs to be settled for full medium calculations to become more precise. In addition, it is essential for the interpretation of the sequential charmonium dissociation in terms of medium temperature.

In 2008 PHENIX recorded much higher-statistics  $d+\text{Au}$  data than had been previously analyzed. The  $J/\psi$  results are being finalized at the time of this writing, and should be published shortly. These results should allow a much better constraint on the cold nuclear matter effects, which in turn will assist in extracting  $J/\psi$ /medium information from  $\text{Au}+\text{Au}$  collisions by reducing one of the current sources of theoretical uncertainty.

In addition, PHENIX is currently installing a silicon-based vertex detector, and is in the pre-planning stages for major detector upgrades during the next decade. There are also planned luminosity upgrades for the accelerator itself, and discussion of adding an electron beam for  $e+A$  collisions.

Moreover, a quarter of the way around the world the LHC is starting up at CERN, and will eventually collide  $\text{Pb}+\text{Pb}$  at  $\sqrt{s_{NN}}=5.5$  TeV/u. The medium temperatures and energy densities produced will be much higher than those at RHIC, allowing exploration of an additional region of the QCD phase-space diagram.

While we now have in hand the measurements first proposed by Matsui and Satz [34], our physical picture has become a complex admixture of different effects, making conclusive interpretation difficult at present. However, the theoretical and experimental advances described above should allow the eventual disentangling of the competing effects on  $J/\psi$  production in high-energy heavy ion collisions.

## Bibliography

- [1] D. Griffiths, **Introduction to Elementary Particles** (John Wiley & Sons, Inc., 1987).
- [2] W. Cottingham and D. Greenwood, **An Introduction to the Standard Model of Particle Physics** (Cambridge University Press, 2007).
- [3] C. Amsler *et al.* (Particle Data Group), [Phys. Lett. B](#), **667**, 1 (2008).
- [4] S. Bethke, [Eur. Phys. J. C](#), **64**, 689 (2009), arXiv:0908.1135.
- [5] H. D. Politzer, [Phys. Rev. Lett.](#), **30**, 1346 (1973).
- [6] D. J. Gross and F. Wilczek, [Phys. Rev. Lett.](#), **30**, 1343 (1973).
- [7] S. Chekanov *et al.* (ZEUS Collaboration), [Phys. Rev. D](#), **67**, 012007 (2003).
- [8] R. Hagedorn, [Nuovo Cim. Suppl.](#), **3**, 147 (1965).
- [9] I. Arsene *et al.* (BRAHMS Collaboration), [Nucl. Phys. A](#), **757**, 1 (2005), arXiv:nucl-ex/0410020.
- [10] C. Wong, **Introduction to High-Energy Heavy-Ion Collisions** (World Scientific, Singapore, 1994).
- [11] R. Vogt, **Ultrarelativistic Heavy Ion Collisions** (Elsevier, 2007).
- [12] F. Karsch, [Lect. Notes Phys.](#), **583**, 209 (2002), arXiv:hep-lat/0106019.
- [13] J. L. Nagle, [Eur. Phys. J. C](#), **49**, 275 (2007), arXiv:nucl-th/0608070.
- [14] B. Müller and J. L. Nagle, [Annu. Rev. Nucl. Part. Sci.](#), **56**, 93 (2006), arXiv:nucl-th/0602029.
- [15] K. Adcox *et al.*, [Nucl. Phys. A](#), **757**, 184 (2005), arXiv:nucl-ex/0410003.
- [16] J. J. Aubert, U. Becker, P. J. Biggs, J. Burger, M. Chen, G. Everhart, P. Goldhagen, J. Leong, T. McCorriston, T. G. Rhoades, M. Rohde, S. C. C. Ting, S. L. Wu, and Y. Y. Lee, [Phys. Rev. Lett.](#), **33**, 1404 (1974).
- [17] J. Paterson, M. Perl, B. Richter, and P. Rapidis, [Phys. Rev. Lett.](#), **33**, 1406 (1974).
- [18] E. Eichten, K. Gottfried, T. Kinoshita, K. Lane, and T. Yan, [Phys. Rev. D](#), **17**, 3090 (1978).
- [19] H. Satz, [Nucl. Phys. A](#), **783**, 249 (2007), arXiv:hep-ph/0609197.

- [20] K. Nakamura *et al.* (Particle Data Group), *J. Phys. G*, **37**, 075021 (2010).
- [21] H. Fritzsch, *Phys. Lett. B*, **67**, 217 (1977).
- [22] F. Halzen, *Phys. Lett. B*, **69**, 105 (1977).
- [23] J. F. Amundson, O. J. P. E'boli, E. M. Gregores, and F. Halzen, *Phys. Lett. B*, **372**, 127 (1996), arXiv:hep-ph/9512248.
- [24] J.-P. Lansberg, Presented at the JJC2001 -Journees Jeunes Chercheurs-, La Hume, France, 10-14 December 2001 (2002), arXiv:hep-ph/0201111.
- [25] F. Abe *et al.* (CDF Collaboration), *Phys. Rev. Lett.*, **79**, 573 (1997).
- [26] F. Abe *et al.* (CDF Collaboration), *Phys. Rev. Lett.*, **79**, 578 (1997).
- [27] M. Krämer, *Prog. Part. Nucl. Phys.*, **47**, 141 (2001), arXiv:hep-ph/0106120.
- [28] G. T. Bodwin, E. Braaten, and G. P. Lepage, *Phys. Rev. D*, **51**, 1125 (1995), arXiv:hep-ph/9407339.
- [29] A. Abulencia *et al.* (CDF Collaboration), *Phys. Rev. Lett.*, **99**, 132001 (2007), arXiv:0704.0638.
- [30] J. P. Lansberg, J. R. Cudell, and Y. L. Kalinovsky, *Phys. Lett. B*, **633**, 301 (2005), arXiv:hep-ph/0507060.
- [31] J. P. Lansberg and H. Haberzettl, *AIP Conf. Proc.*, **1038**, 83 (2008), arXiv:0806.4001.
- [32] H. Haberzettl and J. P. Lansberg, *Phys. Rev. Lett.*, **100**, 032006 (2008), arXiv:0709.3471.
- [33] A. Adare *et al.* (PHENIX Collaboration), *Phys. Rev. Lett.*, **98**, 232002 (2007), arXiv:hep-ex/0611020.
- [34] T. Matsui and H. Satz, *Phys. Lett. B*, **178**, 416 (1986).
- [35] P. Petreczky, *J. Phys. G*, **37**, 094009 (2010), arXiv:1001.5284.
- [36] Á. Mócsy and P. Petreczky, *Phys. Rev. D*, **77**, 014501 (2008), arXiv:0705.2559.
- [37] K. J. Eskola, V. J. Kolhinen, and R. Vogt, *Nucl. Phys. A*, **696**, 729 (2001), arXiv:hep-ph/0104124.
- [38] B. Alessandro *et al.* (NA50 Collaboration), *Eur. Phys. J. C*, **33**, 31 (2004).
- [39] R. Arnaldi (NA60 Collaboration), *Nucl. Phys. A*, **830**, 345c (2009), arXiv:0907.5004 [nucl-ex].
- [40] A. Adare *et al.* (PHENIX Collaboration), *Phys. Rev. C*, **77**, 024912 (2008), arXiv:0711.3917.
- [41] R. Vogt, *Phys. Rev. C*, **71**, 054902 (2005), arXiv:hep-ph/0411378.
- [42] D. de Florian and R. Sassot, *Phys. Rev. D*, **69**, 074028 (2004), arXiv:hep-ph/0311227.
- [43] E. G. Ferreiro, F. Fleuret, J. P. Lansberg, and A. Rakotozafindrabe, *Phys. Lett. B*, **680**, 50 (2009), arXiv:0809.4684.

- [44] M. Abreu *et al.* (NA50 Collaboration), *Physics Letters B*, **477**, 28 (2000).
- [45] A. Abbott, *Nature*, **403**, 581 (2000).
- [46] U. Heinz and M. Jacob, (2000), arXiv:nucl-th/0002042.
- [47] A. Adare *et al.* (PHENIX Collaboration), *Phys. Rev. Lett.*, **98**, 232301 (2007), arXiv:nucl-ex/0611020.
- [48] X. Zhao and R. Rapp, *Eur. Phys. J. C*, **62**, 109 (2009), arXiv:0810.4566.
- [49] R. L. Thews and M. L. Mangano, *Phys. Rev. C*, **73**, 014904 (2006), arXiv:nucl-th/0505055.
- [50] F. Karsch, D. Kharzeev, and H. Satz, *Phys. Lett. B*, **637**, 75 (2006), arXiv:hep-ph/0512239.
- [51] H. Liu, K. Rajagopal, and U. A. Wiedemann, *Phys. Rev. Lett.*, **98**, 182301 (2007), arXiv:hep-ph/0607062.
- [52] T. Gunji, H. Hamagaki, T. Hatsuda, T. Hirano, and Y. Akamatsu, *J. Phys. G*, **35**, 104137 (2008), arXiv:hep-ph/0703061.
- [53] X. Zhao and R. Rapp, *Phys. Lett. B*, **664**, 253 (2008), arXiv:0712.2407.
- [54] B. Abelev *et al.* (STAR Collaboration), *Phys. Rev. C*, **80**, 041902 (2009), arXiv:0904.0439.
- [55] K. Adcox *et al.* (PHENIX Collaboration), *Nucl. Inst. and Meth. A*, **499**, 469 (2003).
- [56] K. Adcox *et al.* (PHENIX Collaboration), *Nucl. Inst. and Meth. A*, **499**, 489 (2003).
- [57] L. Aphecetche *et al.* (PHENIX Collaboration), *Nucl. Inst. and Meth. A*, **499**, 521 (2003).
- [58] M. Aizawa *et al.* (PHENIX Collaboration), *Nucl. Inst. and Meth. A*, **499**, 508 (2003).
- [59] H. Akikawa *et al.* (PHENIX Collaboration), *Nucl. Inst. and Meth. A*, **499**, 537 (2003).
- [60] M. Allen *et al.* (PHENIX Collaboration), *Nucl. Inst. and Meth. A*, **499**, 549 (2003).
- [61] A. Glenn, **Single Muon Production and Implications for Charm in  $\sqrt{s_{NN}} = 200$  GeV Au+Au Collisions**, Ph.D. thesis, University of Tennessee, Knoxville (2004).
- [62] S. Aronson *et al.* (PHENIX Collaboration), *Nucl. Inst. and Meth. A*, **499**, 480 (2003).
- [63] M. L. Miller, K. Reygers, S. J. Sanders, and P. Steinberg, *Annu. Rev. Nucl. Part. Sci.*, **57**, 205 (2007), arXiv:nucl-ex/0701025.
- [64] W. J. Knox, *Phys. Rev. D*, **10**, 65 (1974).
- [65] M. Planck, *Sitzungsber. Deutsch Akad. Wiss. Berlin*, **33**, 355 (1923).
- [66] R. Fröhlich, *Nucl. Inst. and Meth. A*, **262**, 444 (1987).
- [67] G. Cowan, **Statistical Data Analysis** (Oxford University Press, New York, 1998).
- [68] S. S. Adler (PHENIX Collaboration), *Phys. Rev. C*, **69**, 014901 (2004), arXiv:nucl-ex/0305030v2.

- [69] W. H. Press, S. A. Teukolsky, W. T. Vetterling, and B. P. Flannery, **Numerical Recipes in C, Second Edition** (Cambridge University Press, Cambridge, 1992).
- [70] S. Baker and R. D. Cousins, *Nucl. Inst. and Meth.*, **221**, 437 (1984).
- [71] T. Sjöstrand, P. Edén, C. Friberg, L. Lönnblad, G. Miu, S. Mrenna, and E. Norrbin, *Comput. Phys. Commun.*, **135**, 238 (2001), [arXiv:hep-ph/0010017](https://arxiv.org/abs/hep-ph/0010017).
- [72] R. Brun *et al.*, CERN Program Library Long Write-up W5013 (1994).
- [73] P. R. Bevington and D. K. Robinson, **Data Reduction and Error Analysis** (McGraw-Hill, New York, 2003).
- [74] A. Capella and E. G. Ferreiro, *The European Physical Journal C*, **42**, 419 (2005), [arXiv:hep-ph/0505032](https://arxiv.org/abs/hep-ph/0505032).
- [75] A. Capella, L. Bravina, E. G. Ferreiro, A. B. Kaidalov, K. Tywoniuk, and E. Zabrodin, *Eur. Phys. J. C*, **58**, 437 (2008), [arXiv:0712.4331](https://arxiv.org/abs/0712.4331).
- [76] D. Kharzeev, E. Levin, M. Nardi, and K. Tuchin, *Nucl. Phys. A*, **826**, 230 (2009), [arXiv:0809.2933](https://arxiv.org/abs/0809.2933).
- [77] B. Z. Kopeliovich, I. K. Potashnikova, and I. Schmidt, *Phys. Rev. C*, **82**, 024901 (2010), [arXiv:1006.3042](https://arxiv.org/abs/1006.3042).
- [78] A. Andronic *et al.*, *Phys. Lett. B*, **652**, 259 (2007), [arXiv:nucl-th/0701079](https://arxiv.org/abs/nucl-th/0701079)

## Appendix A

### Tables

#### A.1 Signal Tables

Table A.1:  $J/\psi$  signal in 10% centrality bins combining both like-sign and mixed background-subtracted results, with their statistical and systematic uncertainties. Also included are the 90% confidence limits using only the mixed background histograms. For those bins where  $N_{J/\psi} < \sqrt{\sigma_{stat}^2 + \sigma_{sys}^2}$ , the text is in red, and only the confidence limit will be used.

10% Centrality bins								
Cent	South Arm				North Arm			
	signal	stat	sys	90% conf	signal	stat	sys	90% conf
0-10%	1612.9	261.2	280.8	2576.4	220.9	240.6	206.3	1582.3
10-20%	1939.0	216.7	156.0	3035.8	668.3	172.0	149.6	1543.2
20-30%	1754.1	176.6	101.7	2599.8	985.8	129.5	58.3	1592.3
30-40%	1424.3	113.2	67.7	1831.6	940.4	91.5	45.1	1505.2
40-50%	1019.1	82.0	39.9	1335.7	870.5	63.1	42.2	1132.4
50-60%	675.9	47.7	18.8	785.2	630.4	43.4	17.3	762.3
60-70%	392.4	32.2	11.3	441.0	309.9	26.4	10.2	384.3
70-80%	215.0	20.8	4.1	251.7	191.6	17.9	3.3	216.6
80-93%	97.6	12.7	1.8	127.4	125.2	13.6	3.0	150.3

Table A.2:  $J/\psi$  signal in 5% centrality bins combining both like-sign and mixed background-subtracted results, with their statistical and systematic uncertainties. Also included are the 90% confidence limits using only the mixed background histograms. For those bins where  $N_{J/\psi} < \sqrt{\sigma_{stat}^2 + \sigma_{sys}^2}$ , the text is in red, and only the confidence limit will be used.

Cent	5% Centrality bins							
	South Arm				North Arm			
	signal	stat	sys	90% conf	signal	stat	sys	90% conf
0-5%	864.4	192.5	148.5	1389.6	252.4	173.5	161.6	918.6
5-10%	743.5	174.9	139.5	1311.1	20.2	313.1	34.1	793.0
10-15%	946.8	165.3	97.1	1518.8	280.5	138.7	90.9	722.5
15-20%	971.4	141.0	47.8	1616.3	402.7	120.0	73.1	916.9
20-25%	849.4	133.9	75.8	1391.4	430.2	98.4	35.7	823.0
25-30%	879.8	104.2	41.7	1282.3	569.6	84.1	44.3	837.2
30-35%	770.3	90.4	41.6	1024.6	469.5	67.0	42.8	788.1
35-40%	647.0	68.4	41.7	859.1	484.4	60.3	23.3	764.9
40-45%	630.8	62.0	27.2	791.3	482.1	49.6	25.0	671.4
45-50%	398.1	51.6	19.9	579.3	385.6	40.2	12.5	493.5
50-55%	344.2	36.7	9.8	441.5	297.4	32.0	14.2	419.2
55-60%	333.0	31.2	10.0	366.3	334.9	26.2	7.1	364.6
60-65%	231.2	24.1	5.5	265.8	170.6	21.7	5.1	228.1
65-70%	161.3	20.0	6.1	190.0	131.3	16.0	1.5	170.0
70-75%	118.4	15.8	2.0	147.7	113.4	13.8	2.2	129.0
75-80%	95.6	12.7	1.9	114.2	74.1	11.2	2.8	97.4

Table A.3:  $J/\psi$  signal in 20% centrality and 1 GeV/c  $p_T$  bins combining both like-sign and mixed background-subtracted results, with their statistical and systematic uncertainties. Also included are the 90% confidence limits using only the mixed background histograms. For those bins where  $N_{J/\psi} < \sqrt{\sigma_{stat}^2 + \sigma_{sys}^2}$ , the text is in red, and only the confidence limit will be used.

		South Arm				North Arm			
Cent	$p_T$	signal	stat	sys	90% conf	signal	stat	sys	90% conf
0-20%	0-1	1031.5	156.6	159.6	1848.0	377.7	137.8	106.5	1187.6
0-20%	1-2	1315.2	184.8	164.9	2149.5	398.0	211.8	119.7	1219.3
0-20%	2-3	663.5	128.3	74.3	1244.7	128.0	125.9	64.7	607.4
0-20%	3-4	202.1	73.2	31.1	408.3	33.4	132.7	29.2	160.2
0-20%	4-5	202.4	47.3	34.3	219.8	143.4	54.8	75.2	157.4
0-20%	5-6	18.4	27.4	18.4	59.2	36.2	46.1	67.1	80.1
20-40%	0-1	714.7	97.0	64.8	1373.2	528.8	85.6	35.9	978.6
20-40%	1-2	1192.4	108.3	50.7	1785.0	673.8	93.1	51.4	1210.9
20-40%	2-3	711.7	74.7	25.3	982.3	434.1	62.9	18.4	603.3
20-40%	3-4	262.1	40.5	13.3	344.4	182.3	36.8	16.7	292.7
20-40%	4-5	86.2	21.0	6.3	83.0	102.5	27.5	10.9	100.1
20-40%	5-6	50.0	15.7	2.6	52.3	60.6	17.9	4.7	55.3
40-60%	0-1	492.8	44.9	17.0	647.8	450.1	42.7	16.0	579.3
40-60%	1-2	639.6	52.4	25.9	939.9	566.1	46.3	21.4	760.7
40-60%	2-3	300.9	34.1	9.1	361.4	288.3	31.0	11.9	376.0
40-60%	3-4	127.6	21.8	3.7	164.5	124.7	16.0	2.8	150.3
40-60%	4-5	60.4	11.4	1.2	65.7	55.8	9.5	0.5	69.6
40-60%	5-6	17.6	5.5	0.2	13.7	17.6	5.4	0.2	19.1
60-93%	0-1	251.1	21.5	4.7	301.6	232.9	20.7	3.2	275.6
60-93%	1-2	244.6	22.6	10.1	297.3	243.4	21.0	4.6	287.7
60-93%	2-3	117.5	15.2	2.3	146.8	90.2	13.2	2.8	117.6
60-93%	3-4	36.3	8.9	1.0	53.1	41.3	8.6	1.2	59.2
60-93%	4-5	21.8	5.4	0.1	22.5	21.0	4.9	0.1	21.1
60-93%	5-6	10.9	3.4	0.0	12.2	9.0	3.1	0.0	10.3

Table A.4:  $J/\psi$  signal RMS variation due to varying a particular parameter, listed in 10% and 5% centrality bins.

		South Arm			North Arm		
Cent	$p_T$	DGausFrac	FitRange	BgndNorm	DGausFrac	FitRange	BgndNorm
0-10%	all	3.8%	4.2%	14.1%	6.0%	29.9%	63.7%
10-20%	all	2.7%	2.0%	5.3%	2.7%	19.1%	12.8%
20-30%	all	2.6%	4.7%	2.7%	2.8%	4.3%	5.7%
30-40%	all	3.8%	3.2%	3.1%	2.3%	7.6%	1.9%
40-50%	all	3.4%	1.0%	0.9%	2.3%	5.8%	1.3%
50-60%	all	0.9%	1.1%	2.3%	1.7%	1.0%	1.0%
60-70%	all	0.2%	0.9%	0.7%	1.0%	0.7%	0.5%
70-80%	all	0.5%	0.8%	0.3%	0.8%	0.7%	0.2%
80-93%	all	0.3%	2.1%	0.0%	0.9%	1.5%	0.1%
0-5%	all	3.4%	4.4%	15.1%	5.1%	29.9%	42.8%
5-10%	all	4.1%	5.1%	12.5%	10.5%	62.0%	94.0%
10-15%	all	3.0%	3.9%	6.3%	3.6%	16.5%	27.4%
15-20%	all	3.0%	1.3%	4.4%	2.0%	19.1%	14.5%
20-25%	all	2.5%	6.7%	6.3%	3.0%	3.8%	6.9%
25-30%	all	1.8%	3.6%	1.7%	6.6%	5.9%	1.7%
30-35%	all	3.1%	3.4%	0.7%	2.7%	7.8%	4.9%
35-40%	all	2.4%	2.9%	2.3%	2.0%	6.6%	1.3%
40-45%	all	2.4%	1.4%	0.5%	1.9%	7.1%	1.5%
45-50%	all	2.0%	1.6%	2.5%	5.1%	2.1%	0.3%
50-55%	all	1.6%	2.6%	1.0%	1.7%	5.9%	0.9%
55-60%	all	0.4%	1.1%	1.2%	0.9%	0.2%	1.3%
60-65%	all	0.4%	0.3%	0.3%	1.4%	2.1%	4.1%
65-70%	all	0.5%	0.3%	0.5%	0.9%	0.6%	0.2%
70-75%	all	1.0%	0.8%	0.3%	0.9%	0.6%	0.5%
75-80%	all	0.2%	1.5%	0.3%	1.3%	4.2%	0.1%

Table A.5:  $J/\psi$  signal RMS variation due to varying a particular parameter, listed in 20% centrality and 1 GeV/c  $p_T$  bins.

Cent	$p_T$	South Arm			North Arm		
		DGausFrac	FitRange	BgndNorm	DGausFrac	FitRange	BgndNorm
0-20%	0-1	2.5%	8.0%	2.4%	1.6%	10.7%	20.2%
0-20%	1-2	2.9%	1.6%	5.5%	4.6%	12.8%	6.9%
0-20%	2-3	3.4%	8.8%	1.8%	2.8%	40.5%	1.0%
0-20%	3-4	5.0%	15.0%	3.8%	3.8%	27.9%	35.0%
20-40%	0-1	2.5%	9.1%	6.3%	2.5%	3.3%	2.7%
20-40%	1-2	5.3%	3.7%	1.5%	2.5%	10.6%	2.0%
20-40%	2-3	2.5%	2.0%	1.8%	2.3%	1.0%	0.0%
20-40%	3-4	2.9%	5.7%	3.5%	1.8%	8.7%	0.5%
40-60%	0-1	1.7%	2.2%	1.7%	2.7%	3.2%	1.4%
40-60%	1-2	2.1%	2.9%	1.2%	1.7%	2.9%	0.4%
40-60%	2-3	1.8%	1.8%	0.4%	1.8%	2.0%	0.3%
40-60%	3-4	1.9%	0.4%	0.8%	1.6%	1.4%	1.3%
60-93%	0-1	1.4%	0.7%	0.5%	0.7%	1.4%	0.3%
60-93%	1-2	1.7%	3.4%	0.1%	1.1%	0.9%	0.2%
60-93%	2-3	1.5%	0.4%	0.1%	3.8%	1.5%	0.7%
60-93%	3-4	0.1%	0.1%	0.6%	1.0%	0.6%	0.1%

Table A.6:  $J/\psi$  signal/background over [2.6,3.6] and (subtracted counts)/background over [1.8,2.0], in 10% and 5% centrality bins.

Cent	$p_T$	South Arm		North Arm	
		1.8-2.0	2.6-3.6	1.8-2.0	2.6-3.6
0-10%	all	-0.000	0.031	0.001	0.004
10-20%	all	0.004	0.072	-0.000	0.022
20-30%	all	0.000	0.117	-0.000	0.073
30-40%	all	-0.010	0.208	-0.004	0.164
40-50%	all	0.025	0.386	0.009	0.376
50-60%	all	-0.017	0.757	0.074	0.811
60-70%	all	-0.053	1.649	0.135	1.521
70-80%	all	0.115	4.340	-0.294	3.344
80-93%	all	1.192	10.904	-0.373	9.362
<hr/>					
0-5%	all	0.007	0.029	0.006	0.007
5-10%	all	-0.009	0.035	-0.006	0.001
10-15%	all	0.001	0.061	-0.003	0.015
15-20%	all	0.008	0.087	0.004	0.033
20-25%	all	-0.007	0.099	0.000	0.057
25-30%	all	0.010	0.142	-0.001	0.101
30-35%	all	0.007	0.181	-0.012	0.132
35-40%	all	-0.037	0.250	0.007	0.221
40-45%	all	0.004	0.371	0.024	0.331
45-50%	all	0.062	0.416	-0.015	0.445
50-55%	all	0.009	0.599	0.072	0.651
55-60%	all	-0.065	1.072	0.076	1.104
60-65%	all	-0.090	1.396	0.090	1.279
65-70%	all	0.026	2.166	0.232	1.972
70-75%	all	0.151	3.557	-0.428	2.888
75-80%	all	0.035	5.945	0.037	4.243

Table A.7:  $J/\psi$  signal/background over [2.6,3.6] and (subtracted counts)/background over [1.8,2.0], in 20% centrality and 1 GeV/c  $p_T$  bins.

Cent	$p_T$	South Arm		North Arm	
		1.8-2.0	2.6-3.6	1.8-2.0	2.6-3.6
0-20%	0-1	0.005	0.041	0.000	0.018
	1-2	0.000	0.042	-0.001	0.012
	2-3	-0.016	0.063	0.009	0.013
	3-4	-0.003	0.057	-0.027	0.008
	4-5	0.171	0.172	0.042	0.033
	5-6	0.190	0.041	-0.036	0.009
20-40%	0-1	0.004	0.100	-0.010	0.088
	1-2	-0.016	0.135	-0.003	0.090
	2-3	-0.005	0.205	0.014	0.144
	3-4	0.002	0.285	0.080	0.176
	4-5	0.082	0.205	-0.044	0.219
	5-6	0.371	0.395	-0.289	0.152
40-60%	0-1	0.027	0.380	-0.006	0.402
	1-2	-0.021	0.431	0.050	0.457
	2-3	0.065	0.536	0.062	0.624
	3-4	0.069	0.830	0.096	0.775
	4-5	0.158	1.113	-0.655	1.036
	5-6	0.254	0.531	0.606	0.648
60-93%	0-1	0.063	2.459	0.017	2.257
	1-2	-0.104	1.949	0.008	2.268
	2-3	0.100	2.482	0.012	2.080
	3-4	0.136	2.410	0.397	2.952
	4-5	0.549	3.654	1.191	4.464
	5-6	5.646	3.933	4.256	5.015

Table A.8:  $J/\psi$  signal summed across the 10% centrality bins or 1 GeV/c  $p_T$  bins, within a given 20% centrality bin.

Arm	Centrality	cent-summed	stat error	$p_T$ -summed	stat error
South	0-20%	3730.0	292.8	3724.6	244.6
	20-40%	3367.6	170.2	3239.3	146.1
	40-60%	1758.7	86.2	1672.3	73.3
	60-93%	715.5	36.6	686.2	34.4
North	0-20%	849.8	247.1	1189.8	222.0
	20-40%	2053.7	131.6	2102.5	125.4
	40-60%	1535.3	66.8	1527.6	65.8
	60-93%	637.5	32.4	640.8	32.5

Table A.9: Subtracted counts in the  $J/\psi$  mass region [2.6,3.6] for the  $++$  and  $--$  pair distributions in the South Arm in 10% and 5% centrality bins. Also included are the  $\chi^2/\text{ndf}$  and ndf for a fit to a flat line over the mass range [0.6, 6.0].

Cent	$p_T$	Arm	++ Pairs			-- Pairs		
			counts	$\chi^2/\text{ndf}$	ndf	counts	$\chi^2/\text{ndf}$	ndf
0-10%	all	South	$217.8 \pm 187.6$	0.9	53	$-84.4 \pm 140.5$	1.1	53
10-20%	all	South	$226.7 \pm 147.0$	1.3	53	$194.1 \pm 109.6$	0.9	53
20-30%	all	South	$145.4 \pm 106.9$	0.7	53	$221.1 \pm 80.2$	1.3	53
30-40%	all	South	$25.7 \pm 72.5$	2.3	53	$161.8 \pm 54.5$	1.0	53
40-50%	all	South	$23.6 \pm 45.0$	1.0	53	$72.2 \pm 34.4$	1.5	53
50-60%	all	South	$10.5 \pm 25.4$	1.2	53	$13.7 \pm 19.4$	0.7	53
60-70%	all	South	$3.1 \pm 13.3$	1.2	52	$-3.0 \pm 9.6$	0.7	51
70-80%	all	South	$9.7 \pm 6.5$	0.8	47	$1.8 \pm 4.7$	0.7	44
80-93%	all	South	$0.8 \pm 2.5$	0.9	37	$0.2 \pm 2.3$	0.6	34
0-5%	all	South	$220.3 \pm 139.9$	1.1	53	$-147.2 \pm 104.1$	1.2	53
5-10%	all	South	$-2.3 \pm 125.0$	0.9	53	$62.2 \pm 94.3$	0.9	53
10-15%	all	South	$47.8 \pm 110.9$	1.2	53	$70.6 \pm 82.7$	0.8	53
15-20%	all	South	$178.9 \pm 96.6$	1.2	53	$123.5 \pm 72.0$	0.9	53
20-25%	all	South	$72.3 \pm 82.0$	0.8	53	$119.3 \pm 61.3$	1.0	53
25-30%	all	South	$73.1 \pm 68.5$	0.6	53	$101.8 \pm 51.7$	1.2	53
30-35%	all	South	$-12.4 \pm 56.1$	1.9	53	$90.3 \pm 42.4$	1.0	53
35-40%	all	South	$38.1 \pm 45.9$	1.5	53	$71.5 \pm 34.2$	1.1	53
40-45%	all	South	$32.8 \pm 36.0$	1.4	53	$29.3 \pm 26.9$	1.2	53
45-50%	all	South	$-9.2 \pm 27.0$	1.0	53	$42.9 \pm 21.4$	1.1	53
50-55%	all	South	$9.0 \pm 20.6$	1.0	53	$18.0 \pm 15.9$	0.6	53
55-60%	all	South	$1.6 \pm 14.8$	1.1	53	$-4.2 \pm 11.0$	0.6	52
60-65%	all	South	$0.0 \pm 11.0$	1.3	52	$-8.5 \pm 7.4$	0.9	49
65-70%	all	South	$3.1 \pm 7.5$	0.6	49	$5.5 \pm 6.1$	0.6	49
70-75%	all	South	$9.3 \pm 5.7$	1.0	44	$1.8 \pm 4.0$	1.0	39
75-80%	all	South	$0.4 \pm 3.1$	0.4	41	$0.0 \pm 2.5$	0.7	39

Table A.10: Subtracted counts in the  $J/\psi$  mass region [2.6,3.6] for the  $++$  and  $--$  pair distributions in the South Arm in 20% centrality and 1 GeV/ $c$   $p_T$  bins. Also included are the  $\chi^2/\text{ndf}$  and ndf for a fit to a flat line over the mass range [0.6, 6.0].

Cent	$p_T$	Arm	++ Pairs			-- Pairs		
			counts	$\chi^2/\text{ndf}$	ndf	counts	$\chi^2/\text{ndf}$	ndf
0-20%	0-1	South	$286.2 \pm 140.5$	1.4	53	$35.4 \pm 107.2$	0.8	53
0-20%	1-2	South	$107.0 \pm 153.1$	1.1	53	$52.1 \pm 113.6$	0.9	53
0-20%	2-3	South	$98.4 \pm 94.7$	1.4	53	$47.7 \pm 68.7$	1.0	53
0-20%	3-4	South	$29.4 \pm 51.8$	0.8	53	$-6.3 \pm 37.4$	1.1	53
0-20%	4-5	South	$11.5 \pm 29.3$	1.0	53	$-11.7 \pm 22.1$	0.9	53
0-20%	5-6	South	$7.0 \pm 19.9$	1.0	53	$15.2 \pm 15.4$	1.3	53
20-40%	0-1	South	$236.6 \pm 78.1$	1.6	53	$122.0 \pm 59.0$	1.2	52
20-40%	1-2	South	$23.9 \pm 83.2$	1.2	53	$247.7 \pm 62.9$	1.7	53
20-40%	2-3	South	$-7.8 \pm 50.7$	1.1	53	$8.7 \pm 36.3$	0.9	53
20-40%	3-4	South	$-18.5 \pm 26.4$	1.1	53	$19.3 \pm 20.1$	0.9	53
20-40%	4-5	South	$-1.8 \pm 14.7$	1.6	53	$-18.7 \pm 10.1$	1.6	53
20-40%	5-6	South	$-7.3 \pm 8.0$	1.0	53	$8.2 \pm 7.3$	0.8	52
40-60%	0-1	South	$11.4 \pm 30.8$	0.9	52	$24.3 \pm 23.9$	0.8	51
40-60%	1-2	South	$-11.0 \pm 33.0$	0.8	53	$47.1 \pm 25.4$	0.8	53
40-60%	2-3	South	$30.8 \pm 21.2$	0.9	53	$0.4 \pm 15.1$	1.2	53
40-60%	3-4	South	$10.4 \pm 11.2$	1.0	53	$12.8 \pm 8.8$	0.8	52
40-60%	4-5	South	$0.5 \pm 5.9$	0.7	53	$1.1 \pm 4.6$	0.8	52
40-60%	5-6	South	$2.5 \pm 3.5$	0.3	52	$-2.6 \pm 2.8$	0.5	50
60-93%	0-1	South	$1.6 \pm 8.7$	0.8	45	$-6.9 \pm 6.1$	1.1	42
60-93%	1-2	South	$5.0 \pm 9.4$	0.7	47	$-2.0 \pm 7.0$	0.5	48
60-93%	2-3	South	$0.7 \pm 6.1$	1.2	48	$5.2 \pm 4.7$	0.6	44
60-93%	3-4	South	$5.8 \pm 4.2$	1.0	44	$0.9 \pm 2.5$	0.3	43
60-93%	4-5	South	$1.1 \pm 2.3$	0.2	44	$2.9 \pm 2.0$	0.3	33
60-93%	5-6	South	$-0.9 \pm 1.1$	0.2	32	$-0.5 \pm 0.2$	0.1	18

Table A.11: Subtracted counts in the  $J/\psi$  mass region [2.6,3.6] for the  $++$  and  $--$  pair distributions in the North Arm in 10% and 5% centrality bins. Also included are the  $\chi^2/\text{ndf}$  and  $\text{ndf}$  for a fit to a flat line over the mass range [0.6, 6.0].

Cent	$p_T$	Arm	++ Pairs			-- Pairs		
			counts	$\chi^2/\text{ndf}$	ndf	counts	$\chi^2/\text{ndf}$	ndf
0-10%	all	North	$74.7 \pm 190.6$	0.9	53	$-39.6 \pm 156.4$	1.1	53
10-20%	all	North	$28.8 \pm 138.8$	1.1	53	$69.2 \pm 111.0$	1.2	53
20-30%	all	North	$89.7 \pm 98.3$	1.4	53	$48.7 \pm 76.4$	1.6	53
30-40%	all	North	$67.7 \pm 66.0$	1.3	53	$109.5 \pm 50.8$	1.0	53
40-50%	all	North	$46.5 \pm 40.9$	1.0	53	$33.4 \pm 31.6$	0.8	53
50-60%	all	North	$-15.8 \pm 23.1$	0.9	53	$-12.8 \pm 17.4$	1.1	53
60-70%	all	North	$13.3 \pm 12.9$	0.8	53	$0.9 \pm 9.3$	0.8	53
70-80%	all	North	$-7.0 \pm 5.7$	0.8	49	$-3.5 \pm 4.5$	0.7	48
80-93%	all	North	$2.5 \pm 3.7$	0.9	36	$1.9 \pm 2.6$	0.7	37
0-5%	all	North	$-105.2 \pm 144.1$	0.8	53	$-111.4 \pm 119.4$	1.1	53
5-10%	all	North	$180.0 \pm 124.7$	1.3	53	$71.8 \pm 101.1$	1.3	53
10-15%	all	North	$-38.4 \pm 105.3$	0.9	53	$-3.1 \pm 84.9$	1.1	53
15-20%	all	North	$66.2 \pm 90.4$	1.4	53	$72.4 \pm 71.5$	1.0	53
20-25%	all	North	$40.4 \pm 75.4$	0.7	53	$113.8 \pm 59.5$	1.4	53
25-30%	all	North	$48.9 \pm 63.1$	1.6	53	$-65.3 \pm 47.8$	1.2	53
30-35%	all	North	$2.7 \pm 51.1$	1.0	53	$82.4 \pm 39.9$	0.9	53
35-40%	all	North	$65.1 \pm 41.7$	1.1	53	$27.2 \pm 31.5$	1.1	53
40-45%	all	North	$42.3 \pm 32.5$	0.9	53	$12.6 \pm 25.0$	0.9	53
45-50%	all	North	$4.4 \pm 24.7$	1.1	53	$20.9 \pm 19.4$	0.9	53
50-55%	all	North	$-12.0 \pm 18.5$	0.8	53	$6.4 \pm 14.4$	1.1	53
55-60%	all	North	$-3.9 \pm 13.9$	1.0	53	$-19.2 \pm 9.7$	1.4	53
60-65%	all	North	$12.5 \pm 10.6$	0.8	53	$4.3 \pm 7.9$	1.1	52
65-70%	all	North	$0.8 \pm 7.2$	0.5	49	$-3.5 \pm 5.0$	0.7	51
70-75%	all	North	$-5.7 \pm 4.5$	0.7	46	$-2.7 \pm 3.6$	0.7	48
75-80%	all	North	$-1.3 \pm 3.5$	0.9	43	$-0.8 \pm 2.6$	0.5	39

Table A.12: Subtracted counts in the  $J/\psi$  mass region [2.6,3.6] for the  $++$  and  $--$  pair distributions in the North Arm in 20% centrality and 1 GeV/ $c$   $p_T$  bins. Also included are the  $\chi^2/\text{ndf}$  and ndf for a fit to a flat line over the mass range [0.6, 6.0].

Cent	$p_T$	Arm	++ Pairs			-- Pairs		
			counts	$\chi^2/\text{ndf}$	ndf	counts	$\chi^2/\text{ndf}$	ndf
0-20%	0-1	North	$103.2 \pm 127.5$	0.8	53	$-10.1 \pm 102.8$	1.4	53
0-20%	1-2	North	$51.0 \pm 143.3$	1.0	53	$-7.2 \pm 115.1$	1.1	53
0-20%	2-3	North	$72.5 \pm 97.8$	1.4	53	$72.6 \pm 79.0$	0.8	53
0-20%	3-4	North	$-11.5 \pm 62.4$	1.0	53	$-7.1 \pm 52.3$	1.2	53
0-20%	4-5	North	$-55.3 \pm 42.5$	0.8	53	$-48.5 \pm 35.4$	0.9	53
0-20%	5-6	North	$-13.1 \pm 32.3$	0.7	53	$24.6 \pm 27.9$	1.0	53
20-40%	0-1	North	$89.7 \pm 68.8$	1.3	53	$77.7 \pm 53.9$	1.1	53
20-40%	1-2	North	$108.7 \pm 74.7$	1.2	53	$63.0 \pm 57.7$	1.4	53
20-40%	2-3	North	$10.1 \pm 47.5$	1.1	53	$40.1 \pm 35.7$	0.8	53
20-40%	3-4	North	$2.7 \pm 27.5$	1.1	53	$8.9 \pm 20.7$	1.0	53
20-40%	4-5	North	$-14.2 \pm 16.5$	0.9	53	$-4.1 \pm 13.1$	1.0	53
20-40%	5-6	North	$-8.1 \pm 11.8$	1.2	53	$-1.7 \pm 9.2$	1.4	53
40-60%	0-1	North	$16.0 \pm 28.2$	0.8	52	$21.8 \pm 22.4$	0.9	50
40-60%	1-2	North	$46.4 \pm 30.4$	0.7	53	$3.6 \pm 22.8$	0.5	53
40-60%	2-3	North	$-12.0 \pm 18.0$	1.0	53	$-4.1 \pm 13.3$	0.6	53
40-60%	3-4	North	$-13.1 \pm 9.8$	1.0	53	$-0.5 \pm 7.8$	1.3	53
40-60%	4-5	North	$1.4 \pm 5.6$	1.1	53	$2.5 \pm 4.8$	0.7	53
40-60%	5-6	North	$0.7 \pm 3.4$	0.5	51	$-6.5 \pm 1.6$	0.5	52
60-93%	0-1	North	$7.5 \pm 8.9$	0.5	45	$9.5 \pm 7.1$	0.7	40
60-93%	1-2	North	$3.4 \pm 9.3$	0.9	45	$-5.2 \pm 6.6$	0.8	49
60-93%	2-3	North	$-2.8 \pm 5.2$	0.8	47	$-5.0 \pm 3.5$	1.1	44
60-93%	3-4	North	$0.3 \pm 3.4$	0.7	45	$1.6 \pm 2.5$	0.4	42
60-93%	4-5	North	$2.8 \pm 2.3$	0.2	43	$-0.2 \pm 1.0$	0.1	35
60-93%	5-6	North	$-1.3 \pm 0.3$	0.2	29	$-0.7 \pm 0.2$	0.1	26

Table A.13:  $J/\psi$  signal in 10% and 5% centrality bins with statistical and systematic uncertainties added in quadrature, for both mixed and like-sign background subtraction. For those bins where  $N_{J/\psi} < \sqrt{\sigma_{stat}^2 + \sigma_{sys}^2}$ , the text is in red, and only the confidence limit will be used.

		South Arm				North Arm			
		Mixed		Likesign		Mixed		Likesign	
Cent	$p_T$	signal	err	signal	err	signal	err	signal	err
0-10%	all	1571.6	301.0	1654.1	469.5	226.5	266.7	215.4	367.3
10-20%	all	2161.9	214.5	1716.1	320.1	623.3	187.5	713.4	268.3
20-30%	all	1853.6	167.2	1654.6	240.8	1037.3	120.0	934.4	164.3
30-40%	all	1514.0	111.5	1334.5	152.3	1016.5	99.3	864.4	109.5
40-50%	all	1079.6	81.9	958.6	100.4	895.6	79.9	845.4	75.9
50-60%	all	679.1	47.9	672.8	54.8	639.7	41.2	621.2	52.3
60-70%	all	399.4	28.4	385.3	40.1	319.0	27.8	300.7	29.3
70-80%	all	217.5	20.6	212.6	21.8	191.3	17.5	191.8	19.0
80-93%	all	98.6	12.6	96.6	13.1	127.2	13.2	123.1	14.8
0-5%	all	789.6	188.1	939.3	300.0	215.7	187.3	289.0	287.8
5-10%	all	768.4	175.3	718.7	273.2	34.6	512.9	5.7	117.0
10-15%	all	1050.6	160.6	843.1	223.3	248.9	140.0	312.1	192.5
15-20%	all	1119.7	120.4	823.0	177.4	398.5	119.2	406.9	162.1
20-25%	all	922.6	129.3	776.2	179.7	477.3	85.4	383.0	124.0
25-30%	all	928.7	90.2	830.8	134.3	580.9	85.1	558.4	107.1
30-35%	all	805.3	90.4	735.2	109.3	501.8	71.8	437.1	87.6
35-40%	all	713.1	66.1	580.9	95.0	527.2	57.0	441.6	73.1
40-45%	all	653.3	59.9	608.4	75.5	496.7	54.5	467.5	58.8
45-50%	all	429.2	48.6	367.1	62.0	391.6	38.8	379.7	45.8
50-55%	all	354.2	34.1	334.2	41.9	325.1	33.0	269.8	37.1
55-60%	all	327.9	32.6	338.1	33.5	319.0	24.0	350.7	30.4
60-65%	all	231.1	20.8	231.2	28.8	182.1	22.4	159.1	22.3
65-70%	all	165.9	18.2	156.6	23.8	132.9	15.2	129.6	17.0
70-75%	all	121.6	15.4	115.2	16.3	113.3	13.3	113.5	14.6
75-80%	all	94.9	12.2	96.3	13.6	76.0	11.4	72.3	11.8

Table A.14:  $J/\psi$  signal in 20% centrality and 1 GeV/c  $p_T$  bins with statistical and systematic uncertainties added in quadrature, for both mixed and like-sign background subtraction. For those bins where  $N_{J/\psi} < \sqrt{\sigma_{stat}^2 + \sigma_{sys}^2}$ , the text is in red, and only the confidence limit will be used.

		South Arm				North Arm			
Cent	$p_T$	Mixed		Likesign		Mixed		Likesign	
		signal	err	signal	err	signal	err	signal	err
0-20%	0-1	1154.3	171.7	908.7	278.0	454.6	129.1	300.7	219.6
0-20%	1-2	1368.0	176.0	1262.4	327.3	387.1	157.9	408.9	330.1
0-20%	2-3	764.6	128.4	562.3	168.6	189.8	120.9	66.1	165.2
0-20%	3-4	207.2	69.2	197.1	90.1	47.2	68.9	19.5	204.5
0-20%	4-5	207.8	44.6	196.9	72.7	94.9	69.9	191.9	116.7
0-20%	5-6	22.6	22.1	14.2	44.2	16.0	55.9	56.4	107.6
20-40%	0-1	842.7	114.7	586.8	121.3	610.6	79.6	447.0	106.0
20-40%	1-2	1294.4	111.5	1090.3	129.8	721.8	95.5	625.9	118.6
20-40%	2-3	715.2	69.1	708.1	88.8	456.8	54.2	411.3	77.1
20-40%	3-4	281.9	36.4	242.2	49.6	187.2	37.1	177.4	43.9
20-40%	4-5	62.1	15.3	110.3	28.7	93.5	24.2	111.5	34.9
20-40%	5-6	43.0	12.8	57.0	19.1	32.6	12.6	88.5	24.5
40-60%	0-1	509.2	43.7	476.4	52.4	465.0	43.3	435.1	48.0
40-60%	1-2	657.6	53.9	621.7	63.2	587.7	48.2	544.5	54.4
40-60%	2-3	307.1	31.2	294.6	39.4	291.6	31.6	285.1	35.0
40-60%	3-4	135.7	21.3	119.4	23.0	121.6	12.5	127.7	20.0
40-60%	4-5	53.0	10.3	67.8	12.6	50.7	9.1	60.9	9.9
40-60%	5-6	9.7	4.5	25.5	6.6	11.1	4.5	24.0	6.4
60-93%	0-1	252.8	21.0	249.3	22.9	237.2	20.1	228.6	21.8
60-93%	1-2	245.3	23.2	243.9	26.3	248.4	20.7	238.4	22.4
60-93%	2-3	120.7	14.9	114.3	15.9	89.8	13.1	90.5	13.8
60-93%	3-4	38.8	7.8	33.9	10.2	42.0	8.5	40.5	8.9
60-93%	4-5	20.6	5.1	22.9	5.6	16.3	4.4	25.8	5.5
60-93%	5-6	8.0	3.0	13.8	3.8	7.0	2.9	11.0	3.3

Table A.15:  $J/\psi$  signal in 10% and 5% centrality bins with statistical and systematic uncertainties added in quadrature, for both mixed background and like-sign subtraction. Collisions vertex cuts are applied such that the signal for those events closer to that arm are used ( $-30 \text{ cm} < z < 0 \text{ cm}$  for South,  $0 \text{ cm} < z < 30 \text{ cm}$  for North). For those bins where  $N_{J/\psi} < \sqrt{\sigma_{\text{stat}}^2 + \sigma_{\text{sys}}^2}$ , the text is in red.

		South Arm ( $z < 0$ )				North Arm ( $z > 0$ )			
Cent	$p_T$	Mixed		Likesign		Mixed		Likesign	
		signal	err	signal	err	signal	err	signal	err
0-10%	all	731.7	143.7	724.4	226.0	58.9	224.7	52.9	172.5
10-20%	all	1111.0	123.7	934.0	174.2	368.4	106.4	394.4	148.3
20-30%	all	857.4	100.2	607.2	126.9	388.6	71.6	372.9	96.0
30-40%	all	730.2	75.4	652.6	101.4	397.3	63.6	316.2	68.1
40-50%	all	512.0	45.0	481.5	56.7	359.7	36.6	360.1	48.3
50-60%	all	304.2	34.2	305.0	33.9	293.2	25.4	305.8	31.4
60-70%	all	212.4	18.3	220.0	22.1	134.0	16.0	125.6	19.0
70-80%	all	111.2	14.5	108.4	14.2	87.2	11.5	81.1	12.4
80-93%	all	45.9	8.8	45.4	8.8	54.3	8.5	49.8	8.9
0-5%	all	325.8	108.4	417.0	162.7	37.1	170.1	106.0	364.8
5-10%	all	414.6	94.8	285.9	137.1	25.2	145.7	0.0	74.8
10-15%	all	586.4	94.6	437.3	124.7	175.2	76.8	207.3	103.2
15-20%	all	530.3	78.3	460.0	98.2	197.4	68.7	199.0	86.4
20-25%	all	470.7	70.0	270.5	91.2	201.9	50.0	170.0	67.3
25-30%	all	396.4	64.4	324.4	81.9	190.5	42.0	203.2	60.5
30-35%	all	405.5	51.9	371.2	71.8	143.8	45.8	124.5	62.2
35-40%	all	327.4	40.7	291.0	49.8	244.6	39.4	189.2	39.4
40-45%	all	287.0	37.4	276.5	40.8	214.4	25.5	234.8	33.7
45-50%	all	227.0	36.5	210.4	37.9	143.9	30.8	133.8	27.7
50-55%	all	156.3	28.4	162.7	25.5	149.0	19.8	130.7	22.2
55-60%	all	146.5	18.2	142.1	22.2	150.8	16.2	165.3	18.8
60-65%	all	127.1	14.4	133.5	16.2	79.7	13.4	74.7	15.2
65-70%	all	75.8	12.6	77.1	13.7	53.7	9.5	51.0	10.7
70-75%	all	55.6	10.3	50.9	10.8	53.4	8.8	48.2	10.3
75-80%	all	55.5	8.7	57.8	9.1	34.3	8.1	30.8	7.9

Table A.16:  $J/\psi$  signal in 20% centrality and 1 GeV/c  $p_T$  bins with statistical and systematic uncertainties added in quadrature, for both mixed background and like-sign subtraction. Collisions vertex cuts are applied such that the signal for those events closer to that arm are used ( $-30 \text{ cm} < z < 0 \text{ cm}$  for South,  $0 \text{ cm} < z < 30 \text{ cm}$  for North). For those bins where  $N_{J/\psi} < \sqrt{\sigma_{\text{stat}}^2 + \sigma_{\text{sys}}^2}$ , the text is in red.

		South Arm ( $z < 0$ )				North Arm ( $z > 0$ )			
		Mixed		Likesign		Mixed		Likesign	
Cent	$p_T$	signal	err	signal	err	signal	err	signal	err
0-20%	0-1	601.1	90.3	449.8	157.0	130.6	69.8	99.0	260.7
0-20%	1-2	565.7	103.4	517.8	161.8	269.3	92.4	216.8	143.6
0-20%	2-3	422.9	72.2	386.0	92.4	157.6	69.0	119.5	86.3
0-20%	3-4	118.2	39.9	91.1	53.4	0.7	98.3	1.4	68.6
0-20%	4-5	111.5	25.1	103.1	35.3	18.7	39.1	58.9	58.0
0-20%	5-6	12.2	12.7	-2.1	17.7	39.8	32.8	83.1	49.2
20-40%	0-1	403.3	58.6	234.1	73.6	188.1	46.1	118.3	60.2
20-40%	1-2	658.9	64.5	539.1	81.3	259.4	57.6	197.9	76.8
20-40%	2-3	298.9	41.3	283.6	52.7	180.9	31.1	202.2	43.5
20-40%	3-4	122.7	22.8	83.4	30.4	102.3	24.2	89.7	30.8
20-40%	4-5	40.9	11.0	45.8	15.9	49.5	15.8	73.5	20.5
20-40%	5-6	8.3	5.4	12.0	7.1	27.4	12.1	60.3	17.4
40-60%	0-1	240.9	25.6	246.8	29.6	181.6	24.8	176.6	28.1
40-60%	1-2	282.8	31.5	265.5	36.4	250.6	29.7	254.9	32.6
40-60%	2-3	153.6	21.3	147.4	24.5	116.6	18.3	118.5	20.0
40-60%	3-4	70.1	12.9	68.0	15.2	64.8	7.2	68.4	13.4
40-60%	4-5	25.9	6.4	41.4	7.8	26.4	6.8	51.8	8.5
40-60%	5-6	2.8	2.6	19.7	5.0	6.3	3.3	22.4	5.1
60-93%	0-1	143.0	14.7	144.6	15.3	107.5	12.9	107.4	13.8
60-93%	1-2	104.7	14.6	99.4	16.5	92.3	12.8	70.2	14.1
60-93%	2-3	76.2	11.1	78.4	11.9	50.9	9.3	47.5	9.0
60-93%	3-4	22.5	5.2	19.0	7.4	16.5	5.2	15.1	5.4
60-93%	4-5	7.4	2.9	11.0	3.5	6.5	2.6	6.6	2.8
60-93%	5-6	6.0	nan	6.0	2.5	6.0	nan	6.0	nan

## A.2 Acc $\times$ Eff Tables

Table A.17: Acceptance $\times$ Efficiency correction factors for run-to-run variations for six reference runs.

$p_T$	$y$	$A \times \epsilon$ Run-to-Run Correction Factors					
		230956	231429	231920	232005	232460	240100
all	[-2.2, -1.2]	1.01	0.99	1.00	1.00	0.99	0.99
[0, 1]	[-2.2, -1.2]	1.00	0.99	0.99	0.99	0.98	0.99
[1, 2]	[-2.2, -1.2]	1.01	1.00	1.00	1.00	0.99	0.99
[2, 3]	[-2.2, -1.2]	0.99	0.99	0.99	0.99	0.98	0.99
[3, 4]	[-2.2, -1.2]	1.04	1.00	1.00	0.99	0.98	1.04
[4, 5]	[-2.2, -1.2]	1.00	0.95	1.00	0.99	0.97	0.94
all	[1.2, 2.2]	0.98	0.98	0.99	0.99	1.03	1.00
[0, 1]	[1.2, 2.2]	0.98	0.98	0.99	0.99	1.03	1.00
[1, 2]	[1.2, 2.2]	0.98	0.97	0.99	0.99	1.03	1.00
[2, 3]	[1.2, 2.2]	0.99	0.98	1.00	1.00	1.04	1.00
[3, 4]	[1.2, 2.2]	0.98	0.97	0.98	0.98	1.01	1.00
[4, 5]	[1.2, 2.2]	0.96	1.00	0.96	0.96	1.03	1.05

Table A.18:  $J/\psi$  embedded acceptance $\times$ efficiency for six reference runs as a function of centrality, as well as the weighted average.

Cent.	$p_T$	$y$	Embedded $A \times \epsilon$ (%)						Averaged
			230956	231429	231920	232005	232460	240100	
[0, 10]	all	[-2.2, -1.2]	2.85 $\pm$ 0.07	2.69 $\pm$ 0.07	2.94 $\pm$ 0.07	2.72 $\pm$ 0.07	2.98 $\pm$ 0.07	2.97 $\pm$ 0.07	2.91 $\pm$ 0.04
[10, 20]	all	[-2.2, -1.2]	3.87 $\pm$ 0.08	3.55 $\pm$ 0.08	3.92 $\pm$ 0.09	3.57 $\pm$ 0.08	3.98 $\pm$ 0.13	3.43 $\pm$ 0.08	3.68 $\pm$ 0.06
[20, 30]	all	[-2.2, -1.2]	4.66 $\pm$ 0.11	4.17 $\pm$ 0.13	4.50 $\pm$ 0.18	4.20 $\pm$ 0.10	4.57 $\pm$ 0.10	3.94 $\pm$ 0.15	4.28 $\pm$ 0.07
[30, 40]	all	[-2.2, -1.2]	5.05 $\pm$ 0.13	4.70 $\pm$ 0.12	5.05 $\pm$ 0.13	4.49 $\pm$ 0.12	5.05 $\pm$ 0.13	4.32 $\pm$ 0.12	4.70 $\pm$ 0.07
[40, 50]	all	[-2.2, -1.2]	5.30 $\pm$ 0.14	4.94 $\pm$ 0.13	5.28 $\pm$ 0.14	4.92 $\pm$ 0.14	5.44 $\pm$ 0.14	4.74 $\pm$ 0.13	5.06 $\pm$ 0.07
[50, 60]	all	[-2.2, -1.2]	5.65 $\pm$ 0.15	5.05 $\pm$ 0.14	5.60 $\pm$ 0.15	5.16 $\pm$ 0.15	5.58 $\pm$ 0.15	4.76 $\pm$ 0.13	5.20 $\pm$ 0.08
[60, 70]	all	[-2.2, -1.2]	5.70 $\pm$ 0.15	5.25 $\pm$ 0.14	5.53 $\pm$ 0.15	5.17 $\pm$ 0.19	5.86 $\pm$ 0.16	4.87 $\pm$ 0.14	5.35 $\pm$ 0.08
[70, 80]	all	[-2.2, -1.2]	5.90 $\pm$ 0.16	5.25 $\pm$ 0.14	5.73 $\pm$ 0.16	5.19 $\pm$ 0.15	5.74 $\pm$ 0.15	4.99 $\pm$ 0.14	5.40 $\pm$ 0.08
[80, 93]	all	[-2.2, -1.2]	5.83 $\pm$ 0.15	5.21 $\pm$ 0.14	5.79 $\pm$ 0.15	5.25 $\pm$ 0.14	5.95 $\pm$ 0.16	4.99 $\pm$ 0.13	5.45 $\pm$ 0.08
[0, 10]	all	[1.2, 2.2]	1.29 $\pm$ 0.07	1.32 $\pm$ 0.08	1.32 $\pm$ 0.08	1.51 $\pm$ 0.07	1.35 $\pm$ 0.08	1.34 $\pm$ 0.08	1.35 $\pm$ 0.03
[10, 20]	all	[1.2, 2.2]	2.46 $\pm$ 0.09	2.48 $\pm$ 0.09	2.59 $\pm$ 0.10	2.70 $\pm$ 0.10	2.54 $\pm$ 0.10	2.42 $\pm$ 0.10	2.52 $\pm$ 0.04
[20, 30]	all	[1.2, 2.2]	3.76 $\pm$ 0.09	3.79 $\pm$ 0.09	3.80 $\pm$ 0.09	3.72 $\pm$ 0.09	3.59 $\pm$ 0.09	3.66 $\pm$ 0.09	3.70 $\pm$ 0.04
[30, 40]	all	[1.2, 2.2]	4.79 $\pm$ 0.08	4.87 $\pm$ 0.08	4.76 $\pm$ 0.09	4.77 $\pm$ 0.08	4.78 $\pm$ 0.08	4.72 $\pm$ 0.08	4.76 $\pm$ 0.03
[40, 50]	all	[1.2, 2.2]	5.66 $\pm$ 0.09	5.47 $\pm$ 0.09	5.59 $\pm$ 0.09	5.49 $\pm$ 0.16	5.42 $\pm$ 0.09	5.33 $\pm$ 0.09	5.47 $\pm$ 0.04
[50, 60]	all	[1.2, 2.2]	6.20 $\pm$ 0.10	6.07 $\pm$ 0.10	6.03 $\pm$ 0.10	6.03 $\pm$ 0.10	5.80 $\pm$ 0.09	5.90 $\pm$ 0.10	5.98 $\pm$ 0.04
[60, 70]	all	[1.2, 2.2]	6.37 $\pm$ 0.10	6.44 $\pm$ 0.10	6.18 $\pm$ 0.10	6.14 $\pm$ 0.10	6.04 $\pm$ 0.10	6.09 $\pm$ 0.10	6.18 $\pm$ 0.04
[70, 80]	all	[1.2, 2.2]	6.42 $\pm$ 0.10	6.56 $\pm$ 0.11	6.35 $\pm$ 0.10	6.30 $\pm$ 0.10	6.06 $\pm$ 0.10	6.26 $\pm$ 0.10	6.30 $\pm$ 0.04
[80, 93]	all	[1.2, 2.2]	6.63 $\pm$ 0.10	6.54 $\pm$ 0.10	6.64 $\pm$ 0.11	6.56 $\pm$ 0.10	6.29 $\pm$ 0.09	6.42 $\pm$ 0.10	6.48 $\pm$ 0.04

Table A.19:  $J/\psi$  embedded acceptance $\times$ efficiency for six reference runs as a function of  $p_T$  in 0-20% centrality, as well as the weighted average.

Cent.	$p_T$	$y$	Embedded $A \times \epsilon$ (%)					Averaged
			230956	231429	231920	232005	232460	
[0, 20]	[0, 1]	[-2.2, -1.2]	3.75 $\pm$ 0.10	3.55 $\pm$ 0.09	3.70 $\pm$ 0.10	3.50 $\pm$ 0.10	3.98 $\pm$ 0.10	3.69 $\pm$ 0.10
[0, 20]	[1, 2]	[-2.2, -1.2]	3.42 $\pm$ 0.07	3.29 $\pm$ 0.07	3.57 $\pm$ 0.07	3.27 $\pm$ 0.07	3.60 $\pm$ 0.07	3.28 $\pm$ 0.07
[0, 20]	[2, 3]	[-2.2, -1.2]	3.29 $\pm$ 0.10	2.92 $\pm$ 0.09	3.32 $\pm$ 0.10	2.96 $\pm$ 0.09	3.23 $\pm$ 0.10	3.01 $\pm$ 0.09
[0, 20]	[3, 4]	[-2.2, -1.2]	3.62 $\pm$ 0.10	3.45 $\pm$ 0.09	3.62 $\pm$ 0.10	3.38 $\pm$ 0.09	3.70 $\pm$ 0.10	3.37 $\pm$ 0.09
[0, 20]	[4, 5]	[-2.2, -1.2]	5.19 $\pm$ 0.30	4.28 $\pm$ 0.27	4.71 $\pm$ 0.28	4.47 $\pm$ 0.30	5.17 $\pm$ 0.29	4.31 $\pm$ 0.29
[0, 20]	[0, 1]	[1.2, 2.2]	2.32 $\pm$ 0.08	2.41 $\pm$ 0.08	2.35 $\pm$ 0.08	2.57 $\pm$ 0.09	2.42 $\pm$ 0.08	2.21 $\pm$ 0.09
[0, 20]	[1, 2]	[1.2, 2.2]	1.97 $\pm$ 0.06	2.04 $\pm$ 0.06	2.15 $\pm$ 0.06	2.30 $\pm$ 0.06	2.18 $\pm$ 0.06	2.11 $\pm$ 0.06
[0, 20]	[2, 3]	[1.2, 2.2]	1.93 $\pm$ 0.08	1.93 $\pm$ 0.08	1.89 $\pm$ 0.07	2.09 $\pm$ 0.09	1.93 $\pm$ 0.07	1.90 $\pm$ 0.08
[0, 20]	[3, 4]	[1.2, 2.2]	2.24 $\pm$ 0.06	2.23 $\pm$ 0.07	2.23 $\pm$ 0.07	2.36 $\pm$ 0.07	2.25 $\pm$ 0.07	2.15 $\pm$ 0.07
[0, 20]	[4, 5]	[1.2, 2.2]	2.33 $\pm$ 0.22	2.36 $\pm$ 0.26	2.64 $\pm$ 0.23	2.62 $\pm$ 0.22	2.77 $\pm$ 0.23	2.55 $\pm$ 0.22
								2.53 $\pm$ 0.09

Table A.20:  $J/\psi$  embedded acceptance $\times$ efficiency for six reference runs as a function of  $p_T$  in 20-40% centrality, as well as the weighted average.

Cent.	$p_T$	$y$	Embedded $A \times \epsilon$ (%)					Averaged
			230956	231429	231920	232005	232460	
[20, 40]	[0, 1]	[-2.2, -1.2]	5.43 $\pm$ 0.12	4.89 $\pm$ 0.11	5.33 $\pm$ 0.12	5.06 $\pm$ 0.11	5.33 $\pm$ 0.11	4.59 $\pm$ 0.11
[20, 40]	[1, 2]	[-2.2, -1.2]	4.94 $\pm$ 0.09	4.66 $\pm$ 0.09	4.91 $\pm$ 0.09	4.46 $\pm$ 0.08	4.99 $\pm$ 0.09	4.34 $\pm$ 0.08
[20, 40]	[2, 3]	[-2.2, -1.2]	4.73 $\pm$ 0.12	4.16 $\pm$ 0.12	4.60 $\pm$ 0.12	4.02 $\pm$ 0.11	4.52 $\pm$ 0.12	3.88 $\pm$ 0.11
[20, 40]	[3, 4]	[-2.2, -1.2]	5.05 $\pm$ 0.13	4.88 $\pm$ 0.13	5.15 $\pm$ 0.13	4.65 $\pm$ 0.12	5.27 $\pm$ 0.13	4.60 $\pm$ 0.12
[20, 40]	[4, 5]	[-2.2, -1.2]	6.02 $\pm$ 0.31	6.12 $\pm$ 0.32	6.89 $\pm$ 0.34	5.90 $\pm$ 0.32	6.15 $\pm$ 0.32	5.48 $\pm$ 0.30
[20, 40]	[0, 1]	[1.2, 2.2]	4.85 $\pm$ 0.11	4.90 $\pm$ 0.11	4.89 $\pm$ 0.11	4.82 $\pm$ 0.11	4.84 $\pm$ 0.11	4.87 $\pm$ 0.11
[20, 40]	[1, 2]	[1.2, 2.2]	4.31 $\pm$ 0.08	4.38 $\pm$ 0.08	4.26 $\pm$ 0.08	4.24 $\pm$ 0.08	4.12 $\pm$ 0.07	4.26 $\pm$ 0.08
[20, 40]	[2, 3]	[1.2, 2.2]	3.97 $\pm$ 0.10	3.91 $\pm$ 0.10	4.01 $\pm$ 0.10	3.94 $\pm$ 0.10	3.93 $\pm$ 0.10	3.75 $\pm$ 0.10
[20, 40]	[3, 4]	[1.2, 2.2]	4.46 $\pm$ 0.09	4.72 $\pm$ 0.09	4.38 $\pm$ 0.09	4.48 $\pm$ 0.09	4.51 $\pm$ 0.09	4.44 $\pm$ 0.09
[20, 40]	[4, 5]	[1.2, 2.2]	5.39 $\pm$ 0.28	5.50 $\pm$ 0.28	5.47 $\pm$ 0.29	5.53 $\pm$ 0.29	5.62 $\pm$ 0.28	5.48 $\pm$ 0.29

Table A.21:  $J/\psi$  embedded acceptance $\times$ efficiency for six reference runs as a function of  $p_T$  in 40-60% centrality, as well as the weighted average.

Cent.	$p_T$	$y$	Embedded $A \times \epsilon$ (%)					Averaged
			230956	231429	231920	232005	232460	
[40, 60]	[0, 1]	[-2.2, -1.2]	6.11 $\pm$ 0.13	5.79 $\pm$ 0.12	6.12 $\pm$ 0.13	5.69 $\pm$ 0.12	6.32 $\pm$ 0.13	5.22 $\pm$ 0.12
[40, 60]	[1, 2]	[-2.2, -1.2]	5.71 $\pm$ 0.10	5.09 $\pm$ 0.10	5.60 $\pm$ 0.10	5.27 $\pm$ 0.10	5.71 $\pm$ 0.11	4.97 $\pm$ 0.09
[40, 60]	[2, 3]	[-2.2, -1.2]	5.19 $\pm$ 0.14	4.78 $\pm$ 0.13	5.29 $\pm$ 0.14	4.68 $\pm$ 0.14	5.22 $\pm$ 0.14	4.62 $\pm$ 0.13
[40, 60]	[3, 4]	[-2.2, -1.2]	5.88 $\pm$ 0.15	5.50 $\pm$ 0.14	6.03 $\pm$ 0.15	5.42 $\pm$ 0.14	5.85 $\pm$ 0.15	5.17 $\pm$ 0.14
[40, 60]	[4, 5]	[-2.2, -1.2]	7.16 $\pm$ 0.36	6.16 $\pm$ 0.32	6.86 $\pm$ 0.35	6.39 $\pm$ 0.34	7.13 $\pm$ 0.35	6.67 $\pm$ 0.34
[40, 60]	[0, 1]	[1.2, 2.2]	6.54 $\pm$ 0.14	6.37 $\pm$ 0.13	6.41 $\pm$ 0.13	6.27 $\pm$ 0.13	6.27 $\pm$ 0.13	6.14 $\pm$ 0.13
[40, 60]	[1, 2]	[1.2, 2.2]	5.87 $\pm$ 0.10	5.70 $\pm$ 0.10	5.71 $\pm$ 0.10	5.61 $\pm$ 0.10	5.54 $\pm$ 0.09	5.54 $\pm$ 0.09
[40, 60]	[2, 3]	[1.2, 2.2]	5.25 $\pm$ 0.12	5.04 $\pm$ 0.12	5.28 $\pm$ 0.12	5.33 $\pm$ 0.12	4.93 $\pm$ 0.12	5.20 $\pm$ 0.12
[40, 60]	[3, 4]	[1.2, 2.2]	6.02 $\pm$ 0.11	6.18 $\pm$ 0.12	6.10 $\pm$ 0.12	6.07 $\pm$ 0.12	5.87 $\pm$ 0.11	6.01 $\pm$ 0.12
[40, 60]	[4, 5]	[1.2, 2.2]	7.40 $\pm$ 0.33	7.35 $\pm$ 0.32	7.03 $\pm$ 0.31	6.84 $\pm$ 0.32	6.89 $\pm$ 0.31	6.84 $\pm$ 0.31
								7.01 $\pm$ 0.13

Table A.22:  $J/\psi$  embedded acceptance $\times$ efficiency for six reference runs as a function of  $p_T$  in 60-93% centrality, as well as the weighted average.

Cent.	$p_T$	$y$	Embedded $A \times \epsilon$ (%)					Averaged
			230956	231429	231920	232005	232460	
[60, 93]	[0, 1]	[-2.2, -1.2]	6.72 $\pm$ 0.12	6.04 $\pm$ 0.10	6.59 $\pm$ 0.14	6.03 $\pm$ 0.10	6.71 $\pm$ 0.11	5.56 $\pm$ 0.10
[60, 93]	[1, 2]	[-2.2, -1.2]	5.99 $\pm$ 0.10	5.46 $\pm$ 0.09	5.90 $\pm$ 0.09	5.40 $\pm$ 0.09	6.12 $\pm$ 0.10	5.14 $\pm$ 0.09
[60, 93]	[2, 3]	[-2.2, -1.2]	5.61 $\pm$ 0.13	4.84 $\pm$ 0.11	5.35 $\pm$ 0.12	4.94 $\pm$ 0.12	5.56 $\pm$ 0.12	4.83 $\pm$ 0.11
[60, 93]	[3, 4]	[-2.2, -1.2]	6.35 $\pm$ 0.15	5.79 $\pm$ 0.14	6.21 $\pm$ 0.17	5.62 $\pm$ 0.13	6.20 $\pm$ 0.15	5.26 $\pm$ 0.13
[60, 93]	[4, 5]	[-2.2, -1.2]	7.24 $\pm$ 0.30	6.53 $\pm$ 0.28	6.96 $\pm$ 0.29	6.83 $\pm$ 0.29	7.02 $\pm$ 0.29	6.37 $\pm$ 0.28
[60, 93]	[0, 1]	[1.2, 2.2]	7.16 $\pm$ 0.12	7.20 $\pm$ 0.12	7.16 $\pm$ 0.12	7.05 $\pm$ 0.12	6.86 $\pm$ 0.12	6.95 $\pm$ 0.12
[60, 93]	[1, 2]	[1.2, 2.2]	6.42 $\pm$ 0.10	6.47 $\pm$ 0.09	6.23 $\pm$ 0.16	6.23 $\pm$ 0.09	5.98 $\pm$ 0.09	6.16 $\pm$ 0.09
[60, 93]	[2, 3]	[1.2, 2.2]	5.81 $\pm$ 0.11	5.78 $\pm$ 0.11	5.80 $\pm$ 0.11	5.76 $\pm$ 0.11	5.51 $\pm$ 0.10	5.65 $\pm$ 0.11
[60, 93]	[3, 4]	[1.2, 2.2]	6.79 $\pm$ 0.11	6.89 $\pm$ 0.11	6.59 $\pm$ 0.10	6.84 $\pm$ 0.11	6.40 $\pm$ 0.10	6.62 $\pm$ 0.11
[60, 93]	[4, 5]	[1.2, 2.2]	7.81 $\pm$ 0.31	8.06 $\pm$ 0.27	8.03 $\pm$ 0.32	8.28 $\pm$ 0.31	7.34 $\pm$ 0.25	7.85 $\pm$ 0.27

### A.3 Invariant Yield Tables

Table A.23: South Arm  $J/\psi$  invariant yields vs. centrality

10% Centrality bins								
Cent.	$N^{J/\psi}$	$A\epsilon$	$N^{MB}$	$B dN/dy \times 10^8$	$\pm$ stat.	$\pm$ type A	$+$ type B	$-$ type B
[0, 10]	1612.9	0.029	3.94e+08	14072.17	2286.93	2450.11	2510.66	1020.83
[10, 20]	1939.0	0.037	3.94e+08	13389.32	1510.24	1077.03	1764.70	1301.59
[20, 30]	1754.1	0.043	3.93e+08	10428.31	1064.40	604.52	906.74	815.56
[30, 40]	1424.3	0.047	3.93e+08	7710.90	622.85	366.26	618.37	615.29
[40, 50]	1019.1	0.051	3.93e+08	5119.13	418.47	200.19	403.70	403.70
[50, 60]	675.9	0.052	3.93e+08	3306.48	238.45	92.06	235.00	235.00
[60, 70]	392.4	0.053	3.93e+08	1864.92	155.43	53.81	133.86	133.86
[70, 80]	215.0	0.054	3.93e+08	1014.03	99.34	19.23	72.32	72.32
[80, 93]	97.6	0.055	5.12e+08	349.47	45.66	6.48	24.91	24.91
5% Centrality bins								
Cent.	$N^{J/\psi}$	$A\epsilon$	$N^{MB}$	$B dN/dy \times 10^8$	$\pm$ stat.	$\pm$ type A	$+$ type B	$-$ type B
[0, 5]	864.4	0.029	1.97e+08	15371.52	3436.61	2640.23	2838.98	1334.91
[5, 10]	743.5	0.031	1.97e+08	12104.85	2856.47	2270.88	1398.00	890.93
[10, 15]	946.8	0.035	1.97e+08	13681.18	2400.74	1403.64	1401.42	1301.42
[15, 20]	971.4	0.039	1.97e+08	12585.43	1840.05	619.46	1428.74	1425.19
[20, 25]	849.4	0.042	1.97e+08	10336.84	1639.19	922.99	896.28	896.28
[25, 30]	879.8	0.044	1.97e+08	10086.01	1206.14	477.68	786.07	786.07
[30, 35]	770.3	0.046	1.97e+08	8514.01	1009.79	459.67	644.73	644.73
[35, 40]	647.0	0.048	1.97e+08	6867.63	734.94	442.64	633.94	633.94
[40, 45]	630.8	0.049	1.97e+08	6518.36	649.99	281.31	481.95	481.95
[45, 50]	398.1	0.052	1.97e+08	3892.45	508.45	194.36	327.33	327.33
[50, 55]	344.2	0.052	1.97e+08	3392.70	366.37	96.97	247.54	247.54
[55, 60]	333.0	0.052	1.97e+08	3234.39	308.12	96.83	231.50	231.50
[60, 65]	231.2	0.053	1.97e+08	2209.04	233.38	52.59	156.89	156.89
[65, 70]	161.3	0.054	1.97e+08	1524.70	190.75	57.35	111.18	111.18
[70, 75]	118.4	0.054	1.96e+08	1116.84	149.96	18.98	81.22	81.22
[75, 80]	95.6	0.054	1.97e+08	901.24	121.15	17.76	64.12	64.12
[80, 93]	97.6	0.054	5.12e+08	353.14	46.25	6.55	25.17	25.17

Table A.24: North Arm  $J/\psi$  invariant yields vs. centrality

10% Centrality bins								
Cent.	$N^{J/\psi}$	$A\epsilon$	$N^{MB}$	$B \ dN/dy \times 10^8$	± stat.	± type A	+ type B	- type B
[0, 10]	220.9	0.013	3.81e+08	4294.80	4678.24	4010.26	756.23	286.01
[10, 20]	668.3	0.025	3.81e+08	6956.20	1793.08	1556.85	813.04	527.02
[20, 30]	985.8	0.037	3.81e+08	6991.63	920.69	413.72	567.03	500.93
[30, 40]	940.4	0.048	3.81e+08	5185.44	505.63	248.57	417.05	414.98
[40, 50]	870.5	0.055	3.81e+08	4179.17	304.51	202.74	280.42	280.42
[50, 60]	630.4	0.060	3.81e+08	2768.48	191.67	75.84	181.46	181.46
[60, 70]	309.9	0.062	3.81e+08	1315.95	112.43	43.30	88.42	88.42
[70, 80]	191.6	0.063	3.8e+08	799.43	75.03	13.91	51.97	51.97
[80, 93]	125.2	0.065	4.96e+08	389.30	42.52	9.42	25.57	25.57

5% Centrality bins								
Cent.	$N^{J/\psi}$	$A\epsilon$	$N^{MB}$	$B \ dN/dy \times 10^8$	± stat.	± type A	+ type B	- type B
[0, 5]	252.4	0.013	1.91e+08	10301.74	7084.95	6597.12	2003.80	1093.41
[5, 10]	20.2	0.018	1.9e+08	590.98	9172.52	999.64	252.73	247.19
[10, 15]	280.5	0.024	1.9e+08	6055.44	2996.37	1961.92	602.59	556.92
[15, 20]	402.7	0.031	1.91e+08	6902.62	2058.55	1252.33	453.96	450.59
[20, 25]	430.2	0.036	1.9e+08	6209.74	1425.73	515.58	563.35	563.35
[25, 30]	569.6	0.041	1.9e+08	7273.66	1081.14	565.70	480.00	480.00
[30, 35]	469.5	0.046	1.9e+08	5384.11	770.10	491.31	410.33	410.33
[35, 40]	484.4	0.049	1.9e+08	5149.95	642.36	247.63	425.52	425.52
[40, 45]	482.1	0.053	1.9e+08	4757.46	490.80	246.87	320.24	320.24
[45, 50]	385.6	0.056	1.9e+08	3606.09	377.17	117.26	236.59	236.59
[50, 55]	297.4	0.059	1.9e+08	2640.16	284.61	125.77	222.54	222.54
[55, 60]	334.9	0.060	1.9e+08	2910.50	229.00	61.97	205.19	205.19
[60, 65]	170.6	0.061	1.9e+08	1467.85	187.16	43.83	111.19	111.19
[65, 70]	131.3	0.063	1.9e+08	1100.82	134.84	12.90	71.98	71.98
[70, 75]	113.4	0.063	1.9e+08	949.85	115.55	18.50	61.74	61.74
[75, 80]	74.1	0.063	1.9e+08	616.65	93.46	23.48	41.03	41.03
[80, 93]	125.2	0.064	4.96e+08	392.50	42.93	9.50	25.78	25.78

Table A.25: Arm-averaged  $J/\psi$  Invariant Yields vs. Centrality

10% Centrality bins					
Cent.	$B dN/dy \times 10^8$	$\pm$ stat.	$\pm$ type A	+ type B	- type B
[0, 10]	11739.01	2068.35	956.96	2157.43	996.59
[10, 20]	10731.88	1155.12	643.11	1458.19	1101.82
[20, 30]	8297.02	699.62	256.57	747.57	677.83
[30, 40]	6064.42	394.54	162.06	506.57	504.24
[40, 50]	4527.31	246.54	127.65	372.39	372.39
[50, 60]	2971.89	149.46	47.17	222.35	222.35
[60, 70]	1496.07	91.14	29.09	112.96	112.96
[70, 80]	875.07	59.89	9.01	65.69	65.69
[80, 93]	370.42	31.12	4.96	27.79	27.79
5% Centrality bins					
Cent.	$B dN/dy \times 10^8$	$\pm$ stat.	$\pm$ type A	+ type B	- type B
[0, 5]	14496.97	3095.29	1138.02	2745.16	1397.18
[5, 10]	10496.74	2771.39	139.62	1318.77	930.80
[10, 15]	10681.86	1873.58	771.65	1158.31	1084.86
[15, 20]	10192.18	1373.35	527.41	1202.36	1199.59
[20, 25]	7780.16	1081.26	319.40	700.05	700.05
[25, 30]	8524.07	805.06	314.18	696.31	696.31
[30, 35]	6575.96	612.57	304.22	522.04	522.04
[35, 40]	5797.40	486.75	154.29	552.05	552.05
[40, 45]	5387.77	391.70	158.50	417.77	417.77
[45, 50]	3707.18	302.93	75.87	324.05	324.05
[50, 55]	2930.49	224.80	77.25	224.53	224.53
[55, 60]	3026.70	183.80	39.74	228.17	228.17
[60, 65]	1738.57	146.22	27.82	130.05	130.05
[65, 70]	1232.68	110.23	8.89	94.50	94.50
[70, 75]	1011.93	91.53	11.62	77.31	77.31
[75, 80]	720.91	74.01	14.88	54.00	54.00
[80, 93]	373.91	31.47	5.01	28.05	28.05

Table A.26: South Arm ( $-2.2 < y < -1.2$ )  $J/\psi$  Invariant Yields vs.  $p_T$  in four bins of centrality.

Cent.	$p_T$	$N^{J/\psi}$	$A\epsilon$	$N^{MB}$	Inv Yield $\times 10^9$	stat.	type A	+B	-B
[0, 20]	[0, 1]	1031.5	0.038	7.87e+08	11118.76	1696.16	1720.87	1148.43	1148.43
[0, 20]	[1, 2]	1315.2	0.034	7.87e+08	5213.09	734.71	653.51	419.69	419.69
[0, 20]	[2, 3]	663.5	0.031	7.87e+08	1732.63	336.44	194.08	202.72	202.72
[0, 20]	[3, 4]	202.1	0.036	7.87e+08	325.50	117.98	50.02	25.53	25.53
[0, 20]	[4, 5]	202.4	0.046	7.87e+08	198.08	46.79	33.54	15.58	15.58
[20, 40]	[0, 1]	714.7	0.050	7.87e+08	5805.29	790.72	526.70	748.60	748.60
[20, 40]	[1, 2]	1192.4	0.047	7.87e+08	3442.53	314.72	146.24	315.25	315.25
[20, 40]	[2, 3]	711.7	0.042	7.87e+08	1363.61	144.57	48.52	105.20	105.20
[20, 40]	[3, 4]	262.1	0.050	7.87e+08	302.85	46.98	15.33	26.85	26.85
[20, 40]	[4, 5]	86.2	0.057	7.87e+08	68.56	16.80	5.05	12.25	12.25
[40, 60]	[0, 1]	492.8	0.057	7.87e+08	3467.31	318.62	119.63	275.50	275.50
[40, 60]	[1, 2]	639.6	0.053	7.87e+08	1613.35	133.35	65.42	127.10	127.10
[40, 60]	[2, 3]	300.9	0.049	7.87e+08	498.64	56.98	15.12	38.91	38.91
[40, 60]	[3, 4]	127.6	0.056	7.87e+08	130.56	22.42	3.78	11.15	11.15
[40, 60]	[4, 5]	60.4	0.066	7.87e+08	40.99	7.82	0.79	4.29	4.29
[60, 100]	[0, 1]	251.1	0.061	1.3e+09	1001.35	86.08	18.83	77.31	77.31
[60, 100]	[1, 2]	244.6	0.056	1.3e+09	354.99	32.89	14.65	27.37	27.37
[60, 100]	[2, 3]	117.5	0.052	1.3e+09	111.67	14.53	2.14	8.79	8.79
[60, 100]	[3, 4]	36.3	0.059	1.3e+09	21.54	5.30	0.62	1.86	1.86
[60, 100]	[4, 5]	21.8	0.065	1.3e+09	9.09	2.26	0.05	0.75	0.75

Table A.27: North Arm ( $1.2 < y < 2.2$ )  $J/\psi$  Invariant Yields vs.  $p_T$  in four bins of centrality.

Cent.	$p_T$	$N^{J/\psi}$	$A\epsilon$	$N^{MB}$	Inv Yield $\times 10^9$	stat.	type A	+B	-B
[0, 20]	[0, 1]	377.7	0.024	7.62e+08	6670.63	2436.34	1880.57	918.45	918.45
[0, 20]	[1, 2]	398.0	0.021	7.62e+08	2618.91	1394.20	787.68	191.98	191.98
[0, 20]	[2, 3]	128.0	0.019	7.62e+08	548.28	539.50	277.06	157.95	157.95
[0, 20]	[3, 4]	33.4	0.022	7.62e+08	89.84	357.37	78.54	22.53	22.53
[0, 20]	[4, 5]	143.4	0.025	7.62e+08	262.85	100.89	137.81	54.65	54.65
[20, 40]	[0, 1]	528.8	0.048	7.62e+08	4573.86	741.26	310.45	523.50	523.50
[20, 40]	[1, 2]	673.8	0.042	7.62e+08	2215.17	306.42	168.82	182.87	182.87
[20, 40]	[2, 3]	434.1	0.039	7.62e+08	924.29	134.35	39.19	71.83	71.83
[20, 40]	[3, 4]	182.3	0.044	7.62e+08	245.19	49.48	22.46	17.96	17.96
[20, 40]	[4, 5]	102.5	0.055	7.62e+08	87.16	23.42	9.23	7.64	7.64
[40, 60]	[0, 1]	450.1	0.063	7.62e+08	2989.21	284.49	106.34	221.51	221.51
[40, 60]	[1, 2]	566.1	0.056	7.62e+08	1400.42	114.89	53.06	104.89	104.89
[40, 60]	[2, 3]	288.3	0.052	7.62e+08	465.28	50.22	19.25	33.45	33.45
[40, 60]	[3, 4]	124.7	0.060	7.62e+08	124.86	16.03	2.85	9.11	9.11
[40, 60]	[4, 5]	55.8	0.070	7.62e+08	36.98	6.31	0.36	3.29	3.29
[60, 100]	[0, 1]	232.9	0.070	1.26e+09	840.32	74.83	11.52	60.83	60.83
[60, 100]	[1, 2]	243.4	0.062	1.26e+09	330.64	28.66	6.27	23.99	23.99
[60, 100]	[2, 3]	90.2	0.057	1.26e+09	79.74	11.65	2.51	5.71	5.71
[60, 100]	[3, 4]	41.3	0.066	1.26e+09	22.61	4.74	0.66	1.64	1.64
[60, 100]	[4, 5]	21.0	0.078	1.26e+09	7.55	1.77	0.02	1.12	1.12

Table A.28: Arm-averaged ( $1.2 < |y| < 2.2$ )  $J/\psi$  Invariant Yields vs.  $p_T$  in four bins of centrality.

Cent.	$p_T$	$N^{J/\psi}$	$A\epsilon$	$N^{MB}$	Inv Yield $\times 10^9$	stat.	type A	+B	-B
[0, 20]	[0, 1]	-	-	-	9361.16	1406.89	743.08	1013.00	1013.00
[0, 20]	[1, 2]	-	-	-	4457.86	660.30	229.31	398.24	398.24
[0, 20]	[2, 3]	-	-	-	1372.29	285.89	84.30	170.52	170.52
[0, 20]	[3, 4]	-	-	-	299.24	112.14	8.75	27.47	27.47
[0, 20]	[4, 5]	-	-	-	204.89	43.19	14.49	18.18	18.18
[20, 40]	[0, 1]	-	-	-	5075.71	544.71	183.93	665.31	665.31
[20, 40]	[1, 2]	-	-	-	2775.11	219.95	91.81	263.85	263.85
[20, 40]	[2, 3]	-	-	-	1110.54	98.72	22.57	89.84	89.84
[20, 40]	[3, 4]	-	-	-	275.75	34.07	10.56	25.48	25.48
[20, 40]	[4, 5]	-	-	-	74.72	13.65	3.06	13.51	13.51
[40, 60]	[0, 1]	-	-	-	3191.88	212.38	61.26	264.43	264.43
[40, 60]	[1, 2]	-	-	-	1486.76	87.12	31.54	122.17	122.17
[40, 60]	[2, 3]	-	-	-	480.10	37.68	10.70	39.12	39.12
[40, 60]	[3, 4]	-	-	-	126.84	13.04	1.86	11.26	11.26
[40, 60]	[4, 5]	-	-	-	38.55	4.91	0.22	4.14	4.14
[60, 100]	[0, 1]	-	-	-	905.29	56.56	6.87	73.03	73.03
[60, 100]	[1, 2]	-	-	-	340.35	21.65	3.77	27.43	27.43
[60, 100]	[2, 3]	-	-	-	91.88	9.09	1.56	7.55	7.55
[60, 100]	[3, 4]	-	-	-	22.13	3.53	0.36	1.98	1.98
[60, 100]	[4, 5]	-	-	-	8.13	1.39	0.01	0.70	0.70

#### A.4 $R_{AA}$ Tables

Table A.29: Arm-averaged  $J/\psi$   $R_{AA}$  vs. Centrality. Statistical errors are folded into Type A uncertainties.

10% Centrality bins				
Cent.	$R_{AA}$	$\pm$ type A	+ type B	- type B
[0, 10]	0.19	0.04	0.02	0.04
[10, 20]	0.27	0.03	0.04	0.04
[20, 30]	0.34	0.03	0.04	0.04
[30, 40]	0.41	0.03	0.05	0.05
[40, 50]	0.56	0.03	0.08	0.08
[50, 60]	0.71	0.04	0.12	0.12
[60, 70]	0.77	0.05	0.15	0.15
[70, 80]	1.07	0.07	0.25	0.25
[80, 93]	1.35	0.11	0.26	0.26

5% Centrality Bins				
Cent.	$R_{AA}$	$\pm$ type A	+ type B	- type B
[0, 5]	0.21	0.05	0.03	0.04
[5, 10]	0.19	0.05	0.02	0.03
[10, 15]	0.24	0.05	0.03	0.03
[15, 20]	0.29	0.04	0.04	0.04
[20, 25]	0.28	0.04	0.04	0.04
[25, 30]	0.39	0.04	0.05	0.05
[30, 35]	0.39	0.04	0.05	0.05
[35, 40]	0.46	0.04	0.07	0.07
[40, 45]	0.56	0.03	0.08	0.08
[45, 50]	0.71	0.04	0.12	0.12
[50, 55]	0.77	0.05	0.15	0.15
[55, 60]	1.07	0.07	0.25	0.25
[60, 65]	1.35	0.11	0.26	0.26

Table A.30: Arm-averaged  $J/\psi$   $R_{\text{AA}}$  vs.  $p_{\text{T}}$  in four bins of centrality. Statistical errors are folded into Type A uncertainties.

		$p_{\text{T}}$ bins			
Cent.	$p_{\text{T}}$	$R_{\text{AA}}$	$\pm$ type A	+B	-B
[0, 20]	[0, 1]	0.19	0.03	0.02	0.02
	[1, 2]	0.20	0.03	0.02	0.02
	[2, 3]	0.22	0.05	0.03	0.03
	[3, 4]	0.19	0.07	0.02	0.02
	[4, 5]	0.57	0.14	0.06	0.06
[20, 40]	[0, 1]	0.27	0.03	0.04	0.04
	[1, 2]	0.32	0.03	0.04	0.04
	[2, 3]	0.47	0.05	0.05	0.05
	[3, 4]	0.46	0.06	0.05	0.05
	[4, 5]	0.55	0.11	0.10	0.10
[40, 60]	[0, 1]	0.55	0.04	0.06	0.06
	[1, 2]	0.55	0.04	0.06	0.06
	[2, 3]	0.65	0.06	0.07	0.07
	[3, 4]	0.67	0.08	0.07	0.07
	[4, 5]	0.90	0.14	0.11	0.11
[60, 93]	[0, 1]	1.02	0.07	0.10	0.10
	[1, 2]	0.81	0.06	0.08	0.08
	[2, 3]	0.81	0.09	0.08	0.08
	[3, 4]	0.76	0.13	0.08	0.08
	[4, 5]	1.23	0.24	0.13	0.13

## Appendix B

### Mass Plots

Figure B.1: Dimuon spectra after mixed (left) and like-sign (right) background subtraction. Fits are over the mass ranges [2.2,6.0], [1.8,7.0], and [0.5,8.0] both with and without low-mass Gaussians.

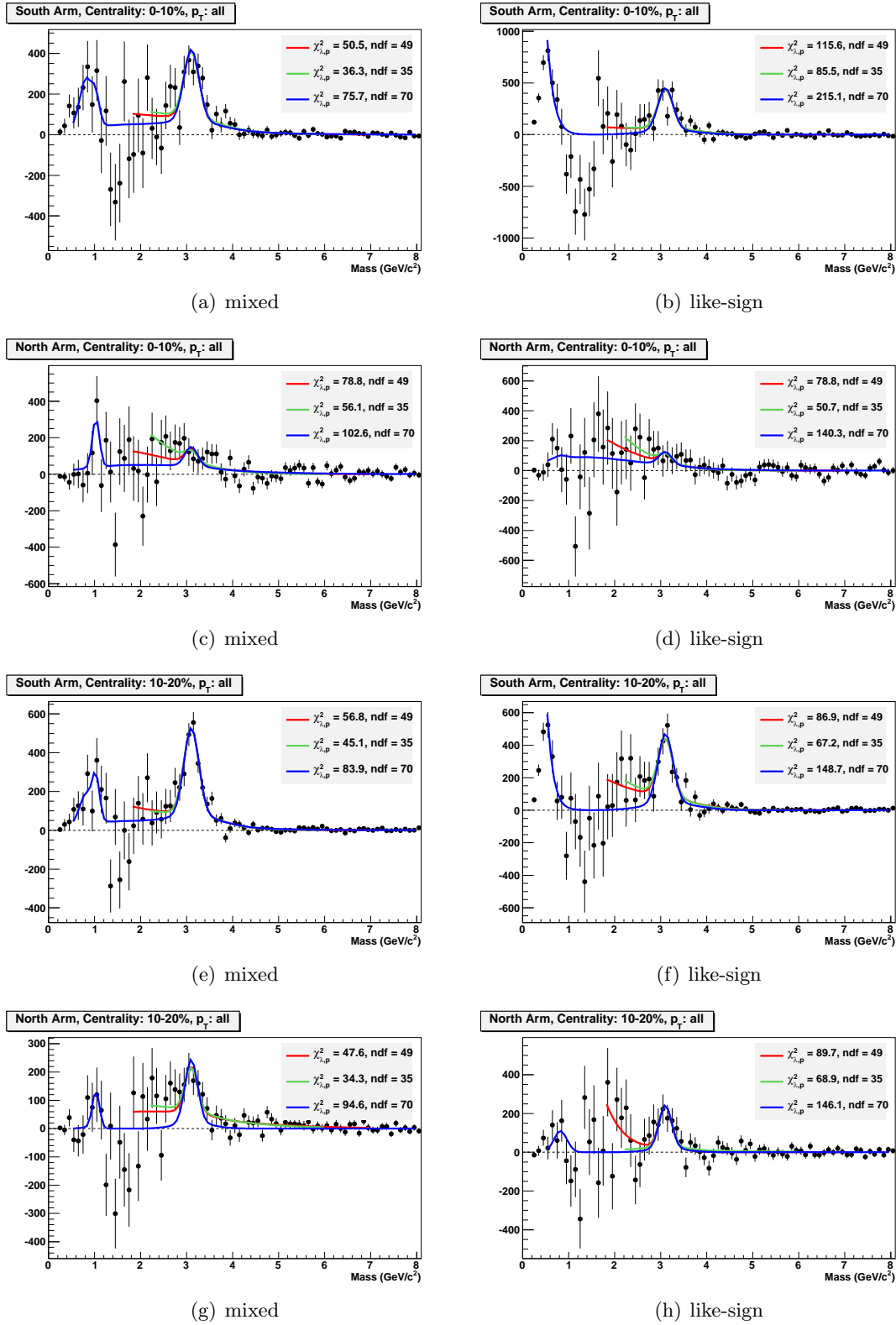


Figure B.2: Dimuon spectra after mixed (left) and like-sign (right) background subtraction. Fits are over the mass ranges [2.2,6.0], [1.8,7.0], and [0.5,8.0] both with and without low-mass Gaussians.

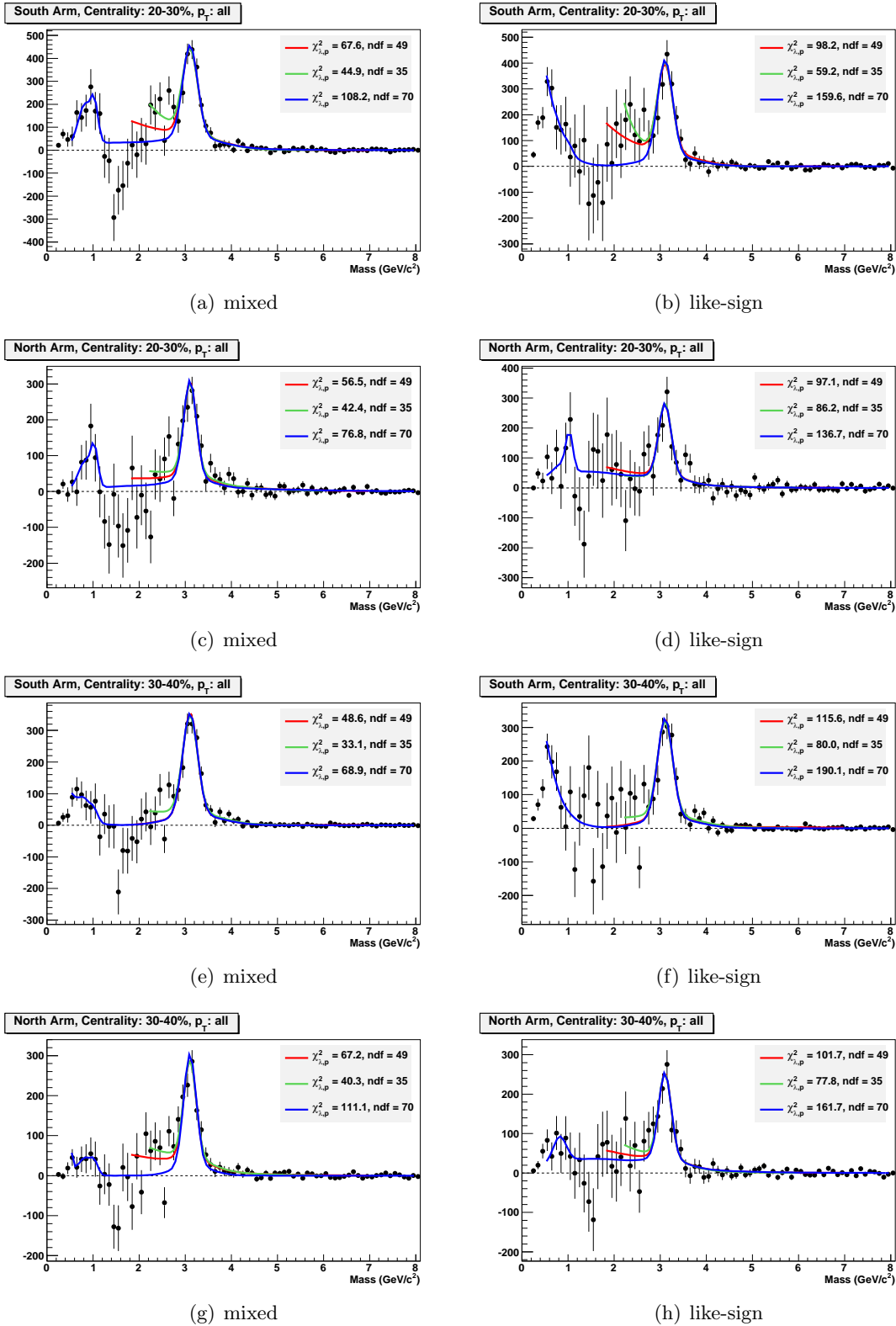


Figure B.3: Dimuon spectra after mixed (left) and like-sign (right) background subtraction. Fits are over the mass ranges [2.2,6.0], [1.8,7.0], and [0.5,8.0] both with and without low-mass Gaussians.

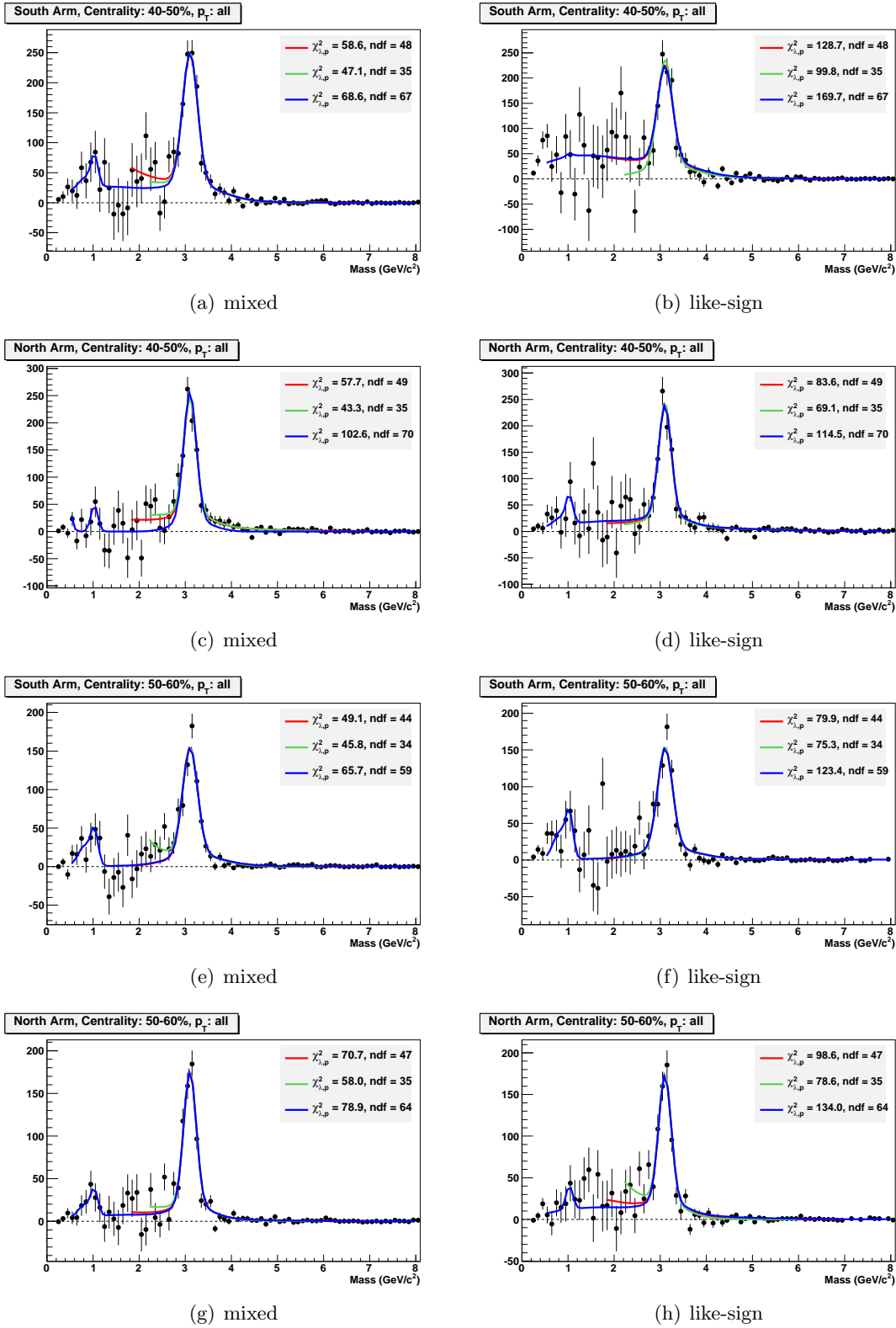


Figure B.4: Dimuon spectra after mixed (left) and like-sign (right) background subtraction. Fits are over the mass ranges [2.2,6.0], [1.8,7.0], and [0.5,8.0] both with and without low-mass Gaussians.

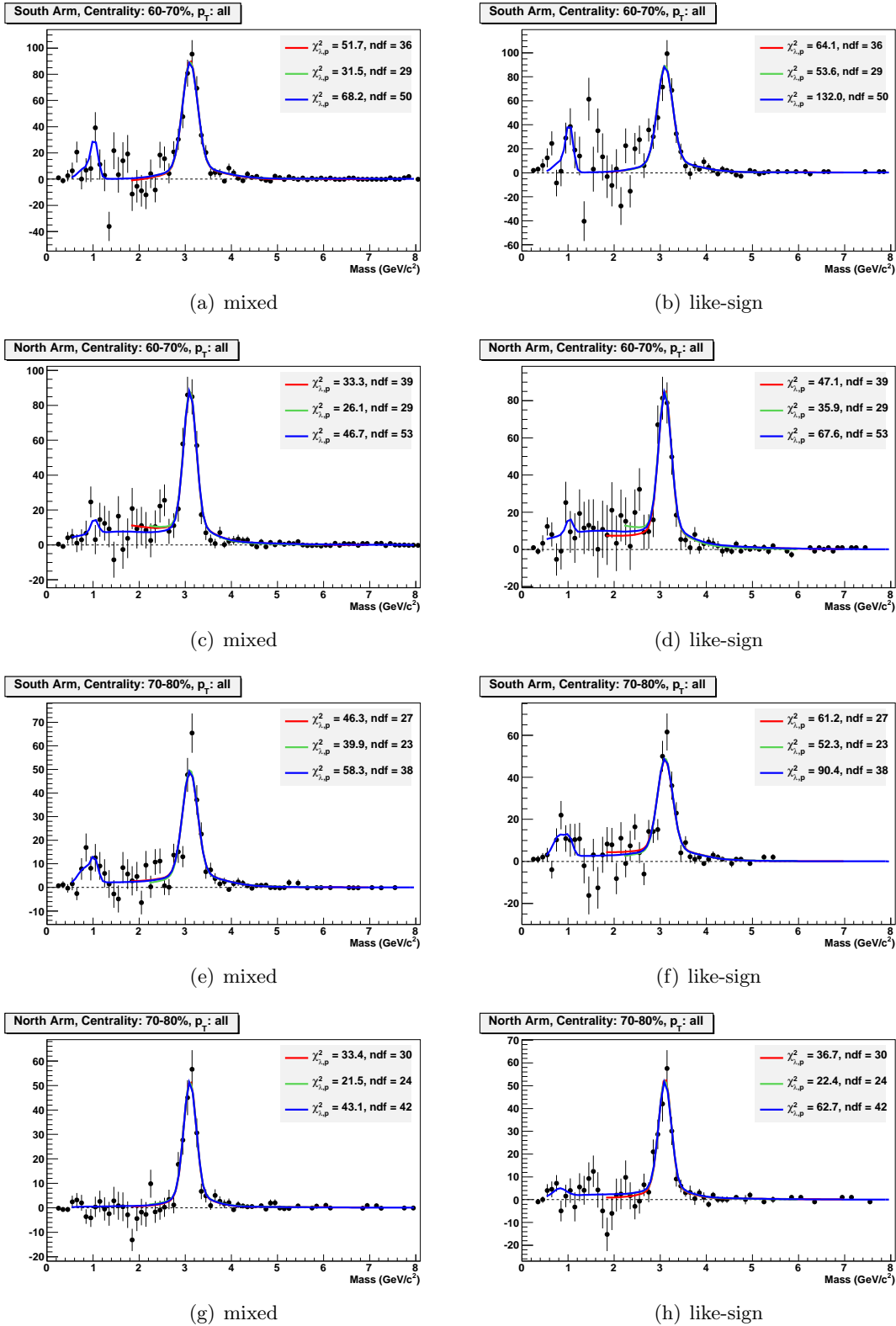


Figure B.5: Dimuon spectra after mixed (left) and like-sign (right) background subtraction. Fits are over the mass ranges [2.2,6.0], [1.8,7.0], and [0.5,8.0] both with and without low-mass Gaussians.

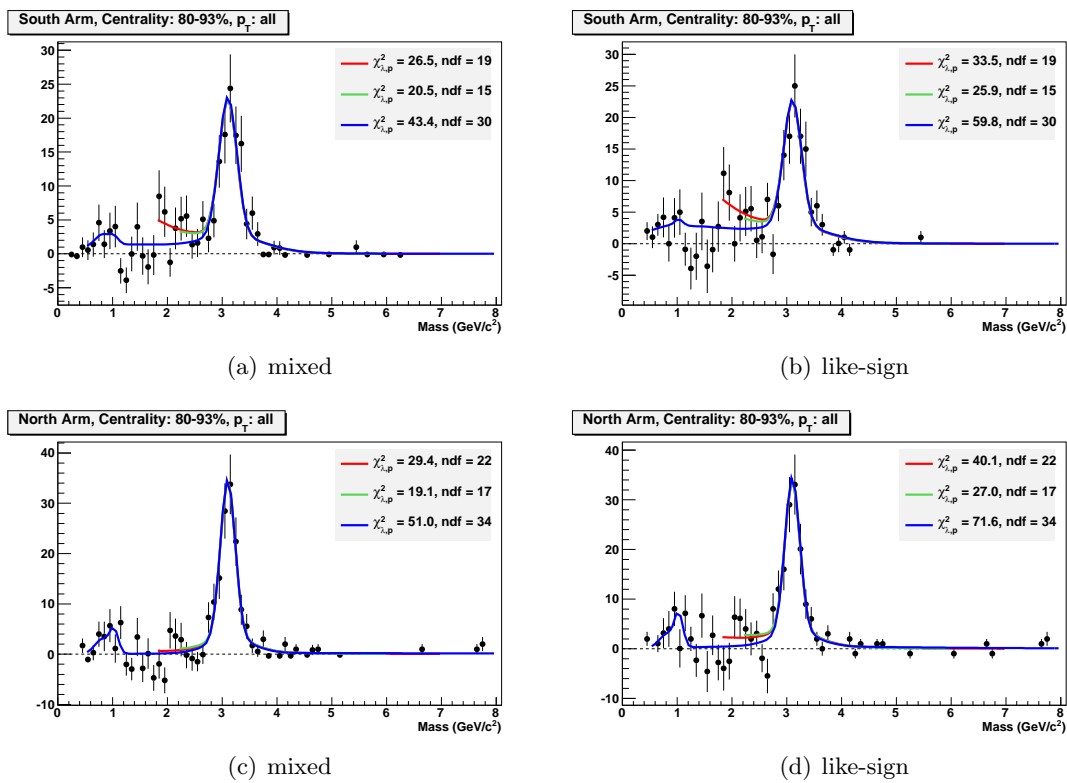


Figure B.6: Dimuon spectra after mixed (left) and like-sign (right) background subtraction. Fits are over the mass ranges [2.2,6.0], [1.8,7.0], and [0.5,8.0] both with and without low-mass Gaussians.

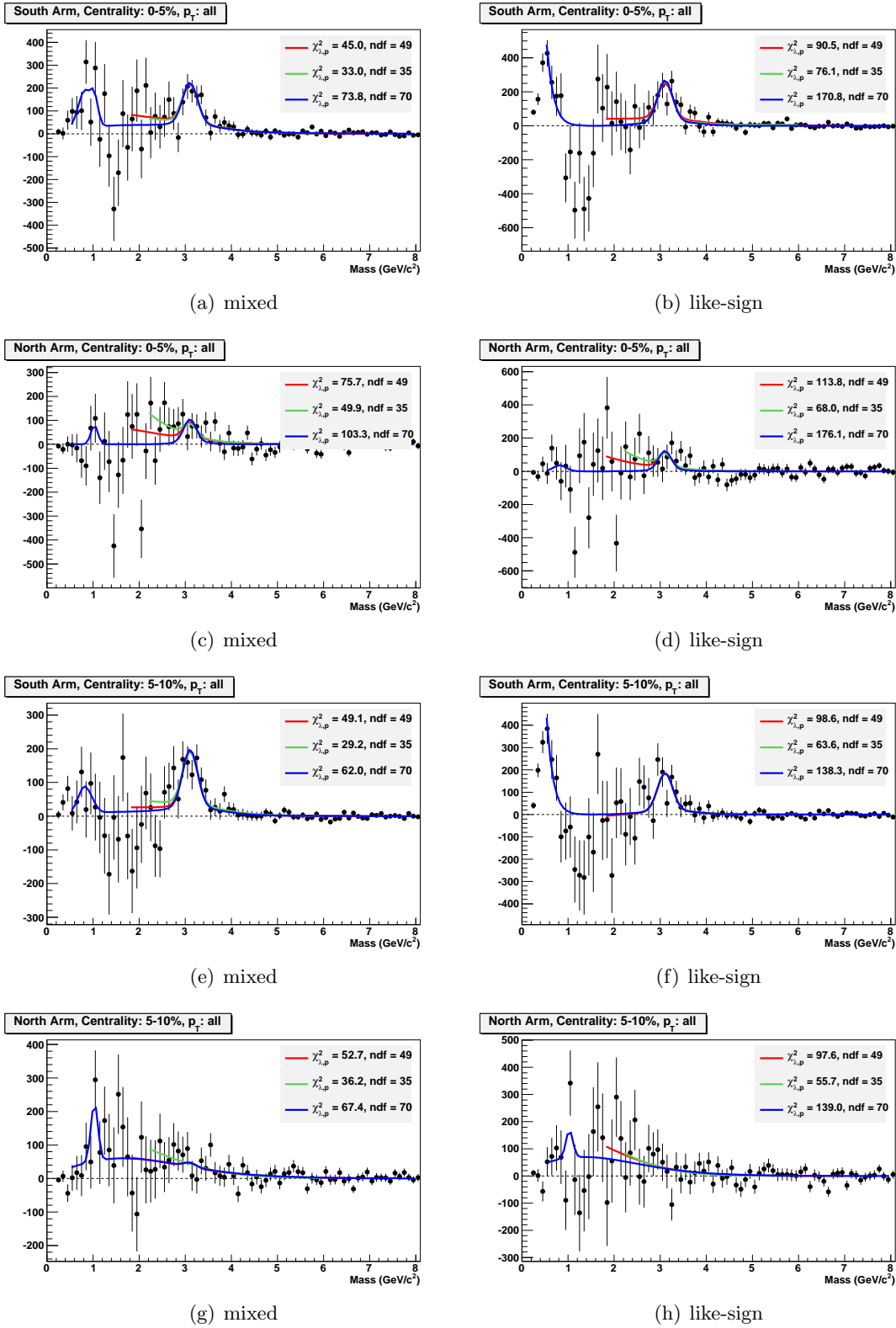


Figure B.7: Dimuon spectra after mixed (left) and like-sign (right) background subtraction. Fits are over the mass ranges [2.2,6.0], [1.8,7.0], and [0.5,8.0] both with and without low-mass Gaussians.

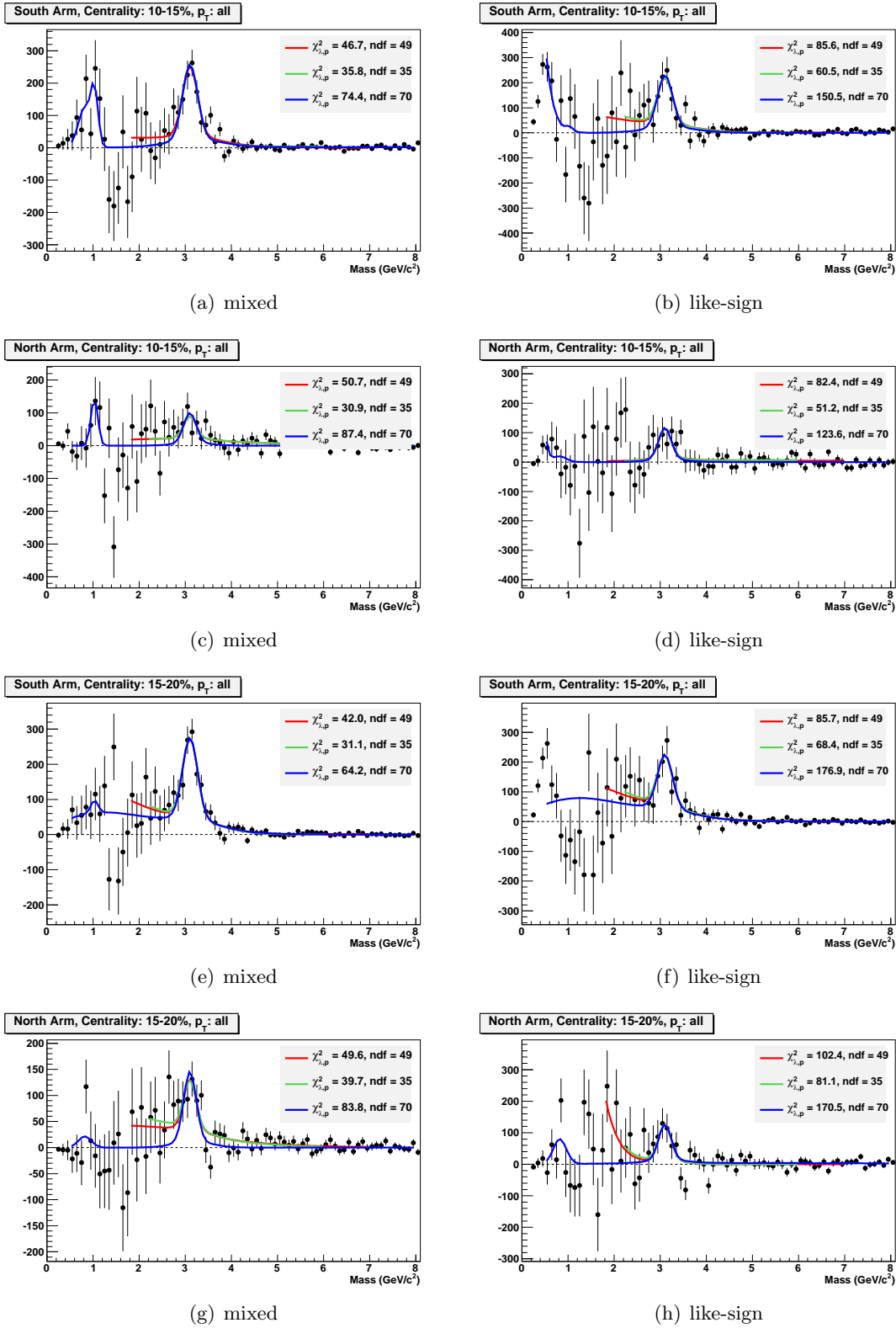


Figure B.8: Dimuon spectra after mixed (left) and like-sign (right) background subtraction. Fits are over the mass ranges [2.2,6.0], [1.8,7.0], and [0.5,8.0] both with and without low-mass Gaussians.

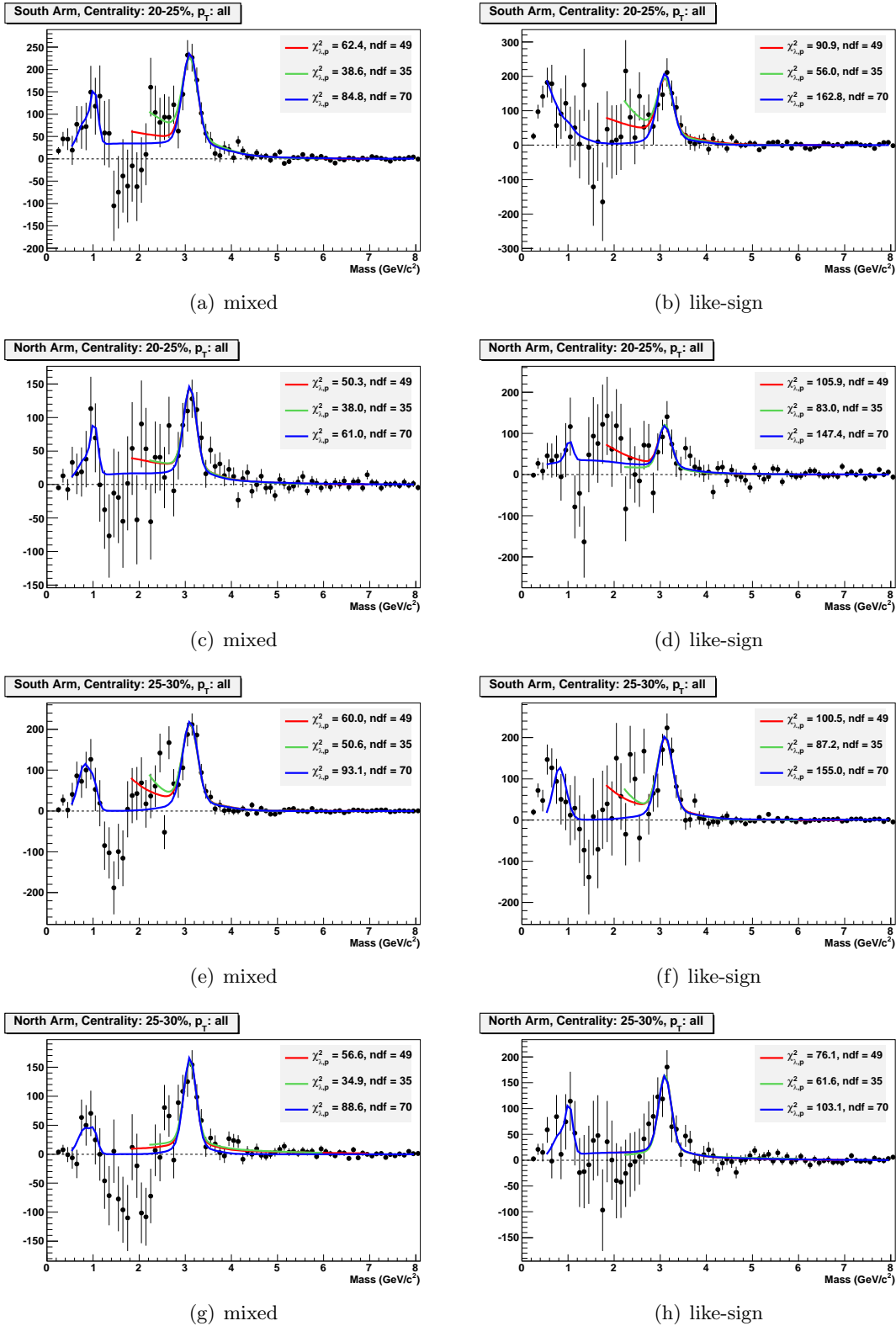


Figure B.9: Dimuon spectra after mixed (left) and like-sign (right) background subtraction. Fits are over the mass ranges [2.2,6.0], [1.8,7.0], and [0.5,8.0] both with and without low-mass Gaussians.

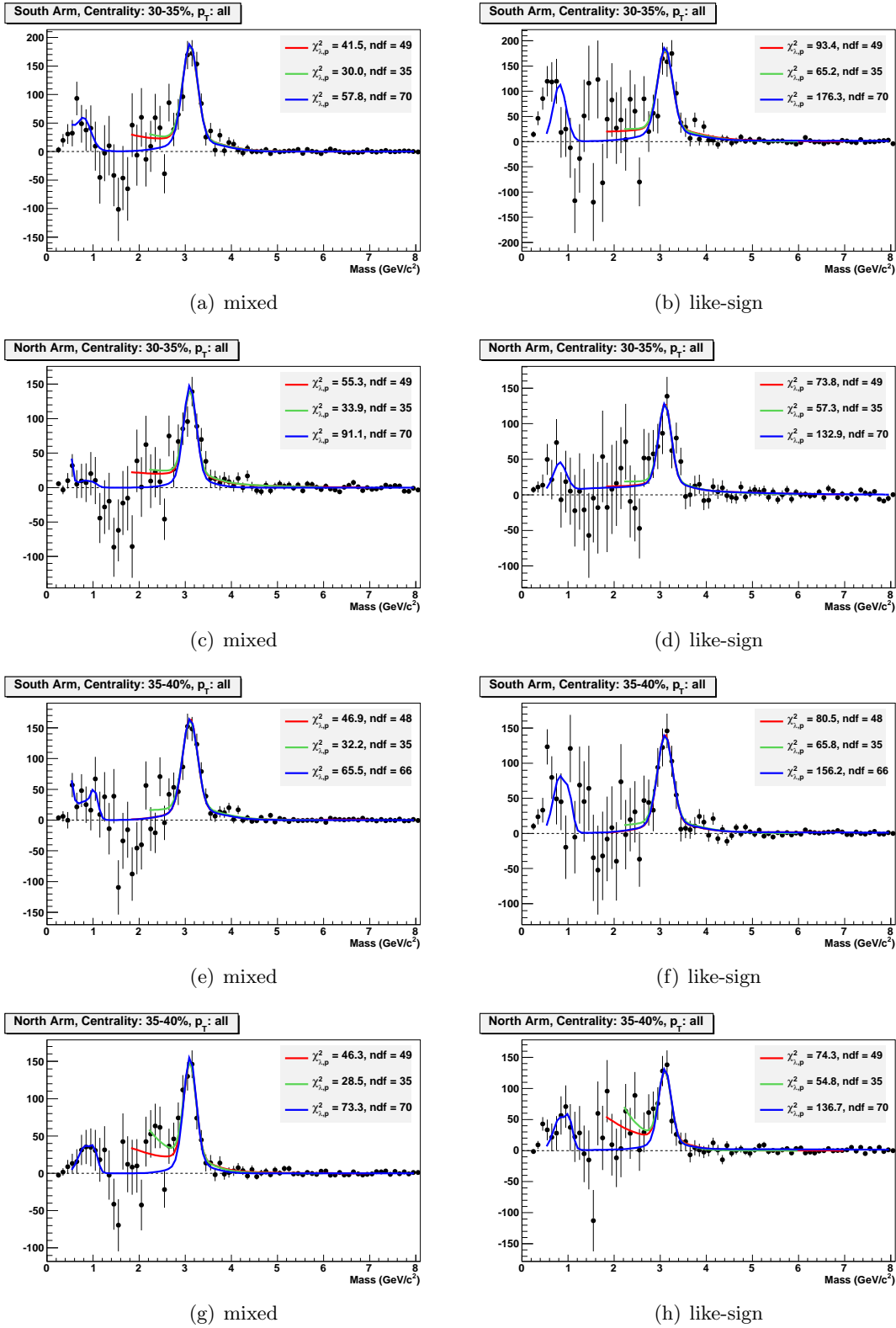


Figure B.10: Dimuon spectra after mixed (left) and like-sign (right) background subtraction. Fits are over the mass ranges [2.2,6.0], [1.8,7.0], and [0.5,8.0] both with and without low-mass Gaussians.

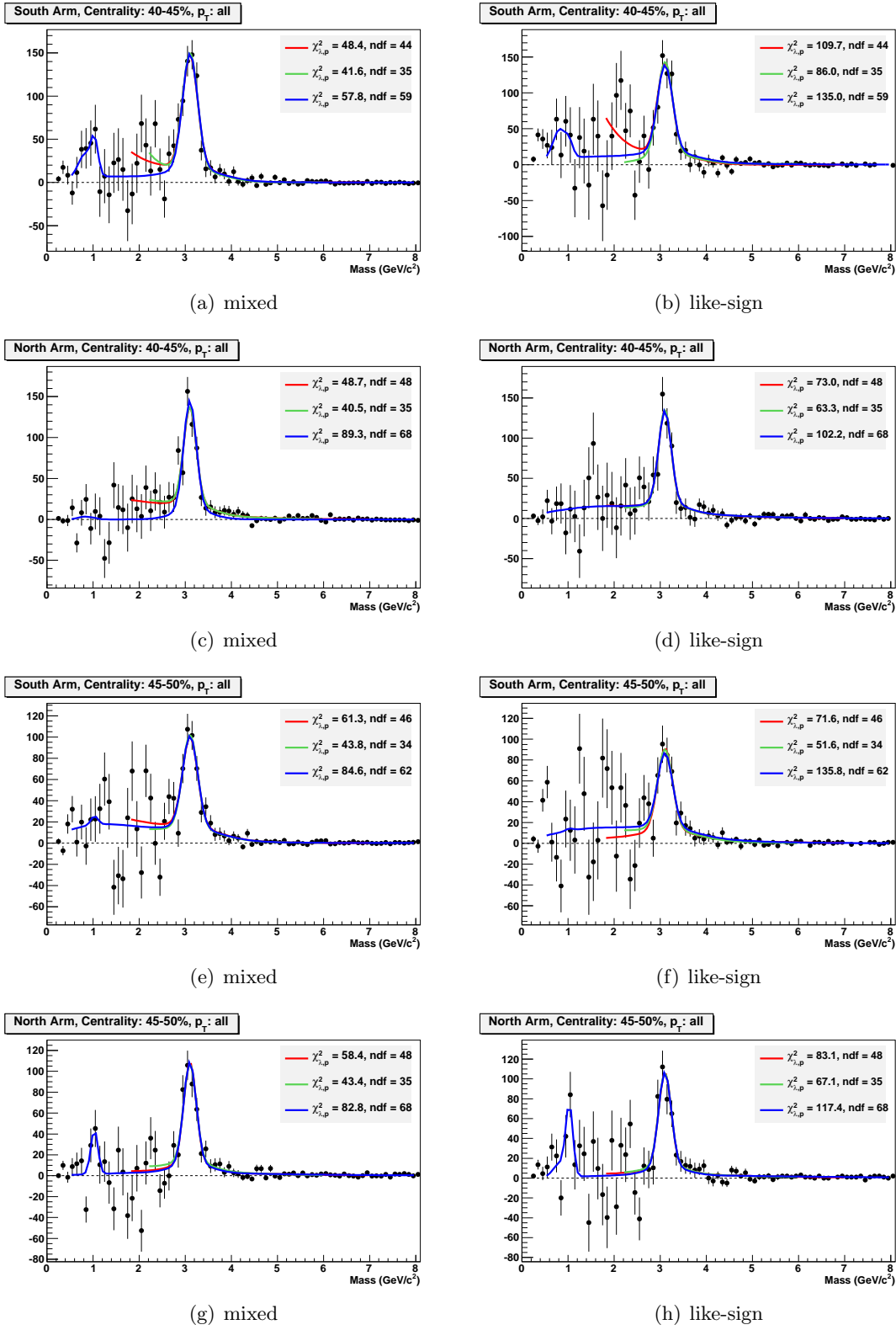


Figure B.11: Dimuon spectra after mixed (left) and like-sign (right) background subtraction. Fits are over the mass ranges [2.2,6.0], [1.8,7.0], and [0.5,8.0] both with and without low-mass Gaussians.

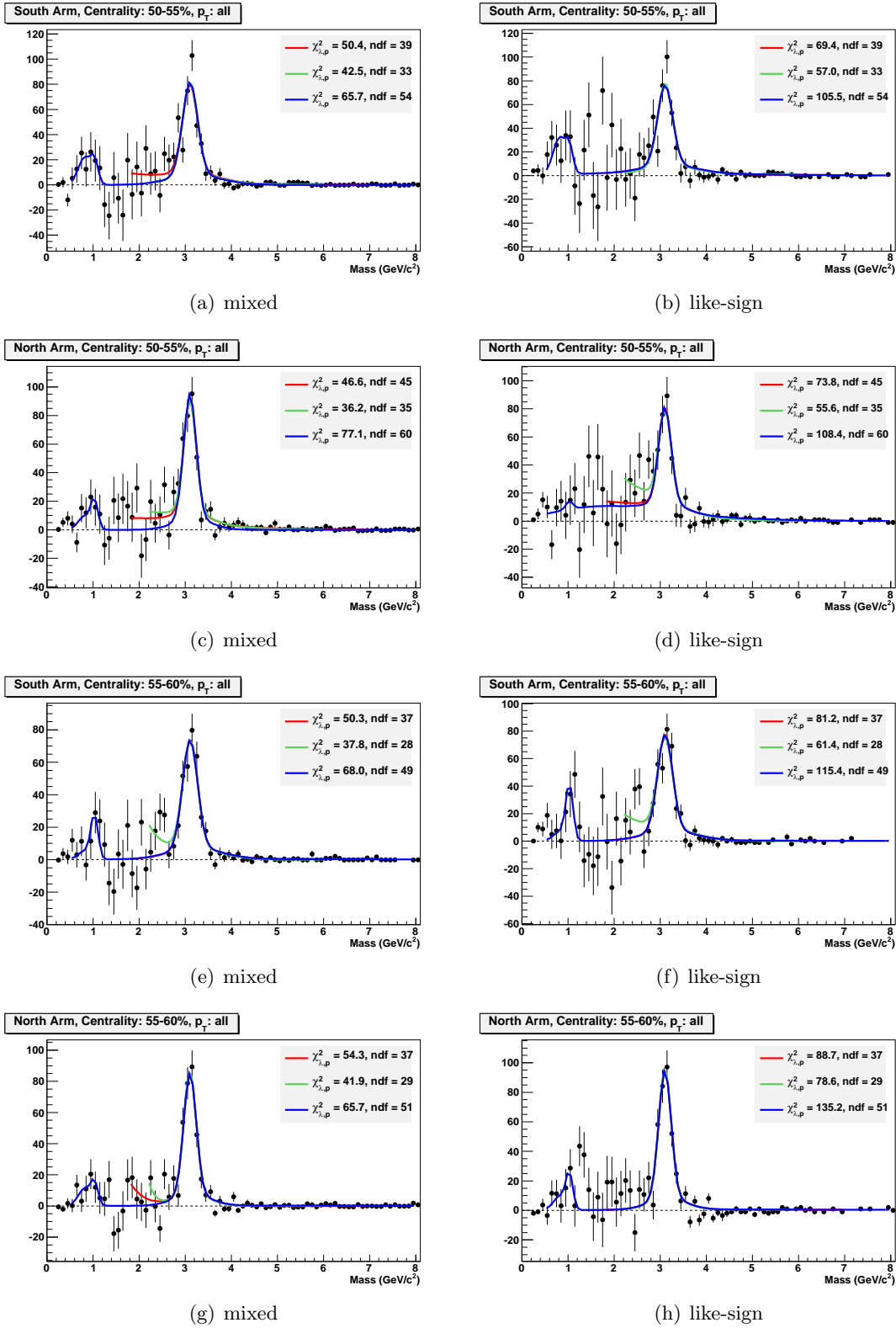


Figure B.12: Dimuon spectra after mixed (left) and like-sign (right) background subtraction. Fits are over the mass ranges [2.2,6.0], [1.8,7.0], and [0.5,8.0] both with and without low-mass Gaussians.

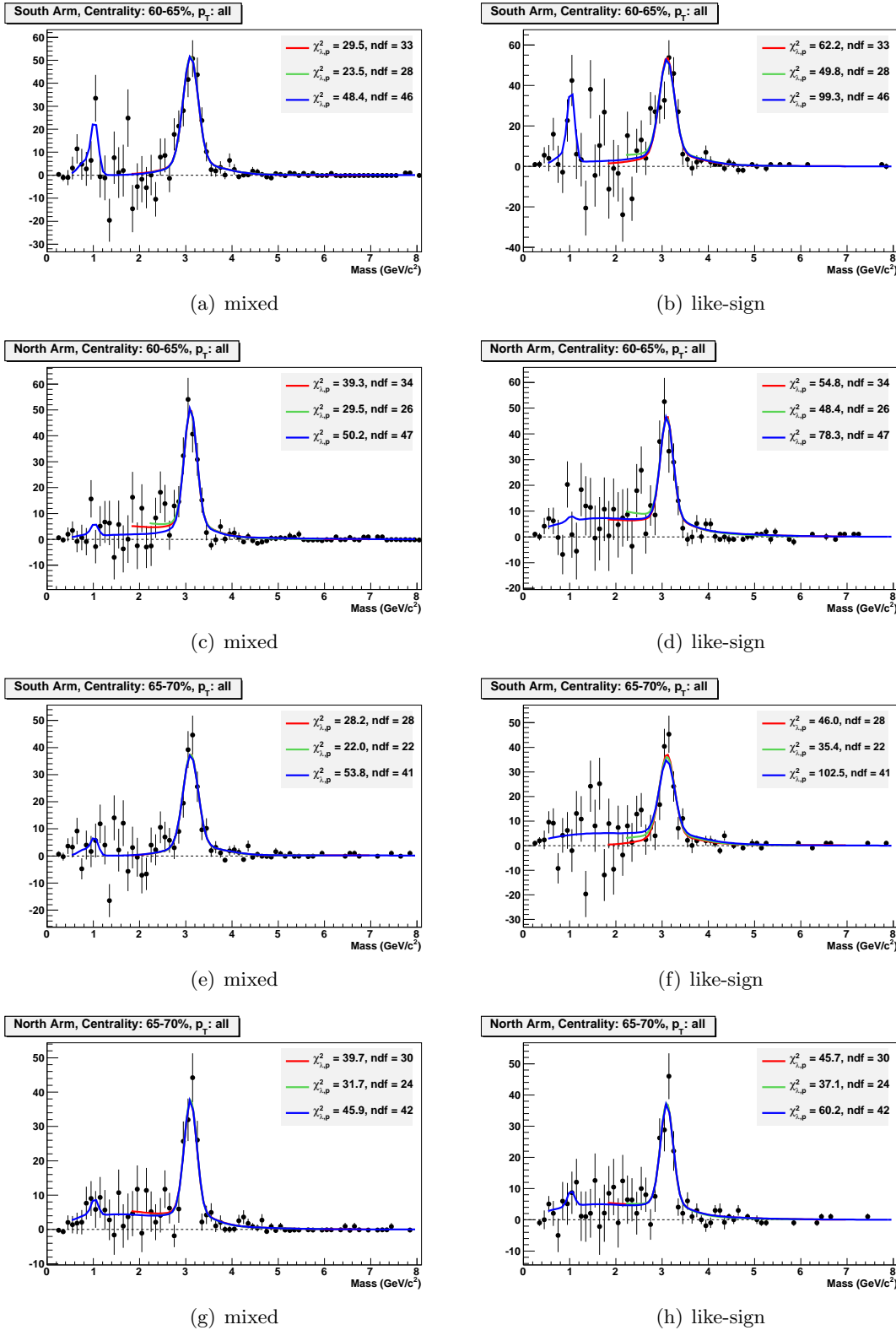


Figure B.13: Dimuon spectra after mixed (left) and like-sign (right) background subtraction. Fits are over the mass ranges [2.2,6.0], [1.8,7.0], and [0.5,8.0] both with and without low-mass Gaussians.

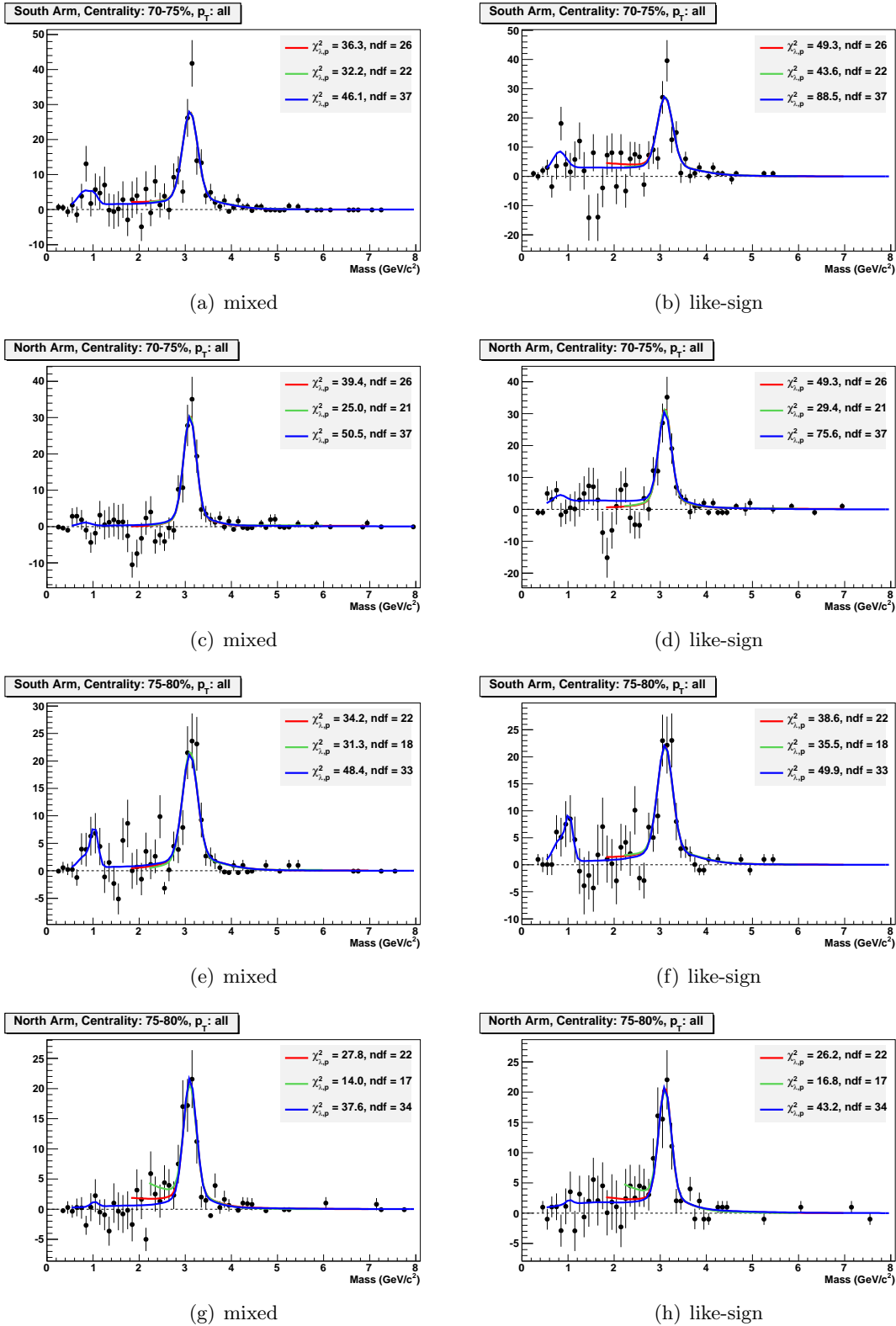


Figure B.14: Dimuon spectra after mixed (left) and like-sign (right) background subtraction. Fits are over the mass ranges [2.2,6.0], [1.8,7.0], and [0.5,8.0] both with and without low-mass Gaussians.

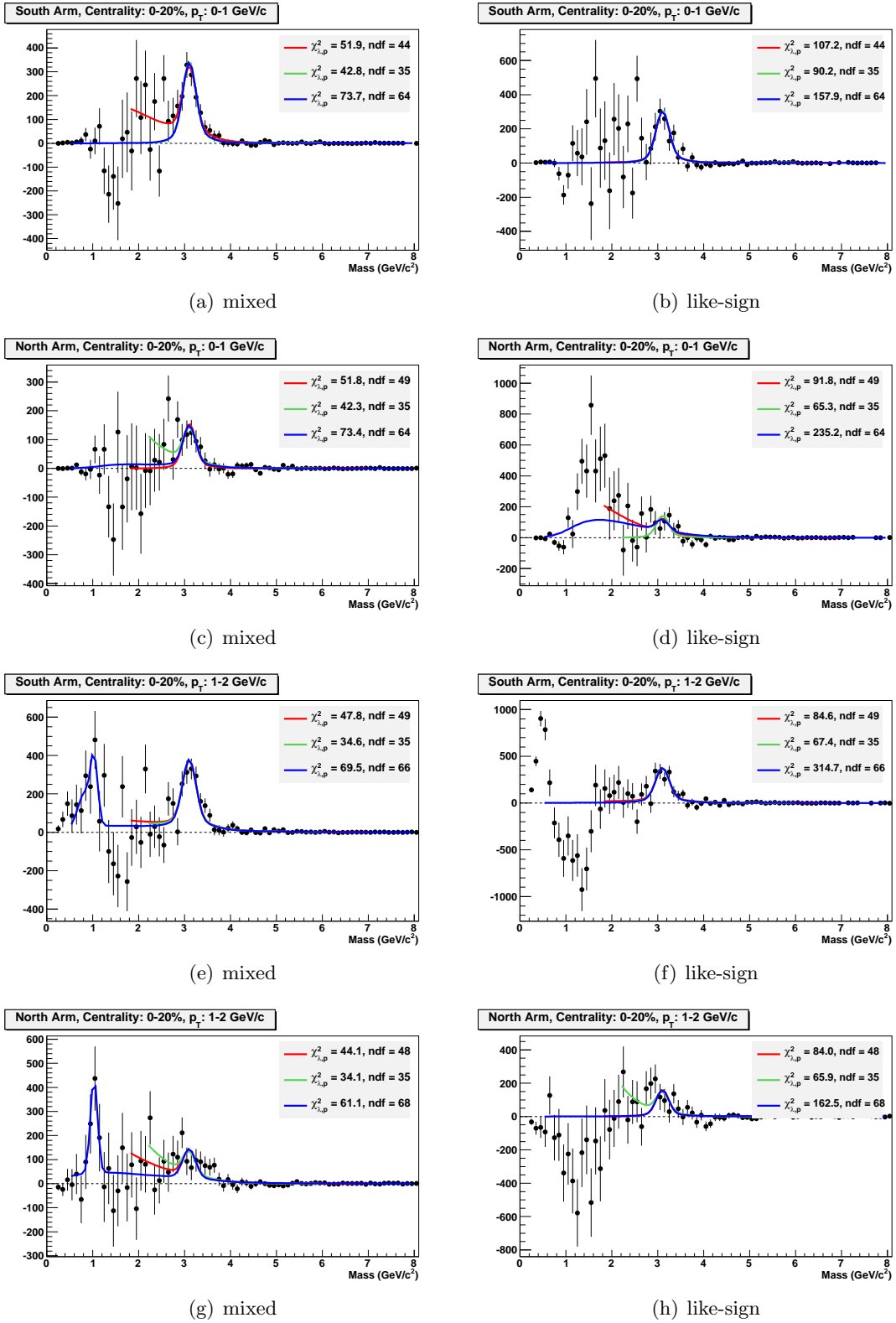


Figure B.15: Dimuon spectra after mixed (left) and like-sign (right) background subtraction. Fits are over the mass ranges [2.2,6.0], [1.8,7.0], and [0.5,8.0] both with and without low-mass Gaussians.

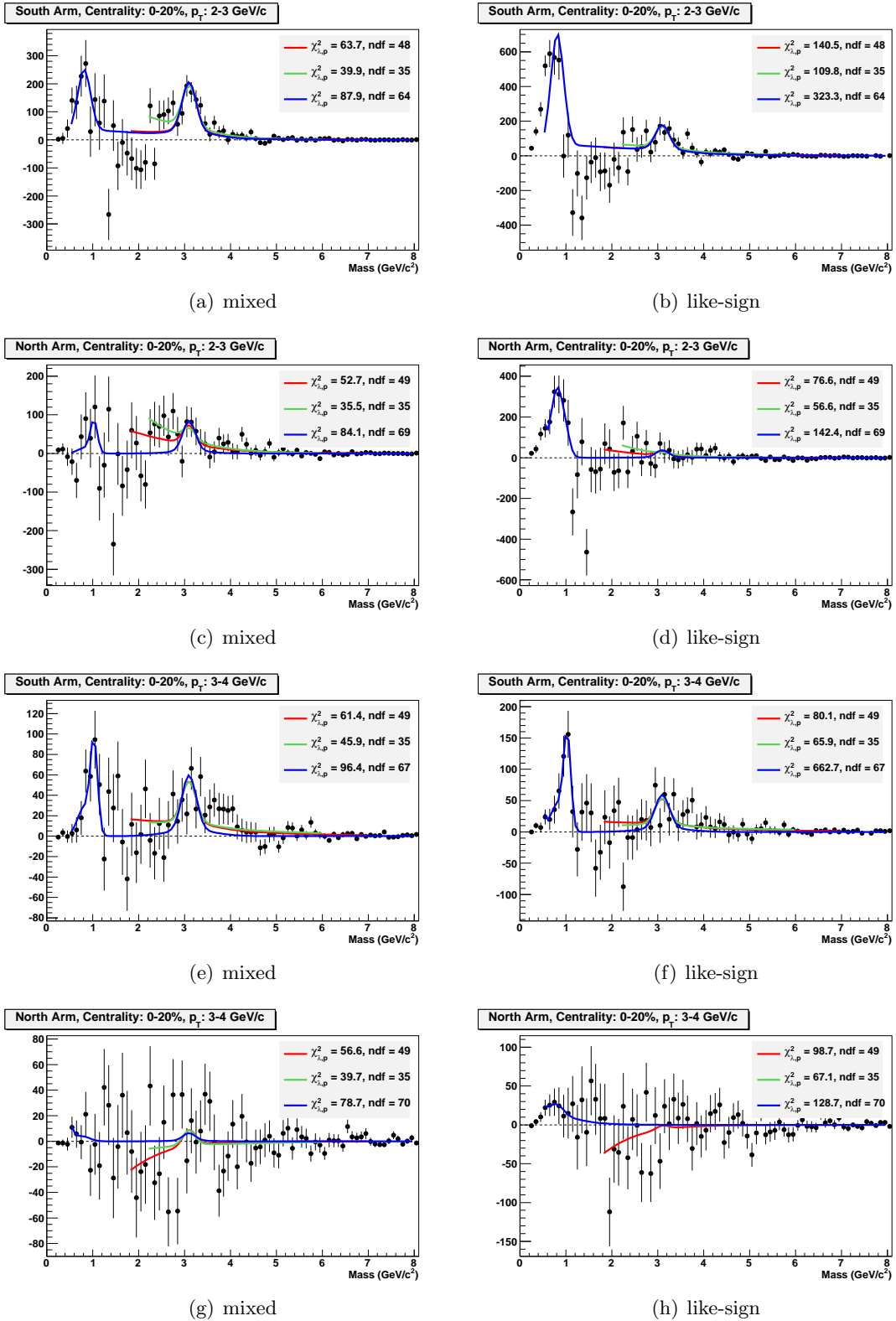


Figure B.16: Dimuon spectra after mixed (left) and like-sign (right) background subtraction. Fits are over the mass ranges [2.2,6.0], [1.8,7.0], and [0.5,8.0] both with and without low-mass Gaussians.

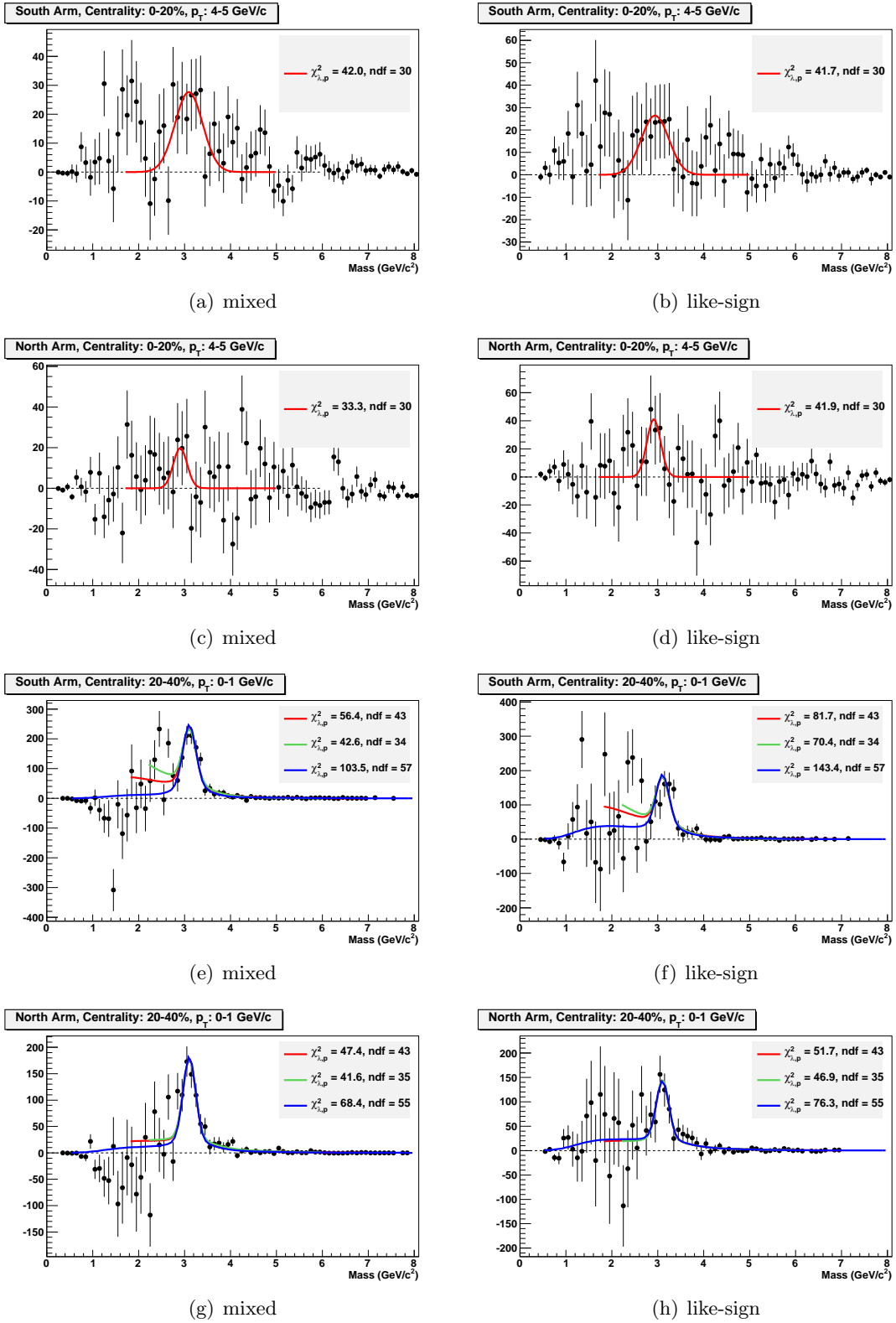


Figure B.17: Dimuon spectra after mixed (left) and like-sign (right) background subtraction. Fits are over the mass ranges [2.2,6.0], [1.8,7.0], and [0.5,8.0] both with and without low-mass Gaussians.

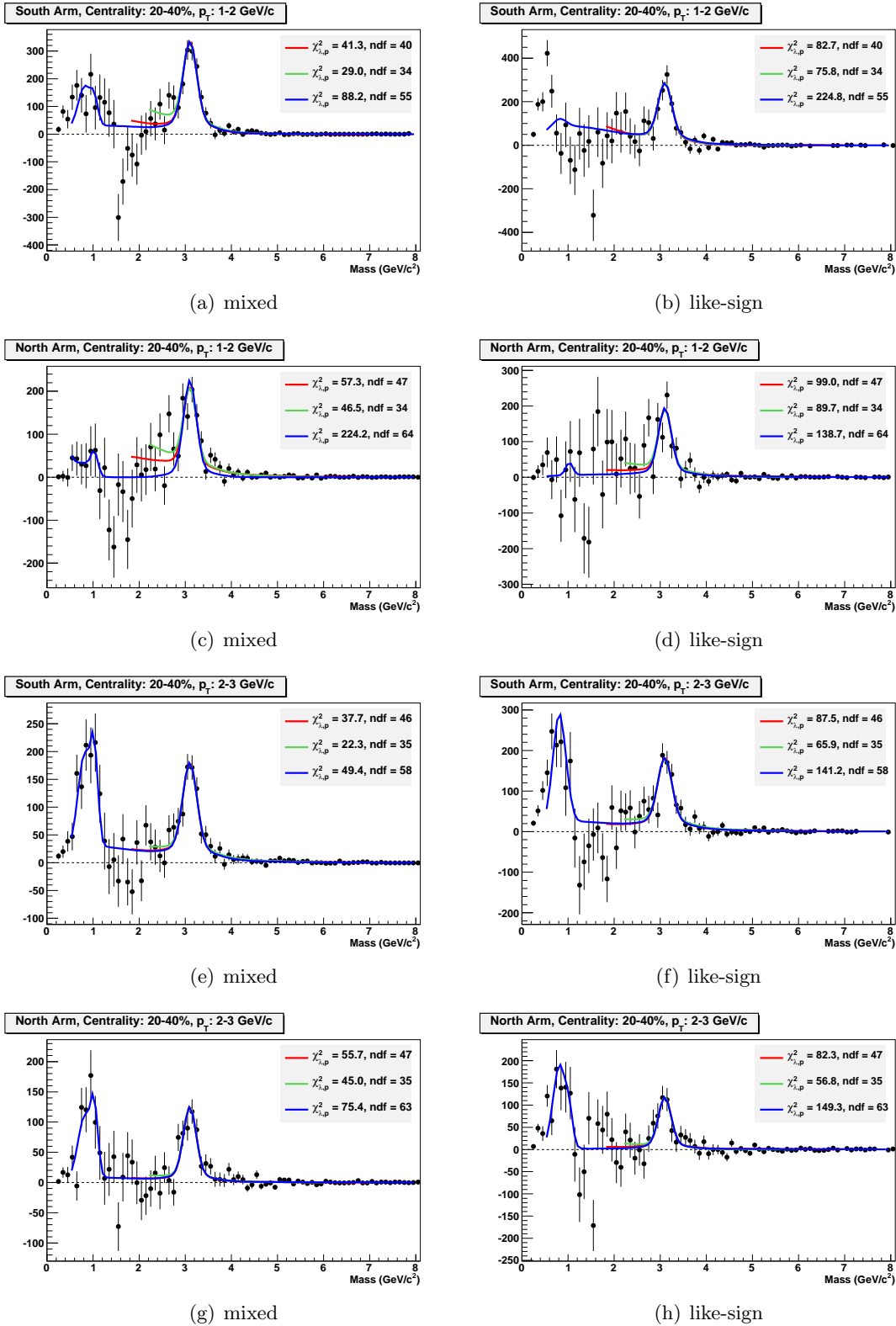


Figure B.18: Dimuon spectra after mixed (left) and like-sign (right) background subtraction. Fits are over the mass ranges [2.2,6.0], [1.8,7.0], and [0.5,8.0] both with and without low-mass Gaussians.

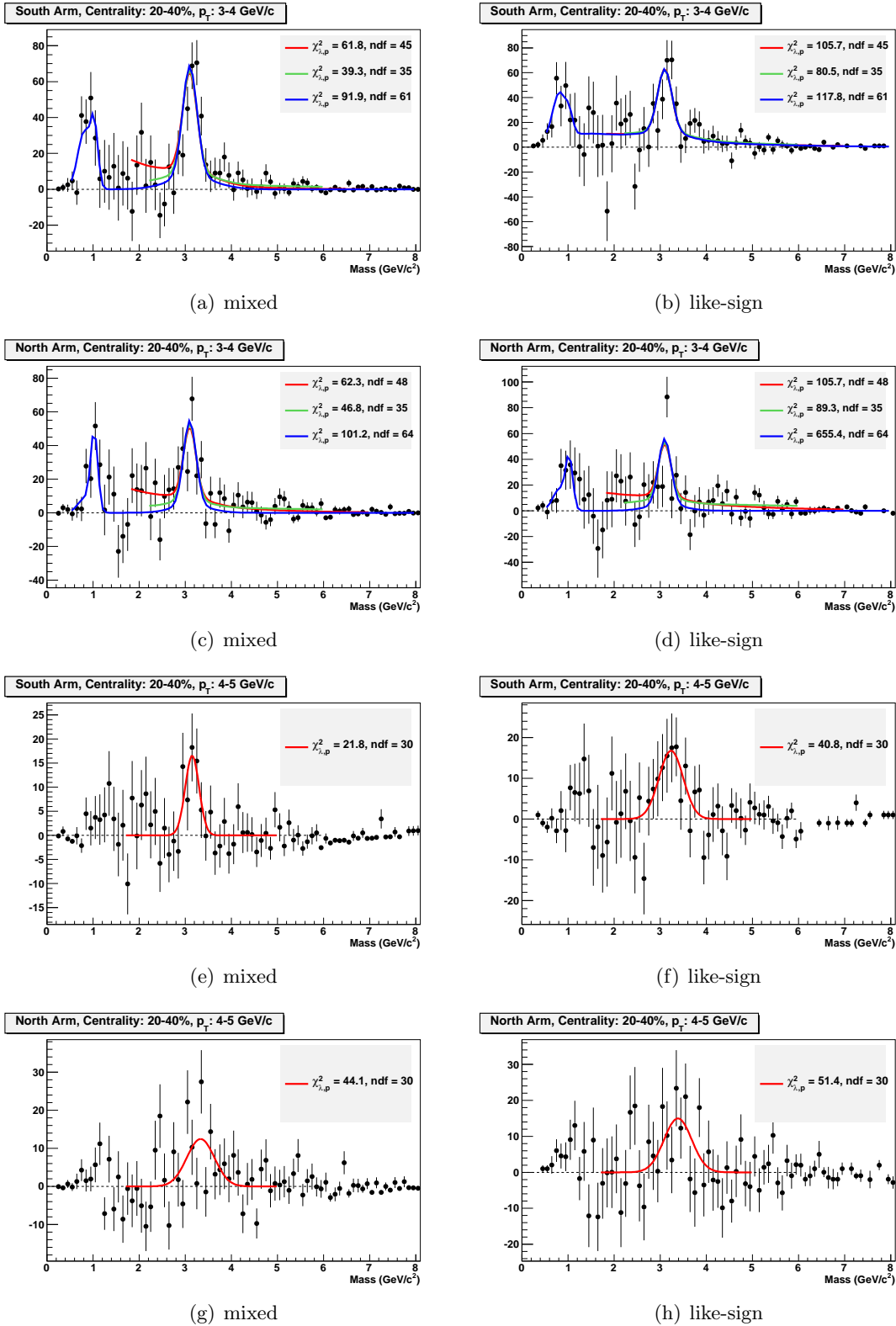


Figure B.19: Dimuon spectra after mixed (left) and like-sign (right) background subtraction. Fits are over the mass ranges [2.2,6.0], [1.8,7.0], and [0.5,8.0] both with and without low-mass Gaussians.

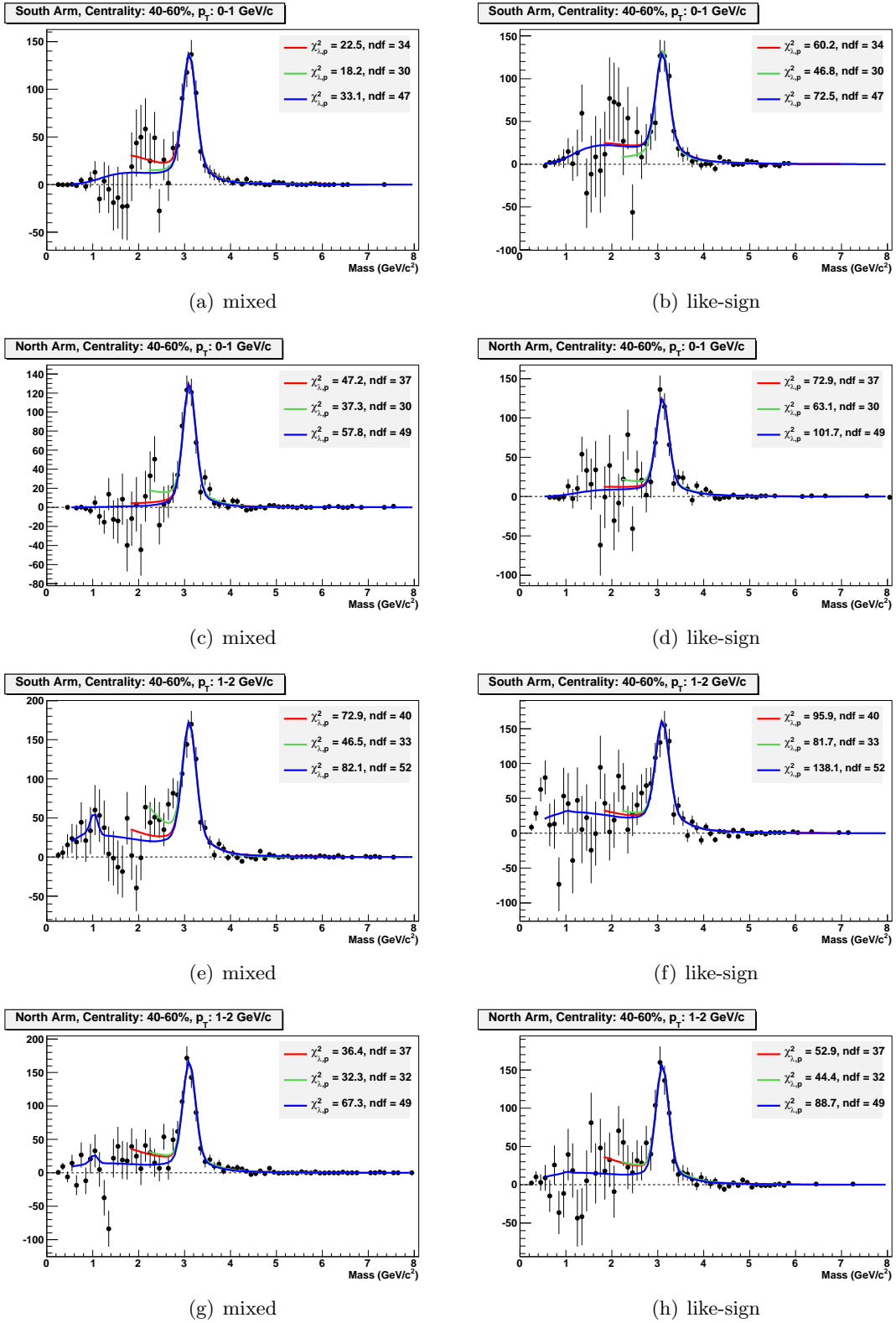


Figure B.20: Dimuon spectra after mixed (left) and like-sign (right) background subtraction. Fits are over the mass ranges [2.2,6.0], [1.8,7.0], and [0.5,8.0] both with and without low-mass Gaussians.

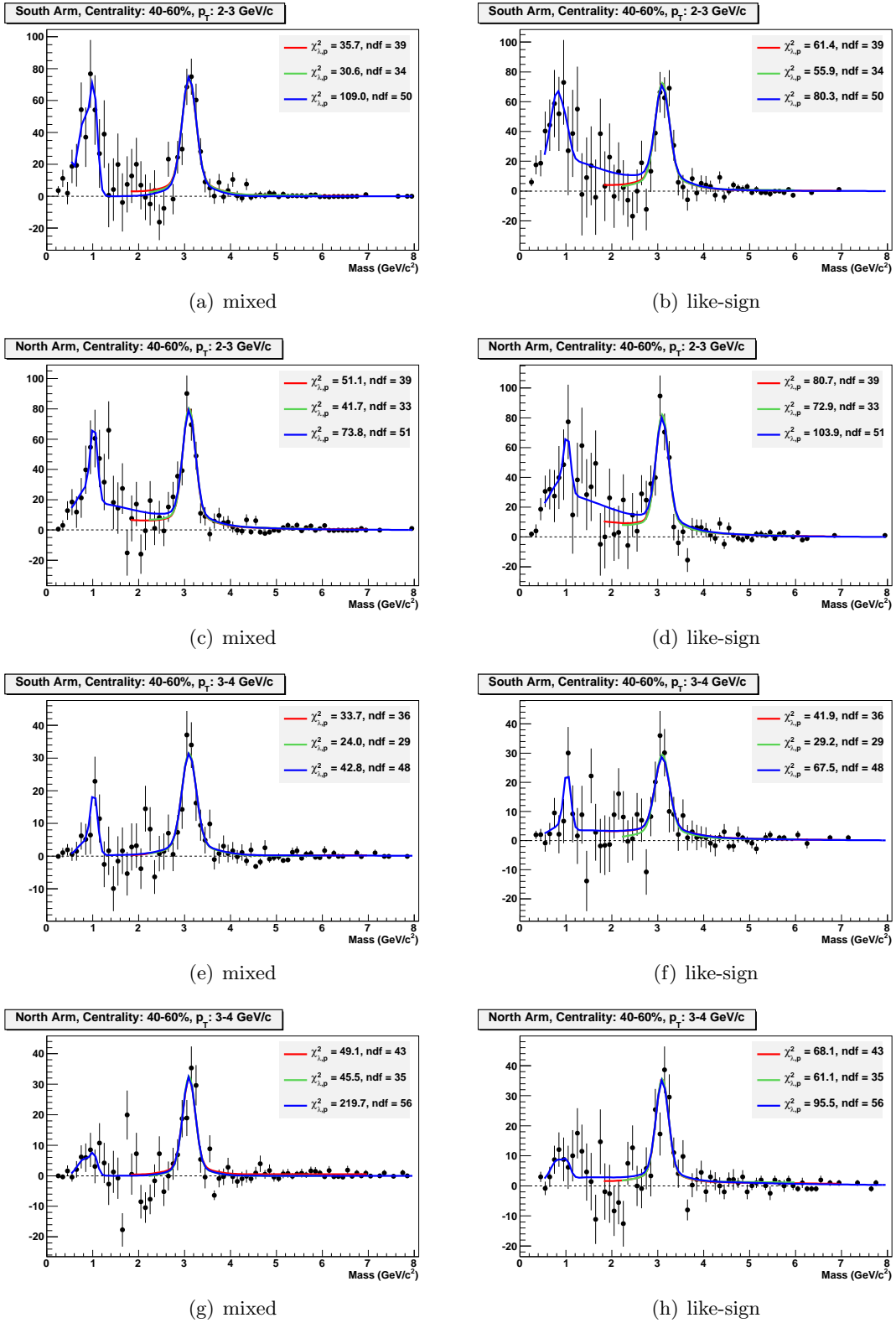


Figure B.21: Dimuon spectra after mixed (left) and like-sign (right) background subtraction. Fits are over the mass ranges [2.2,6.0], [1.8,7.0], and [0.5,8.0] both with and without low-mass Gaussians.

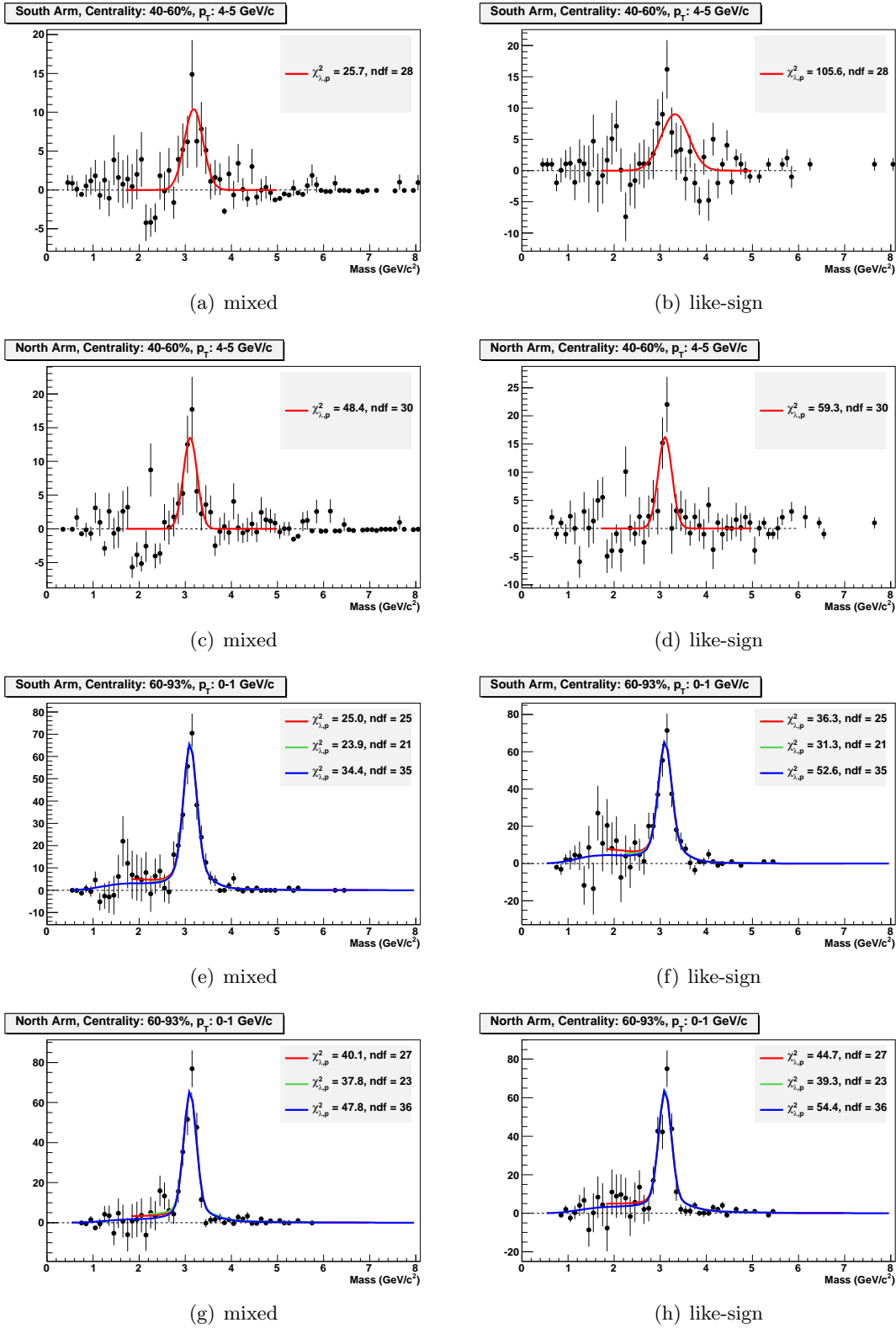


Figure B.22: Dimuon spectra after mixed (left) and like-sign (right) background subtraction. Fits are over the mass ranges [2.2,6.0], [1.8,7.0], and [0.5,8.0] both with and without low-mass Gaussians.

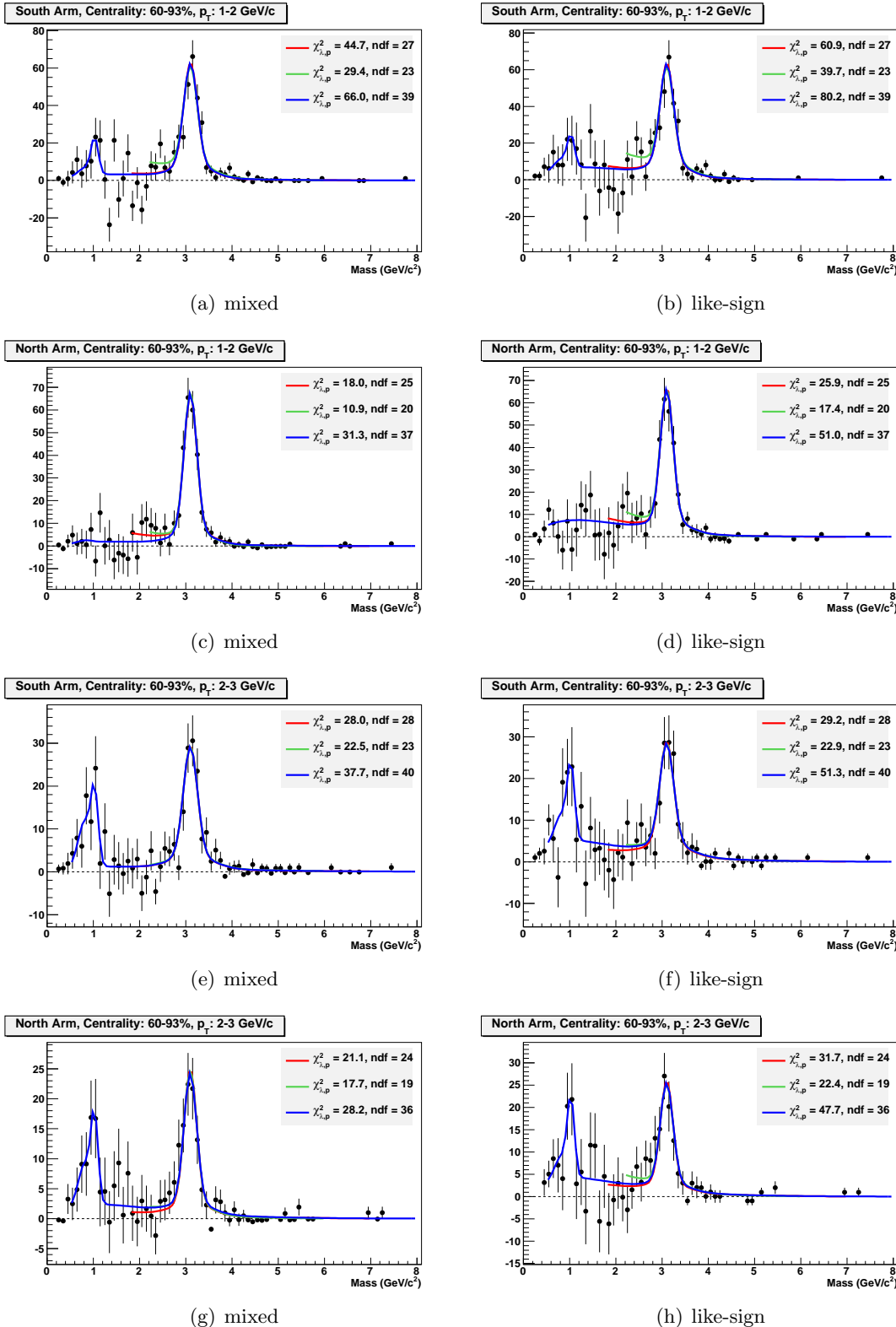


Figure B.23: Dimuon spectra after mixed (left) and like-sign (right) background subtraction. Fits are over the mass ranges [2.2,6.0], [1.8,7.0], and [0.5,8.0] both with and without low-mass Gaussians.

